Development of a novel light-frame wood panelized roof system

by

Md Saiful Islam

A thesis submitted in partial fulfillment of the requirements for the degree of

Doctor of Philosophy

in

Civil (Cross-disciplinary)

Department of Civil and Environmental Engineering
University of Alberta

Abstract

Panelized fabrication of light-frame wood buildings has higher productivity than the traditional stick-built method. However, the roof production process is inefficient due to the structural system and construction method. This research proposes a novel roof system to improve the productivity of the panelized construction process for light-frame wood residential building fabrication. The system includes several roof components, such as ceiling frames, roof panels and support walls designed to comply with structural requirements, manufacturing efficiency, and on-site installation factors. A case study of the gable roof of a two-story building demonstrates the implementation of this system. Ceiling frames can be fabricated using three options in the current offsite setting. Meanwhile, roof panels can be produced in the wall line without altering existing processes. The design requirements for the roof panels were determined based on nail connection tests and finite element analysis. The most critical factor for successfully implementing this panelized roof system is efficient connections. Therefore, self-tapping screws were explored to connect the roof assembly components. An experimental study on timber screw connections was conducted to determine the short-term mechanical performance of five different connection configurations. This data was used to develop a numerical model of the novel roof assembly. The study also invented a novel apex connection to facilitate a folding mechanism in the panelized light-frame wood roof system. Proof of concept of the proposed connection assembly was presented by a 3D printout of the developed connection. Following the steel design and timber codes, the initial estimation of different parameters, such as the pinhole diameter and number of screws, was established. A detailed finite element analysis was performed to determine the connection strength requirement for different load case scenarios. The analysis and 3D printout demonstrated that the proposed connection could provide the required folding mechanism before roof installation and withstand the load in the unfolding state at service. Finally, a three-dimensional finite-element analysis of the proposed light-frame wood panelized gable roof was performed. Macro elements representing the major roof components were developed using analytical models of the diaphragm and shear wall. The most critical load response of the panelized roof was obtained by considering the governing load cases, including the partial load case for snow load. The load path analysis revealed that the panelized roof had a two-way load distribution due to the deep beam action of the support wall. The study also revealed the replicability of this holistic approach to other offsite facilities. A feasibility study shows that this roof system could be a potential solution to building homes offsite for remote locations such as Northern Canada.

Preface

This thesis is an original work by Md Saiful Islam, executed under the supervision of Professor Dr. Ying Hei Chui. The identification and design of the research program were performed independently with the direct supervision of Dr. Chui. Four journal papers and three conference papers related to this thesis have been published or submitted and are listed below. This thesis is organized in paper format by following the paper-based thesis guidelines.

Journal Papers:

1. **Islam M.S.**, Chui, Y.H., Chen Z. (2022) Novel Apex Connection for Light Wood Frame Panelized Roof. Materials. 2022; 15(21):7457.
2. **Islam, M. S.**, Chui, Y. H., Altaf, M. S. (2022) Design and Experimental Analysis of Connections for a Panelized Wood Frame Roof System. Buildings 12(6): 847.
3. **Islam, M. S.**, Chui, Y. H., Altaf, M. S. (2023) Novel Panelized Roof Design for Offsite Fabrication of Light-Frame Wood Residential Homes. (Submitted to a journal and under review)
4. **Islam, M. S.**, Chui, Y. H. (2023) Finite element analysis of a light-frame wood panelized gable roof. (Submitted to a journal and under review)

Conference Papers:

1. **Islam, M.S**.; Chui, Y.H., Al-Hussein, M.; Altaf, M. (2021) A New Panelized Roof Design Approach for Offsite Fabrication of Light-Frame Wood Residential Construction Projects. In Proceedings of the Canadian Society of Civil Engineering Annual Conference May 26-29.

2. **Islam, M.S.**, Chui, Y.H., Altaf, M.S. (2021) A Holistic Design Approach for Innovative Panelized Light-Wood Frame Roof Construction. In Proceedings of the WCTE 2021 - World Conference on Timber Engineering 9-12 August; Chile.
3. **Islam, M.S**., Chui, Y.H. (2023) Numerical Investigation of Timber Screw Connection for Panelized Light Wood Frame Roof. Canadian Society of Civil Engineering Annual Conference May 24-26, 2023.

Acknowledgements

Throughout my Ph.D. study, I have received enormous help and support from different people. Firstly, I would like to express my sincere gratitude to my supervisor Prof. Ying Hei Chui, for his continuous support of my Ph.D. study. His patience, insightful feedback, and immense knowledge of timber engineering pushed me to sharpen my thinking and brought my work to a higher level. Through this journey, I have lost my father and sister. Also, COVID-19 has put tremendous mental pressure. Without Dr. Chui's mental support and patience, it was impossible to overcome these situations. I would like to thank the rest of my advisory committee, Dr. Ahmed Bouferguene and Dr. Yuxiang Chen, for their constructive comments, encouragement, and guidance throughout my research.

I would like to acknowledge the financial support from the Natural Sciences and Engineering Research Council of Canada (NSERC) through the Industrial Research Chair program that was granted to Dr. Ying Hei Chui. I am also grateful to ACQBUILT Inc., Rothoblaas, and Simpson Strong-Tie for providing the materials used in my research.

My sincere gratitude also goes to Dr. Jan Niederwestberg, Dr. Mohammed Sadiq Altaf, Suat Demirer and Dr. Haitao Yu for their continuous advice and feedback on the different phases of research.

Last but not least, I would like to thank my beautiful wife, mother and daughters for their unconditional love, sacrifice and support throughout my PhD study.

Table of Contents

List of Tables

List of Figures

List of Symbols

ν = maximum shear due to specified loads at the top of the wall, N/mm

H_s = height of shearwall segment, mm

E = modulus of elasticity of vertical boundary framing members, N/mm^2

A = cross-sectional area of the boundary member, mm^2

L_s = length of shearwall segment, mm

Bv = shear-through-thickness rigidity of the sheathing, N/mm

e_n = sheathing-to-framing connection deformation, mm

d_a= total vertical elongation of the wall overturning restraint system

d_F = diameter of the sheathing fastener, mm

K_m = service-creep factor

P_{ij} = specified uplift restraint force for storey i at the bottom of the end stud of a shearwall segment j, N

s_n = sheathing fastener spacing along panel edge, mm

L_s = length of shearwall segment, mm

n_u = unit lateral strength resistance per shear plane of sheathing-to-framing connection, N

f_y = yield strength of steel

f_{up}= the ultimate tensile strength of steel pin

$f_{h,1}$ = embedment strength of the head side wood member

$f_{h,2}$ = embedment strength of the point side wood member

$\mathrm{M_y}$ = the yield moment of the screw

$\mathrm{R_{ax,1}}$= withdrawal strength of the screw from the head side wood member

$\mathrm{R_{ax,2}}$= withdrawal strength of the screw from the point side wood member

$\mathrm{s_1}$ = the anchorage length of the screw into the first wood element measured orthogonally to the shear plane

s_2 = the anchorage length of the screw into the second wood element measured orthogonally to the shear plane

d = the effective diameter of the screw

$F_{v,R}$ = the load carrying capacity of timber-to-timber connection with inclined screw

μ = the friction coefficient at the interface between wood elements

PEEQ = the equivalent plastic strain of a material

G = mean realtive density of wood

Chapter 1 : Introduction

1.1 Prefabricated Home Building

Prefabricated home construction adapts traditional construction by integrating manufacturing design and optimization tools to solve complex challenges in construction projects (Qi et al. 2021). In general terms, prefabrication covers several different construction practices: manufactured housing (formerly known as “mobile homes” or “trailers”), modular, panelized, component-based, and hybrids of these different systems (Crosbie 2009). Panelized construction is an offsite method of fabricating homes in which large sections or panels of a building are pre-manufactured in a factory and then transported to the construction site for assembly. These panels include walls and floors in case of a light-frame wood building. This prefabricated home construction has been widely recognized as a promising approach over traditional on-site construction due to the following reasons (Ahn et al. 2019; Ahn 2019; Altaf 2016; Altaf et al. 2018a; b; Li et al. 2014):

a) Reduced construction time: Panelized construction can be completed faster than traditional construction, as the panels are manufactured in a controlled factory environment and then transported to the site for assembly.

b) Lower labour costs: Panelized construction requires less on-site labour, as much of the work is done in the offsite facility. This leads to lower labour costs and a more efficient construction process.

c) Improved quality control: Panelized construction allows for greater precision and quality control, as the panels are fabricated using specialized equipment and tools in a controlled environment.

d) Reduced waste: Panelized construction generates less waste than traditional on-site construction, as the panels are manufactured to precise specifications and material waste is reused or recycled.

The efficiencies mentioned above are obtained through implementing complex manufacturing technology, including CNC machines, advanced sensors such as RFID, and software such as Building Information Modelling (BIM). As can be observed from Figure 1.1, wall production in an offsite facility located in Edmonton, Alberta, Canada, utilizes several workstations. The fabrication of the wall begins by supplying precut lumbers to the framing station (Figure 1.1 b). An operator uses in-feed rollers to insert the top and bottom plates of the wall into the clamp system of the framing table first. Then supplied studs are re-fed into the machine by the operator for nailing. Following this, the machine automatically makes all panel adjustments, including width adjustment and plate tightening, based on the panel design specified in the drawing file loaded into the machine. Once these adjustments are complete, the machine initiates the nailing operation. The finished frame is labelled and transferred to the following table, where a quality check of nailing is performed. In the next phase, workers utilize a vacuum lifter to place sheathing materials onto wall frames and secure them using a nail gun. At this production stage, the multi-function bridge machine automatically performs the nailing operation to attach the sheathing according to the design drawing (Figure 1.1d). Finally, the finished wall panel is flipped vertically using the butterfly table (Figure 1.1c) and transferred to the loading zone or the window/ door installing station. Due to full automation, this wall production process is very efficient such that, on average, 112 m^2 of panel per hour can be manufactured (ACQBUILT Inc. 2019).

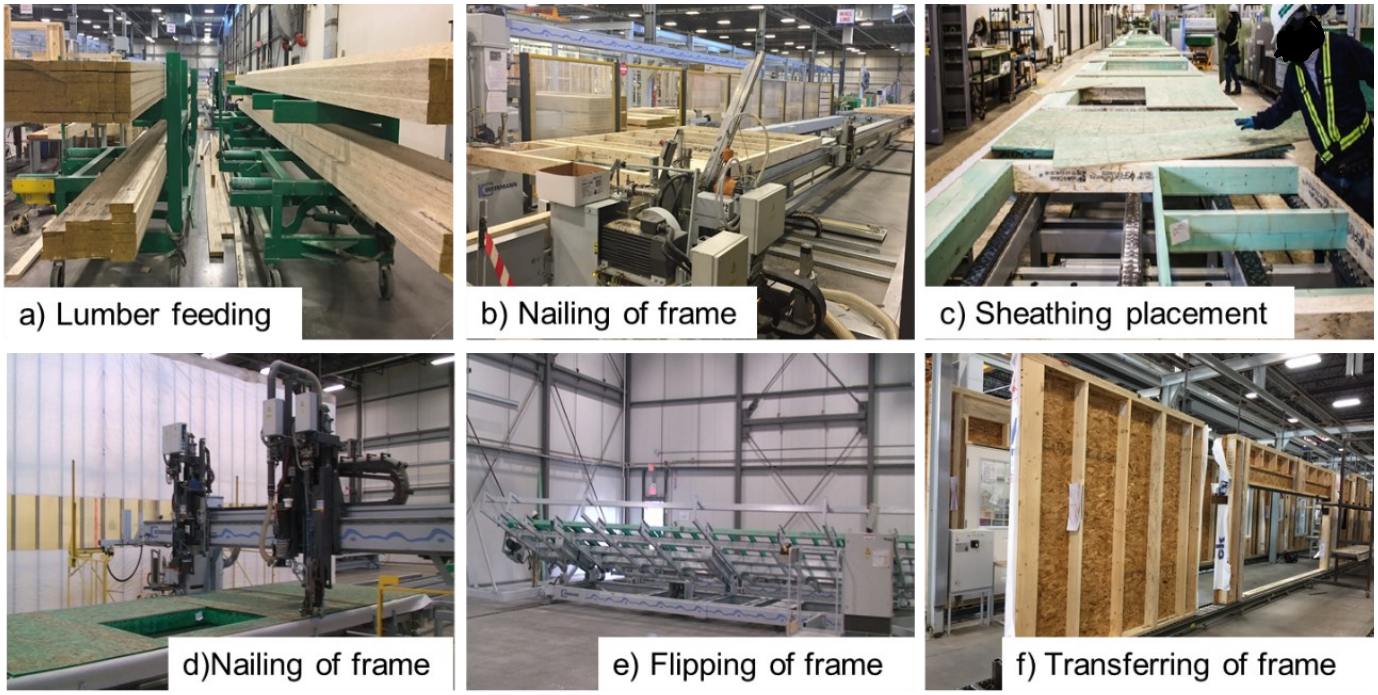

Figure 1.1. Wall production process (source: ACQBUILT Inc. 2019).

The floor production process is illustrated in Figure 1.2. Using a conveyor cart, two workers transfer timber joists from the CNC cutting machine to the pin table (Figure 1.2 a and b). Following this, a worker inspects the panel drawings and layouts of the joists according to the plan (Figure 1.2 c). Then the worker manually connects the joist hangers to the specified joists or joists to the rim boards or beams using a nail gun. Upon completing the floor joist connection, the worker initiates the multi-function bridge machine to apply glue on the joist edges. In the next stage, using a vacuum lifter, a worker transports sheathing to the pin table and positions it onto the floor joist frame as specified by the panel drawings. Finally, the worker again initiates the multi-function bridge machine to perform nailing to connect the sheathing on the floor joist frame. It is evident from the above discussion that the floor line is semi-automated and involves manual activities synchronized with CNC machines. Therefore, it has a relatively low production rate compared to the wall production line (Figure 1.3).

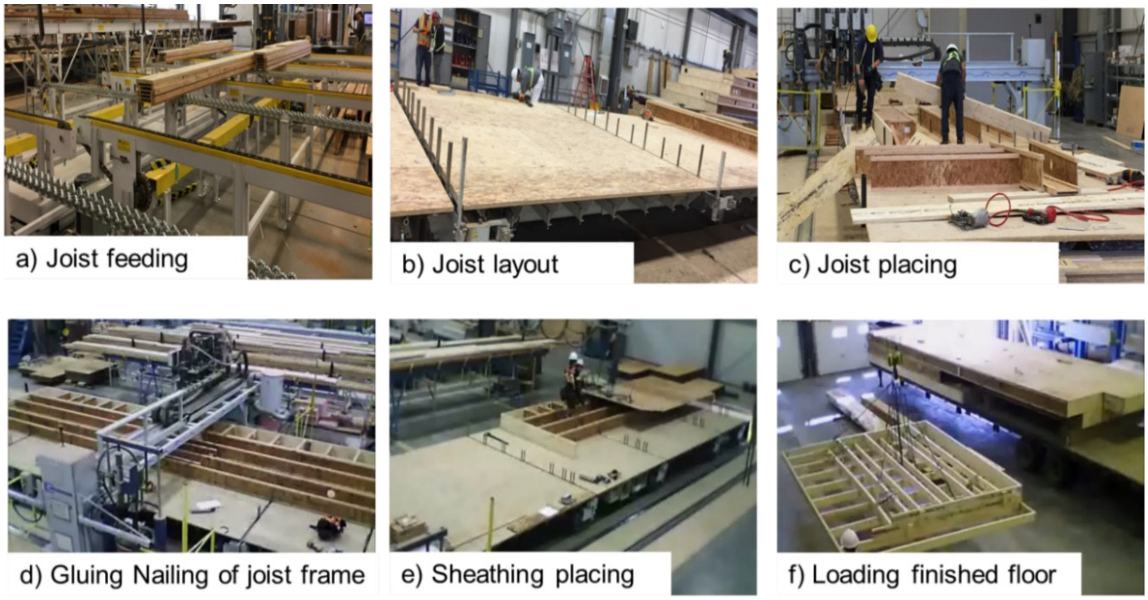

Figure 1.2. Floor line production process (source:ACQBUILT Inc. 2019).

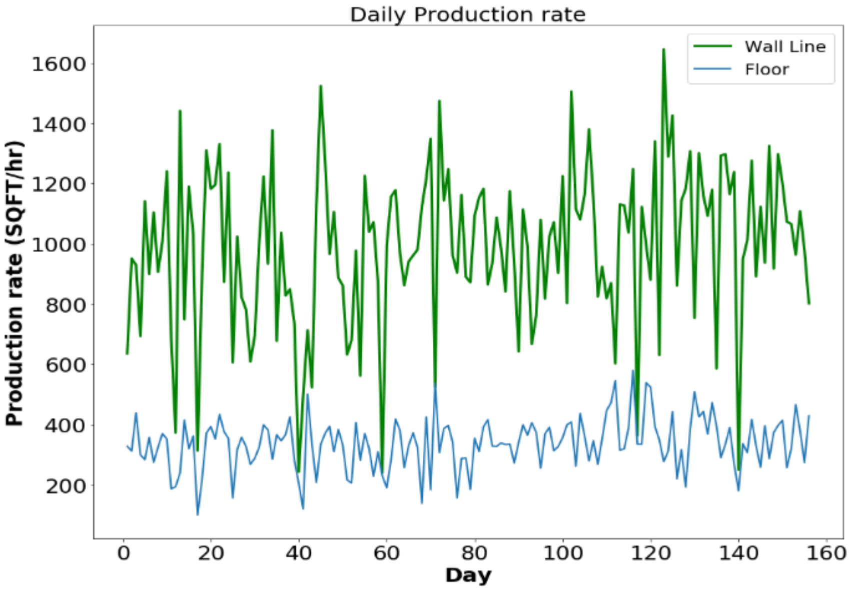

Figure 1.3. Historical production rate of wall and floor line for 156 days (data source: ACQBUILT Inc. 2019).

1.2. Problems in Roof Fabrication in Panelized Construction

Despite high productivity, panelized home fabrication faces a significant drawback in delivering complete buildings due to the roof manufacturing process. Currently, panelized home fabrication employs traditional on-site construction production techniques to build roofs. Figure 1.4 illustrates the current roof production station of the offsite facility in Edmonton, Alberta, Canada. In the current process, a gable roof is subdivided into several small volumetric units to comply with the transportation limitation. Ideally, the roof fabrication process has the same procedure as the traditional stick-framing process. The only difference is that roof modules are built within factory space and transported to the site as several single-piece modules.

Figure 1.4. Roof production station (source: ACQBUILT Inc. 2019).

To begin roof production, a worker initially sets up a roof jig platform according to the dimensions of the second-floor plan in the case of two storey building (Figure 1.5). Then using the overhead crane, two workers unload trusses from the trailer and load them on the roof jig to lay out the individual trusses according to the roof plan (Figure 1.6). In summary, current roof production in the panelized construction method has the following five key steps and involves 19 manual tasks, as illustrated in Figure 1.7 :

1. The roof trusses are designed and fabricated by a truss fabricator.
2. The roof trusses are shipped to the panelized production facility.
3. Trusses are unloaded and transferred to the designated roof production workspace, where they are laid out according to the plan.
4. Wood-based sheathing panels and blocking are attached to the trusses using fasteners to form a roof module.
5. Roof finishing is added to the completed module.

Figure 1.5. Roof jig platform (source: ACQBUILT Inc. 2019).

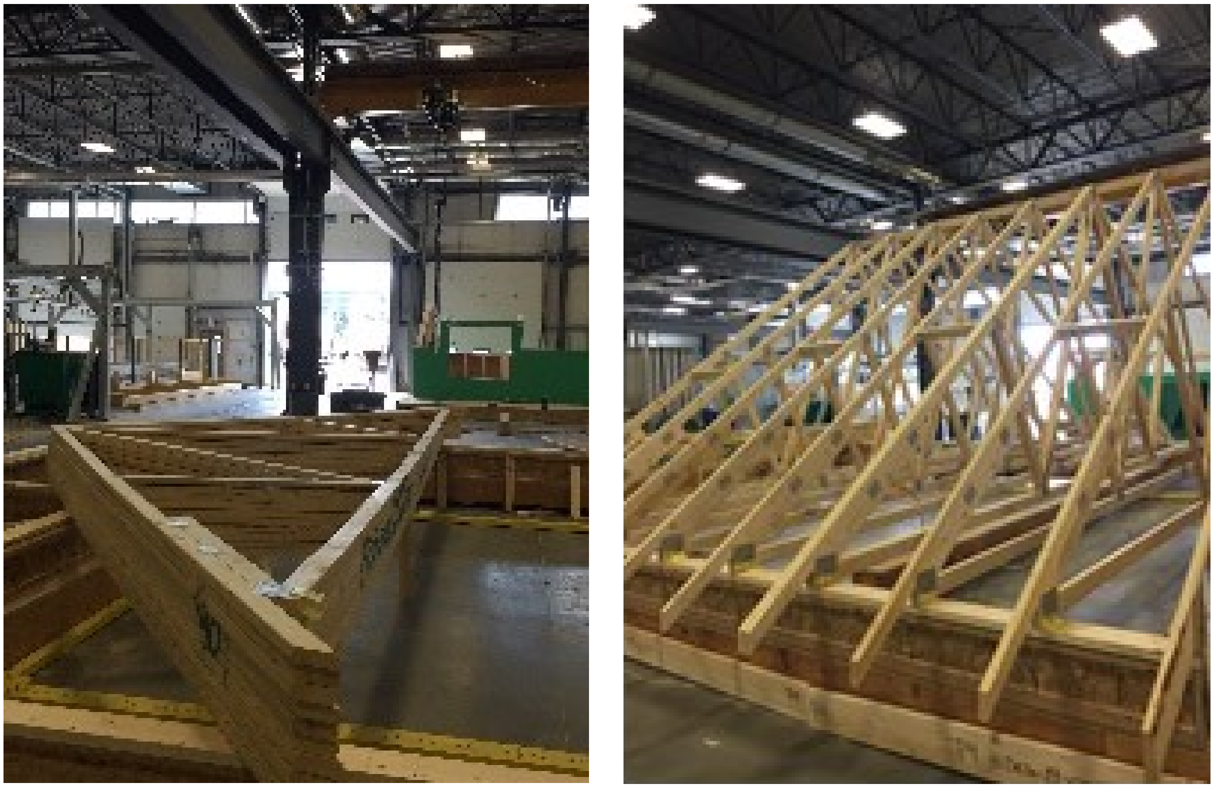

(a) (b)

Figure 1.6. (a) Unloading and (b) Loading of Truss (source: ACQBUILT Inc. 2019).

Producing roof structures in this manner entails the following deficiencies that can be addressed through innovation:

a) From a production management viewpoint, loading and unloading trusses are regarded as non-value-added activities. This led to a relatively long setup time in the roof production jig.

b) If the production flow rate of other workstations, such as wall or floor lines, is taken into account, then the manual (stick-built) approach employed for roof fabrication results in an imbalance of the overall production of the complete building.

c) Transporting the complete roof requires a relatively large number of trailers (according to the local manufacturer in Alberta, four trailers for a 149 m^2 single-family home), and on-site loading and unloading increases the overall work duration, leading to high transportation costs (Altaf et al. 2018b). Therefore, this fabrication process is not viable for building home offsite for remote project locations.

d) The site installation process is complex due to the size of the roof modules. In the case of very congested construction sites, it becomes impossible to transport large roof modules. Consequently, the roof must be built entirely at the site (similar to the traditional stick-built process), increasing project cost and duration. Thus, the offsite construction goal still needs to be achieved.

e) Considerable space is occupied in the factory while producing the roof module, again making it difficult to balance wall and floor panel production with roof fabrication for a given number of homes.

f) The additional cost of sub-contracting the roof trusses to the truss manufacturer raises the price of a home package.

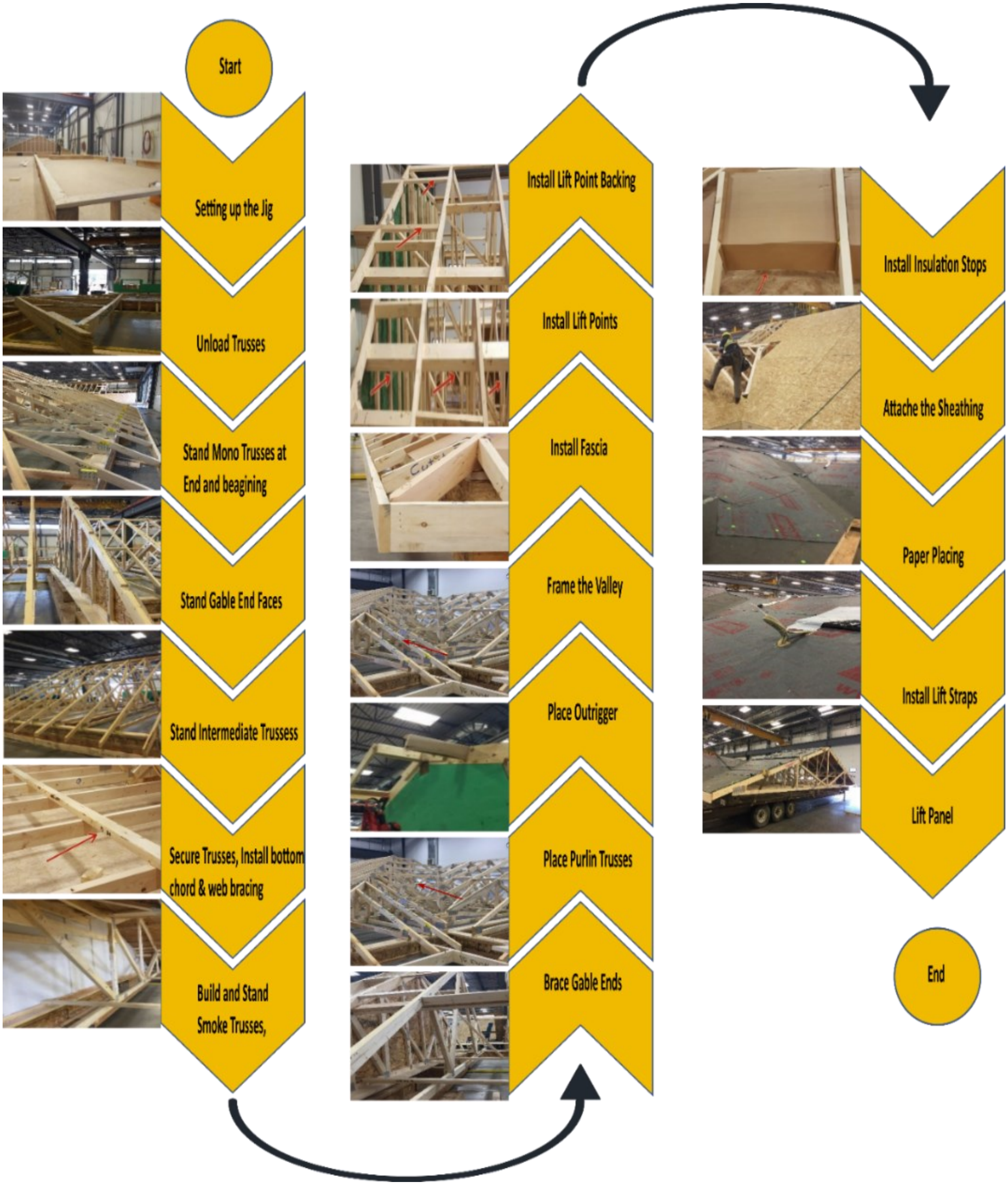

Figure 1.7. Current roof production process.

1.3. Novel Solution for Roof Fabrication in Panelized Construction

It is evident from the above discussion that the roof production process faces a significant challenge in improving productivity. The primary constraint is the structural system of the roof. As can be observed from Figure 1.5, the gable roof is built using closely spaced wood trusses that support sheathing and roofing materials (on the upper chord) and ceiling materials (on the lower chord). These trusses are arranged at a spacing of 610 mm or less. The lateral bracing of such a wood roof truss system is provided by wood-based sheathing panels, thereby achieving a highly efficient structural design. However, this system prevents the current partial panelized construction toward a fully panelized system. Producing several roof modules fails to fully capitalize on the advantages of prefabricated construction, which include increased productivity, reduced costs, and minimized waste (Altaf et al. 2018b). Therefore, a novel type of structural system is required to improve roof manufacturing efficiency. The novel structural system of the roof will allow home manufacturers to produce the roof components in-house using the existing production facility, thus overcoming the challenges mentioned earlier and facilitating complete panelized construction.

A fully panelized building package would lead to improving the overall construction process due to the following factors: a) reduced transportation cost; (b) complete utilization of the existing wall and floor panel assembly lines, thereby reducing idle times. However, further research is required to engineer this new roof system to maximize its potential and to ensure that the new system meets the building code requirements as it would deviate from the traditional construction method, which is recognized by the national and provincial building codes due to its long history of providing safe and affordable housing for Canadians.

The review of previous studies on roof panelization reveals a noticeable gap in the design of panelized gable roofs, particularly in the context of manufacturing building components in offsite facilities (see section 1.5 for details of literature review). In order to address the challenges associated with roof fabrication for the industrialized production of homes, this thesis presents a comprehensive approach to designing panelized gable roofs that considers manufacturing, site installation, and transportation aspects of structural design. To ensure the structural integrity of the panelized gable roof system, it is crucial to develop effective connection mechanisms. Therefore, this study introduces innovative connections that facilitate convenient onsite installation and transportation of roof components. A noteworthy contribution of this thesis is the introduction of a novel folding apex connection concept, which holds significant scientific value in the realm of light-frame timber structure design. Furthermore, this research includes numerical analysis of the assembly of panelized gable roof systems, providing valuable insights into the behaviour of such constructions in North America. These findings significantly contribute to the body of knowledge on the analysis of light-frame wood structures.

1.4. Research Objectives

The main objective of this study is to develop a panelized gable roof system that uses a holistic approach to design light frame timber roofs for residential building manufacturing in North America. To achieve this goal, several specific objectives are addressed in this thesis. The first objective is to develop a detailed analysis of the current panelized home manufacturing system and find the possible option to incorporate the roof component fabrication using automated or semi-automated production lines. Analyzing the current production system provides the basic input parameters that must be accounted for to move forward in developing the novel roof design process.

The second objective is roof component design, such as roof panel and ceiling frames and manufacturing process identification aligned with the panelized home fabricator facility assembly lines. The input parameter includes different types of engineered timber products, nail connection test, the roof panel diaphragm, ceiling frame, gable wall and support wall analysis.

The third objective of this work is to develop an efficient connection system for a novel roof system. The specific connection design requirement includes the location, such as eave line, panel to panel, roof panel to support wall and apex connection. Experimental evaluation of individual connection configuration would provide the design requirement in all possible load cases.

The final objective of the study is to develop a finite element model of the case study gable roof to evaluate the system performance of the novel roof system under different load cases.

1.5. Review of the Early Development of Panelized Roof

The roof penalization concept originated in the 1980s. With the evolution of factory-based or off-site construction of buildings, research was motivated by the potential benefits of the panelized roof, including higher energy savings, utilization of attic space, improved quality, and reduction in manufacturing costs associated with off-site fabrication (Briscoe et al. 2011; Mullens and Arif 2006; Nahmens and Reichel 2013). However, roof penalization poses unique structural challenges (Briscoe et al. 2011). A thorough review of the literature shows that the most of roof panels developed in the past are structurally insulated panels (SIP) and can be classified into two types: a) panels with foam core and b) panels with web core. Although this study seeks to develop a panelized roof that can serve as similar to a truss-based system, a review of the SIP roof panel system provides the basis to conceptualize the factors involved in the structural design of current research. The two types of SIP comprised two face sheets, but in the case of the web-core roof panel design, lumber webs are added to connect the two faces (Briscoe et al. 2011; Crowley et al.

1993; Fam and Sharaf 2010; Sharaf and Fam 2011). It is possible to design roof panels that can sustain all structural loads for an unsupported span by themselves and eliminate the need for a truss or rafter (Dentz 1991).

Kucirka (1989) introduced three types of the structural system for the SIP panelized roof (Figure 1.8): (a) Folded plate roof panels spanning between the end gable walls; (b) Roof panels spanning between the longitudinal wall and the ridge beam; (c) Roof panels connected to the floor unit which acts as a tie to resist lateral force.

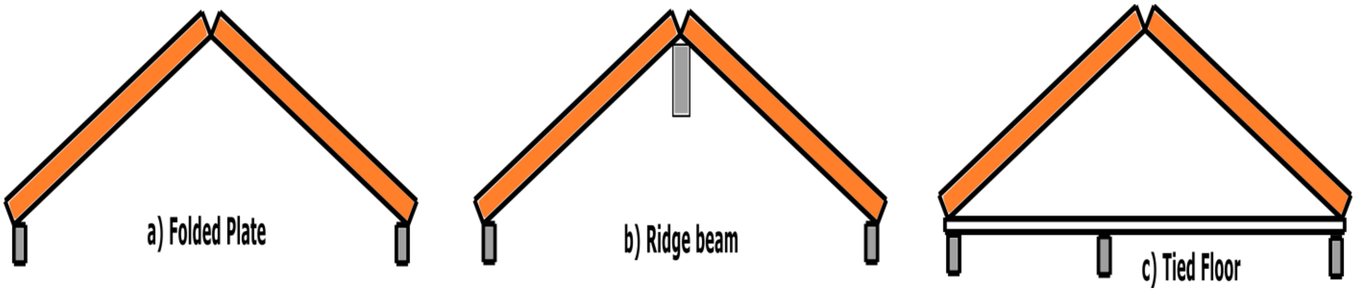

Figure 1.8. Three types of structural system for roof panels (Kucirka 1989).

In a folded plate system, two panels in a single bay gable roof perform as an inverted 'V' to transfer the vertical load to end supports at the gables, eliminating any truss or ridge beam requirement. The gravity load path of this system is illustrated in Figure 1.9. Loads normal to the roof surface are carried to the fold, eave and gable lines by the bending action of the panel face and the shear capacity of the core material. In contrast, in-plane loads are transferred through the "plate" action analogy of adjacent panels (Figure 1.9a). The uniform projected load, as shown in Figure 1.9b, is distributed to the eave and fold line supports by the "slab" action of the planner element (Kucirka 1989). The eave line load is ultimately transferred to the load-bearing wall. Kucirka (1989) assumed a perfect pin connection design at the apex of this system.

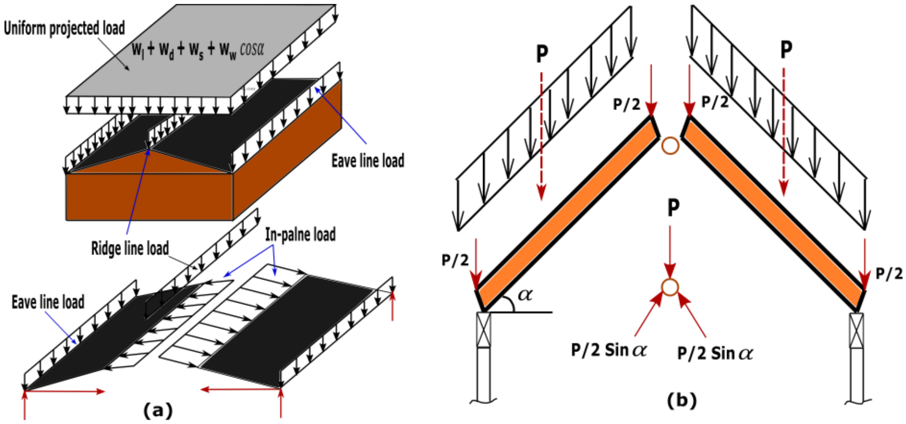

Figure 1.9. Folded plate roof system idealization (a) In-plane and out-of-plane load distribution of roof panel (b) gravity load path of the system.

Therefore, at the apex, the load is resisted by force developed in the plane of the roof panel, as indicated in Figure 1.9b. Hence, Kucirka (1989) applied simply supported deep girder beam analogy to analyze the roof panel system. In the case of the ridge beam system, the roof panel is supported by a framing element at the fold line, and the reaction at the peak of the roof is transferred to the gable end by the one-way beam action of the panel itself. The sustained lateral load on the ridge beam system is solved by the diaphragm action of the roof. The tied-floor system incorporates a horizontal diaphragm unit in the roof cavity. The in-plane load of this system is the same as the folded-plate system, except the load resistance is provided through the truss analogy (Kucirka 1989).

Dentz (1991) developed a panelized system for a complicated residential roof shape incorporating a gable, turn gable, and hip end. The roof panels were designed to sustain load without truss or rafter framing. A beam was used at the ridge that divides the roof structure into two simple spans between the eave and ridge of the roof to carry vertical loads to gable ends and supporting walls (Figure 1.10). As a result, the roof panels spanned between the ridge to the eave, transferring self-weight and snow load through one-way bending action. Horizontal wind and seismic loads are resisted by the diaphragm action of the roof panel. The study considered the manufacturing, in-plant handling, and transportation constraints for fabricating the roof panels, which only led to the production of 4 feet wide panels.

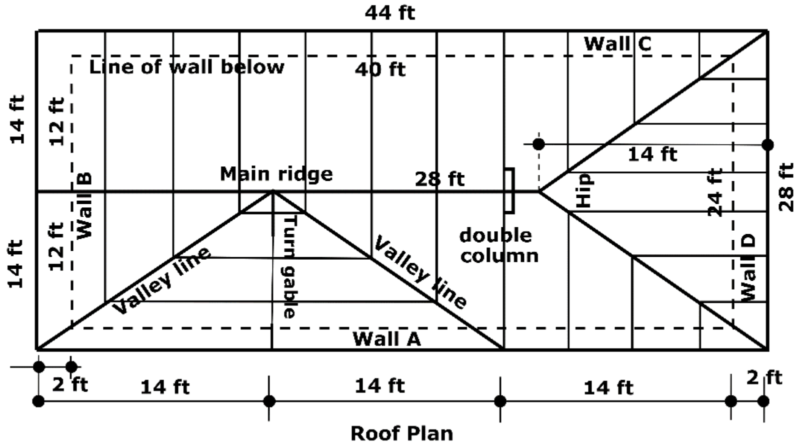

Figure 1.10. Panelized roof by Dentz (1991)

As a result, many panel-to-panel connections were required for a case study roof plan (13.4 m × 8.5 m). Dentz (1991) stated that the panel-to-panel joint was the most critical and structurally challenging because of the out-of-plane shear force in addition to in-plane shear, tension, and compression. This out-of-panel shear originates due to the differential deflection of panels. Differential deflection is the effect of different spans of adjacent panels or asymmetrical loading due to live load on the roof or snow melting unevenly.

As shown in Figure 1.11, Dentz (1991) designed a tapered spline panel-to-panel connection to join the adjacent panels using a bevelled spline element and 1-inch drywall screws. From a constructability point of view, this type of connection increases the on-site activity duration and becomes less productive. This type of panelized roof can be an excellent replacement for traditional rafter-based cathedral attic roof construction. However, self-supporting panel design brings challenges with respect to structural stability to withstand roof loads, the adaptation to fit the home architecture and cost competitiveness with the traditional rafter/truss-based system (Thomas et al. 2006). For a simply supported roof panel (SIP), the maximum deflection due to bending at the midpoint is directly proportional to the quadratic power of the roof span (Zenkert 1997). As a consequence, the panel depth increases with a longer span. For example, a case study by Thomas et al. (2006) shows that 9.0 m long roof span panels required a total depth of 350 mm, whereas traditional cathedral ceiling design is possible with 38 x 292 mm rafter and 16 mm thick OSB for the same span to support 3.9 kPa gravity load.

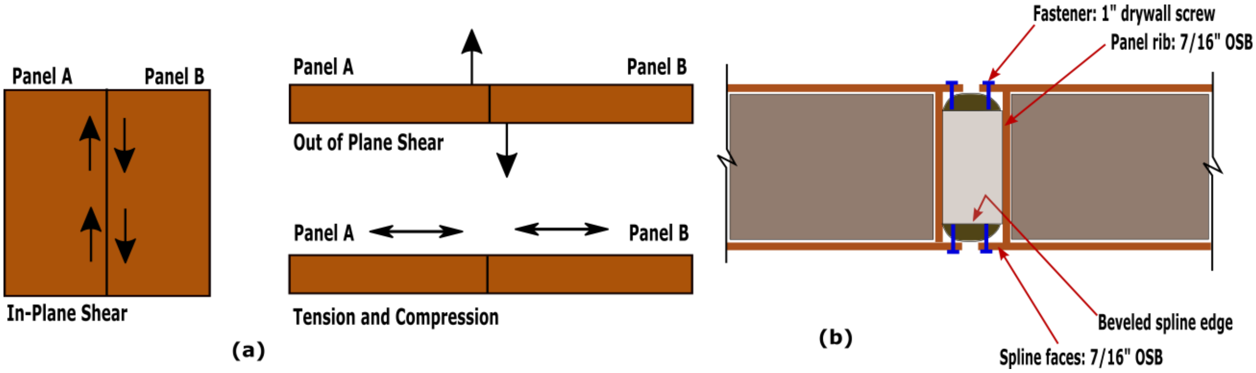

Figure 1.11. Structural requirements of the panel-to-panel joint (Dentz 1991)

A recent study by Altaf et al. (2018b) experimented with a gable roof penalization approach using girder trusses. Figure 1.12 illustrates the panelized roof concept introduced in Altaf et al. (2018b). For a case study home with an 11 m × 6.1 m roof footprint, two roof panels (9.8 m × 3.4 m) were fabricated manually in the roof-built sections of the offsite facility in Edmonton, Alberta. Six girder trusses were used to support the two roof panels. Four ceiling frames (5 m × 3.4 m) were fabricated in the wall line to accommodate the drywall.

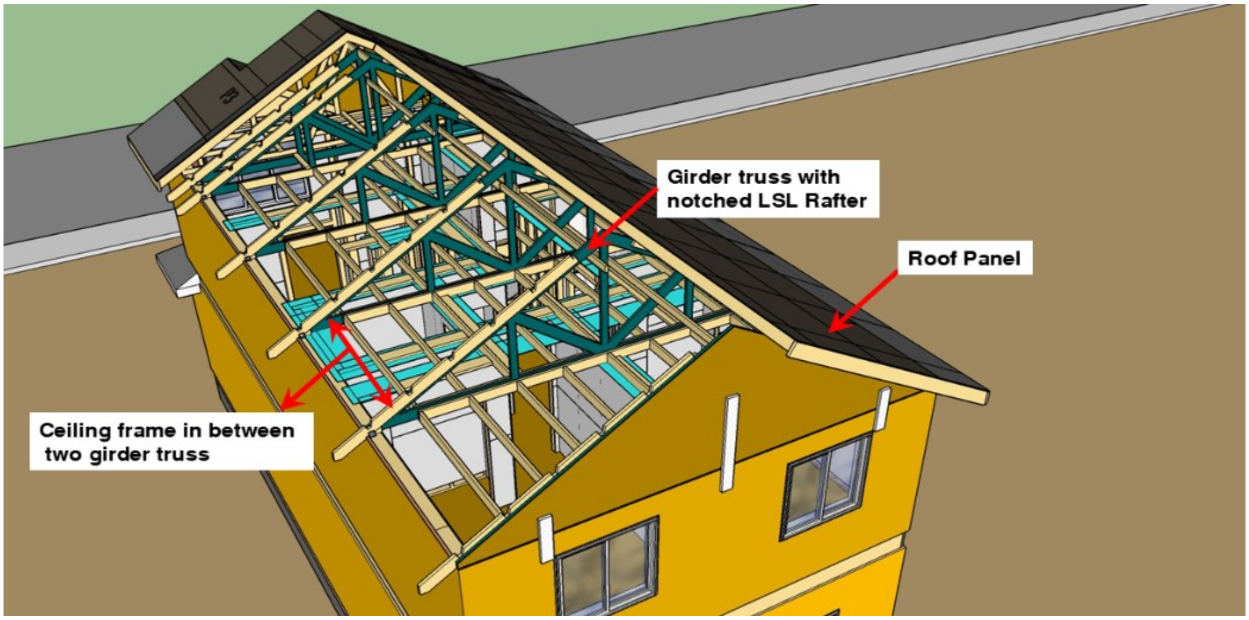

Figure 1.12. Panelized roof design with howe type girder truss and ceiling frame (Altaf et al. 2018b).

Most roof components were fabricated using manual labour except for the ceiling frames. To produce roof panels, some materials cut was performed at the wall line, so two factory stations have to synchronize for the production. Overall, framing operations took 45.5 manhours which is 20 additional manhours compared to regular framing work (ACQBUILT Inc. 2019). The panel design is the main reason for the higher manhour requirement. As can be observed from Figure 1.13, the rafters of the roof panel run in the longer direction of the house and are supported by the girder truss using notched 38 mm × 140 mm LSL. The blocking of the panel framing was provided in a staggered pattern. This type of construction characteristic requires extra work hours. Due to the 3.4 m width of the panel, fabrication was not possible in the wall line.

Notching on 12 LSL rafters was created using the CNC machine in the stair production line and then transferred to the roof sections for attaching them to the girder trusses by nailing. Consequently, the CNC machine was overloaded, and extra notching slowed down the other productions, i.e. stairs and balcony (ACQBUILT Inc. 2019). Figure 1.14 shows the onsite construction sequence for this panelized roof. Since this roof system had several components, the crane lifting number was higher than the volumetric roof unit approach.

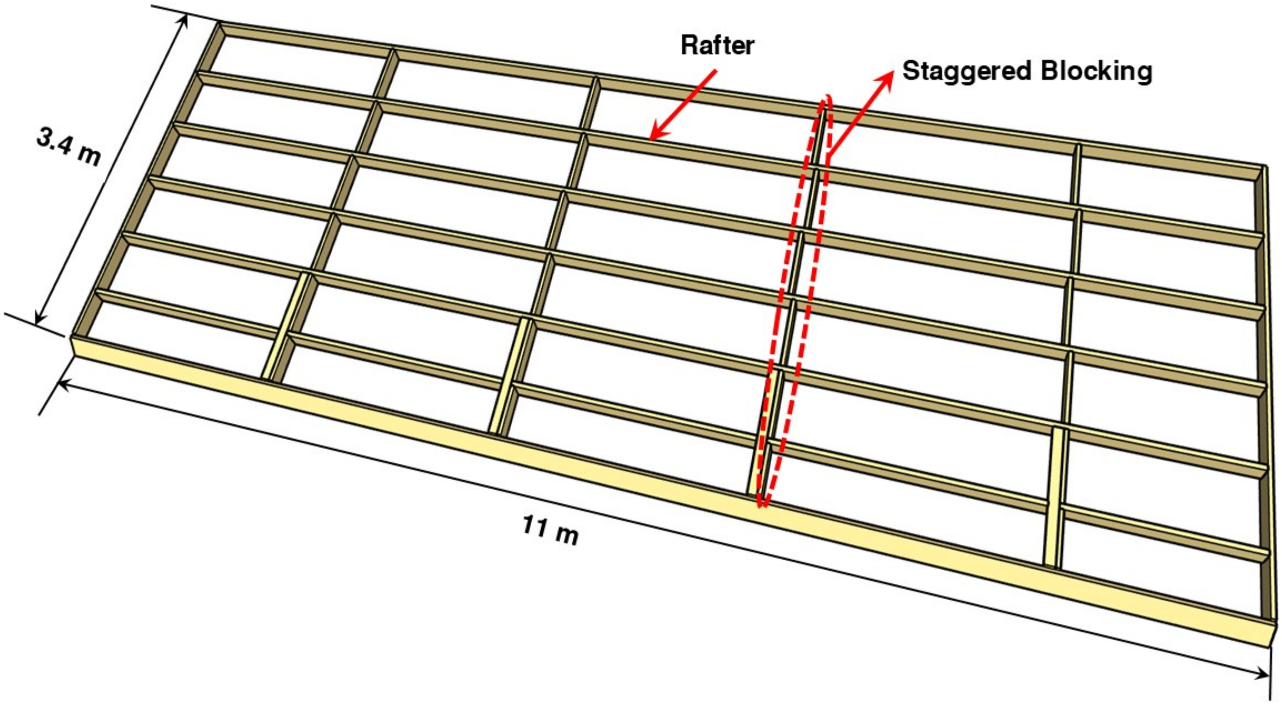

Figure 1.13. Roof panel framing (Altaf et al. 2018b).

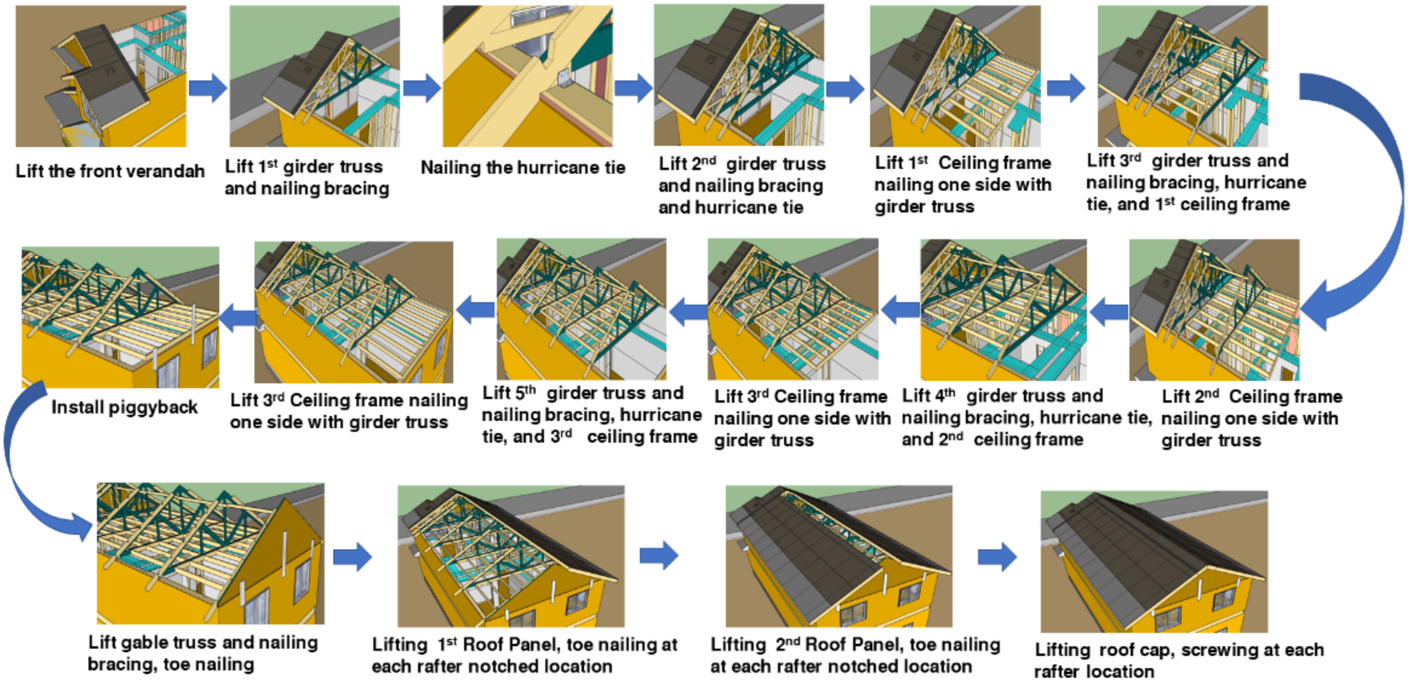

Figure 1.14. Onsite works contributed to higher installation time (Altaf et al. 2018b).

Additionally, the roof panel rafters required toenail with the notched LSL pre-attached to the girder truss at each notched cavity. This connection installation activity required workers to climb on the ceiling frame and involved extra effort. Each girder truss had to connect to the load-bearing wall using steel angle plates to sustain the wind uplift. The individual ceiling frame end was nailed to the bottom chord of the truss. Hence, higher connection installation works resulted in increased site installation time. It is evident from the above discussion that this type of panelized roof used extra timber material than traditional truss built. Because of the manual production of most of the components, the manufacturing plant did not save any manhours. The onsite installation was complex and time-consuming because of too many nailing works and the higher number of crane lifting. Since on-site labour is more expensive than plant labour, site installation of this type of construction added additional costs. As a result, the cost of this production could not compete with the existing truss-built approach.

1.6. Structure of the Thesis

This thesis is organized into the following chapters: Chapter 1 (Introduction), Chapter 2 (Novel Panelized Roof Elements), Chapter 3 (Screw Connection Design and Analysis), Chapter 4 (Novel Apex Connection Design), Chapter 5 (System Behaviour of Panelized Roof), Chapter 6 (Fabrication, Onsite Installation, and Replicability of the System), Chapter 7 (Conclusion and Future Works).

The introduction chapter (Chapter 1) describes the background, current issues in roof fabrication, and previous attempts to solve roof fabrication in panelized form and defines the objective of the study. Chapter 2 provides an overview of a holistic approach to designing a panelized gable roof primary components. Chapter 3 introduces screw connection design and analysis for the proposed panelized roof. This chapter was published in the Buildings journal.

Chapter 4 presents a novel apex connection system for the proposed panelized roof that facilitates easy transportation and onsite installation of roof panels. This chapter was published in the Materials journal. Chapter 5 presents the finite element analysis of the light frame panelized gable roof to understand the system behaviour and connection design requirement for the complete roof assembly. Chapter 6 presents how the panelized roof components can be fabricated in an existing automated and semi-automated production line of an offsite facility, onsite installation consideration for this roof, and replicability of the holistic approach in another type of offsite facilities, such as the robotic arms system.

Finally, Chapter 7 summarizes the outcomes of the study and potential contributions to the body of knowledge and limitations. Moreover, future research directions in panelized roof construction are also suggested.

Chapter 2 : Panelized Gable Roof

This chapter summarizes the overall concept of the panelized gable roof, different aspects of producing roof components in an offsite facility, ceiling frame analysis, nail connection test and roof panel design and analysis. This chapter is based on a paper submitted to a peer-reviewed journal and a published conference paper Islam et al. (2022a).

Novel Panelized Roof Design for Offsite Fabrication of Light-Frame Wood Residential Homes

Md Saiful Islam [1,3], Ying Hei Chui [1] and Mohammed Sadiq Altaf [2]
Dept. of Civil and Environmental Engineering, University of Alberta, Canada;
ACQBUILT Inc., 4303 55 Ave NW, Edmonton, AB T6B 3S8, Canada
*Correspondence: mdaiful@ualberta.ca

Abstract: Panelized fabrication of light-frame wood buildings has higher productivity than the traditional stick-built method. However, the roof production process is inefficient due to the structural system and construction method. This study proposes a novel roof system to improve the productivity of the panelized construction process for light-frame wood residential building fabrication. This unique system uses a holistic approach to design several roof components considering structural requirements, manufacturing efficiency, and on-site installation factors. This chapter presents a case study of the gable roof of a two-storey building to demonstrate the implementation of this novel system. The two main components of the novel roof system are the ceiling frame and roof panels. Ceiling frame analysis shows three different fabrication options are possible in the current offsite setting. Twenty-four nail connection specimens were tested under shear and uplift loading to determine the load-slip response of nail connections used in structural composite wood such as OSB and LSL. The roof panel design requirement was determined based on the nail connection test and finite element analysis. The results show that ceiling frames for a gable-type roof can be produced economically using a floor panel production line, whereas roof panel fabrication is possible using the current wall panel production line.

Keywords: finite element analysis; roof panel; ceiling frame; wall line; floor line; nail connection test.

2.1. Introduction

Off-site construction is a manufacturing process where building components, elements, or modules are pre-assembled in a controlled plant environment and subsequently transported to the construction site for installation (Goodier and Gibb 2007). This process reduces project duration, reworks, safety risks, life cycle costs, and adverse environmental effects. At the same time, it improves predictability, productivity, life-cycle performance, sustainability, and profitability (Goodier and Gibb 2007; Pan and Goodier 2012). By relocating approximately 80% of the building construction activity from the original location, significant site disruption and vehicular traffic are reduced, which increases overall safety and security from the owner's perspective (MBI 2015). The panelized construction process is popular among the several off-site construction approaches because of its design flexibility and associated on-site assembly cost savings. Panelized construction subdivides a building model into subassemblies such as wall panels, floor panels, and volumetric roof elements. These components are manufactured in an off-site facility and then shipped to the site for installation. In Canada, all offsite building manufacturers implement automated and semi-automated manufacturing processes (Koo et al. 2020). The manufacturing process uses several workstations, such as the wall line, floor line, and jig platform for roof assembly (Figure 2.1).

In the production phase, building components travel through several stages. For example, to fabricate a wall panel, the first step is feeding precut timber studs and plates to the framing station (Figure 2.2a), then they travel towards the sheathing station (Figure 2.2c), where wood sheathing panels are attached to the wall frame. These production stations have some dimensional limitations. For instance, an Alberta-based panelized home manufacturer's wall framing station can produce wall frames with a maximum height of 3.2 m, whereas for floor production lines, the maximum framing height is 12.2 m (Figure 2.2) (ACQBUILT Inc. 2019). So, the abovementioned constraints must be considered to produce building components using these production lines.

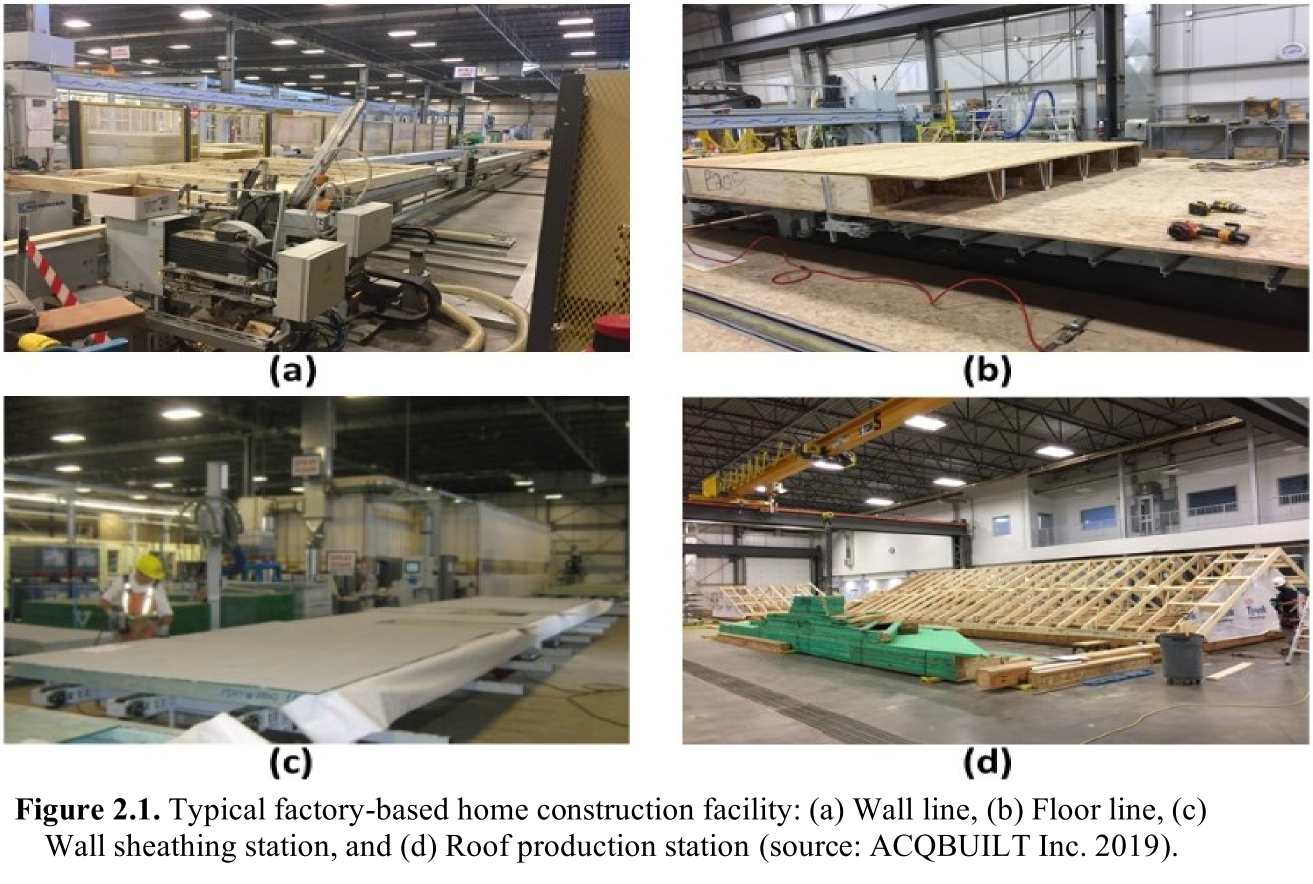
(a)
(b)
(c)
(d)

Figure 2.1. Typical factory-based home construction facility: (a) Wall line, (b) Floor line, (c) Wall sheathing station, and (d) Roof production station (source: ACQBUILT Inc. 2019).

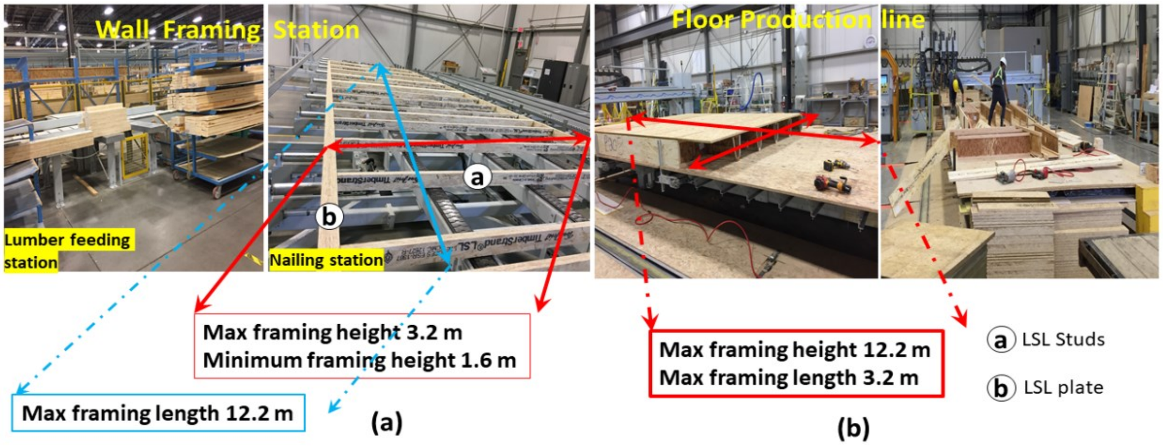

Figure 2.2. Production facility constraints (a) Wall framing station (b) Floor production line (source: ACQBUILT Inc. 2019).

Furthermore, in the current panelized construction process, the roof is built using closely spaced wood trusses that support sheathing and roofing materials (on the upper chord) and ceiling materials (on the lower chord). These trusses are arranged at a spacing of 610 mm or less. Wood-based sheathing panels provide lateral bracing of such a wood roof truss system. The entire roof of a single detached home is subdivided into four or five small volumetric units based on floor area and manufactured on the roof production line (ACQBUILT Inc. 2019). The production of volumetric roof modules in a factory consists of five phases (ACQBUILT Inc. 2019; Altaf et al. 2018b): (i) The roof trusses are designed and fabricated by a truss fabricator; (ii) The roof trusses are shipped to the housing production facility; (iii) Trusses are unloaded and transferred to the designated roof production workspace where they are laid out according to the plan. (iv) Wood-based sheathing panels and blocking are attached to the trusses using fasteners to form a roof module. (v) Roof finishing is added to the completed module. All these activities are manual and labour-intensive. Figure 2.3 illustrates the roof fabrication process of an Alberta-based panelized home manufacturer, which shows that its overall roof fabrication consists of 19 manual activities. In summary, this process of roof production is the same as stick-built construction, with the only difference being that construction activities occur inside the factory space. The entire roof is transported to the site as several single-piece modules and finally connected at the site.

Consequently, current roof production is less efficient than other workstations, such as the wall or floor line. For example, in the case of an Alberta-based home pre-fabricator, one complete gable roof production requires an average of 82.5 manhours, whereas the walls of an entire single detached home require only 6.0 manhours (Brown 2020). Additionally, the roof module occupies ample space in the factory because of the geometry during the production phase. As a result, this production line creates an imbalance in production rate with wall and floor panel lines for a given number of homes (Altaf et al. 2018c). Moreover, transporting the volumetric roof units requires a relatively large number of trailers (specifically, in the case of an Alberta-based home manufacturer, four trailers are needed for transporting a 149 m^2 single-family home) and on-site loading and unloading of trusses increases the overall work duration. This increases transportation costs (Altaf et al. 2018c) and CO_2 emissions during the construction process. A carbon footprint analysis of panelized construction in Alberta shows that 11% of CO_2 emissions are associated with panel transportation (Li et al. 2014). Furthermore, if the construction sites are very congested, it becomes impossible to transport large roof modules. As a consequence, the roof must be built entirely at the site (similar to the traditional stick-built process), thus increasing project cost and duration. Therefore, roof production of panelized construction of homes requires an in-depth analysis to improve the current production.

This chapter discusses the development of a novel panelized roof system that can be produced in-house using an existing panelization facility. Such a panelized roof system can replace the conventional triangulated roof truss system and thereby further improving the efficiency and reducing the cost of prefabricated house construction. By aligning roof production with the automated production line, the novel panelized roof system will potentially improve the off-site home-building process and facilitate the North American prefab sector towards the fully panelized home-building approach.

Figure 2.3. Flow diagram of the existing roof production process

A recent study by Brown (2020) shows that if the Alberta-based prefab company produces panelized roofs for six projects, then the production time is reduced by 38% and the 20% change in lead times of the roof assembly and wall assembly lines allowed for better production balancing between the two. Overall, a 28% manhours savings was also observed in the roof assembly process by the same study. Therefore, roof panelization for the offsite construction of homes is a solution to improve the current roof production. However, components of panelized roofs require a structural assessment to comply with the building code. A study was conducted to determine the structural requirements and feasibility of production using an existing offsite facility, which is the subject of this chapter.

2.2. Holistic Approach to Roof Prefabrication

Several production facility constraints often need to be considered in developing the novel panelized roof system that can be produced in a current panelization facility (Figure 2.2). In this study, the following constraints were imposed based on a typical commercial production facility in Edmonton, Alberta, Canada (ACQBUILT Inc. 2019) : (a) The framing dimension must align with the corresponding workstations constraints as shown in Figure 2.2; (b) The framing direction for the panel should be parallel to the short direction of the component if it is fabricated at the wall framing station; (c) The roof design should minimize the crane lifting sequence on-site. It should be noted that the above constraints may differ to some extent depending on the commercial production facility, but the same approach can be applied to develop an appropriate design that suits a different set of constraints.

In devising this holistic approach, a case architectural 3D model was analyzed first and then subdivided into several rectangular subsections. The dimensions of these sub-elements are determined in accordance with the production line limitations, transportation trailer capacity, crane lifting limitations, and on-site installation considerations. The resulting panelized system for a typical two-storey building with a gable roof (Figure 2.4) comprises the following components (Figure 2.5): a) Roof panels, b) Support wall panels, c) Ceiling frames, d) Beams spanning over two support walls, e) Gable Ends, and f) Inter-component connections, including the inclined roof panel-to-support wall, ceiling frame-to-load-bearing shear wall, and the support wall-to-ceiling frame. In this case study, a simple gable-style roof (Figure 2.4) of a two-story building with a slope of 8/12 was selected for implementing the panelized roof design concept. The case study home has an 11 m x 6.1 m roof footprint. Figure 2.5 shows the different components of the proposed system for this case study.

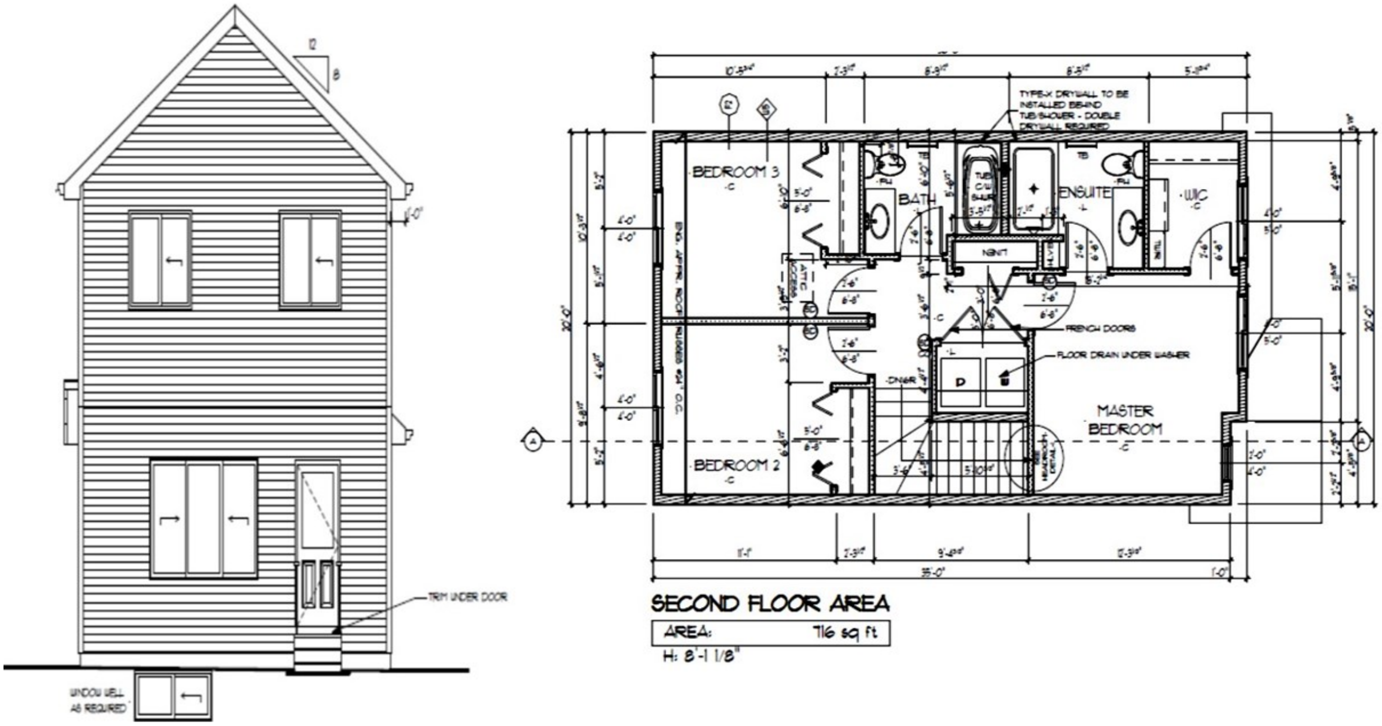

Figure 2.4. Elevation and roof footprint area of the case study

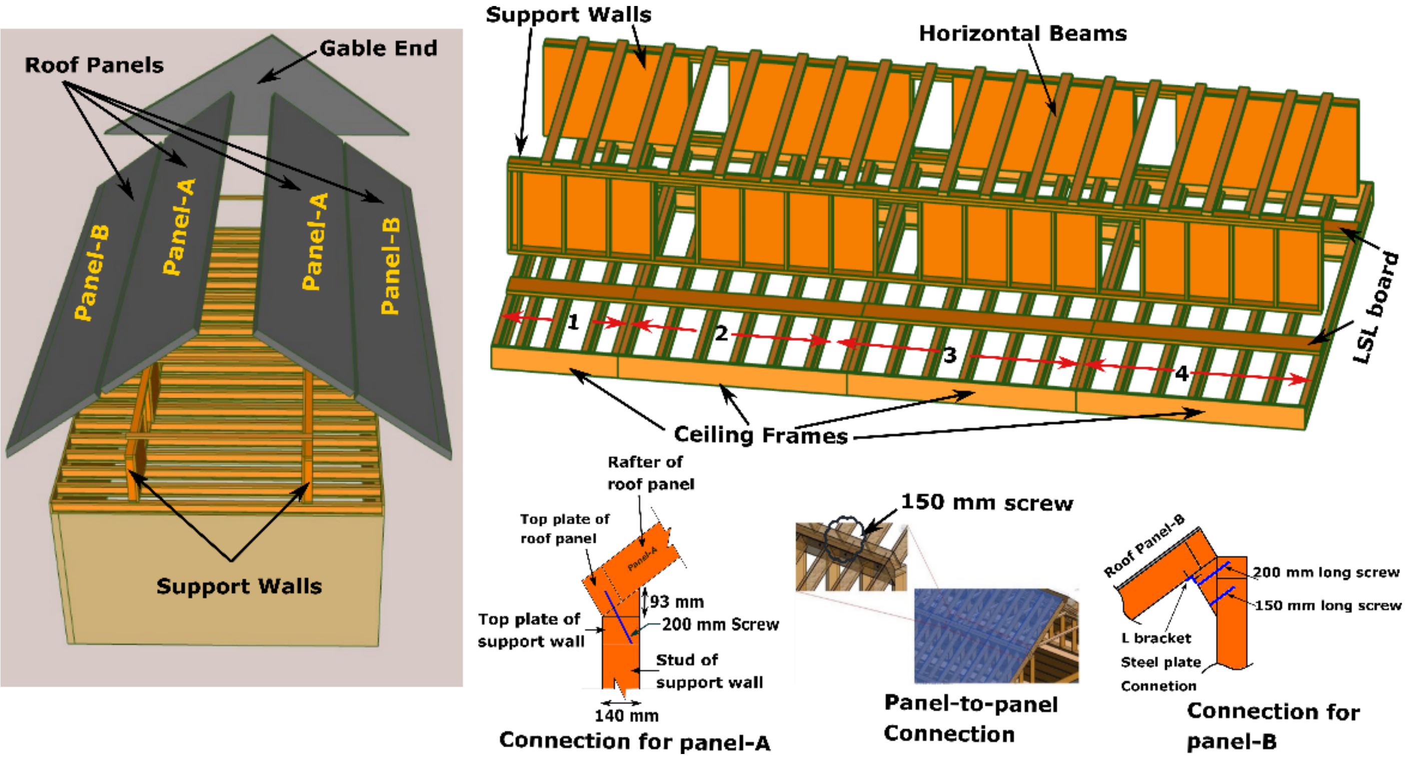

Figure 2.5. Panelized roof concept

The dimensions of the roof panel, the ceiling frame, and the support wall were selected in such a manner that they accommodated the constraints of the production line and transportation limitations, as described in Table 2-1. Analysis of component dimensions shows that this panelized roof system requires only one trailer to transport all the roof components for a single-detached home. The roof panels and support walls are produced in the wall production line using laminated strand lumber (LSL) and Oriented strand board (OSB). Details of the panel design are discussed in a later section. Ideally, following the wall production job sequence, roof panels can be fabricated. For instance, the rafter of the roof panel can be fed in the framing station to connect the LSL rafters (Figure 2.1a) and attach the OSB to the finished roof frames is completed into the multifunction bridge (Figure 2.1c) of the wall line. Whereas the ceiling frame can be produced in the wall line framing station or floor line depending (Figure 2.2) on the cost and efficiency of production. Details of the ceiling frame analysis are presented in the proceeding section.

Table 2-1. Constraints for roof panel and ceiling frame size

Component dimension	Production constraints	Transportation constraints
Maximum height (m)	3.2	3.5
Maximum length (m)	12.2	12.2
Minimum height (m)	1.6	n/a
Minimum length (m)	1.2	n/a

2.2.1. Ceiling Frame Analysis

The first step of the novel panelized roof system design is analyzing the ceiling frame component under gravity and wind loads. To begin with, the gable roof with an 11 m x 6.1m footprint of a two-storey house, as shown in Figure 2.4, was selected for implementing the following analysis. The design loads applied to the roof structure were assigned based on the National Building Code of Canada (NBCC) (NBCC 2020a) and the building location of Edmonton, Alberta. These were specified at a snow load of 1.035 kPa and an hourly wind pressure of 0.45 kPa. The dead load due to the gypsum ceiling is 0.5 kPa, and other non-structural components account for another 0.5 kPa. Ceiling frame analysis and joist size selection are primarily governed by the gravity load case. However, the gravity load path in light-frame timber construction is very complex and redundant. Even for the well-established traditional truss base roof system, a static gravity load test by Doudak et al. (2012) confirmed that by applying a gravity patch load (4.57 kN) to a roof truss over an area of 1.35 × 1.04 m, only 57% of the total applied force was detected by the load cell under the loaded truss and 29% of the load was recorded on the load cell placed under an adjacent truss 680 mm away from the loading location. Hence, to accommodate the system effect, CSA086-19 (CSA 2019) allows increasing the bending capacity of dimension lumber in an assembly of repetitive members by up to 40% if such members are spaced not more than 610 mm apart and OSB sheathing of a minimum of 9.5 mm thickness is attached to the members using common nails. So, for the roof panel rafter and ceiling frame, a maximum rafter and joist spacing of 600 mm is allowed to obtain the system effect in the assembly. Therefore, a tributary width of 600 mm was adopted for the 2D analysis of the ceiling frame for gravity load distribution.

As demonstrated in Figure 2.6, the gravity load distribution path of the panelized roof is idealized. As illustrated in Figure 2.6, Panel B is supported at both ends (at the eave line and support wall). So, half of the gravity load is transferred to the load-bearing shear wall at the eave line, and half of the load is transferred to the support wall. A conservative approach for gravity load distribution in the case of the load transmitted from Panel-A to the support wall is 100% tributary load flows on the top plate of support walls by the adequately designed rigid connection between their interfaces. Thus, the top plate of the support wall is subjected to a line load (UDL) from the roof panel-A and, assuming 600 mm spacing of the ceiling frame joist, two-point loads at x distance from the supporting load-bearing wall are applied. Simply support boundary condition was assumed for the joists of the ceiling frame. The location of the support wall was a critical parameter for both deflection and the roof panel size.

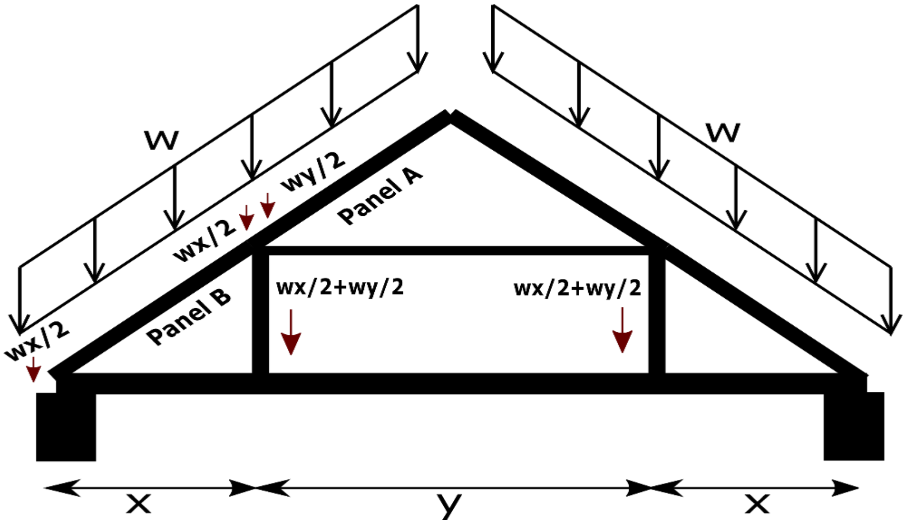

Figure 2.6. Gravity load distribution in a cross-section of the panelized roof

Several iterations were performed in analyzing the ceiling frame, and the results revealed that Span/4 is the optimal location to comply with both the roof panel dimensional constraint (see Table 2-1) and the serviceability limit state criterion (deflection limit L/360 for snow load on the roof). This analysis also found that three different design options with different engineered wood products are possible for the ceiling frame that satisfies the production line constraints of the Alberta-based manufacturer: (a) Option-A: Ceiling frame production utilizing the wall line with LSL; (b) Option-B: use LSL material but production on the floor line, and (c) Option-C: manufacturing ceiling frames using wood I-joist on the floor production line. All these three options have their limitations and advantages. For instance, the floor line is a semi-automated production station, and it has a higher manhour demand compared to the wall line. Consequently, the floor line has a lower production rate than the wall line. Furthermore, the wall line can produce frames using only LSL or SPF timber products, whereas the floor line can accommodate any wood product, including wood I-joist. However, producing a ceiling frame using the wall line will have a high production rate due fully automated system.

A higher number of load-bearing members of the ceiling frame along the shorter span of the roof is preferred to produce uniform load distribution and meet serviceability limit states. However, the minimum height allowed by the wall framing station is 1.60 m. Since the span of ceiling joists is 5.9 m, the maximum height of ceiling framing can be 1.60 m for fabrication Option-A, and the layout plan shown in Figure 2.7 is required to achieve the design moment capacity and deflection limit. The location of the support wall determines the concentrated load position that ultimately affects the moment and deflection of the joists of the ceiling frames. From the analysis, it is evident that the deflection limit governs the number of LSL joists required for the ceiling frame. To meet the deflection limit, the joist of each frame will require a 2-ply LSL beam with cross-sectional dimensions of 44 mm x 241 mm per ply and a grade of 1.55E (Weyerhaeuser 2021). It is worth noting that in producing a ceiling frame, the joists are placed along the long direction, and the blockings are in the short direction of the framing table (Figure 2.2a).

Another alternative for fabricating ceiling frames is to utilize the floor production line. The floor production line of the local manufacturer is capable of building 3.66 m x 12.2 m floor frames. So, it is possible to produce ceiling frames with joists having a maximum length of 12.0 m, and the width must be limited to 3.6 m. For the closely spaced ceiling frames, joists in directions, as indicated in Figure 2.8b, have better load-sharing capacity because of load distribution over several framing members (CSA 2019). Consequently, if the floor production line is used to manufacture ceiling frames, then two types of framing material can be used: a) 1.55 E LSL and b) wood I-joist. Figures 2.8 and 2.9 illustrate the corresponding framing plan for the case study roof, considering the abovementioned hypothesis and Table 2-2 summarizes all the options. In this case, the ceiling joists are spaced at 600 mm c/c in a 3.2 m wide frame.

Table 2-2. Roof ceiling frame production options

	Ceiling Panel Size (mm)	Qty	Ceiling frame Production line	Material	Ceiling frame production cost CAD/m^2	Other component production costs CAD/m^2	Total production cost CAD/m^2
Option A	1651 x 6096 and 1086 x 6096	7	Wall line	LSL (44 mm x 241 mm)	\$59	\$44	\$103
Option B	3200 x 6096 and 1473 x 6096	4	Floor Line	LSL (44 mm x 241 mm)	\$54		\$98
Option C	3100 x 6096 and 1076 x6096	4	Floor Line	Wood I-joists (Flange size 52.8 mm × 31.8 mm, Web 9.5 mm and depth 241 mm)	\$26		\$70

A detailed production cost analysis was performed using the production rate, material and labour cost data obtained from the local home manufacturer for this case study roof production to identify the best option for the manufacturing process. The material costs were representative of the time when this analysis was carried out. The production cost here is defined as the sum of material and labour costs to produce in the offsite facility. The cost estimation also excluded the site installations and transportation costs in both the panelized and current roof production scenarios.

The cost analysis results show that ceiling frame production costs are \$59/m2 for option-A, whereas, in the case of option C, the cost is \$26/m^2. Hence, a cost-effective solution is to produce the ceiling frame with wood I-joists in the floor line. The cost analysis of making a whole roof showed that the case study roof costs \$67/m^2 to make with the roof truss system, but it will cost \$70/m^2 to manufacture following the proposed system if option-C (Table 2-2) is used to fabricate the ceiling frame. Since, at this stage, the shipping and site installation costs are unknown for the panelized roof, it is impossible to compare the two systems equally. However, the panelized system requires only one trailer to transport the whole roof for the case study building. Hence, it has the potential to the shipping cost. Another fact is that this system can be cost-competitive when the project site is located remotely from the offsite facility for the following reason discussed proceeding section.

In panelized construction, transportation operation is a major cost-driving factor in project management since fabricated components are part of buildings and require a complex operation to successfully deliver the finished product (Browne 2015; Li et al. 2016). A recent study by Ahn (2019) on this Alberta-based prefab company found that the cost of transporting building components is linearly related to the serviceable distance, as indicated in Figure 2.10. In the study, the initial serviceable area was within a 30 km radius boundary of the factory (Ahn 2019). To observe the cost sensitivity of the transportation of single-family homes, the study analyzed 221 project data for the default 30 km radius boundary and gradually increased the serviceable project area up to a maximum of 60% of the original area (50 km radius boundary) in a machine learning and rule-based algorithms model. As can be observed from Figure 2.10, the cost increased by 41% for the new serviceable area. Therefore, it is evident that the current roof system is not cost-effective in case of long hauling distance projects since it requires multiple hauling for transporting the roof of a single-family home. Hence, the hidden cost savings in the panelized roof is the primary advantage for the remote project site.

Therefore, the proposed system has the potential to be a cost-competitive alternative to the conventional system. As a matter of fact, this holistic approach is more efficient since the new system delivers higher utilization of automated and semi-automated production lines. As a result, the novel system is expected to reduce environmental impact by reducing the logistic hauling number for a single-detached home roof transportation to one from four and thus lowering CO_2 emissions in the overall project execution cycle.

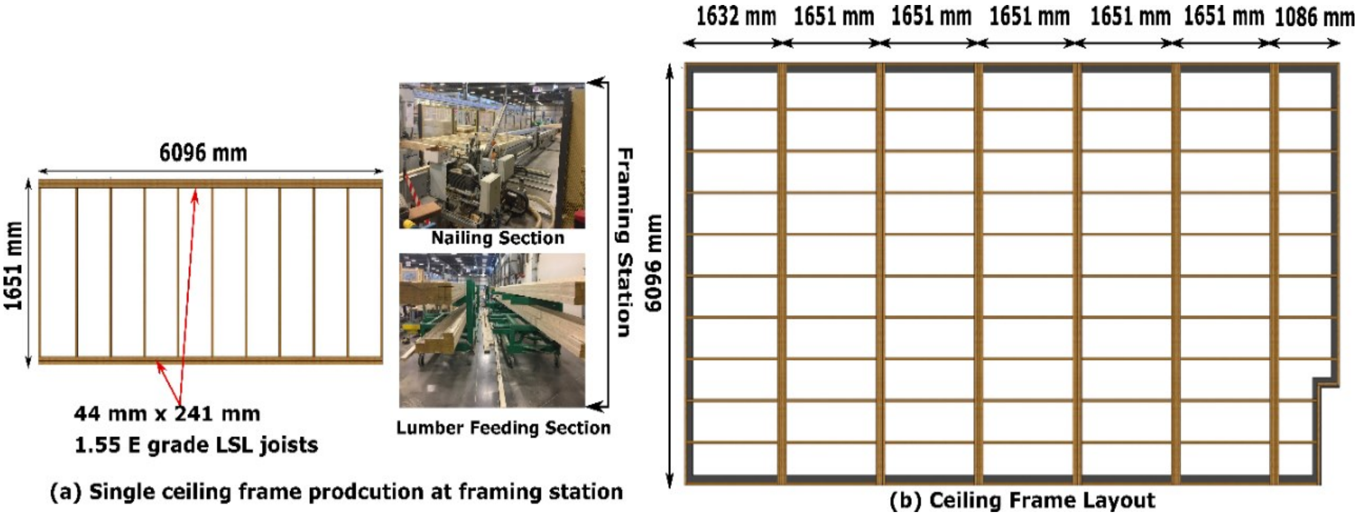

(a) Single ceiling frame prodcution at framing station

(b) Ceiling Frame Layout

Figure 2.7. Ceiling frame layout considering fabrication option-A for the case study.

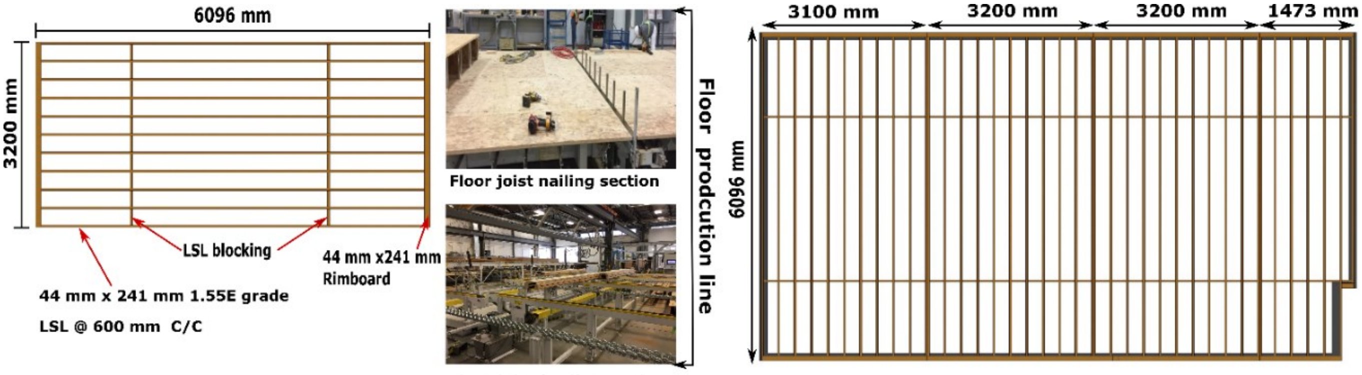

(a) Single ceiling frame production at floor line

(b) Ceiling frame Layout

Figure 2.8. a) Ceiling frame fabrication in Floor Line; b) Ceiling frame layout of the case study

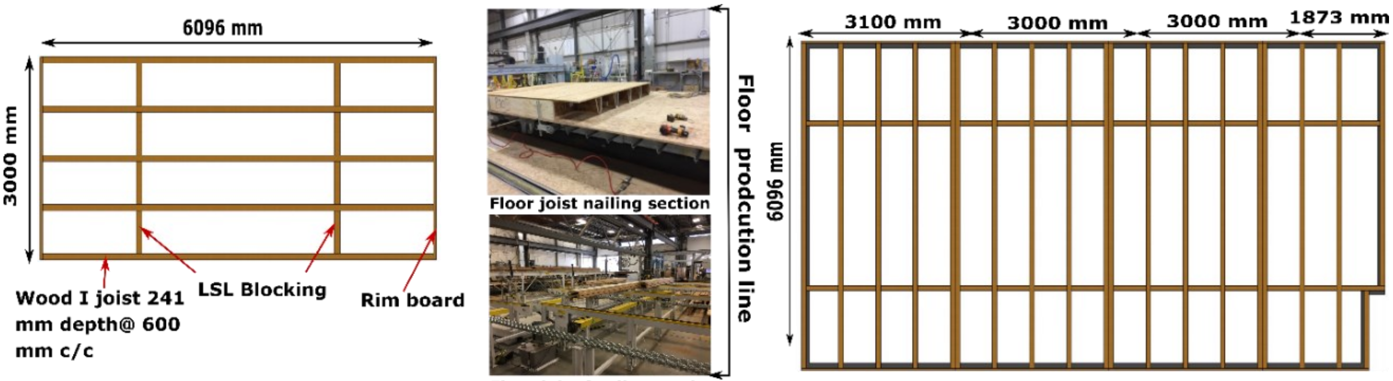

(a) Single ceiling frame at floor line

(b) Ceiling frame layout

Figure 2.9. a) Ceiling Frame Fabrication using wood I-Joist b) Ceiling frame layout of the case study

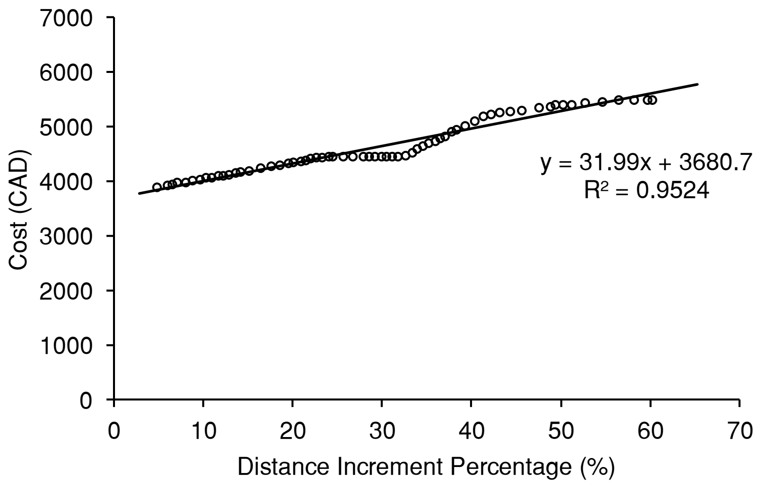

Figure 2.10. Cost sensitivity of transportation of panelized buildings with distance (Ahn 2019).

2.2.2. Roof Panel Analysis

As mentioned in the previous section, the roof panel is produced on the wall line following the same procedure as the wall panel production process. As such, a gable roof with an 8/12 slope and a 6,096 mm span requires four panels. The corresponding width for the panel A type (Figure 2.5) is 1,930 mm, whereas panel B has a width of 1755 mm. The panel design begins with the selection of the OSB sheathing thickness. Following the design tables 5.2.1.2A and 5.2.1.2B in the Wood Design Manual (CWC 2014), for a roof rafter spacing of 600 mm, 9.5 mm thick OSB sheathing can be used for specified roof snow loads less than 2.0 kPa and 15 mm for specified roof snow loads greater than 2.0 kPa. The framing lumber of the panel can be designed similarly to the traditional rafter analysis considering simply supported conditions for a span of the panel width. Since panels A and B are subjected to both out-of-plane and in-plane loading, the lumber design would require checking for bending and compression CSA 086-19 clauses 6.5.4.1 and 6.5.6.2.3) of timber members (CSA 2019). This simplified process gives an estimate as an individual rafter member of the panel. However, the panel is a system itself with LSL plates (76 mm × 140 mm), rafters (38 mm × 140 mm) spaced at 600 mm, and OSB sheathing (9.5 mm to 15 mm thick). Each panel can be characterized as an assemblage rather than an individual rafter system. The nail connections of the roof panel are subjected to shear and withdrawal for gravity and wind uplift. Therefore, a finite element model (FEM) of the roof panel was developed to verify the member strength and nail connection capacity to sustain the design load. A detailed nail connection test was performed to analyze the roof panel to obtain connection input properties, which are discussed in the following section.

2.2.2.1. Nail Connection Tests

Experimental tests were conducted to obtain the load slip behaviour of the OSB-to-LSL rafter and LSL plate-to-LSL rafter nail connections. The test method described in section 13 of ASTM D1761−12 (ASTM 2012) covers the determination of the resistance to lateral movement offered by a single nail in wood members. Following the same loading protocol and measurement process, a modified test setup was designed for this study to obtain the load slip of the nail connections. The test program involved four types of nail connection (Figure 2.11 to 2.14); in total, 24 nail connection specimens were fabricated at the offsite construction facility. All the specimens were fabricated at the factory using the similar nail gun used in the wall framing and the same materials grade in wall panel manufacturing. So, it is evident that the nail connection samples represent a reasonable portion of actual production that accounts for the construction defects and variability.

The test setup used for testing nail joints was similar to the one previously used by Plesnik et al. (2016) and Spasojevic et al. (2021). The setup had two parts: a) the test section at the top and b) a dummy section at the bottom. The dummy section was overdesigned to make it very rigid so that it could maintain the geometry of the specimen. It was fabricated using ten 12-gauge screws that provided the dummy section with high stiffness to minimize any movement at that end. Sample A was fabricated using two 9.5 mm thick OSB and two 38 mm x 191 mm LSL (Figure 2.11a). This sample test provides the load slip behaviour of the nail connection between OSB and LSL in shear. In the test section part of sample A, two nails (83 mm × 3.3 mm nails) per side were used to connect the OSB with LSL, whereas, in the dummy part, six screws per side were utilized to connect the OSB with LSL. To obtain the LSL plate-LSL rafter nail connection load slip curve, three types of specimens were fabricated: a) Sample B for the nail connection behaviour in shear along perpendicular to strand the direction of point side member in plank orientation (Figure 2.11b), b) Sample C for the nail connection behaviour in shear along parallel to strand the direction of point side member in beam orientation (Figure 2.11c) and d) Sample D for the nail connection behaviour in withdrawal.

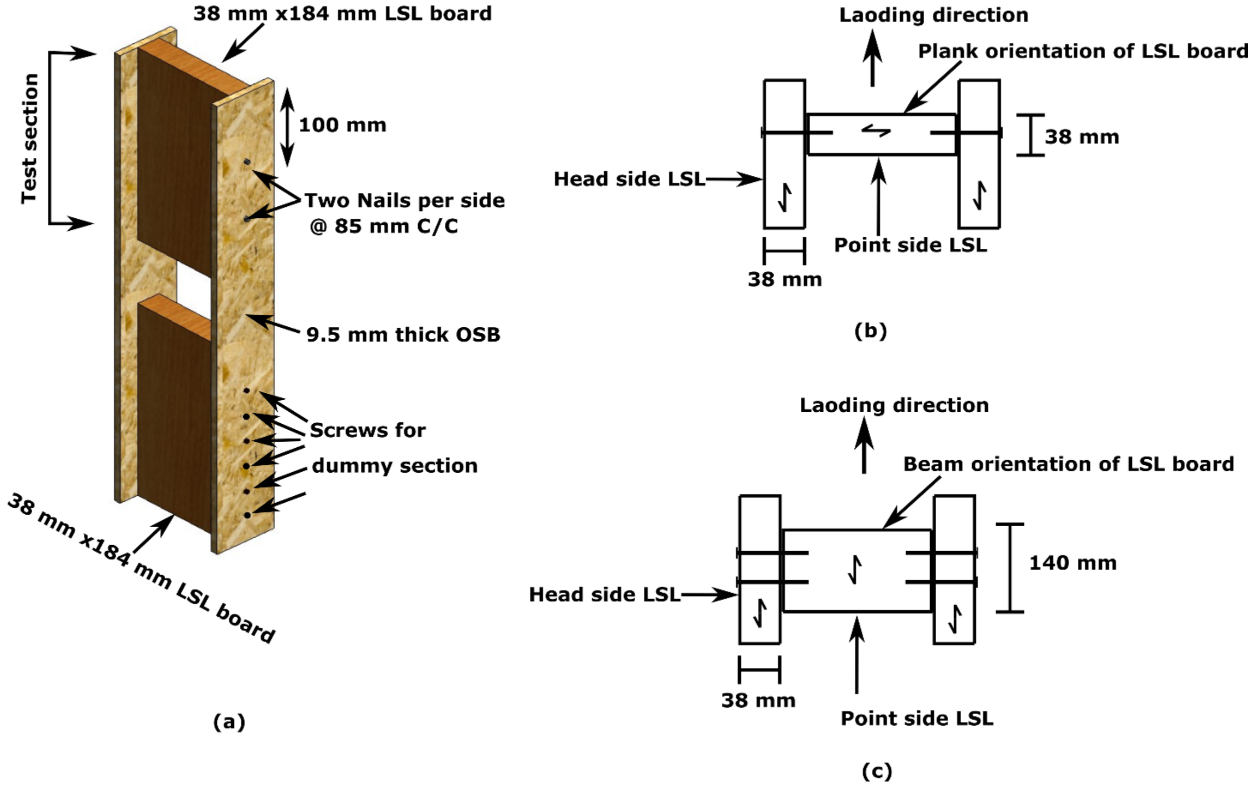

Figure 2.11. (a) Sample A construction details (b) Nail connection loading LSL in plank orientation of LSL point side member (c) Nail connection loading LSL in beam orientation of LSL point side.

Sample B was fabricated using one 38 mm × 140 mm LSL piece in horizontal plank orientation and two 38 mm x 140 mm LSL parts in beam orientation (Figure 2.12a). Two nails (83 mm × 3.5 mm nails) per side were used to connect the LSL parts, which represents the nail connection with a LSL plate to LSL rafter, and the test results of this sample represent the displacement of joints in the x-direction as shown in the coordinate system in Figure 2.13. Sample C was made from eight 38 mm × 140 mm LSL, one 38 mm x 191 mm LSL, and two 9.5 mm thick OSB sheathing (Figure 2.12b). The sheathing provided a surface connecting the dummy and test sections (Figure 2.12b). Sample D was fabricated using one 38 mm × 140 mm LSL piece in horizontal plank orientation and two 38 mm × 140 mm LSL parts in beam orientation with nailing, as indicated in Figure 2.14a.

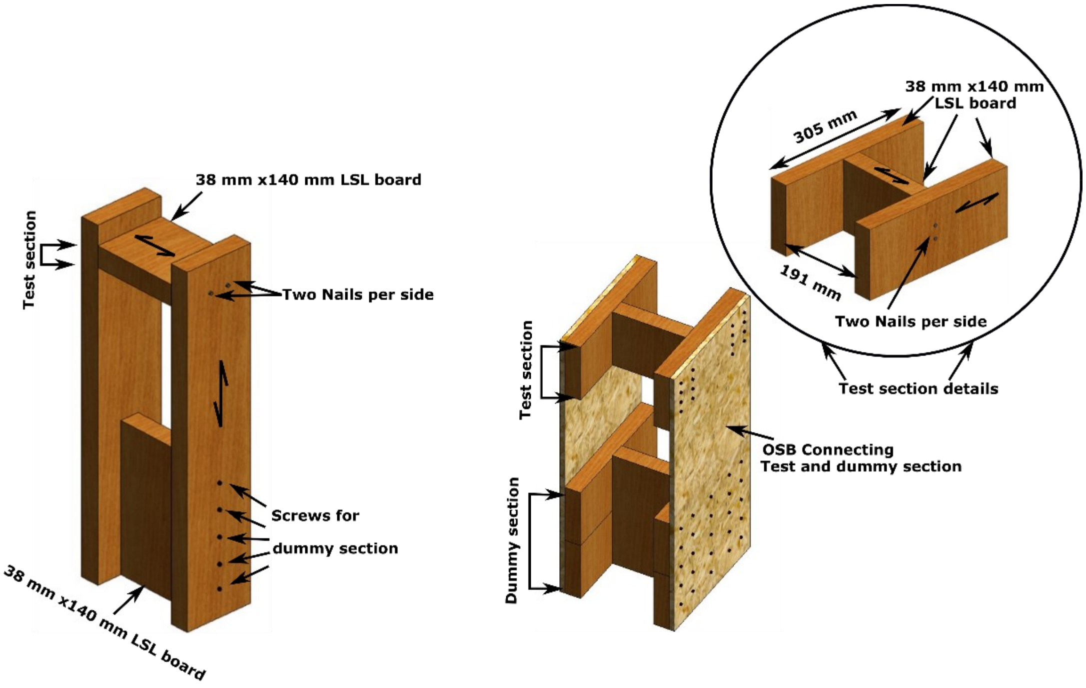

(a) (b)

Figure 2.12. (a) Sample B construction details, (b) Sample C construction details

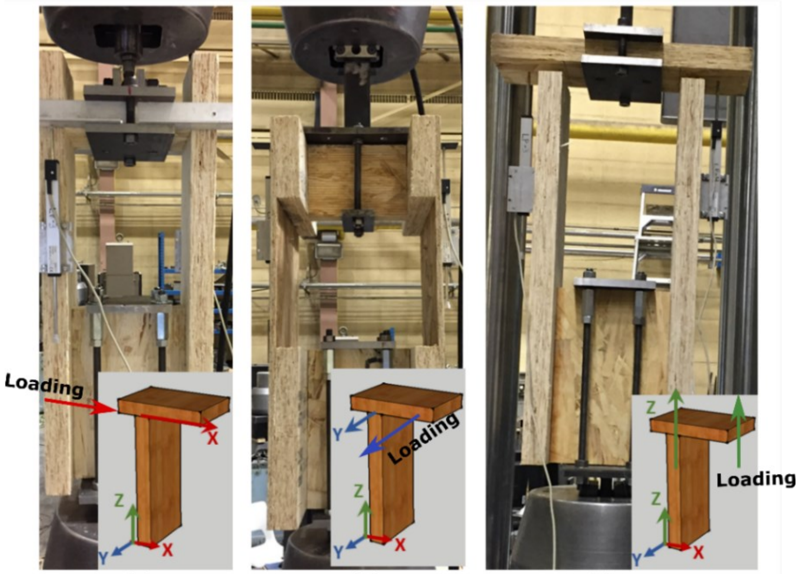

(a) (b) (c)

Figure 2.13. Axis direction of nail connection (a) Sample B, (b) Sample C, and (c) Sample D.

A total of four nails (83 mm × 3.5 mm PD nails) were used to connect the LSL sections in case Sample C, which represents the nail connection of LSL plate-to-rafter in beam orientation, and test results of this sample represent the displacement of joints in the y-direction (Figure 2.13b). Two Linear Variable Differential Transformers (LVDTs) were attached to both sides of the OSB of the specimen to record the relative displacement of the LSL sections.

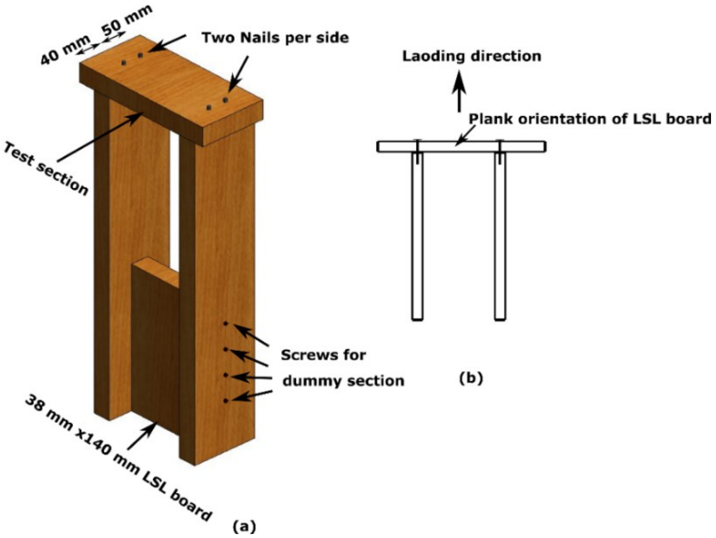

Figure 2.14. (a) Sample D construction details (b) Loading direction along nail withdrawal.

Finally, for the test section of sample D, four nails were used to connect the LSL sections that represent the connection of the LSL plate-LSL rafter in plank orientation, and the test results of this sample represent the displacement of joints in the z-direction (Figure 2.13c). Figure 2.15 shows the test setup for sample A. The same apparatus was used for testing samples B, C, and D. Figure 2.17 illustrates the load-slip plot of the tested sample in which load is expressed per fastener, and Table 2-3 summarizes all the test results. The failure modes of nail connection specimens were bending of nails and crushing of LSL strands for samples B and C, whereas, in the case of sample A, nail head pull throughout was also observed, as shown in Figure 2.16. The characteristics of the individual sheathing-to-rafter and LSL plate-to-rafter joints in the roof panel are crucial in defining the strength and stiffness of the panel. The results of this nail connection test were used to develop a finite element model (FEM) of the panel, which is described in the next section.

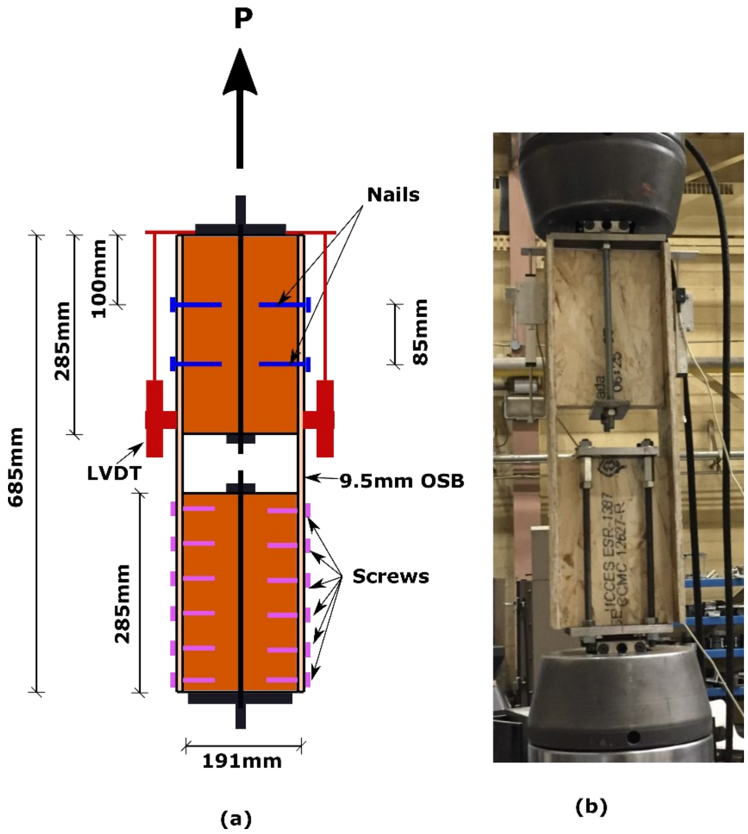

Figure 2.15. Apparatus for nail connection test

Table 2-3. Summary of nail connection test samples

Joint type	Load	Head-side	Point-side	F_{max} (kN)		K_s (N/mm)
				Mean	S.D.	
Framing LSL rafter-to-LSL plate X-axis	Lateral	LSL	LSL	1.403	0.020	712.34
OSB sheathing-to-LSL framing	Lateral	OSB	LSL	1.035	0.188	2,622.93
Framing LSL rafter-to-LSL plate Y-axis	Lateral	LSL	LSL	1.199	0.138	758.51
Framing LSL rafter-to-LSL plate e Z-axis	Axial	LSL	LSL	0.862	0.186	3,608.57

Figure 2.16. Failure modes of nail connections under monotonic loading

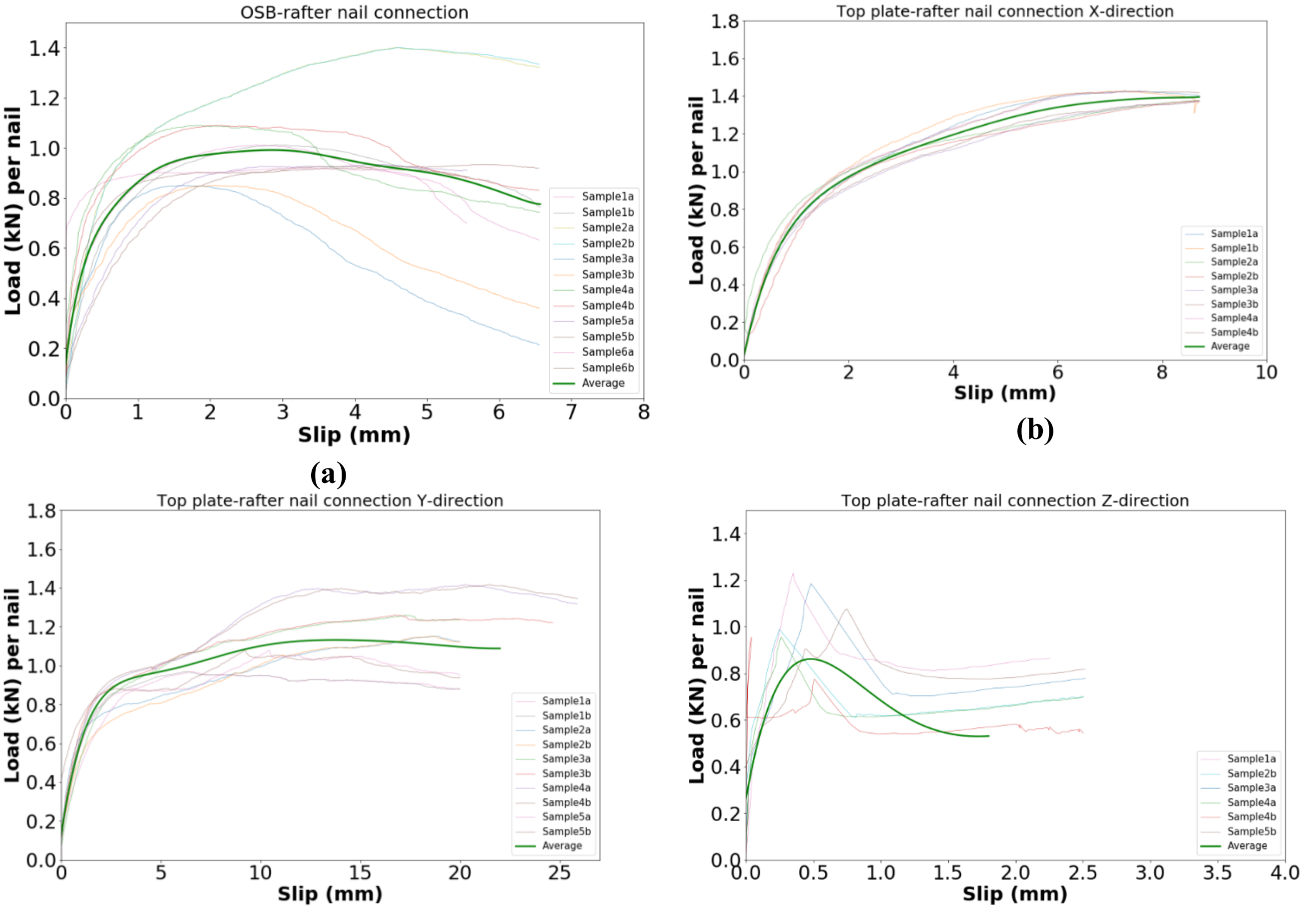

(a)

(b)

(c)

(d)

Figure 2.17. Load slip curves for (a) Sample-A, (b) Sample-B (x-direction), (c) Sample-C (y-direction), and (d) Sample-D (nail withdrawal)

2.2.2.2 Finite Element Analysis of Roof Panel

FEM covers broad structural engineering applications, and it aids research by providing an efficient and cost-effective means of predicting the structural response of a range of light-frame wood buildings (Satheeskumar et al. 2017a; Stevenson et al. 2019). This study used general-purpose finite element software Abaqus to develop a FEM of a roof panel of a gable roof with a slope of 8/12. Due to the nature of the construction, three types of elements are used in the FEM. The OSB panels and LSL rafters were modelled using the S4R shell element. The top and bottom LSL plates were connected to the rafter using nails. They were modelled using an 8-node linear brick element (C3D8R) and connector elements (CONN3D2) representing the nail connection. S4R is a 4-node doubly curved general-purpose shell element with finite membrane strains permitted, and each node has 6 degrees of freedom, whereas C3D8R is a solid (or continuum) element in Abaqus that can be used for both linear and nonlinear analyses involving contact, plasticity, and large deformations.

To assess the roof panel member strength and nail connection status in design load, modelling a part of the roof panel is sufficient due to the symmetry of the gable roof. As can be observed from Figure 2.5, one end of panel A is supported by the support wall component of the roof and the other end is connected to the other panel A on the opposite side via an apex connection. Therefore, pinned boundary condition (U_x=U_y=U_z=0) at both ends of the roof panel at the connection location (e.g., support wall line and apex) was assigned. The details of the connection mechanism can be found in Islam et al. (2021, 2022b). Due to symmetry, only half of the gable geometry was modelled. In the case of panel B, one end is supported by the ceiling frame end near load bearing shear wall and the other end is connected to the support wall. So, a similar boundary condition as panel A applies to the panel model representing panel B. Hence an inclined roof panel with 8/12 was modelled with a representative longitudinal length of 2.40 m and a span of 1.930 m representing panel A. Symmetry boundary condition was defined along the global Z axis for the OSB and LSL plate edges as indicated in Figure 2.18 (see the notation d and e of the figure). To represent proper boundary conditions, the rafter edges were partitioned at both ends according to the contact length of the corresponding connection surface (see note f of Figure 2.18). Also, the 76 mm thick LSL plate at both ends of the panel was partitioned to the width of the rafter width since this portion is an active element in the connection for the roof panel at the eave line, support wall line and apex connection. In the wind withdrawal load case, the pinned boundary condition was removed from the bottom end of the rafters (see note b of Figure 2.18) since the screw connection at the eave line or support wall line only the 76 mm thick LSL plate is an active point side member.

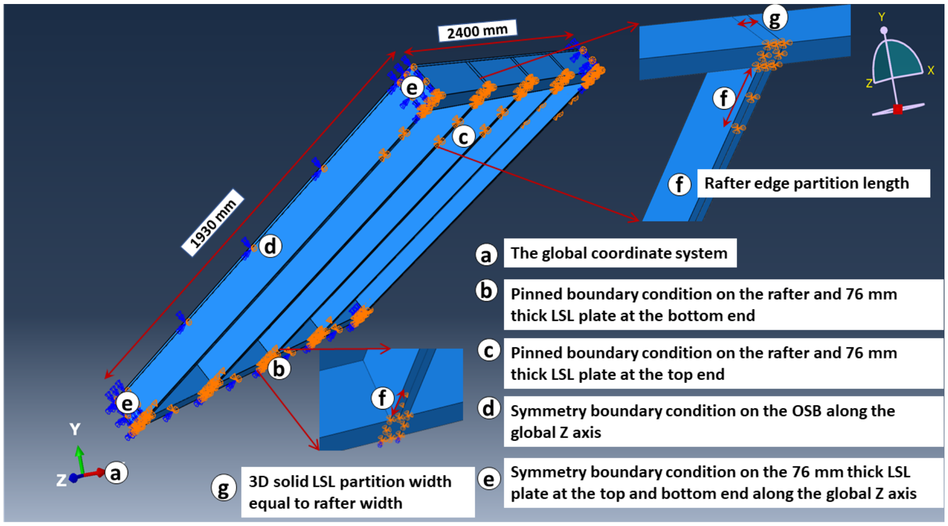

Figure 2.18. Boundary condition of the inclined roof pale Model-A

The connections between the intercomponent members were important components to be modelled in this numerical analysis of the roof panel because the nonlinearity of a wood frame building is mostly governed by these connections (He et al. 2001). A sensitivity study of light frame roof panel uplift capacity by He and Hong (2012) shows that the nonlinear behaviour of nail withdrawal must be considered to predict accurate uplift capacity in the nonlinear static analysis under static wind pressure, quasi-static analysis under time-varying wind pressure and nonlinear dynamic analysis under time-varying wind pressure. So, the nail connection of the sheathing-to-LSL rafter and LSL plate-to-LSL rafter in the FEM was modelled using connector elements in Abaqus (CONN3D2). This element in three-dimensional space (Conn3D2) is a two-node 1D element that effectively substitutes the active parts of a connection and defines a constitutive relationship between the degrees of freedom of the respective nodes (Dassault Systèmes 2021). Since timber connections with dowel-type fasteners generally exhibit non-linear load-deformation behaviour (He and Hong 2012; Satheeskumar et al. 2017b; Shivarudrappa and Nielson 2013; Vessby et al. 2010), nonlinear spring properties were used to define the OSB-to-rafters and LSL plate-to-rafters connector (CONN3D2) behaviour. The load-displacement relationship of the nonlinear springs was obtained from the individual connection tests discussed in the previous section. The connection between the LSL plate and the LSL rafter required two nonlinear springs (x and y axes of the LSL plate-LSL rafter connector's local axis, as shown in Figure 2.19) and one rotational spring (in the LSL plate -LSL rafter connector's local z-axis, as shown in Figure 2.19). The linear, rotational stiffness of the nail connection was adopted from the test data of Mohamadzadeh et al. (2019) due to a similar nail connection. Similarly, the connection between OSB and LSL rafter/plate was defined using three nonlinear springs with a corresponding local coordinate system, as illustrated in Figure 2.19. The properties of OSB and LSL materials were defined based on values reported in the literature. The OSB sheathing properties were adopted from. Karacabeyli et al. (1996), Zhu (2003), and Shahidul Islam et al. (2017). The LSL wood properties were defined based on the test results of Moses et al. (2003), CCMC (2019), and Niederwestberg et al. (2018), and Janowiak et al. (2001) (Table 2-4).

Table 2-4. Elastic material properties for OSB and LSL

Property	OSB	LSL
E_1 (MPa)	5323	8,965
E_2(MPa)	3231	996
E_3 (MPa)	130	1,350
G_{12}(MPa)	1,574	490
G_{13}(MPa)	157.4	195
G_{23}(MPa)	157.4	80
υ_{12}	0.183	0.298
υ_{13}	0.364	0.500
υ_{23}	0.312	0.6

Hard contact was defined between the OSB sheathing surface and the 76 mm thick LSL plate surface. Two different models were developed to observe the response of the roof panel subjected to design load: a) Model-A and Model-B. Model-A had a panel dimension of 1.930 m x 2.40 m with an 8/12 roof slope and assembly elements consisting of 9.5 mm to 15 mm thick main OSB, 76 mm x 140 mm LSL plates at the top and bottom end, and 38 mm x140 mm LSL rafter at 600 mm spacing. It is worthwhile to note that for a specified snow load of less than 2 kPa minimum OSB thickness for rafter spacing 600 mm is 9.5 mm, whereas for a snow load of more than 2 kPa is 15 mm (CWC 2014). The 76 mm thick LSL plate facilities the screw connection between the roof panel and support wall and ceiling frame at the eave line. This dimension is governed by the screw connection requirement at the eave line and support wall line.

Table 2-5. Strength properties for OSB and LSL (Karacabeyli et al. (1996); CCMC (2019))

Material	Bending strength (MPa)	Shear (MPa)
LSL	21.65	5.39
OSB	12.8 [a] 13.4 [b]	1.5

a) for 9.5 mm thick OSB; b) for 15 mm thick OSB

Model-B was the same size and slope as Model-A, but a secondary OSB was added at the top and bottom (Figure 2.19 b). The objective of this model is to obtain roof panel requirements in a specific case where the apex connection is omitted for one alternate rafter. The apex connection is fabricated using steel plates (Islam et al. 2022c). To make an economical design if the cross-section is provided such that it can support 1.2 m spacing of rafter. However, the maximum rafter spacing is 600 mm for the roof. Therefore, it is required to see if the nail connection between the LSL plate and rafter complies with the design capacity to resist gravity in such a boundary condition that has an apex connection spacing of 1.2 m. It was observed in the case of Model-A that the nail connection between the LSL plate and rafter exceeded the design capacity when the above-mentioned boundary condition was applied. The primary OSB-to-rafter nail spacing was 150 mm. As for this specific case (Model-B), the gravity load case governs and factored gravity load of 4 kPa was applied in the FEM in this particular case. The threshold of 4 kPa was selected considering the specific snow load of 2.25 kPa, which accommodates all of the locations in the province of Alberta, Canada.

The nail connection of the secondary OSB in Model-B is subjected to both lateral and axial load because of the slope orientation of the roof panel. This combined loading is not addressed by the design provision in CSA 086-19 (CSA 2019). As shown in Figure 2.19a, symmetry boundary conditions at the ridge were defined for the studs 1.20 m apart to mimic an apex connection spacing at every alternate rafter, as well as a boundary condition (U_x=U_y=U_z=0) at every alternate bottom rafter was assigned to represent the support wall to roof panel connection. Therefore, the rafter between the supported ones had all degrees of freedom in space at the apex and bottom locations.

Thus, the model redistributes the load to adjacent supported studs, and by analyzing the connector force output, the design capacity of the roof panel, as well as the optimum number of nails for the secondary OSB, was obtained. To assess the nail connection status at design load, connector output was compared with the test data for each representative nail connection in the

FEM. It is worthwhile to note that the connector damage threshold was set in accordance with the design capacity obtained using section 12.9 of CSA 086-19 (CSA 2019). For instance, the nonlinear behaviour of nail withdrawal was defined using the load slip curve of the withdrawal test. However, for design, the LSL-LSL connector in withdrawal was considered damaged at a load level of 352N, which is factored maximum withdrawal capacity obtained using CSA 086-19 (CSA 2019). Similarly, the LSL-LSL connector design shear capacity was set at 1052 N, while the OSB-LSL connector's withdrawal and lateral capacity were set at 419 N and 584 N for 9.5 mm thick OSB, respectively.

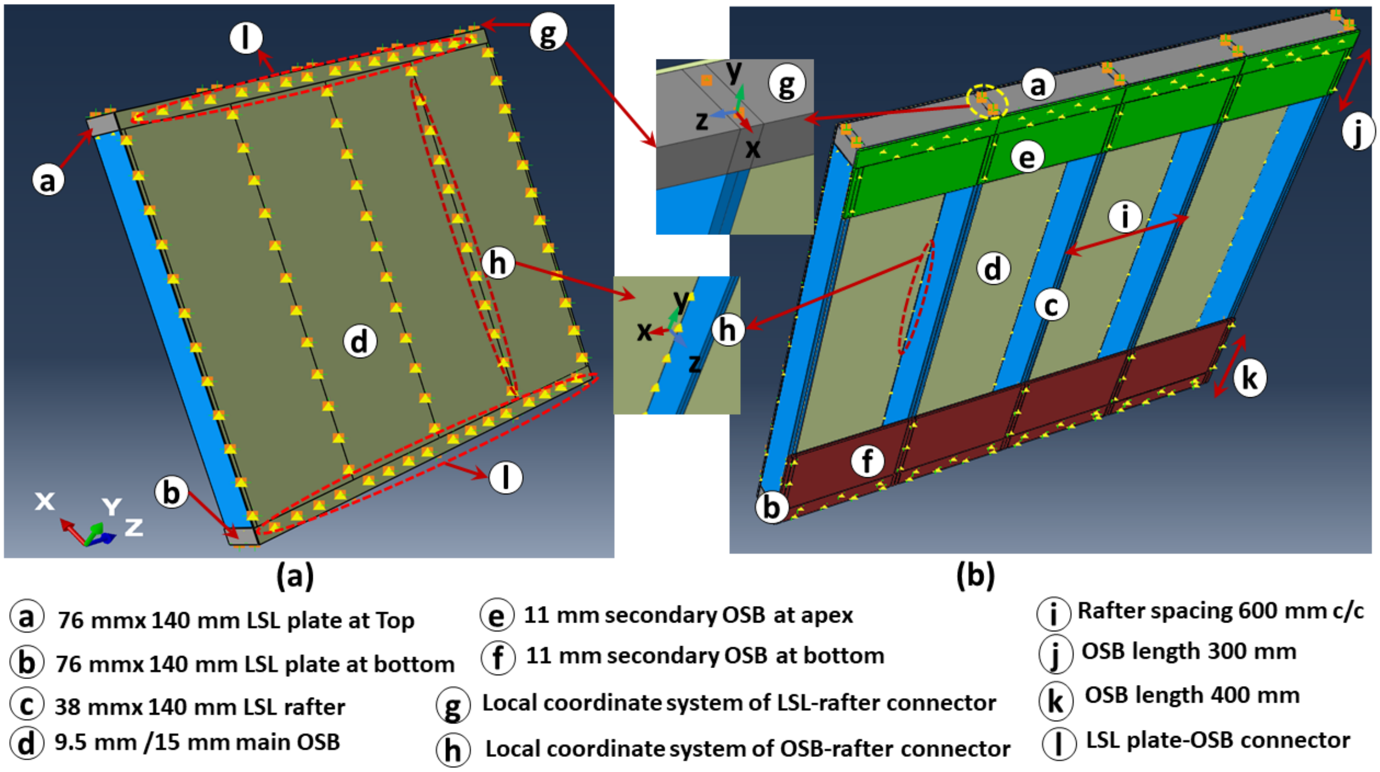

Figure 2.19. a) Model-A nail connections and b) Additional OSB in Model-B

2.2.2.3. Results

The load applied to the roof panel Model-A was according to NBCC (NBCC 2020a). The roof panel was subjected to two governing load cases: a) gravity (1.25 D+1.5S) and b) wind uplift case (0.9D+1.4W) in two different locations in Canada. The first location is in Edmonton, Alberta, Canada, with a specified snow load of less than 2.0 kPa, and the other location is Salliq (Coral Harbour), with a snow load of over 2.0 kPa. Additionally, 0.5 kPa dead load was assumed for roofing materials. For Edmonton, the total specified snow load was 1.035 kPa and wind pressure of 0.45 kPa in 1/50 years return period. In the case of Salliq, the total specified snow load was 2.29 kPa and wind pressure of 0.58 kPa in 1/50 years return period. For the strength of roof panel members governing load case is gravity; however, the partial snow load case has the most critical effect on member strength in the gravity load case. Therefore, snow load was applied based on the partial load case, as explained in NBCC (NBCC 2020a). In the case of wind uplift (wind blowing parallel to ridge direction), the end zone defined as in NBCC has the most critical effect in nail connection withdrawal (NBCC 2020a). Therefore, the end zone uniform pressure was applied for the wind load case (0.9 D+1.4W) to obtain the most critical effect on the roof panel. To assess the roof panel member strength stress output of the OSB, the LSL plate and rafter were compared with the specified strength values reported in Table 2-5. In the case of Edmonton, maximum bending and shear stress for the rafter were 1.86 MPa and 0.78 MPa, respectively. These values for OSB sheathing were 4.27 MPa and 0.63 MPa, respectively. Whereas in the case of Salliq, maximum bending and shear stress for the rafter were 2.96 MPa and 1.2 MPa, respectively. For OSB, these values were 2.5 MPa and 0.44 MPa. Maximum deflection in the rafter was 0.72 mm for Edmonton and 1.2 mm for Salliq. According to NBCC maximum deflection for the rafter is L/180 (9.88 mm) (NBCC 2020b). Therefore, roof panel elements comply with the strength and serviceability. However, the nail connection in the roof panel must have the capacity to sustain the design load.

As can be observed from Figure 2.19, the nail connection between the 76 mm thick LSL plate and rafter is at the inclination angle of the roof slope with the global X-Z plane. Hence, it is subjected to both shear and withdrawal in gravity and wind load case. The OSB-rafter nails are subjected to withdrawal in wind uplift cases. The nail connection between the 76 mm thick LSL plate and OSB is subjected to withdrawal due to the bending of OSB in the gravity load case. All these nail connection statuses were obtained from the connector force output of Model-A.

Table 2-6 summarizes the different nail connections capacity in the roof panel for the governing load cases. As expected, the highest nail withdrawal between the 76 mm thick LSL plate and the rafter at the bottom end for Salliq was observed in the wind uplift case. It is apparent from Table 2-6 that nail connections comply with the design requirement. The nail spacing for OSB to rafter was initially obtained from the diaphragm design of CSA 086-19 (CSA 2019), and the shear check from the gravity load case shows that nails have sufficient shear capacity. Therefore, it can be concluded that the rafters, OSB, LSL and the nails specified in the model for the roof panel meet the design requirement.

Figure 2.20 shows the load-displacement output from the models with (Model-A) and without secondary (Model-B) OSB in withdrawal. It can be observed from Figure 2.20a that in the case of Model-A (without secondary OSB), rafter-to- LSL top plate nail connection (LSL-LSL connector) withdrawal component output is close to the defined connector failure threshold, whereas for Model-B (with secondary OSB), it is well below the limit.

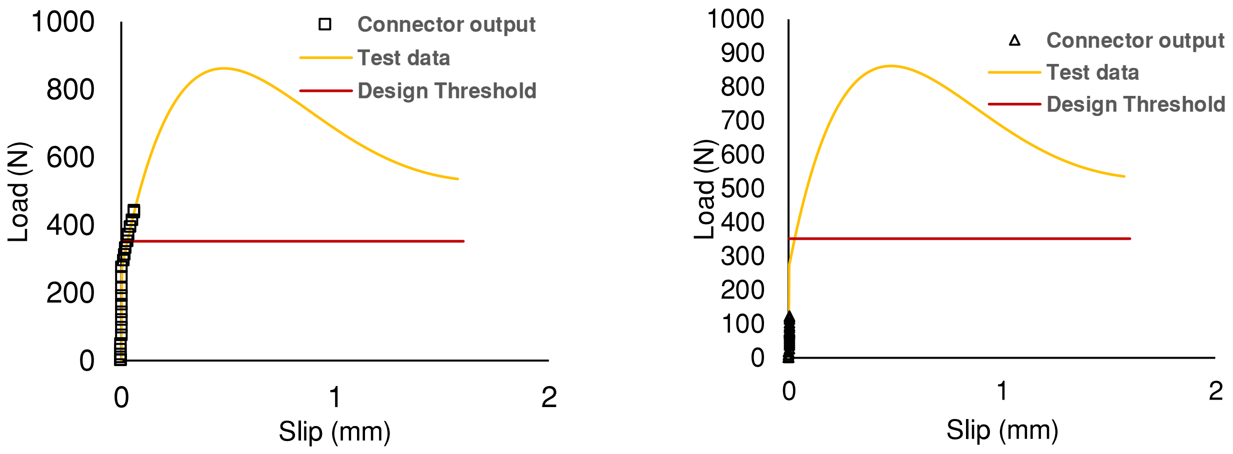

(a) (b)

Figure 2.20. Load-slip responses of LSL plate-to-rafter connections- a) Model-A, b) Model-B

Table 2-6. Summary of nail connection capacity from Model-A

	Connection Type					
Location	76 mm thick LSL Plate-OSB	Rafter-OSB	Design Capacity OSB-LSL nail withdrawal	LSL Plate-Rafter	Design Capacity of LSL-LSL nail connection	Load Case
	Nail withdrawal (N)					
Edmonton	224	112	419	210	352	0.9D+1.4W
Salliq	255	180		252		
	Nail Shear (N)					
Edmonton	29	203	584	182	1052	0.9D+1.4W
Salliq	72	251	710	280		
	Nail withdrawal (N)					
Edmonton	183	-	419	166	352	1.25 D+1.5 S
Salliq	163	-		215		
	Nail Shear (N)					
Edmonton	75	275	584	145	1052	1.25 D+1.5 S
Salliq	166	397	710	166		

Note: The framing station uses nails with 3.33 mm dia and 83 mm long for OSB-rafter connection, and for 76 mm thick LSL to rafter connection, nails have 3.5 mm dia and 130 mm in length

Thus, the FEM confirmed that a roof panel with secondary OSB is required to sustain the design load when the apex connection spacing is 1.2 m. Fastener sensitivity analysis of secondary OSB at the apex of Model-B was also performed by varying the nail number and pattern, as shown in Figures 2.21 and 2.22. As illustrated in Figure 2.21, Model-1B consists of a single row of two nails and Model-2B a single row of four nails attaching the secondary OSB, in contrast to Model-3B with a double row of two nails and Model-4B with a double row of four nails (Figure 2.22). For a design load 4 kPa gravity load, it was revealed that fasteners 1 and 6 (Figure 2.21) have the highest withdrawal force in the case of Model-1B. As the number of fasteners increases, the withdrawal force of fasteners 1 and 6 decreases in succeeding models (Table 2-7). It can be observed from Table 2-7 that the double row four nail pattern (Figure 2.22) has the lowest withdrawal force. Thus, results from the FEM affirm that for a factored gravity load of 4 kPa, two rows of nails 150 mm c/c in jig jag pattern are recommended to attach 11 mm thick secondary OSB.

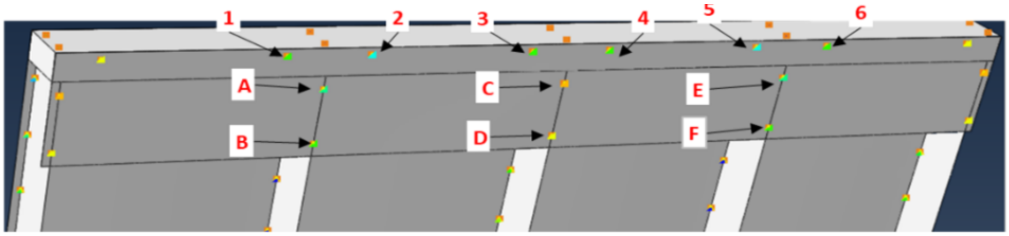

Model-1B: Sigle row two fastener

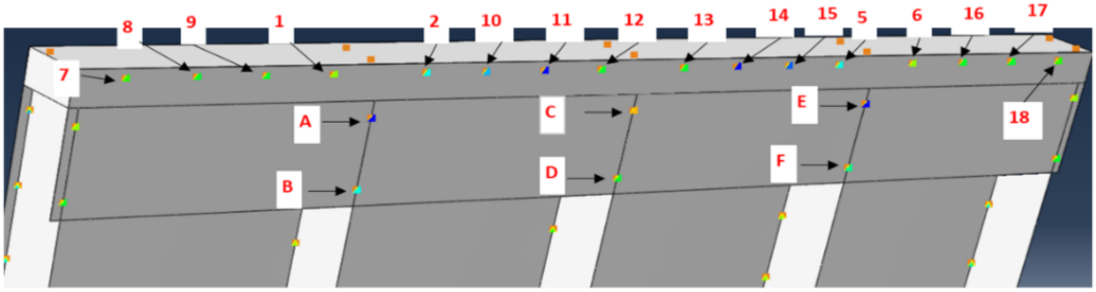

Model-2B: Sigle row four fastener

Figure 2.21. Fastener sensitivity analysis model 1B and 2B

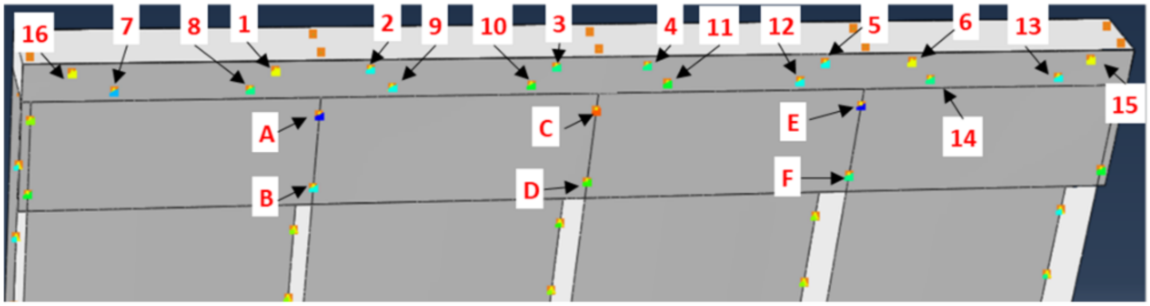

Model-3B: Double row two fastener

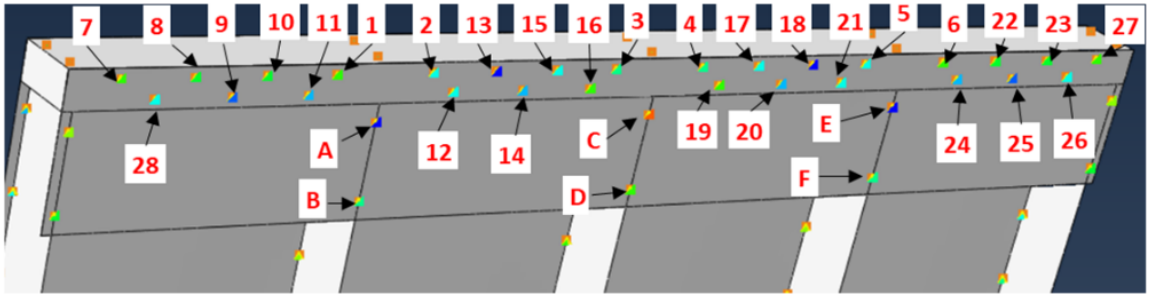

Model-4B : Double row four fastener

Figure 2.22. Fastener sensitivity analysis models 2B and 3B

Table 2-7. Fastener sensitivity analysis force output

	Fastener 1 Withdrawal Force (N)	Fastener 6 Withdrawal Force (N)	Fastener C Lateral force (N)	Fastener D Lateral force (N)
Model 1B	488	490	376	311
Model 2B	343	343	368	303
Model 3B	401	403	363	316
Model 4B	333	333	361	314

2.3. Conclusions

In this chapter, a novel panelized roof system concept was introduced, which integrates offsite manufacturing processes, transportation limitations and onsite installation factors. The holistic approach to designing panelized roofs applies to the fully panelized residential home prefabrication process. The production of the new system is superior in terms of production due to the higher utilization of automated and semi-automated fabrication stations and a reduction in transporting manufactured building components on-site. The structural design requirements of two main components are also presented in this chapter. The ceiling frame analysis and cost estimation show that floor line utilization is the most economical option. However, the 2D analysis ceiling frame ignores the system effect since the support wall and ceiling frame joists will respond as a system itself in actual assembly.

Moreover, due to panelization, there will be two joists side by side at some locations (Figure 2.9b) along the longer direction of the building plan. Those locations will have higher flexural stiffness than other ceiling joists in the assembly. Accommodating this complex system behaviour in design requires three-dimensional analysis. However, this analysis provides the initial basis for further developing an accurate numerical model. Nail connection testing in this study provided the basis for designing some of the main components of a panelized roof, such as the roof panel and support wall. The finite element of the roof panel shows that adding secondary OSB increases the rafter-to-LSL plate connection stiffness. Also, the details of this study are contingent to the specific case of a gable roof. Another limitation of this system is increased on-site workloads due to higher crane lifting activity and connection installation. In terms of future work, a full-scale system-level numerical model would provide more information on system behaviour, allowing for further design optimization.

Chapter 3 : Screw Connection design and analysis

This chapter presents the screw connection design and analysis. These screw connections are intended to be used for roof panel B to ceiling frame at eave line, roof panel A to support wall, and roof panel B to support wall joints. This chapter is based on a published peer-reviewed journal paper Islam et al. (2022b).

Design and experimental analysis of connections for a panelized wood frame roof system

Md Saiful Islam[1,] *, Ying Hei Chui[2] and Mohammed Sadiq Altaf[3]
[1]PhD Candidate, University of Alberta, Canada; mdsaiful@ualberta.ca
[2]Professor, University of Alberta, Canada; yhc@ualberta.ca
[3]Technical Advisor, ACQBUILT Inc., Canada; sadiqa@acqbuilt.com
*Correspondence: mdsaiful@ualberta.ca

Abstract: The results of an experimental study on the short-term mechanical performance of timber screw connections comprising two types of fasteners suitable for a novel panelized roof design process in presented. Thirty-seven specimens of five different connection configurations were tested under quasi-static monotonic loading. The main objective of this study is to provide a preliminary assessment of connection capacity that is key to the successful implementation of a proposed panelized roof design method. It also provides the basis to assist in the development of a numerical model of the novel roof assembly. Additionally, the experimental data is used to check the validity of existing analytical approaches for predicting the strengths of screwed connections comprising engineered wood members. The validation exercise shows that available analytical models can be used to predict the connection capacity of the novel panelized roof.

Keywords: panelized roof, laminated strand lumber, home manufacturing, wall framing stations, self-tapping screw

3.1. Introduction

The panelized fabrication is a form of the off-site construction method. This process subdivides a building model into subassemblies such as wall panels and floor panels to manufacture buildings in a factory environment. Two-dimensional construction of building elements makes it more flexible in various architectural designs with a trade-off that substantial on-site workload in contrast to modular construction. In Canada, all panelized building manufacturers implement digital CAD drafting for building design and adopt automated and semi-automated manufacturing processes (Koo et al. 2020). Typically, a light frame panelized house production facility encompasses several workstations, e.g., wall framing station (Figure 3.1a), sheathing assembly section, floor production line, and roof assembly section. These production lines fabricate the corresponding components using Building Information Modelling (BIM) and CNC machines, which make the process more efficient with minimal wastage of material and higher productivity. As a result, this panelized construction method is faster, and superior compared to the traditional stick-built process. In current residential house construction, the roof structure typically consists of a series of triangulated trusses fabricated with dimension lumber that is connected with light-gauge truss plates. These triangulated trusses are often fabricated in a factory and brought to the job site. The final structure is constructed by connecting the triangulated trusses using wood-based sheathing panels. Because of this type of roof system, the present light frame offsite house construction method is classified as partially panelized since the roof production process is the same as the traditional stick-framing process, with the only difference being they are built within factory space and transported to the site as a volumetric module(s) (Figure 3.2).

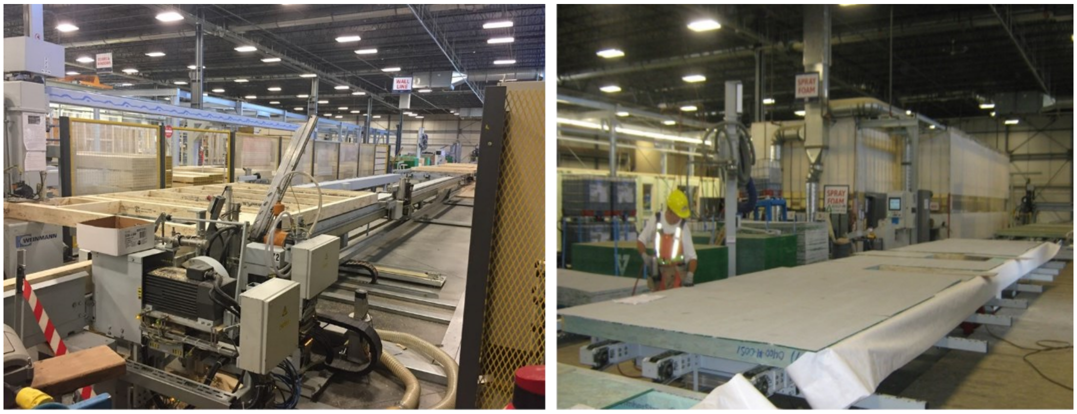

(a) Wall framing station (b) Sheathing station

Figure 3.1. (a) Framing (b) Sheathing stations of wall production line (ACQBUILT Inc. 2019).

This process of roof production is significantly less productive in contrast to the other component production stations such as wall and floor lines. In fact, from the manufacturing perspective, roof workstation imbalances the overall production rate, taking into account the effect on fabrication efficiency at other workstations.

Figure 3.2. A roof production line (ACQBUILT Inc. 2019).

For instance, an Alberta-based home manufacturer's wall production station is capable of producing wall panels for three homes in an 8-hour shift, whereas one roof-framing workstation produces only one complete roof (Altaf 2016). A time study of current roof manufacturing stations shows that one complete gable roof production requires an average of 82.5 man-hours in contrast to only 6 man-hours for the walls (Brown 2020). The penalization of roofs is an improvement to current factory-based house construction that can be introduced to further reduce the cost of houses. The prefabricated roof panels need to be connected on-site to make this innovative panelized roof system perform structurally. Therefore, the development of various panel connections is a key part of the research leading to the implementation of the panelized roof systems. A study was conducted to develop these connection details, which is the subject of this chapter. Gable roofs are arguably the most common roof structure for single-family residences, garages, barns, warehouses, and factories in North America. Hence, this study focuses on the connection development of the new panelized-roof system for the gable-type roof that takes into account manufacturing factors and on-site assembly efficiency.

In the development of the required connection details, the entire gable roof was divided into several subsections. The dimensions of these subsections must comply with the production line constraints, transportation trailer capacity, crane lifting limitations, and on-site installation considerations. The resulting system for a typical two-storey house with a gable roof comprises the following components (Figure 3.3): a) Roof panels, b) Support wall panels, c) Celling frames, d) Beams spanning over two support walls, e) Gable Ends, and f) Inter-component connections, including the inclined roof panel-to-support wall, ceiling frame-to-load-bearing shear wall, and the support wall-to-ceiling frame. The roof panels and support walls are produced in the wall production line using laminated strand lumber (LSL) and Oriented Strand Board (OSB). Whereas the ceiling frames are produced in the floor line using wood I-joists. Details of the panel and ceiling frame design are discussed in Islam et al. (2021, 2022a).

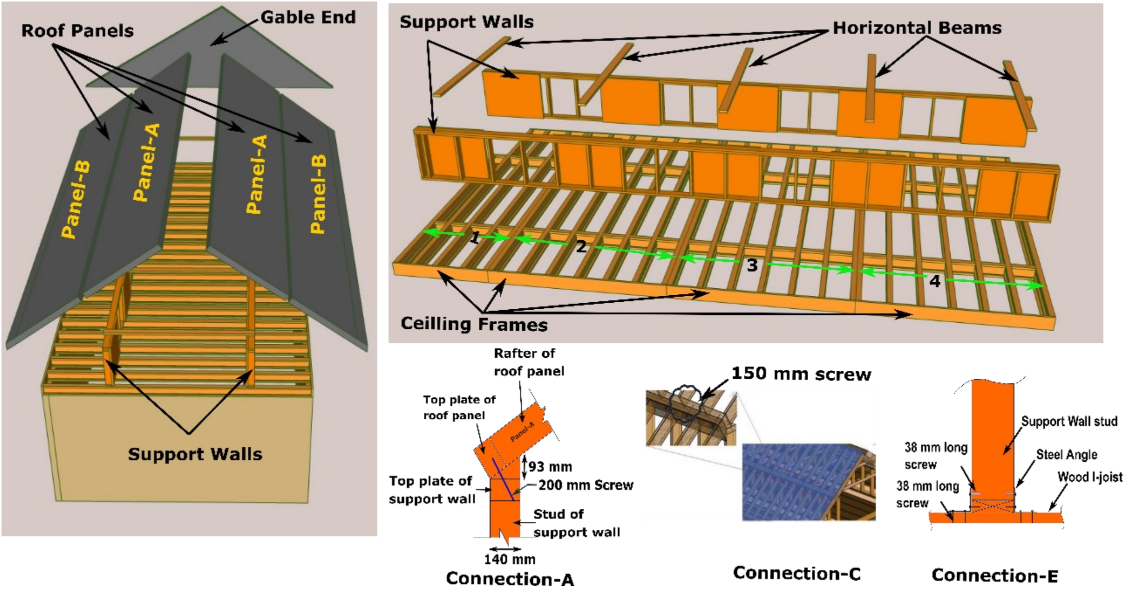

Figure 3.3. Panelized roof concept.

In brief, the production process of the roof panels is the same as the wall production; for example, the framing operation is performed in the framing station (Figure 3.1a) and attaching the OSB to the finished frame is completed in the multifunction bridge (Figure 3.1b) of the wall line. Other components such as roof panel to support wall connection requires a combination of automated and manual operations. For instance, wedge pieces for connection can be produced on a CNC-controlled processing machine which is capable of cutting at any angle and installing screws manually.

3.2. Development of Connection Details

The complete panelized roof is a complex three-dimensional (3D) system, that consists of an assembly of several components, where inter-component connections are a significant factor in the effective implementation of this design. In this system, all the panels are assembled at the site, and the inter-component connections must be easy to install with a minimum workload. In total, the panelized roof has the following eight primary joint types (Figure 3.4): (i) Connection-A: Support wall-to-panel-A connection; (ii) Connection-B: Support wall-to-wedge connection for panel-B; (iii) Connection-C: Panel-to-panel connection; (iv) Connection-D: Panel-B-to-ceiling frame connection at the eave line; (v) Connection-E: Support wall-to-ceiling frame connection; (vi) Connection-F: Apex line connection; vii) Connection-G: Gable end-to-roof panel, viii) Connection-H: Gable end-to-support wall.

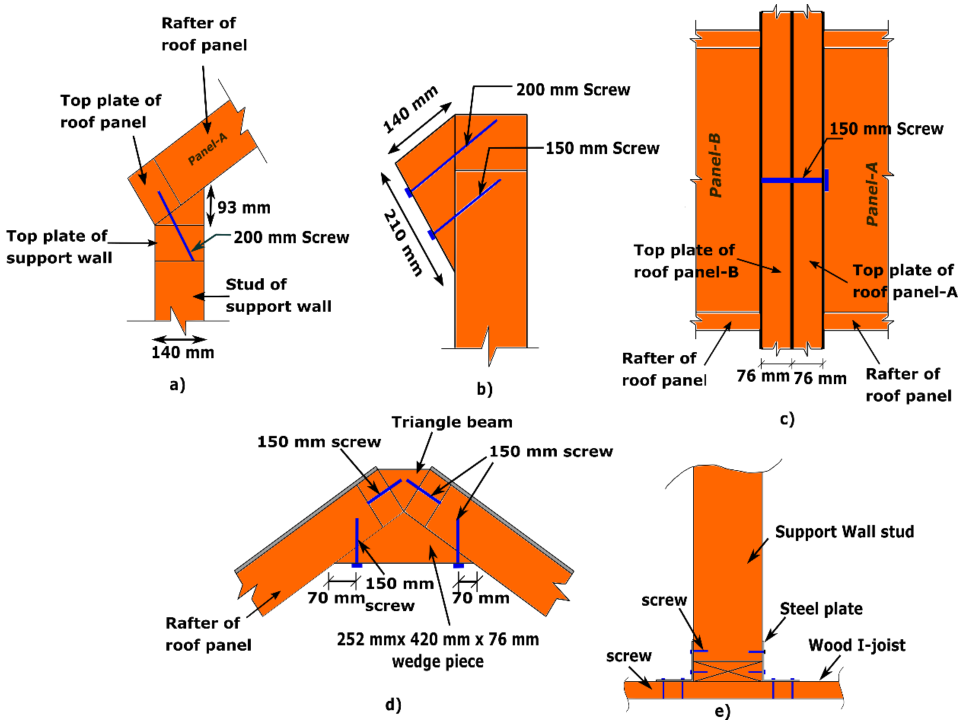

Figure 3.4. a) Connection-A and Connection-D, b) Connection-B c) Connection-C, d) Connection-F, e) Connection-E.

Connection-A comprises a 200 mm screw connecting the top plates of the support wall and roof panel (Figure 3.4a), whereas panel-B is supported on a wedge piece (210 mm × 140 mm × 76 mm) attached to the support wall using two screws (200 mm and 150 mm long) in the case of Connection-B (Figure 3.4b). Connection-C is fabricated using a 150 mm screw to connect the top plate of the roof panels laterally (Figure 3.4c). A similar joint configuration as Connection-A can be used for panel-B-to-ceiling frame connection (Connection-D) at the eave line. Connection-E consists of a 12 ga 90° steel angle plate and 38 mm long screws (Figure 3.4e). These screws are commercially available and an alternative to common 10d nails with a higher load capacity. The apex connection consists of a 150 mm screw joining the two opposite side framing rafters of the roof panel to a 252 mm × 420 mm × 76 mm wedge piece, and the top plate of the two roof panels is connected to a triangular-shaped beam via 150 mm screws (Figure 3.4d). Finally, the gable end-to-roof panel connection is a timber-to-timber screw connection with a 150 mm long screw, whereas in the case of the gable end-to-support wall connection, screws similar to the Connection-E are utilized (Figure 3.5).

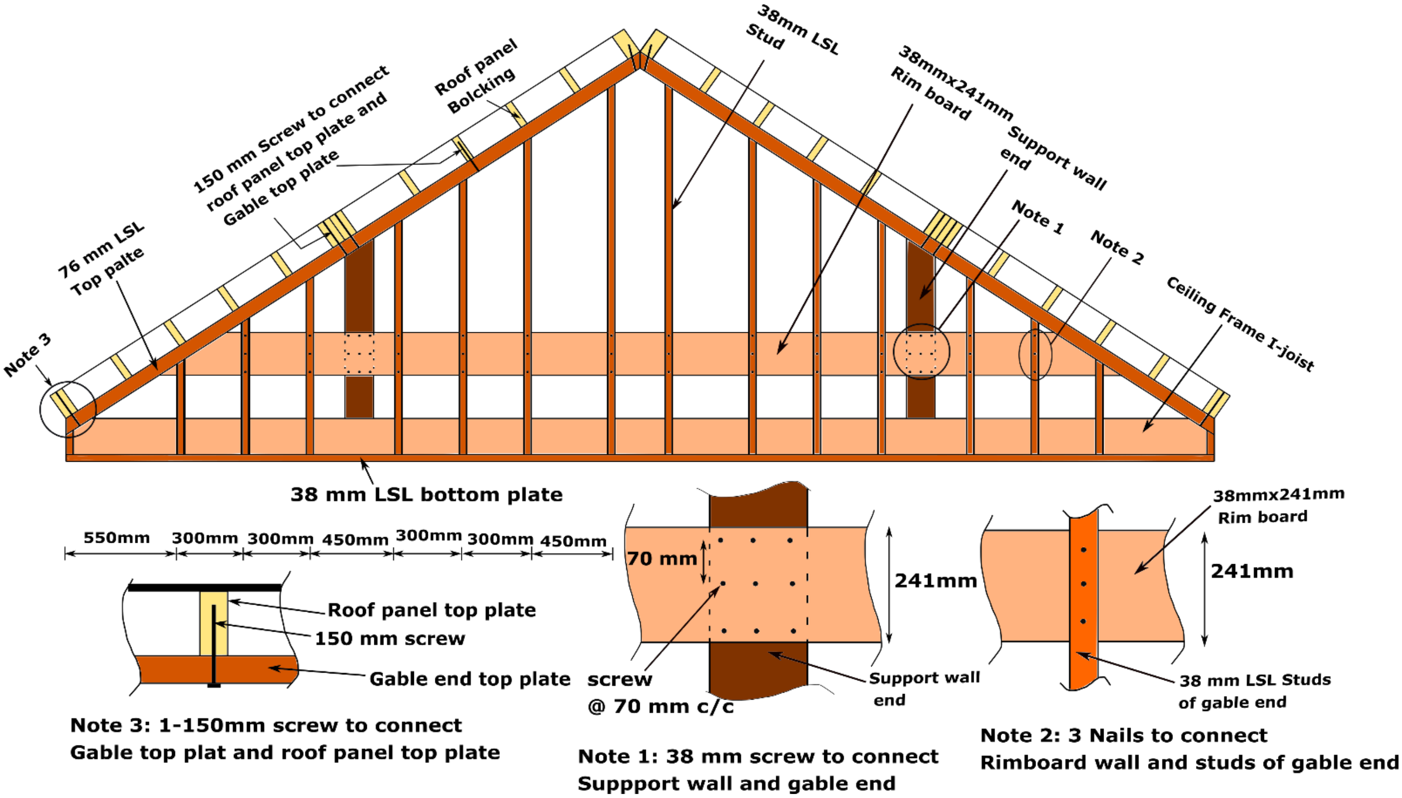

Note 3: 1-150mm screw to connect Gable top plat and roof panel top plate

Note 1: 38 mm screw to connect Suppport wall and gable end

Note 2: 3 Nails to connect Rimboard wall and studs of gable end

Figure 3.5. Connection-G and H.

The location and corresponding load case of the connections explained previously are shown in Figure 3.6. Depending on the load cases the connections are subjected to lateral or withdrawal load.

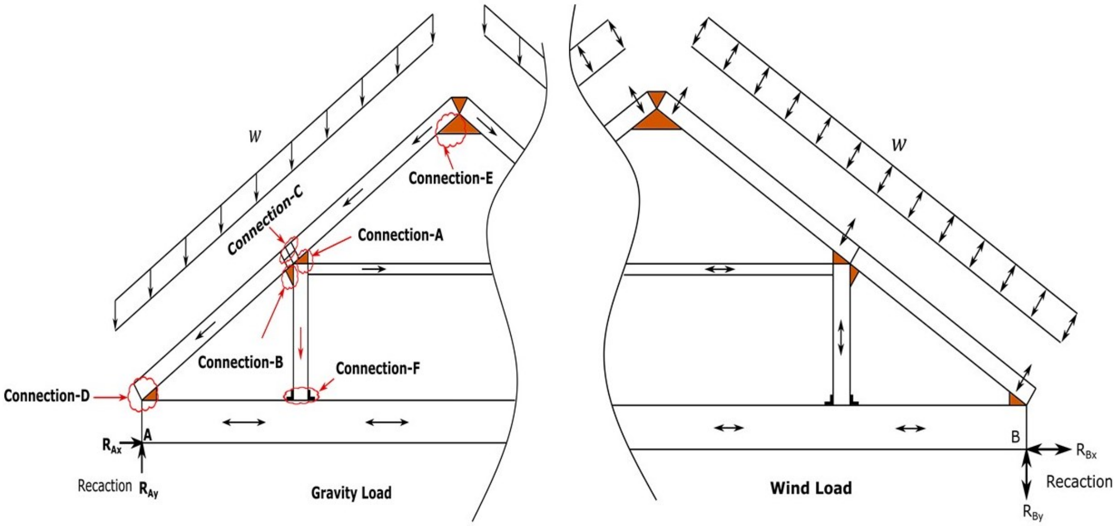

Figure 3.6. Connection location and load cases.

For instance, Connection-A and D are subjected to lateral loading along the inclined plane of the wedge in the gravity load case (Figure 3.7a) whereas withdrawal in the wind uplift load case. For Connection-B, it is required to determine the shear capacity along the vertical plane of the support wall (Figure 3.7c), while connection-C is subjected to lateral load in two different strand directions of LSL (Figure 3.7d and e). Connection-E resists shear load for the angle plate side attached to the support wall and screws withdrawal force for other right-angle parts of the connection, as shown in Figure 3.7h. Connection-F is subjected to shear loading in the gravity load case but a combined axial and lateral load in the wind load case (Figure 3.7g). So, it is evident that experimental evaluation is required to generate test data that can be used to assess their load-carrying capacities for structural design purposes. An experimental study was conducted to test all connections except Connection-G and Connection-H as they are similar to laterally loaded timber-to-timber connections and capacity assessment can be performed using the analytical model available in timber design standards, such as CSA O86-19 (CSA 2019).

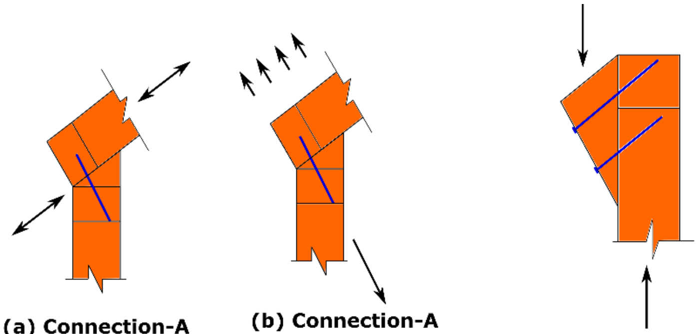

(a) Connection-A in lateral loading

(b) Connection-A in withdrawl

(c) Connection-B in lateral loading

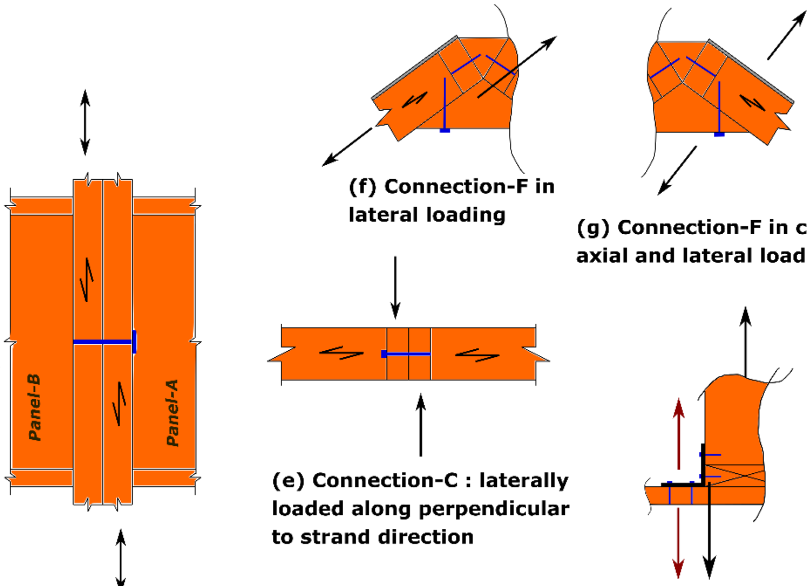

(f) Connection-F in lateral loading

(g) Connection-F in combined axial and lateral loading

(e) Connection-C : laterally loaded along perpendicular to strand direction

(d) Connection-C : laterally loaded along parallel to strand direction

(h) Connection-E : laterally loaded in one side and withdrawl in other side of steel angle

Figure 3.7. Loading conditions of the connections.

3.3 Materials

3.3.1. Screws

There were two types of screws employed in the experimental study: a) partially threaded self-tapping screw primarily used in mass timber products (Rothoblaas HBS) and b) timber screw with flat head predominantly used in light-frame wood construction as an alternative to bolts and traditional lag screw (Simpson Strong-Tie SDWS) for Connection-A and Connection-B (Rothoblaas 2021; Simpson Strong-Tie 2022). The geometries of the HBS and SDWS screws are quite similar to each other, with a milling cutter between the thread and the shank and a pronounced cutter on the tip. The main difference between the two screws lies in the shape of the head, with a countersunk head in the case of the HBS screw. The dimensions and the mechanical properties provided by the relevant European Technical Approval (ETA) (ETA 2019) and Uniform Evaluation Service (UES 2022) reports are summarized in Table 3-1. For Connection-C, only SDWS screw was used in this experimental study since the screw manufacturer's Simpson Strong-Tie (2019) technical data does not have the shear capacity for engineered wood products. The Connection-E test specimen was fabricated using HBS screws only since it can be driven faster than SWDS screws. It is worth mentioning that half of this connection installation will be performed at the site, and faster screw installation is preferred.

Table 3-1. Screw geometry and properties.

Connector	HBS Screw		SDWS Screw	
Commercial name	HBS6150	HBS6200	SDWS22600DB	SDWS22800DB
Fastener length (mm)	150	200	152	203
Shank length (mm)	75	125	82	133
Head diameter (mm)	12.0	12.0	19	19
Shank diameter(mm)	4.3	4.3	5.5	5.5
Nominal diameter (mm)	6.0	6.0	7.7	7.7
Tip diameter (mm)	3.95	3.95	5.0	5.0
Head thickness (mm)	4.5	4.5	-	-
Characteristic yield moment (N-mm)	9494	9494	25590	25590
Characteristic tensile strength (N)	11300	11300	-	-
Allowable tensile strength (N)	-	-	7006	7006

3.3.2 Timber Elements

As previously mentioned, the framing members of the roof panels are structural composite lumber and dimension lumber. The structural composite lumber was Laminated Strand Lumber (LSL) of 1.30E grade (Weyerhaeuser 2021). The product is manufactured from wood strands blended with an isocyanate-based binder adhesive. The manufacturing process of LSL primarily orients the wood strands parallel to the long axis of the mat within a range of ±10° (Lam 2001). As a result of cross laminating between cells in wood strands, LSL has high fracture toughness relative to most other solid wood products (Murty et al. 2007). The mechanical properties and density of the LSL from product documentation (CCMC 2019) and experimental data are reported in Table 3-2.

Table 3-2. LSL properties

Grade	1.30 E
Modulus of Elasticity (MOE) (MPa)	8965
Density (kg/m^3)	≥624.72
Density (experimental) (kg/m^3)	698.80
Equivalent Specific gravity (connection design), SG	0.5

3.4. Fabrication of Connection Specimens

The complete assembly of the Connection-A specimen is comprised of three components, such as 140 mm × 205 mm × 76 mm (representative element of roof panel -A), 140 mm × 330 mm × 76 mm (representative element of support wall top plate) LSL cut pieces, and 93 mm × 140 mm × 76 mm LSL wedge pieces (Figure 3.8). The wedge piece was first glued on the top plate element and a 200 mm screw was inserted at an angle of 30° with the vertical direction of the stud to connect the roof panel part (Figure 3.8). A total of 23 LSL pieces were fabricated to obtain 7 representative samples for the shear capacity test and 9 samples for the wind uplift test of this connection type. Connection-B controls the slope of the roof panel, and it had the most complex fabrication setup. It had two components, i.e., a small representative element of the support wall panel and the wedge piece. First, a total of 16 225 mm × 410 mm small panels (Figure 3.9a) were fabricated using two 38 mm LSL studs, a 76 mm top plate, and 9.5 mm OSB that represent a sample of the support wall, and then the wedge piece was connected using two self-tapping screws (STS) as shown in Figure 3.9b, which resembles the actual connection.

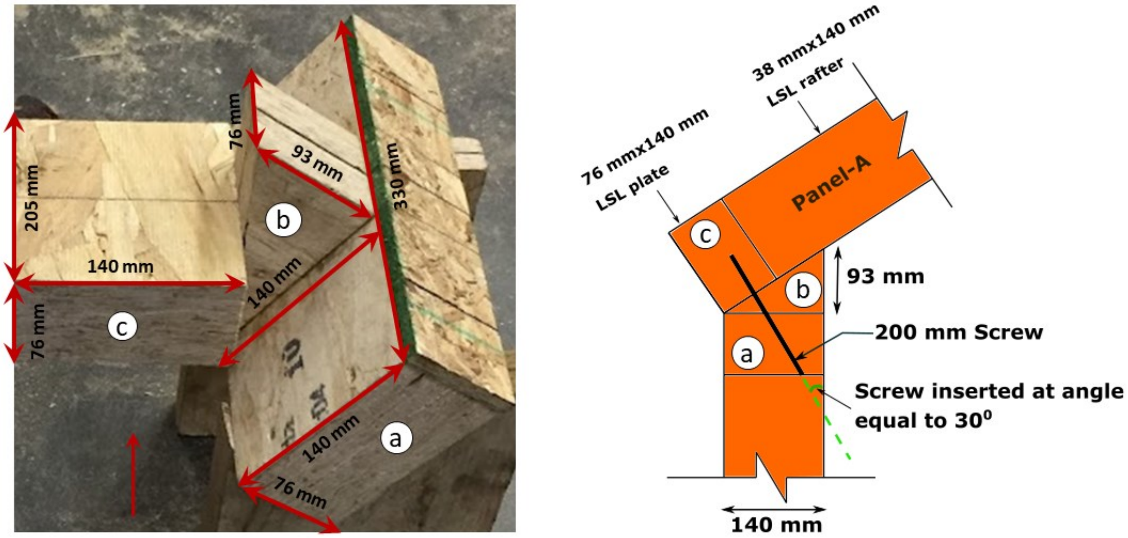

ⓐ Rrepresentative element of Support wall top plate stud ⓑ Wedge piece ⓒ Rrepresentative element of roof panel -A

Figure 3.8. Connection-A specimen.

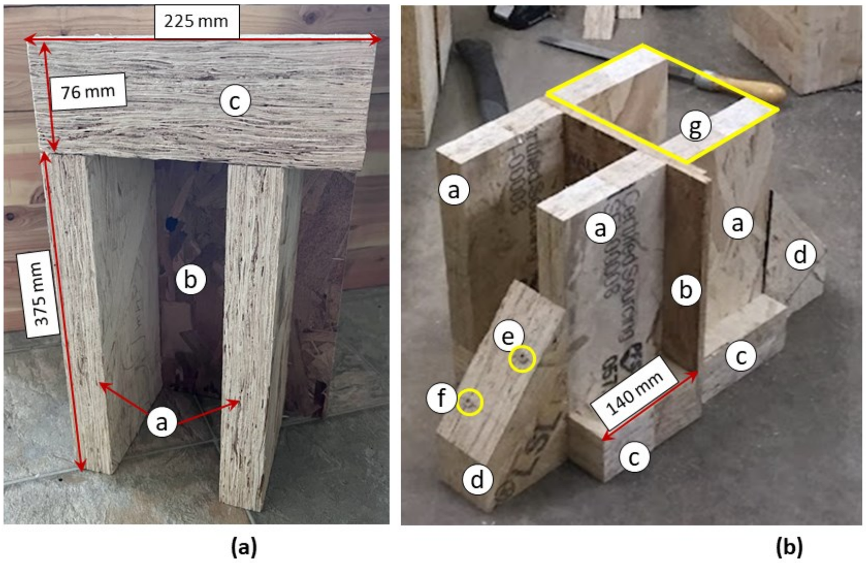

ⓐ LSL Stud (38 mm x 140 mm) connected to the Wedge piece

ⓑ 9.5 mm OSB

ⓒ 76mm x140 mm top plate connecting the Wedge piece

ⓓ 76 mm x 140mmx 210 mm Wedge piece

ⓔ 150 mm Screw connecting the wedge to 38 mm LSL Stud

ⓕ 200 mm Screw connecting the wedge to 76 mm Top Plate

ⓖ Second Panel Connected rigidly with the first panel

Figure 3.9. (a) 225 mm x 410 mm Panel fabrication (b) complete Connection-B specimen.

To create a symmetric pushout test setup, two panels were connected side by side rigidly using small screws so that the assembly acts as a single piece (Figure 3.9b) and thus fabricated sample ensured the desired setup as shown in Figure 3.14. Additionally, 6 panels (225 mm × 410 mm) were also fabricated for Connection-F specimens (Figure 3.10). The difference, in this case, was the use of a 150 mm long screw to connect the wedge and the roof panel rafter (Figure 3.10). It is worthwhile to note that the other part of the apex connection with the triangular beam shear test is similar to the panel-to-panel connection.

Figure 3.10. Connection-F specimen.

Connection-C samples were fabricated by connecting two pieces of 76 mm × 140 mm LSL side by side using SWDS timber screw in two different orientations as shown in Figure 3.15. Connection-F specimens were fabricated by attaching a 38 mm × 140 mm × 600 mm LSL stud with two 76 mm × 140mm × 200 mm LSL blocks using 12-gauge angle plates and screws as illustrated in Figure 3.11.

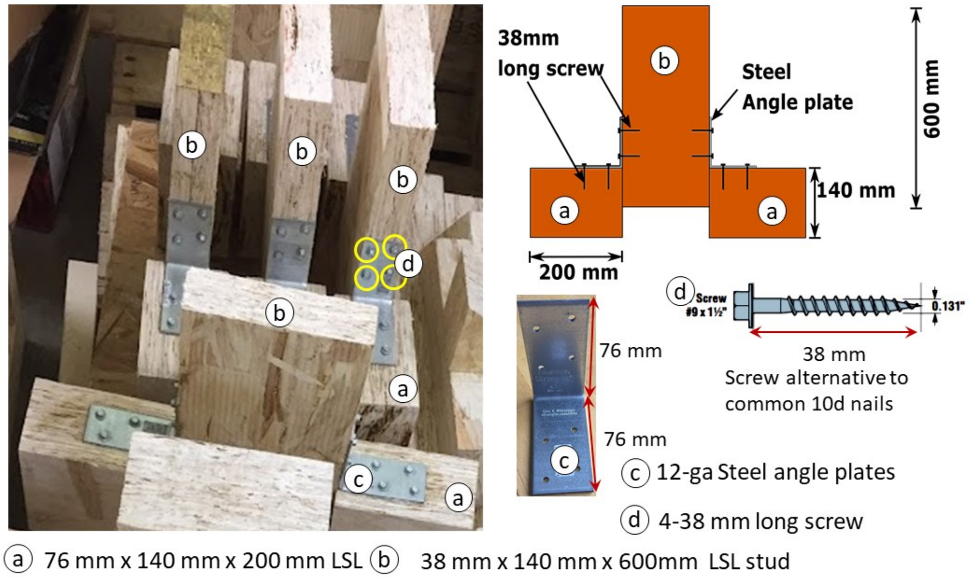

Figure 3.11. Connection-E specimen.

3.5. Test Setup

ASTM D1761 − 12 (ASTM 2012) provides a guideline for the timber screw connection test. According to this standard, the test specimen was subjected to quasi-static monotonic loading at a rate of 2.54 mm/min. Because of the specific orientation of the connection specimens, modified test setups were prepared for each connection type. Although ASTM D1761 – 12 (ASTM 2012) states that displacement should be recorded up to the first drop of load and a slip limit of 15 mm is recommended by EN 26891 (CEN 1991) for ultimate condition, where possible, the specimens were loaded to their actual failure limit state to evaluate the residual capacity. Specimens were tested using an MTS Test Machine with a 1000 kN capacity under displacement control. The proceeding section discusses individual test setup.

3.5.1. Connection-A setup

As can be observed in Figure 3.7a, Connection-A is a single shear connection. Determination of shear capacity requires loading parallel to the plane of the wedge element. So, two connection specimens were placed side by side (Figure 3.12a) on the bottom base steel plate as shown in Figure 3.12b. Then the representative elements of roof panel -A were attached by threaded steel rods passing through the top and bottom steel plates (Figure 3.12b). The representative elements of the support wall top plate were clamped rigidly at the bottom by four threaded steel rods passing through the base steel plate, and an L shaped angle bracket as illustrated in Figure 3.12b. Two cable transducers measured the slip between the central part and the side members.

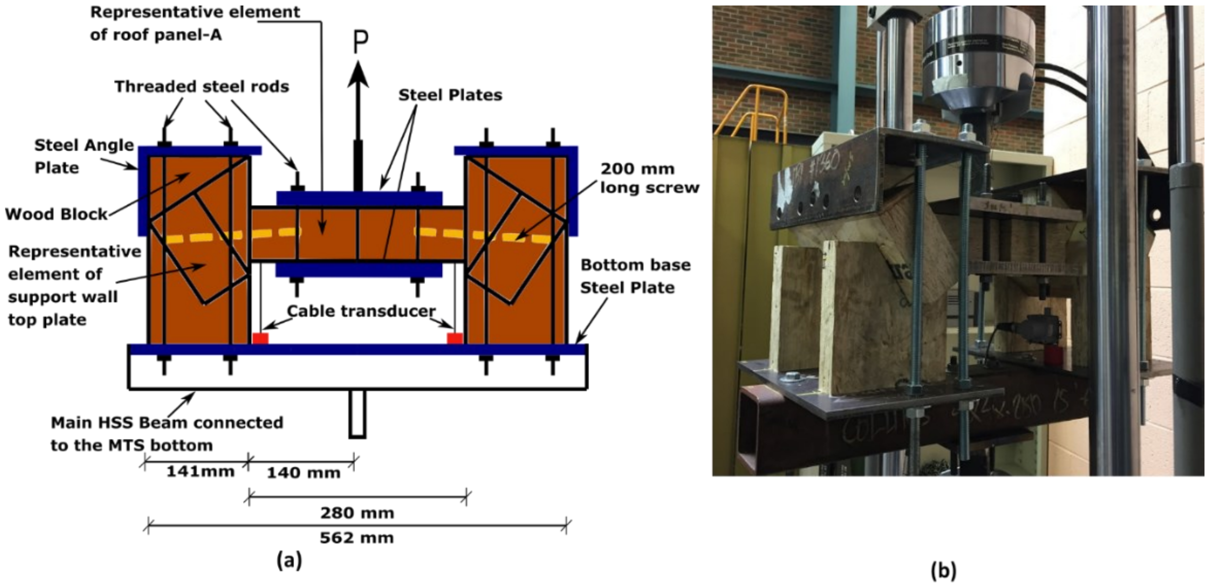

(a)

(b)

Figure 3.12. Connection-A test setup for shear loading: (a) schematics; (b) actual .

The screw withdrawal test apparatus is shown in Figure 3.13. In this case, only one test specimen was placed on the base steel plate (Figure 3.13). The representative element of the support wall top plate part was attached to the base plate using threaded steel rods (Figure 3.13). While the representative element of the panel-A part was connected to the crosshead of the MTS machine by the same mechanism used for the bottom part. MTS head displacement was used to calculate the slip between the connection members.

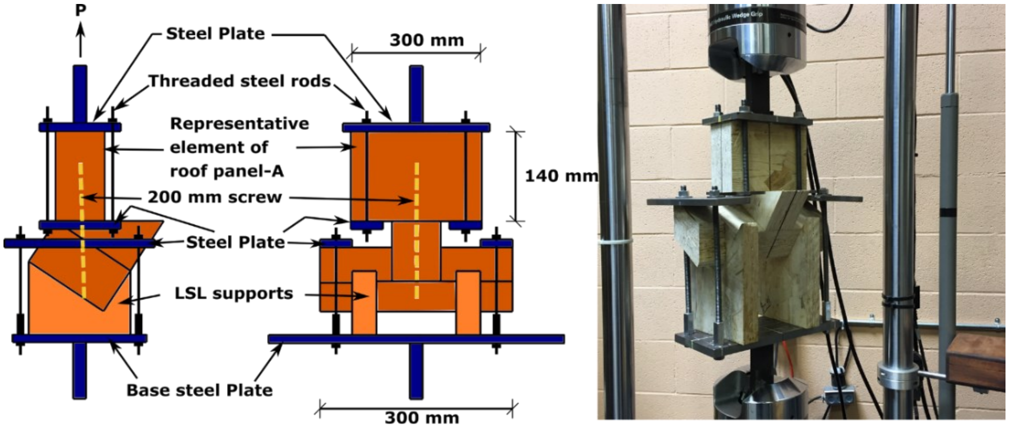

(a) (b)

Figure 3.13. Connection-A withdrawal test setup: (a) schematics; (b) actual image.

3.5.2. Connection-B and Connection-E setup

Connection-B is also a single-shear connection with two screws. The test apparatus to determine the capacity was a modified typical timber connection push-out setup. As can be observed from Figure 3.14, the wedge parts were supported on a small HSS beam, and the L shaped angle plate was clamped to avoid any lateral movement. A steel plate was used to distribute the load evenly on the top of the specimen. Two cable transducers were placed on both sides of the specimen to record the relative slip between the central part and the side members. Connection-F specimens were also tested for shear loading using the same apparatus. Two cable transducers measured the slip of the middle member relative to the side members.

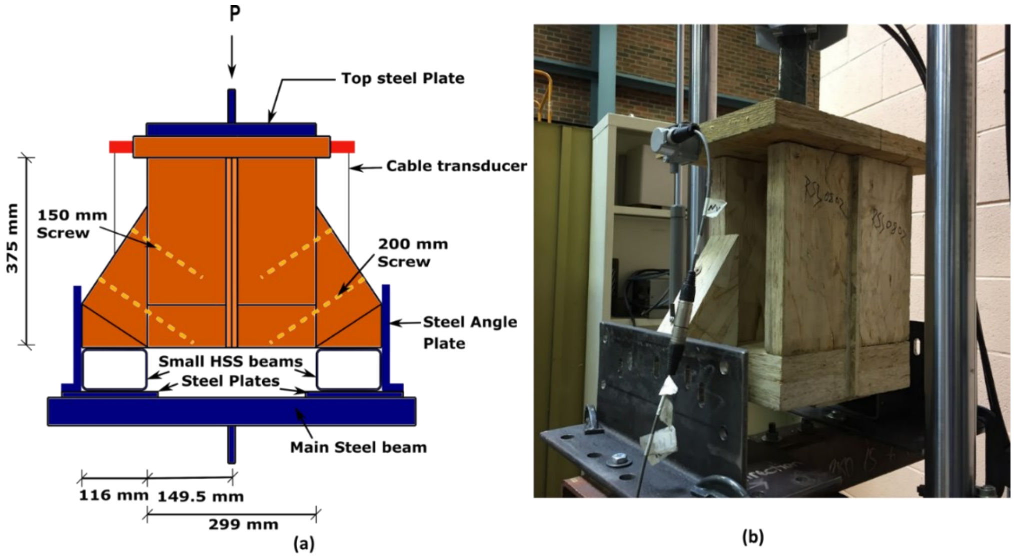

Figure 3.14. Connection-B test setup: (a) schematics; (b) actual image.

3.5.3. Connection-C setup

The Connection-C test assembly was typically pushed out in a single shear plane but two different orientations of the specimen, i.e., (a) loading parallel to the LSL strand direction and (b) loading perpendicular to the LSL strand direction. To reduce minimize friction between the moving side LSL member and the steel beam face, a polypropylene sheet was placed as indicated in Figure 3.15. Two LVDTs measured the relative slip between the connection members.

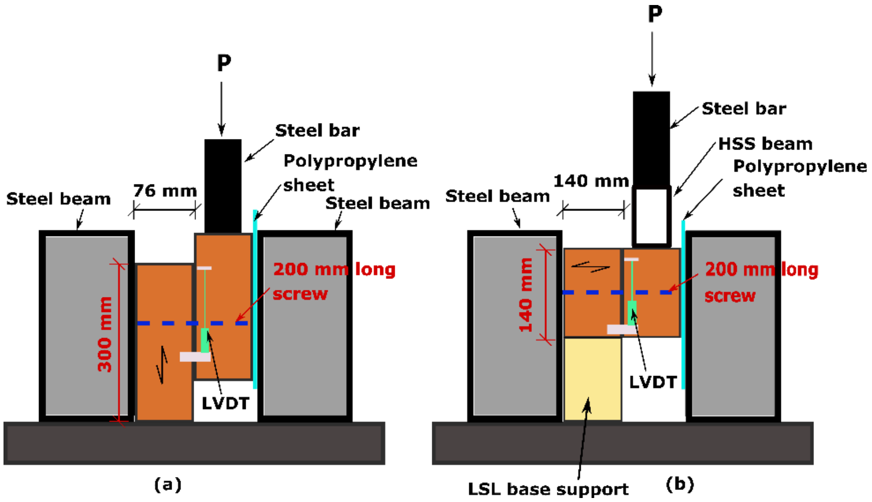

Figure 3.15. Schematics of Connection-C test setup: (a) Loading parallel to strand; (b) perpendicular to strand.

3.5.4. Connection-E setup

Although for this type of connection, the screw manufacturer guide provides shear capacity where screws are inserted on the wider face of timber studs. However, for Connection-B it is required to insert the screws on the narrow face of the LSL. The withdrawal capacity of this connection is available in the screw manufacturer's technical data report (ICC-ES 2021). So, a test setup was developed to determine only the shear capacity of the connection. The side LSL parts were clamped by a threaded steel rod passing through both the bottom base steel plate and upper steel plate as shown in Figure 3.16, whereas the middle LSL part was connected to the crosshead of MTS by the same mechanism. Two LVDTs were placed on either side of the specimen to record the relative slip between the central and side LSL members.

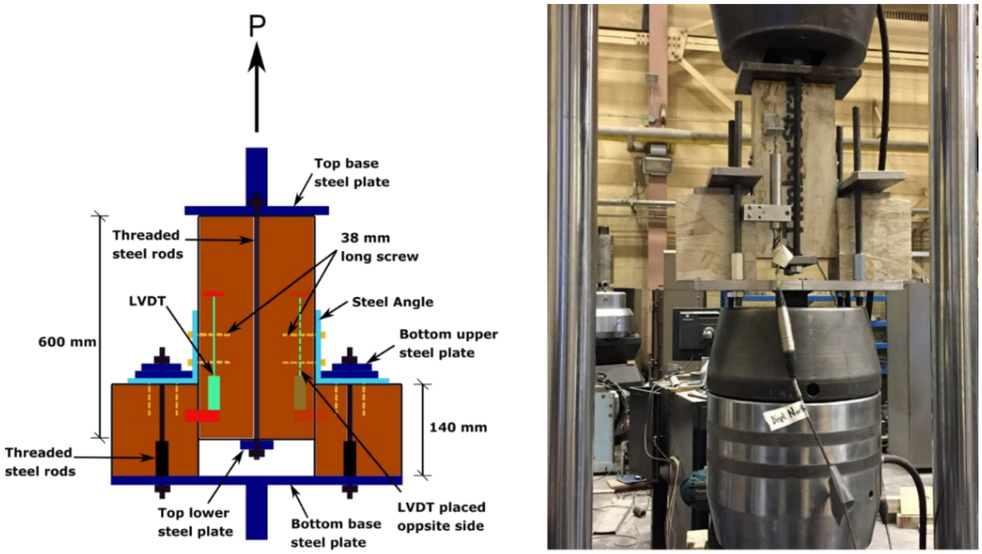

(a) (b)

Figure 3.16. Connection-E test setup: (a) schematics; (b) actual image.

3.6. Assessment of Connection Mechanical Parameters

The connection strength in this study was determined according to EN 26891 (CEN 1991), which defines it as the maximum load before failure of the specimen if the corresponding slip value was less than 15 mm, otherwise the load value at 15 mm slip. The evaluation of the slip modulus, K_s, of all the connections (corresponding to the slip modulus K_{ser} provided by EN 1995-1-1 (CEN 2004)) was calculated by means of the following equation:

$$K_s = \frac{0.4F'_{max} - 0.1F'_{max}}{v_{0.4} - v_{0.1}} \qquad (1)$$

where $v_{0.4}$ *and* $v_{0.1}$ are the connection slips corresponding to loading equal to $0.4F'_{max}$ *and* $0.1F'_{max}$ respectively; F'_{max} is the mean value of the peak load values,

$F'_{max,i}$ recorded peak load for all test repetitions for each connection type (Almeida and Melo Moura 2022; Schiro et al. 2018; Tomasi et al. 2010). The yield load of a timber connection (F_y) is the load value corresponding to the entry into the plastic field. Identifying yield load requires a clear demarcation point between the linear-elastic and plastic regions of the load-slip curve. However, for all load-slip curves, the demarcation point was not easy to identify. Therefore, the ASTM D5764 5% offset method (ASTM 2018) was used to determine the yield point. The 5% offset method defines the yield point as the intersection of a straight line parallel to the initial linear line part (slope between 0% and 40 % of the peak load). The straight parallel line is drawn at an offset of 5% of the diameter of the fastener.

3.7. Results

All the connection test specimens exhibited peak load capacity, and then the loads gradually decreased while deformations increased, except Connection-A specimen fabricated using HBS screws; none of the test specimens failed suddenly with a rapid loss of applied load. The connection performance parameters, such as peak load and slip modulus, that were derived from the test data are reported in Table 3-3. The test mean maximum is reported are normalized by the whole connection, not per screw. For every parameter, the coefficient of variation (CoV), is given. The load-slip curves were obtained by taking the average displacement of two cable transducers/LVDT and the applied load to the specimen which was recorded by a load cell. After the connection test, selected specimens from all the types of connections were cut and opened to examine the deformed shape of the screw, which revealed the failure mode of the joint. In addition to the maximum shear load of the connection specimens, the yield load for each test was also calculated to determine the load at which the connections begin to deform inelastically.

Table 3-3. Test Results

	F_{max} per connection		**K_s (N/mm)**	**F_y (kN)**
	***Mean* (kN)**	***CoV (%)***		
Connection-A in shear loading				
HBS screw	4.53	15.60	823	3.17
SDWS Screw	5.70	13.31	1417	3.37
Connection-B in shear loading				
HBS screw	12.84	10.8	3460	5.89
SDWS Screw	21.27	14.90	5834	12.42
Withdrawal test of Connection-A				
HBS screw Withdrawal	5.88	17	4401	4.38
SDWS Screw Withdrawal	9.20	8.43	5136	5.61
Connection-C				
Loading parallel to the LSL strand	13.72	21.00	5566	6.54
Loading perpendicular to the LSL strand	11.70	20.94	5596	6.5
Connection-E				
Screw and steel side plate	5.46	3.72	3231	2.51
Connection-F				
HBS screw	5.77	17.59	3310	3.76

3.7.1. Connection-A results

Figure 3.17 shows the load-slip curve of the Connection-A test in shear loading. The connection strength and stiffness of the SDWS screw are higher than those of the HBS screw. However, assessment of the failed specimen revealed that the SDWS screw broke inside the point side member, which explains the sharp drop in load after peak value. As can be observed from

Figure 3.18, the failure mode of the HBS screw was yielding followed by two plastic hinges per shear plane, and the bending of the screw continued even after 35 mm of deformation. Thus, the maximum connection strength of the HBS screw connection was defined at 15 mm slip. Figure 3.19 illustrates the load-slip curve of Connection-A in withdrawal. The failure mode of the HBS screw was head pull-through in the side member. As a consequence, there was no well-defined peak point.

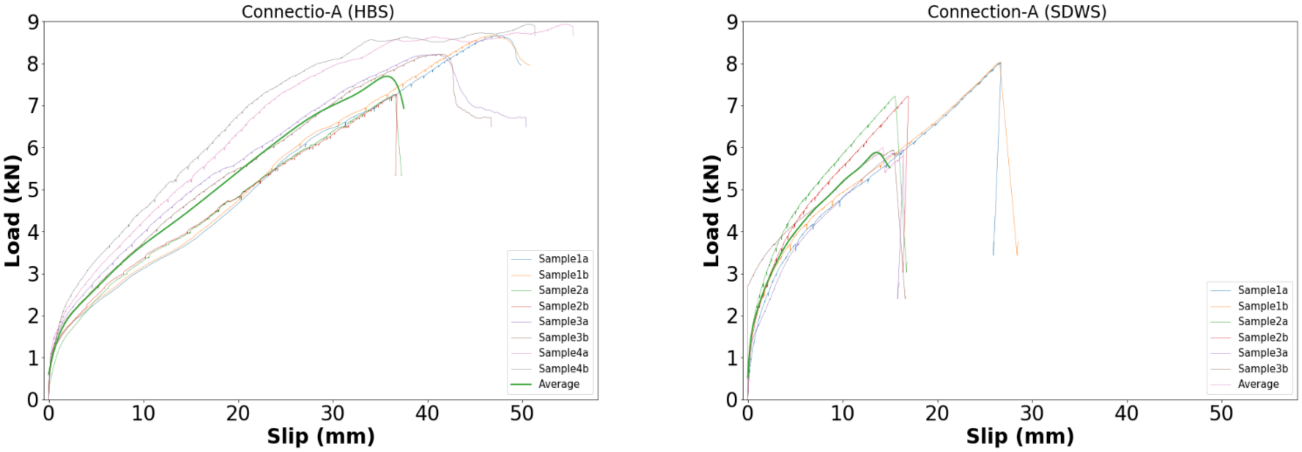

(a) **(b)**

Figure 3.17. Load-slip curve of Connection-A (a) HBS screw (b) SDWS screw.

Figure 3.19 illustrates the load-slip curve of the Connection-A test in withdrawal. Although ASTM D1761 – 12 (ASTM 2012) recommends withdrawal resistance at the peak load value of the test, here maximum withdrawal capacity was defined at 5 mm slip since for standard withdrawal tests of these types of screws have been reported by Almeida and Melo Moura (2022), Gutknecht and Macdougall (2019) and Xu et al. (2021) at slip value of 4 to 6 mm. For SDWS screw Connection-A, specimen failure mode was the withdrawal of the threaded part of the screw.

Figure 3.18. Failure of mode of Connection-A in shear loading (a) HBS screw (b) SDWS screw.

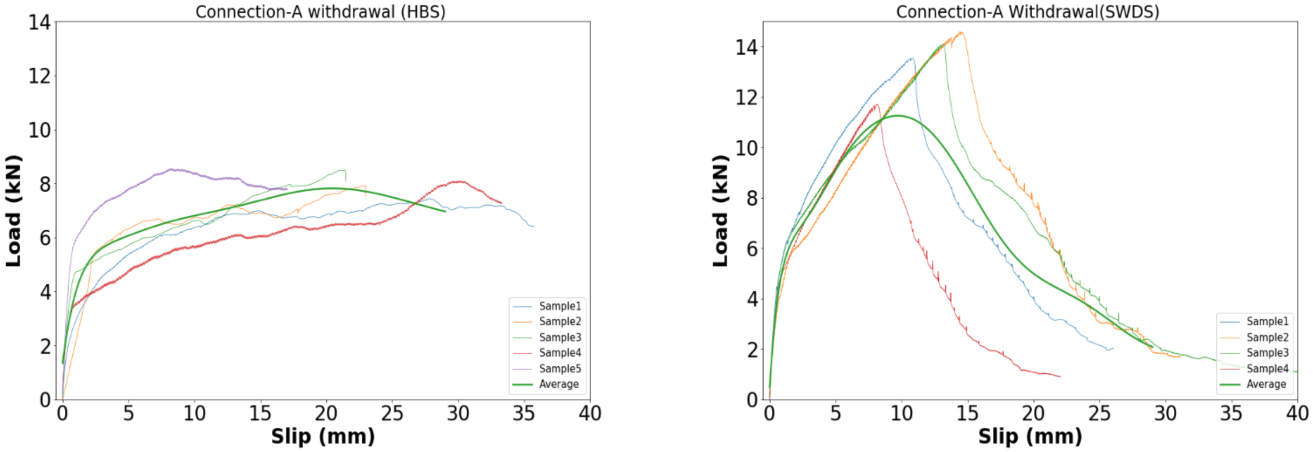

(a) **(b)**

Figure 3.19. Load-slip curve of Connection-A in withdrawal (a) HBS screw (b) SDWS screw.

3.7.2. Connection-B results

For all Connection-B specimens, a crack in the LSL side member was observed after reaching the peak load. Not surprisingly, the connection specimens fabricated using SWDS screws had a higher peak load value than those made with HBS screws, as they have larger nominal diameter and fastener yield moment capacity (Figure 3.20).

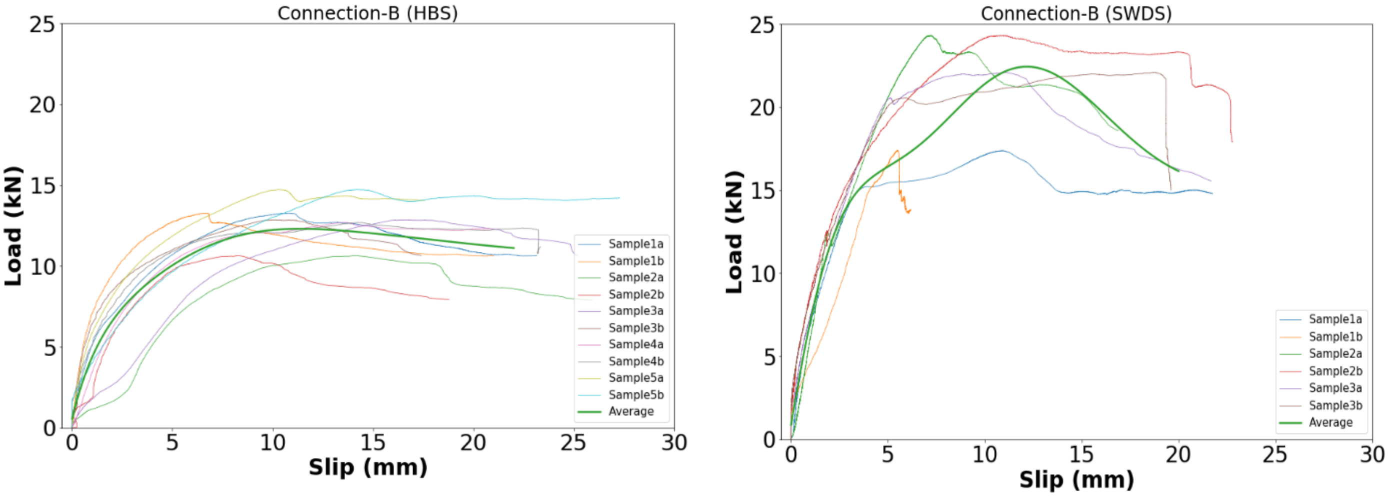

(a)

(b)

Figure 3.20. The load-slip curve of Connection-B (a) HBS screw (b) SDWS screw.

However, the HBS screw connections exhibited more ductile behaviour in contrast to the SDWS screw. Specimen cut of SDWS screw connection revealed the shear failure of the screw itself at the transition location of the beginning of the thread and smooth shank in the case of all Connection-B specimens. As can be observed in Figure 3.22, two plastic hinges were formed on both HBS screws, while for the 150 mm long SDWS screw, one plastic hinge was detected. In addition, to crack development, head pull-through of the fastener into the side member (wedge piece) was also observed in the case of Connection-B made with HBS screws (Figure 3.21). Whereas in the case of the SWDS screw, only crack formation in the side member (wedge piece) and shear failure of the 200 mm long screw inside the main member were noticed.

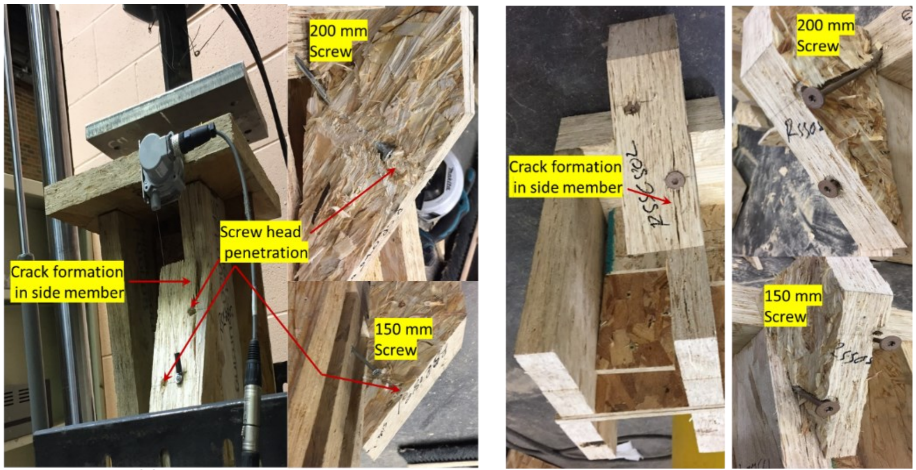

(a) Connection made with HBS screw (b) Connection made with SDWS Screw

Figure 3.21. Failure of Connection-B (a) HBS screw (b) SDWS screw.

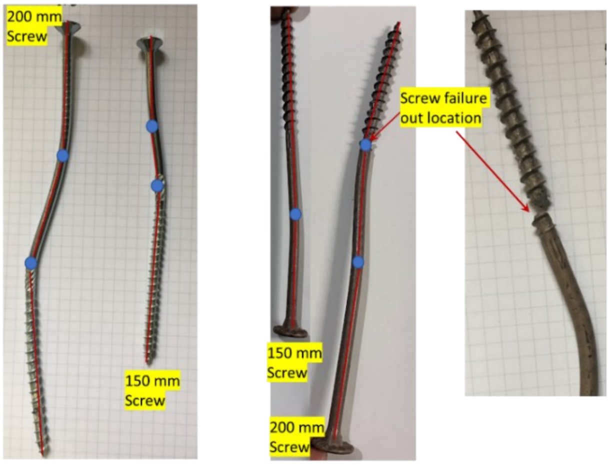

(a) HBS screw (b) SDWS Screw

Figure 3.22. Failure mode: plastic hinge formation of the screws in Connection-B (a) HBS screw (b) SDWS screw.

3.7.3. Connection-C results

Figure 3.23 shows the load-slip curve of Connection-C specimens. There was an insignificant difference in the peak load values for both loading directions. This may be due to the cross-laminating structure of wood strands in LSL, which distinguishes it from natural timber. The failure mode of this connection was yielding of the SDWS screw and ultimately breaking out of the screw inside the point side member (Figure 3.24).

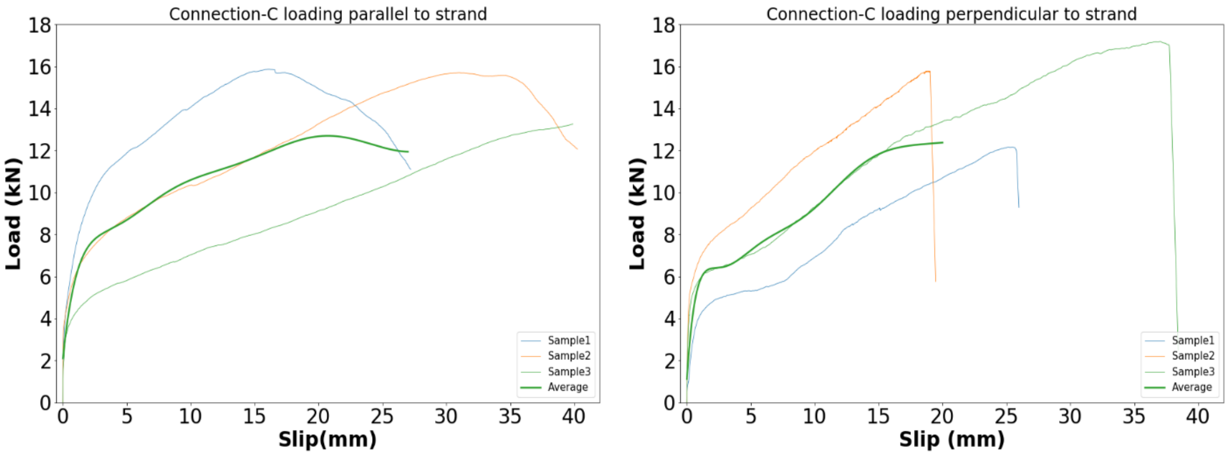

(a) **(b)**

Figure 3.23. Load-slip curve of Connection-C (a) loading perpendicular to the strand (b) loading parallel to the strand.

Figure 3.24. Failure mode of Connection-C.

3.7.4. Connection-E results

As can be observed from Figure 3.25, all the Connection-E specimens exhibited peak load with an average value of 5.77 kN. The failure mode of Connection-E was yielding of screw followed by head pull-through and ultimately forming two plastic hinges. No additional test was performed to assess the connection capacity in withdrawal for Connection-E as it can be estimated using the Eurocode 5 interaction equation (CEN 2004). It should be noted that in wind load, the screw is loaded in a combination of the axial and lateral directions. It was also observed in the Connection-A withdrawal test that the failure mode for HBS screw head was head pull-through. Thus, for Connection-E, it is obvious that screw axial load capacity will be governed by head pull-through. Therefore, only the lateral capacity test for Connection-E was performed.

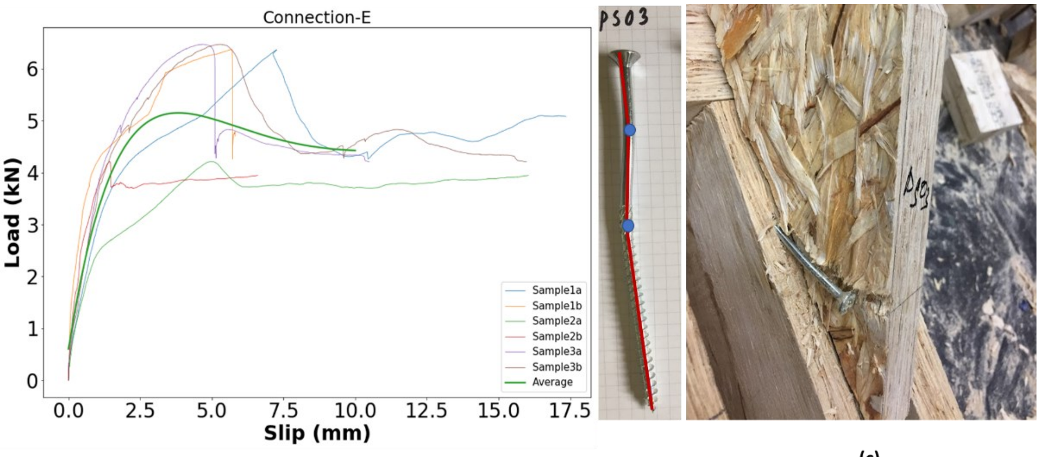

(a) (b) (c)

Figure 3.25. (a) Load-slip curve (b) screw from cut specimen (c) failure mode of Connection-E.

3.7.5. Connection-F results

Connection-F is steel-to-timber connection, and the objective of this test is to check the shear capacity of this connection as screws were inserted on the narrow face of the LSL stud. The maximum mean shear capacity obtained from the test was 5.46 kN, whereas the manufacturer's technical specification (ICC-ES 2021) reported allowable shear resistance of 3.69 kN for timber with SG of 0.5. Since mean test value is higher than the reported value, it is safe to use the design value in the specifier’s guide. However, the withdrawal resistance reported by the manufacturer is 3.1 kN. Therefore, it can be concluded that in the case of Connection-F withdrawal capacity governs. The failure mode of Connection-F was embedment failure in wood, leading to the withdrawal of the screws from the member (Figure 3.26).

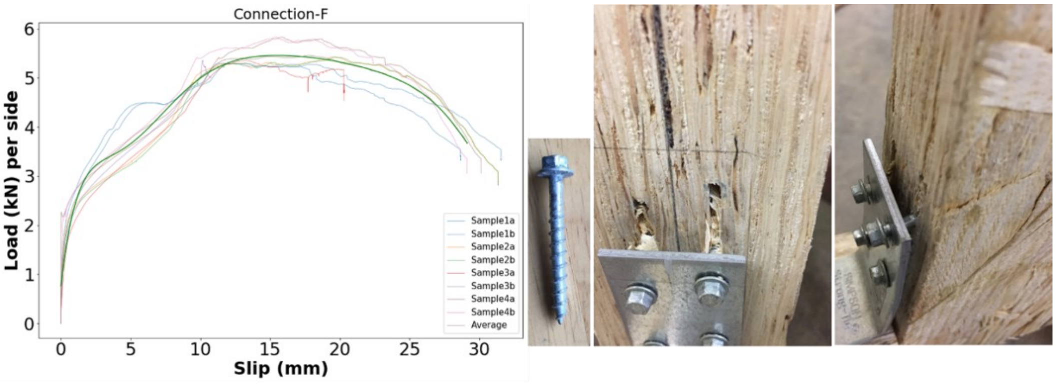

(a) (b) (c)

Figure 3.26. (a) Load slip response, (b) screw from cut specimen (c) failure mode of Connection-F.

The data sets from this study will allow further investigation of the applicability of these connection assemblies with self-tapping screws in designing the panelized roof. As can be observed from the geometry of Connection-A and Connection-B, the angle of the wedge piece depends on the slope of the roof. This study only investigated the connection specimens for one roof slope (8/12), therefore validation of connection capacity using analytical models is discussed in the following section. If the validation with the analytical model can predict the reasonable connection capacity, then it is obvious that for another roof slope, the developed connections can be utilized.

3.8. Comparison Between Experimental Results and Theoretical Models

To facilitate connection design for any roof slope, it is essential to have a methodology that can be used by designers to predict the connection capacity. Hence, a comparison of test data in terms of connection capacity is compared to the values predicted by means of theoretical models available in the literature. The load-bearing capacity ($F_{max,th}$) of screws inserted at 90^{O} with respect to the shear plane can be calculated by using the theoretical model included in the CSA 086-19 (CSA 2019) or CEN (CEN 2004), which is based on Johansen theory (Johansen 1949). However, in Connection-B, the screws were installed at an angle of roof slope with the line perpendicular to the shear plane. A theoretical model for the estimation of the connection capacity of fasteners inserted at an angle with the shear plane was proposed by Bejttka and Blaß (2002). According to their study, the load-carrying capacity of the screws inserted at an angle α with respect to the line perpendicular to the shear plane consists of two components, the bearing resistance and withdrawal resistance. Each of the expressions shown below contains these two component contributions and is associated with a failure mode, with the connection capacity governed by the lowest value of the failure mode a to f:

$$F_{v,R} = min\{R_a;\ R_b; R_c;\ R_d; R_e; R_f\} \qquad (2)$$

$$R_{ax} = min\begin{Bmatrix} R_{ax,1} \\ R_{ax,2} \end{Bmatrix} \qquad (3)$$

The corresponding failure modes are:

$$(a)\ R_a = R_{ax}\ sin\alpha + f_{h,1}\ s_1 d\ cos\alpha$$

$$(b)\ R_b = R_{ax}\ sin\alpha + f_{h,2}\ s_2 d\ cos\alpha$$

$$(c)\ R_c = R_{ax}\ (\mu\ cos\alpha + sin\alpha) + \frac{f_{h,1}\ s_1 d}{1+\beta}\ (1 - \mu\ tan\alpha)\left[\sqrt{\beta + 2\beta^2\left(1 + \frac{s_2}{s_1} + \left(\frac{s_2}{s_1}\right)^2 + \beta^3\left(\frac{s_2}{s_1}\right)^2\right)} - \beta\left(1 + \frac{s_2}{s_1}\right)\right]$$

$$(d)\ R_d = R_{ax}\ (\mu\ cos\alpha + sin\alpha) + \frac{f_{h,1}\ s_1 d}{2+\beta}\ (1 - \mu\ tan\alpha)\left[\sqrt{2\ \beta\ (1+\beta) + \left(\frac{4\ \beta\ (2+\beta) M_y}{f_{h,1}\ d\ s_1^2}\right)} - \beta\right]$$

$$(e)\ R_e = R_{ax}\ (\mu\ cos\alpha + sin\alpha) + \frac{f_{h,1}\ s_1 d}{1+2\beta}\ (1 - \mu\ tan\alpha)\left[\sqrt{2\ \beta^2\ (1+\beta) + \left(\frac{4\ \beta\ (1+2\beta) M_y}{f_{h,1}\ d\ s_1^2}\right)} - \beta\right]$$

$$(f)\ R_f = R_{ax}\ (\mu\ cos\alpha + sin\alpha) +\ (1 - \mu\ tan\alpha)\sqrt{\frac{2\beta}{1+\beta}}\ \left[\sqrt{2\ M_y\, f_{h,1}\ d\ cos^2\alpha}\ \right]$$

where

- $F_{v,R}$ is the load carrying capacity of timber-to-timber connection with inclined screw.
- R_{ax} is withdrawal capacity of the screw.
- s_1 is the anchorage length of the screw into the first wood element measured orthogonally to the shear plane
- s_2 is the anchorage length of the screw into the second wood element measured orthogonally to the shear plane
- $f_{h,1}$ is embedment strength of the head side wood member.
- $f_{h,2}$ is embedment strength of the point side wood member.
- $\beta = \frac{f_{h,2}}{f_{h,1}}$ the ratio of embedment strengths.
- $R_{ax,1}$ is withdrawal strength of the screw from the head side wood member.
- $R_{ax,2}$ is withdrawal strength of the screw from the point side wood member.
- d is the effective diameter of the screw.
- M_y is the yield moment of the screw.
- μ is the friction coefficient at the interface between wood elements (0.25 for wood to wood) and

The characteristics of Connection-B are such that two separate screws and three timber members act together to provide load resistance. The first screw is 150 mm long and connects the 76 mm wide LSL wedge piece (side member) with the 38 mm wide LSL stud member (main member). Whereas the second screw was 200 mm long and attached the LSL wedge piece (side member) to the 76 mm thick top plate of the support wall (Figure 3.27). The two screws have a diagonal spacing of 95 mm (which is greater than the 12 times fastener diameter) in the side member wedge piece (Figure 3.27).

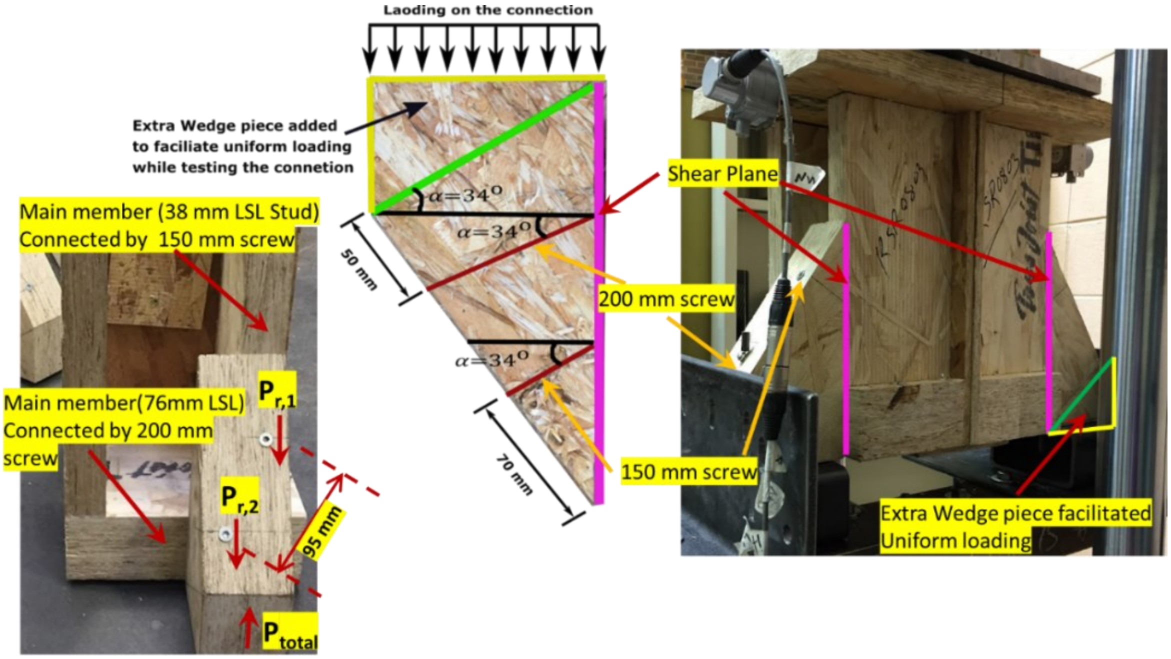

Figure 3.27. Support wall-to-wedge piece connection details for strength prediction.

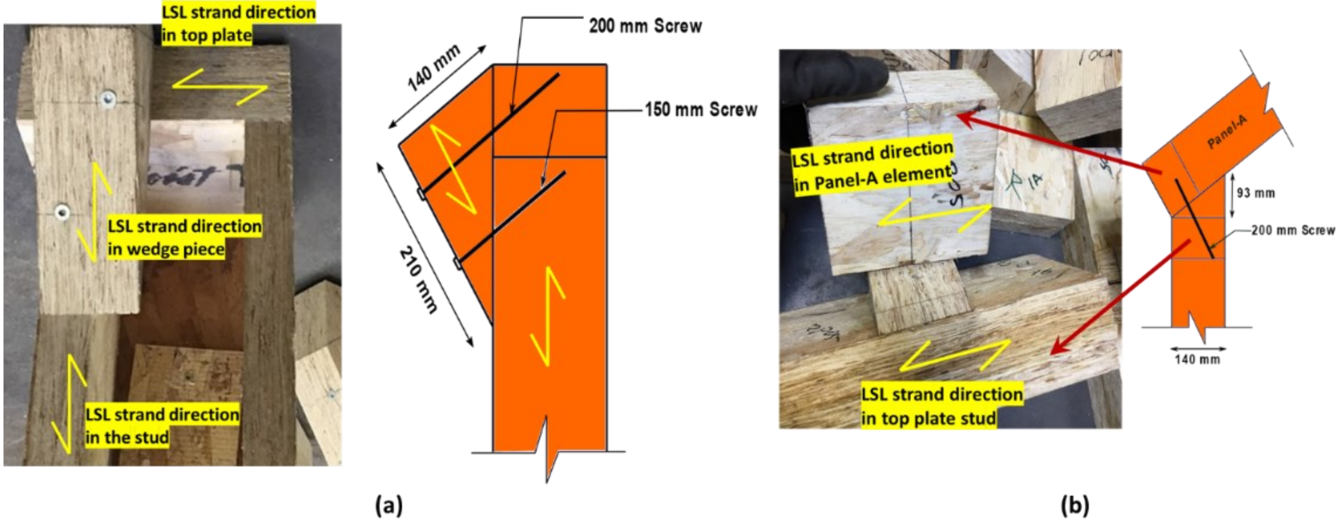

Figure 3.28. Strand direction in the (a) Connection-B, (b) Connection-A.

When the connection is loaded, each screw contributes simultaneously to resist the applied force. So, the theory proposed by Bejttka and Blaß (2002)was applied, adopting the following assumption: a) The total load carrying capacity of the joint will be the combined ultimate loads of the fasteners ($P_{total} = P_{r,1}+P_{r,2}$) as illustrated in Figure 3.27; b) the system parameter, embedment strength of timber (f_h) depends on properties such as screw geometry, surface roughness or load to the grain direction of timber. So, the parallel to grain direction, in this case, is considered along the strand direction of LSL (Figure 3.28a). It should be noted that the side member embedment strength is parallel to the strand direction while the main members are at an inclination equal to (90°-roof angle).

The application of the above model requires estimation of embedment strength (f_h) and screw withdrawal resistance (R_{ax}) of corresponding connection members. The embedment strength of connection members was predicted using the recent Canadian study by Khan et al. (2021) for various inclinations of the screw axis with respect to the grain as follows:

$$f_{h,\alpha} = \frac{0.206\,.\,\rho_k^{0.860}\,.\,d^{-0.0078}}{2.89\,.cos^2\alpha + sin^2\alpha} \qquad (4)$$

For the HBS screw, R_{ax1} of the side member was assumed to equal the minimum value between the head pull-through resistance (R_{head}) and the tensile strength of the screw. In the withdrawal test of HBS screw, head pull-through resistance was observed to be the failure mode. So, R_{ax1} is equal to R_{head} for the HBS screw. For SDWS screw, R_{ax1} of the side member is the tensile strength since the withdrawal test failure was the fracture of the threaded part of the screw. The SDWS screw head diameter is large (19 mm), and the geometry prevents head pull out of the side members. In the case of the main member, R_{ax2} is the axial resistance of the screw corresponding to the lower value of the thread withdrawal resistance (R_{thread}) and the tensile strength of the screw (R_{tens}). The reported value of R_{thread} is governed by both screws. With regards to Equation (3), R_{ax} is the minimum of R_{ax1} and R_{ax2}. So, R_{ax} = R_{head} for the HBS screw and R_{ax}=

R_{thread} for the SDWS screw were used in predicting connection capacity. So, in applying the above model, screw withdrawal capacity (R_{ax}) obtained from the Connection-A withdrawal test was used.

In the case of Connection-A, the wedge piece was glued on the top plate part, and therefore it can be assumed that in connection configuration, they act as a single member (in this case, it is regarded as the side member). The screw was inserted at an angle of 60° with the strand direction of the side member to connect it to the main member that represents the panel-A element (Figure 3.28b), and thus it was inclined at 4° with the line perpendicular to the shear plane (Figure 3.29). For such a small angle, the effect of screw inclination can be ignored since the connection capacity increases with the angle between 15° and 50° (Bejttka and Blaß 2002). So, the analytical validation was performed according to expressions reported in Section 8.7.2 of Eurocode 5 (CEN 2004) and CSA O86-19 (CSA 2019) expressions reported in Section 12.6.

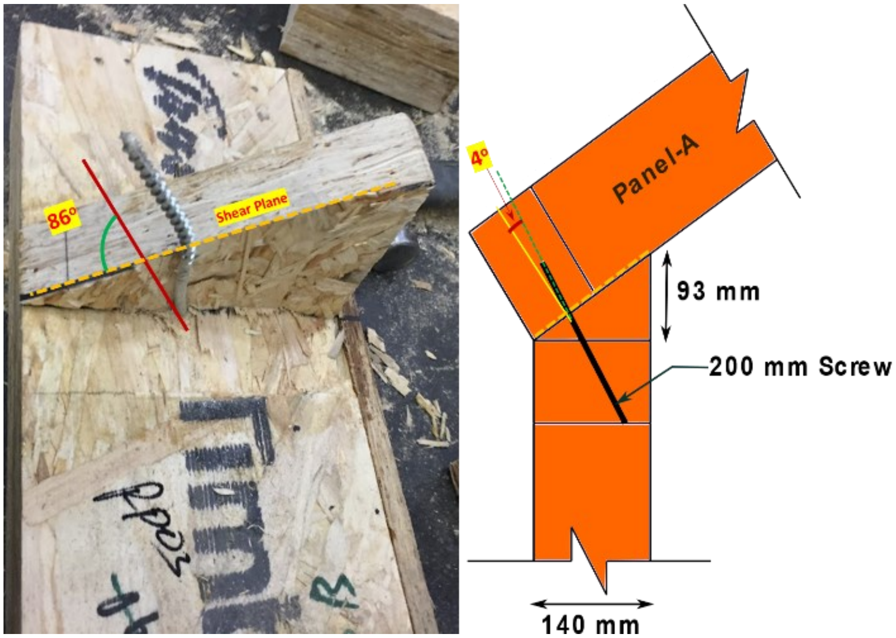

Figure 3.29. Connection -A shear plane.

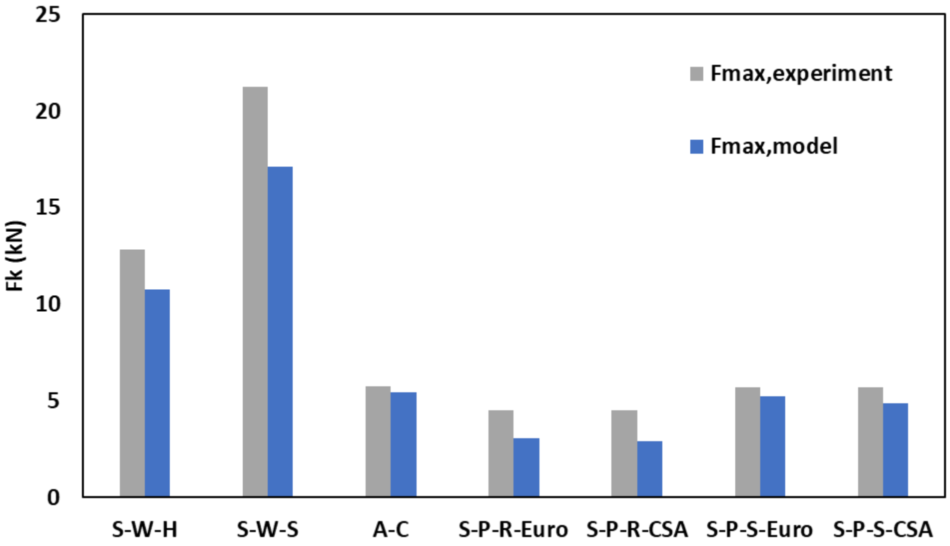

Figure 3.30. Comparison between the experimental and theoretical results in terms of capacity.*

*Note: S-W-R= Connection -B with HBS screw, S-W-S= Connection -B with SDWS, A-C= Apex connection, S-P-R-Euro= Connection -A with HBS screw prediction using Eurocode 5, S-P-S-Euro= Connection -A with SDWS screw prediction using Eurocode 5, S-P-R-CSA= Connection -A with HBS screw prediction using CSA 086-19, S-P-S- CSA = Connection -A with SDWS screw prediction using CSA 086-19. See Appendix-6 the error bar graph for the accuracy of the model in shear capacity prediction.

Table 3-4 summarizes the calculated connection capacities and the failure modes using the above-mentioned models, and Figure 3.30 illustrates the comparison of predicted capacity with experimental mean maximum load values. The model predicted the same failure mode as the test for Connection-B. Overall, it can be concluded that the proposed model by Bejttka and Blaß (2002) predicts reasonable strength of Connection-B (Figure 3.30). Therefore, this model can be used to obtain the design value of this connection for other roof slopes. The predicted capacity of Connection-A using Eurocode 5 (CEN 2004) and CSA 086-19 (CSA 2019) is close to the tested value (Figure 3.30) and the failure mode matched the observed values in the opened tested specimens. So, it is evident from the experimental results that available analytical models can be used to obtain reasonable estimates of design values for the connections of the novel panelized roof. However, there were uncertainties associated with some material input properties, such as embedment strength. Consequently, further studies are highly recommended in order to improve the calibration of material input properties for the theoretical models.

Table 3-4. Theoretical load-bearing capacity calculation

	Connection-B		**Connection-E**	**Connection-A**			
	HBS screw	**SDWS screw**	**HBS screw**	**HBS screw**		**SDWS screw**	
	Bejttka and Blaß model			**Eurocode**	**CSA 086**	**Eurocode**	**CSA 086**
R_{ax}(kN)	5.88	9.20	5.88	5.88	-	9.20	-
$f_{h,1,k}$ (N/mm^2)	12.95	12.70	12.95	25.42	25.42	24.93	24.93
$f_{h,2,k}$ (N/mm^2)	23.52	23.07	23.52	12.99	12.99	12.74	12.74
$M_{y,k}$ (Nmm)	9494	25590	9494	9494	9494	25590	25590
d (mm)	6.00	7.70	6.00	6.00	6.00	7.70	7.70
$F_{max,\ model}$ (kN)	**10.77**	**17.10**	**5.46**	**3.08**	**2.91**	**5.26**	**4.9**
Mean $F_{max,\ experiment}$ (kN)	12.84	21.27	5.77	4.53	4.53	5.70	5.70
Safety factor, $\eta = \frac{F_{max,experiment}}{F_{max,model}}$	1.19	1.24	1.06	1.47	1.56	1.08	1.17
Failure mode	Two plastic hinges per share plane	Two plastic hinges per share plane for 200 mm screw; one plastic hinge for 150 mm screw	Two plastic hinges per share plane	Two plastic hinges per share plane in screw			

3.9. Conclusion

The connections of a novel panelized roof system have been designed and developed. The main goal of this study was to obtain the strengths of proposed connections applicable to roof manufacturing in offsite production facilities. Based on testing of the seven connection configurations, the load-bearing capacity, the load-slip behaviour, and the failure modes were investigated and described. These test data can be used to derive design properties for structural design purposes.

Furthermore, an assessment of maximum wind uplift capacity from the test of common connections used on North American roofs shows the proposed connections have adequate capacity and even, in some cases, are higher than those commonly used in light-frame wood construction. For instance, the average wind uplift capacity of the Connection-A connection capacity varied between 5.88 and 9.2 kN depending on the screw diameter, whereas the tested capacity of the hurricane tie steel plate connection— a very common mechanism used to connect the truss bottom chord with light-frame shear walls in North America, has an average maximum capacity of 3.9 to 5.9 kN as reported in the test conducted by Alhawamdeh and Shao (2020) and Canino et al. (2011). Thus, this study demonstrates self-tapping screws are suitable for connection design in panelized roof fabrication with engineered wood products such as LSL.

The limitation of analytical model validation was the lack of material test data. No embedment test of LSL was performed. Embedment strength depends on the screw diameter and density of the wood. The embedment strength equation used here is primarily developed for wood products, and the LSL density was regarded as the equivalent of Douglas Fir wood species. Consequently, further validation of embedment strength is required before implementing the analytical models. Another limitation was the lack of testing of screw properties. As can be observed from Table 3-1, SDWS screws have a higher yield moment capacity than HBS screws but lower tensile strength. Therefore, future studies should include embedment strength equation development for LSL and experimental evaluation of fastener yield strength in bending.

Chapter 4 : Novel Apex Connection design and analysis

This chapter discusses the novel apex connection invented in this research. The details of connection analysis and design requirement are presented in a published peer-reviewed journal paper Islam et al. (2022c).

Novel Apex Connection for Light Wood Frame Panelized Roof

Md Saiful Islam [1],*, Ying Hei Chui [1],* and Zengtao Chen [2]
[1]Department of Civil and Environmental Engineering, University of Alberta,
Edmonton, AB T6G 1H9, Canada
[2]Department of Mechanical Engineering, University of Alberta, Edmonton, AB T6G 1H9, Canada;
zengtao@ualberta.ca
*Correspondence: mdsaiful@ualberta.ca (M.S.I.); yhc@ualberta.ca (Y.H.C.)

Abstract: Panelized fabrication of light-frame wood buildings has higher productivity than the traditional stick-built method. However, the roof production process is not very efficient due to the structural system and construction method. This study proposes a novel apex connection that allows for a folding mechanism in a panelized light wood frame roof system. Proof of concept of the proposed connection assembly is presented by a 3D printout of the developed connection. Following the steel design code and timber code, the initial estimation of different parameters, such as the pinhole diameter and number screws, were established. A detailed finite element analysis (FEA) was performed to determine the connection strength requirement for different load case scenarios. The results of the FEA and 3D printout of the assembly show that the proposed connection can provide the required folding mechanism before roof installation and can withstand the load in the unfolding state at service.

Keywords: apex connection; folding mechanism; FEA; panelized light frame roof.

4.1. Introduction

The majority of residential buildings constructed in North America are light-frame wood buildings (approximately 90%), mostly in the form of single detached family houses and low-rise multi-story apartments (Asiz et al. 2011; Ellingwood et al. 2004). In light wood frame construction, the primary framing material is dimension lumber, which is often utilized in combination with other wood products such as plywood, I-beams, and oriented strand board (OSB) to fabricate a building (Jellen and Memari 2019; naturally:wood 2022; U.S. Department of Housing and Urban Development 2017). However, in recent decades, application of engineered lumber such as laminated strand lumber (LSL) has increased due to the dimensional stability of this structural composite lumber product and the adoption of an off-site construction process. For example, an Alberta-based prefab company in Canada uses LSL and OSB to produce light frame walls and their wall production is fully automated, whereas floor production uses wood I-joist in combination with a semiautomated process (ACQBUILT Inc. 2019). This type of light wood frame construction is termed panelized construction. Panelized construction of light wood frame homes is drawing attention in North America due to its design flexibility and on-site assembly cost savings (Altaf et al. 2018a; Wang et al. 2020a). It utilizes manufacturing principles to build light-frame wood buildings. This off-site construction process subdivides a building model into subassemblies, such as wall panels, floor panels, and volumetric roof elements, which are manufactured in a factory environment and then shipped to the site for installation. A light-frame panelized-building production facility typically encompasses several workstations such as wall and floor production lines.

As most construction activities in the panelized construction of light wood frame buildings are performed in a manufacturing environment, it is critical to obtain optimal productivity in the production lines (Altaf et al. 2018a; Wang et al. 2020a). In the current panelized construction process, the roof is built using closely spaced wood trusses that support OSB sheathing and roofing materials (on the upper chord) and drywall ceiling materials (on the lower chord). The entire roof of a single detached home is subdivided into four or five small volumetric units based on the floor area and is manufactured on the roof production line (ACQBUILT Inc. 2019). The fabrication of roofs follows the same methodology as stick-built construction. For example, the roof trusses are laid out on a setup jig platform (Figure 4.1a) in the offsite facility according to the building plan, as shown in Figure 4.1b. Then, other roof components are added (Figure 4.1c) to manufacture the small roof modules. All the activities in the roof module production are manual and labour intensive. Consequently, current roof production is not as efficient as other building components, such as the wall or floor.

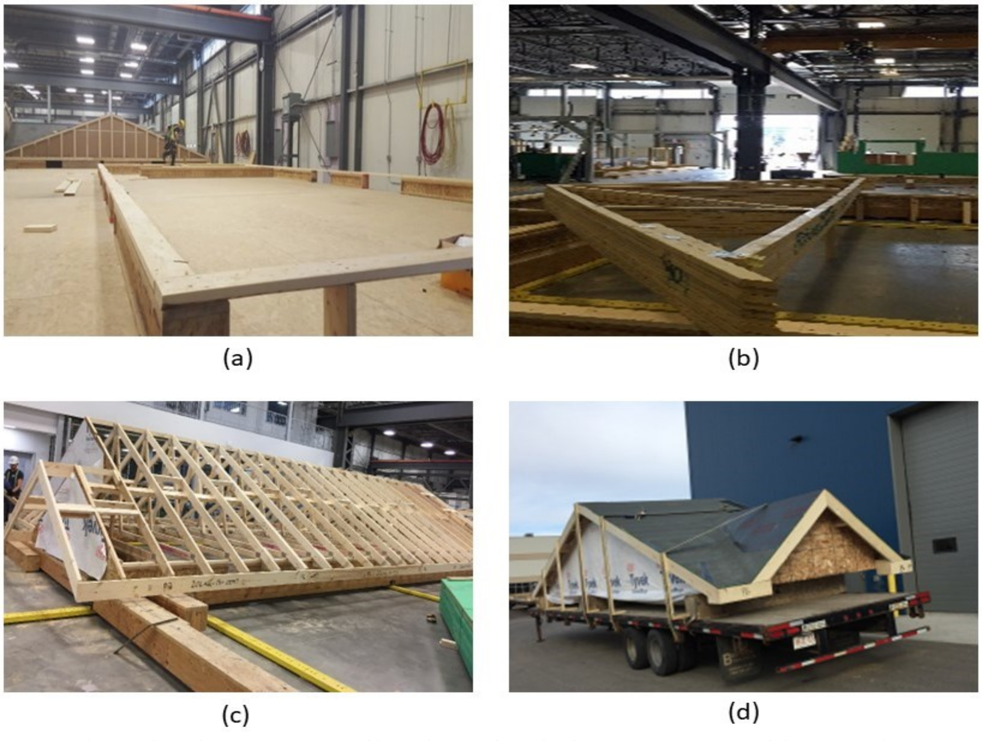

Figure 4.1. Roof production (a) setup jig, (b) unloaded truss, (c) attaching roof components, and (d) small roof module on the transportation trailer (ACQBUILT Inc. 2019).

Moreover, transporting the roof volumetric units requires a relatively large number of trailers (to be specific, in the case of an Alberta-based home manufacturer, four trailers are required to transport a 1600 sq ft single-family home) and on-site loading and unloading of trusses increases the overall work duration (Altaf et al. 2018b). Therefore, to improve the current roof construction a holistic approach was developed by Islam et al. (2021, 2022a; b). In this holistic approach, a gable roof was divided into several sub-elements. The dimensions of these sub-elements were aligned with the production line constraints of offsite facility, transportation trailer capacity, crane lifting limitations, and on-site installation considerations. The complete the panelized roof system for a typical two-storey house with a gable roof comprises the following components (Figure 4.2): (a) Roof panels, (b) support wall panels, (c) celling frames, (d) beams spanning over two support walls, (e) gable ends, and (f) inter-component connections, including the inclined roof panel-to-support wall, ceiling frame-to-load-bearing shear wall, apex connection, and the support wall-to-ceiling frame.

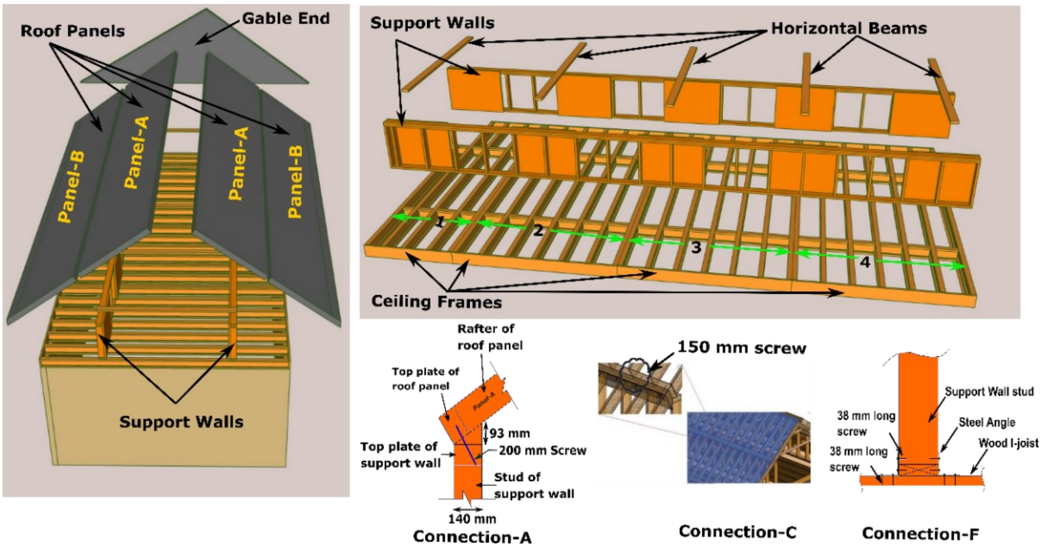

Figure 4.2. Light wood frame panelized roof concept.

Due to panelization, major components, such as roof panels, ceiling frames and support walls, can be produced in the automated and semi-automated production line of an offsite facility

(Islam et al. 2021). For instance, the roof panels (panel-A and panel-B in Figure 4.2) and support walls are produced using LSL and OSB in the wall production line. In contrast, ceiling frames are built using wood I-joist and an LSL rim board. Consequently, major roof component fabrication is expected to require less production time in contrast to the current process due to the utilization of the current wall and floor panel assembly lines. Moreover, transporting the panelized roof requires only one trailer trip in contrast to the current roof system for the same home size (Islam et al. 2022a). However, in the panelized roof system, all the components are assembled at the site. Consequently, onsite workload increases significantly (Altaf et al. 2018b). Thus, installation of the inter-component connections must be easy to minimize the on-site workload. This chapter presents a concept of a novel apex connection that allows assembling two roof panels (Panel-A in Figure 4.2) at the offsite facility and folding of roof panels while transporting and the self-locking mechanism facilitates easy lifting and installation of the two connecting panels (Figure 4.3).

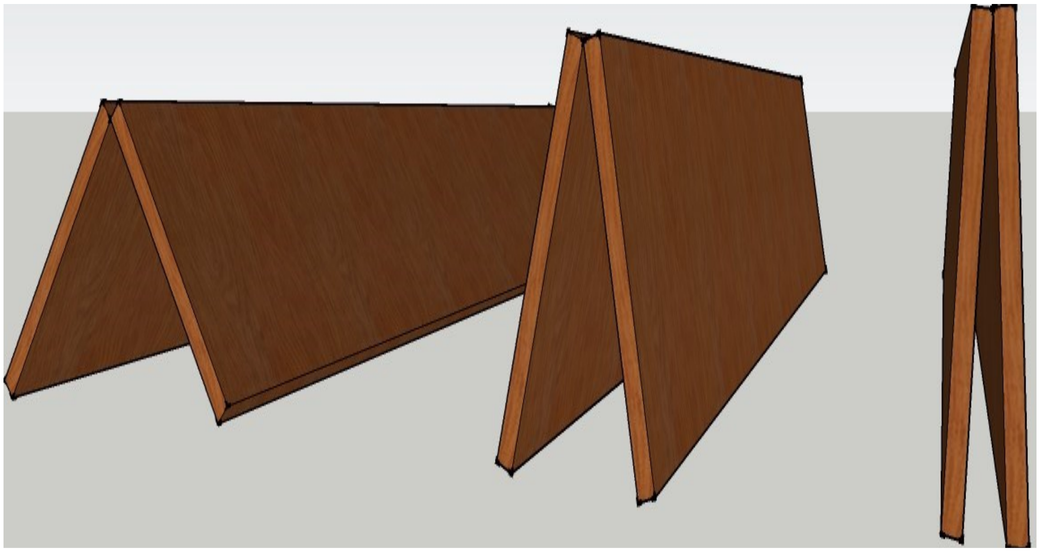

Figure 4.3. Roof panel folding.

4.2. Novel Triangular Hinge Apex Connection

The main limitation of the panelized roof system is the increased crane lifting number while installing the roof at the site. To reduce the onsite workload, a novel connection mechanism is developed so that multiple panels can be lifted at once. The apex connection for a panelized roof with an 8/12 slope can be used to connect the two Panels (in this case panel-A as shown in Figure 4.2). The advantage of this connection is that it is self-locking and foldable. The apex connection can be installed at the offsite facility and thus two panels will form a triangle module that can be folded, as shown in Figure 4.3. This folded state of the panel facilitates easy transportation to the site and a single crane lift is required for installation. Since the connection facilitates a self-locking mechanism, the roof panel installation requires no additional job once the module reaches the proper roof angle. Thereby, this system is expected to reduce a significant amount of the workload at the site. To demonstrate the folding and locking mechanism of the assembly, a full-scale 3D printout using PLA prototyping material was developed. Figure 4.4 illustrates the folding and unfolding state of the 3D full-scale printout. A video link of the folding mechanism can be found in the Appendix-5. The primary components of the connection are shown in Figure 4.5 and consist of the following 8 parts:

1. Secondary bars to connect the panel rafter
2. Primary Folding link bars
3. Main lock channel
4. Middle bar
5. Secondary lock channel
6. Side-bars
7. Secondary Folding link bars
8. Pins

The secondary bars are connected to the roof panel rafter using screws, while the primary folding link bars act as rigid link elements when the connection assembly is completely unfolded at the service condition. The primary folding link bar itself has two bars connected using a pin whereas the two secondary bars are tied using pins to the ends of the folding link bars and with each other at the apex point. In order to act as a rigid link, the folding bar has to resist clockwise and counterclockwise rotation depending on the loading condition. The self-locking mechanism is provided through the main lock channel, middle bar, secondary link bars, secondary lock channel and sidebars. It can be observed from Figure 4.6 that clockwise rotation at point A is resisted by the main lock channel placed at the bottom of the primary folding link bar, whereas counterclockwise rotation is resisted by the secondary lock channel.

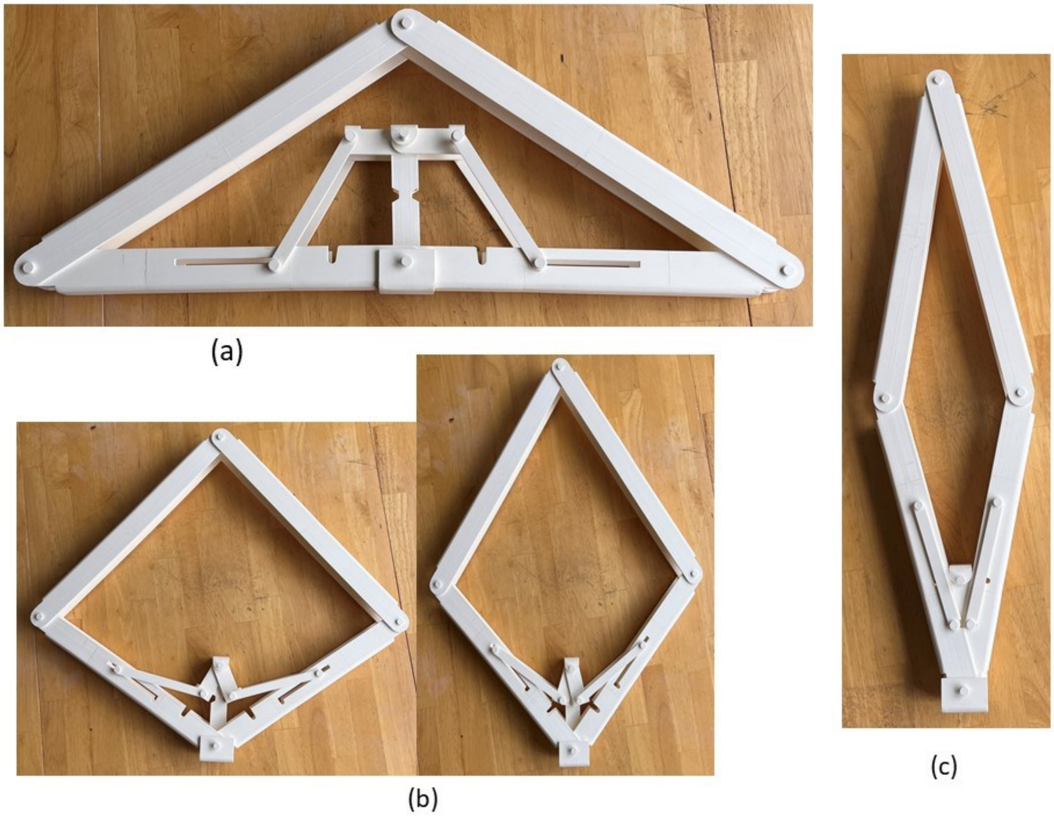

Figure 4.4. 3D printout of full-scale assembly using PLA prototyping material: (a) Unfolded state, (b) partial folding state, and (c) full folding state.

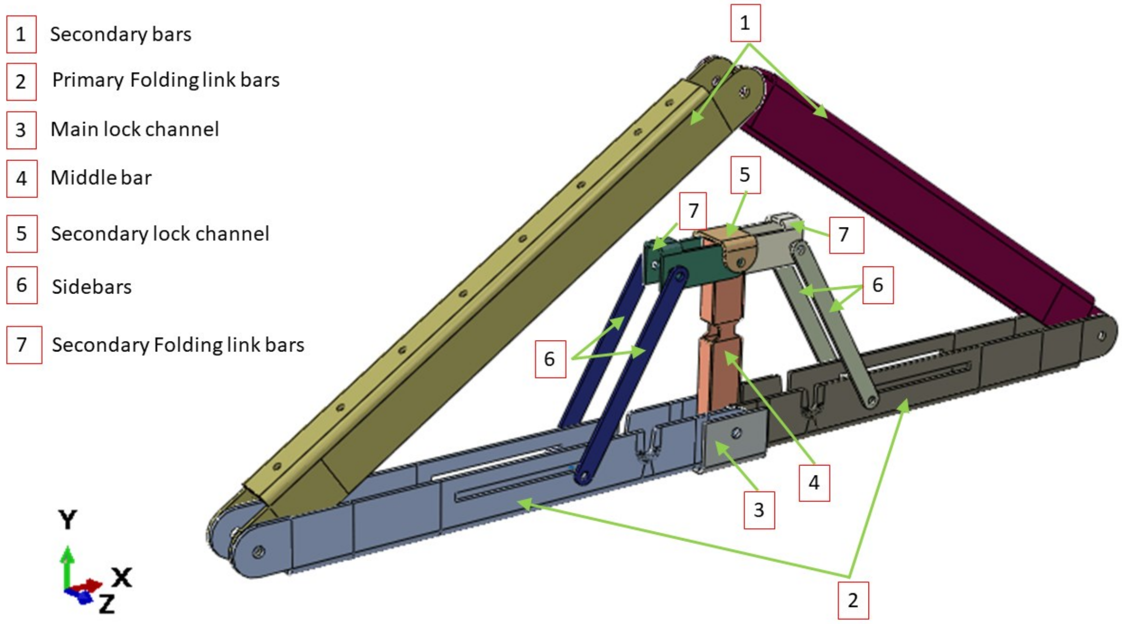

Figure 4.5. Components of the novel apex connection system for a light frame panelized roof.

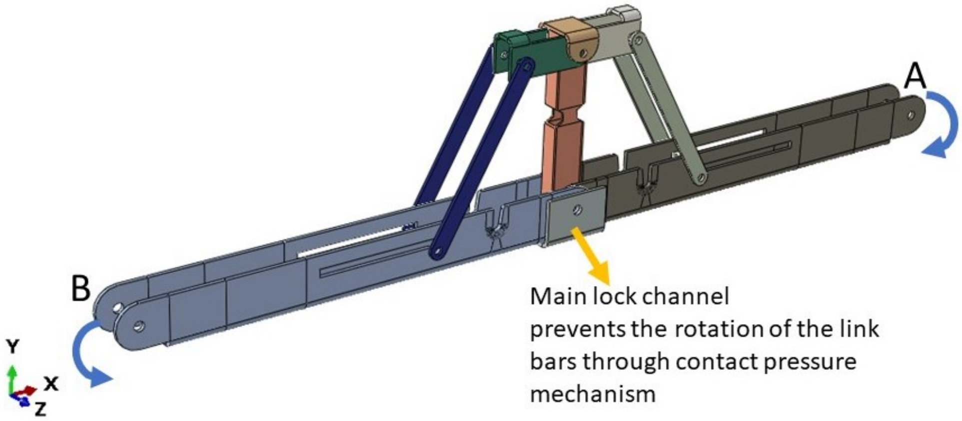

Figure 4.6. The main lock channel resisting clockwise rotation at point A.

All the components can be fabricated using steel sheet metal (12 gauge and 11 gauge). EN 1993-1-8 (2006) provides a general guideline for the edge and end distance of pin holes. Figure 4.7 shows geometrical requirements for pin-ended members according to EN 1993-1-8(2006). The initial estimate of the hole diameter of the assembly was designed considering the steel design guideline by EN 1993-1-8 (2006). For an 11-gauge plate, (yield strength of plate $f_y = 187$ MPa, hole diameter $d_o = 7.35$ mm and design pin force $F_{ED} = 8000$ N) member the corresponding edge distance and end distance are 10.7 mm and 12.3 mm, respectively. Hole dimensions of the main link bar are governed by the pin diameter requirement, which primarily depends on the shear capacity of the pin. To analyze the connection, a reasonable diameter of the pin was obtained using the pin connection shear capacity equation of EN 1993-1-8 (2006) . Following the design guideline and assuming a design value of pin joint dimensions of the parts of apex connection were determined for numerical analysis. Detailed dimensions of all the components of the novel apex connection for a case study roof slope 8/12 are illustrated in Figures 4.8 – 4.14.

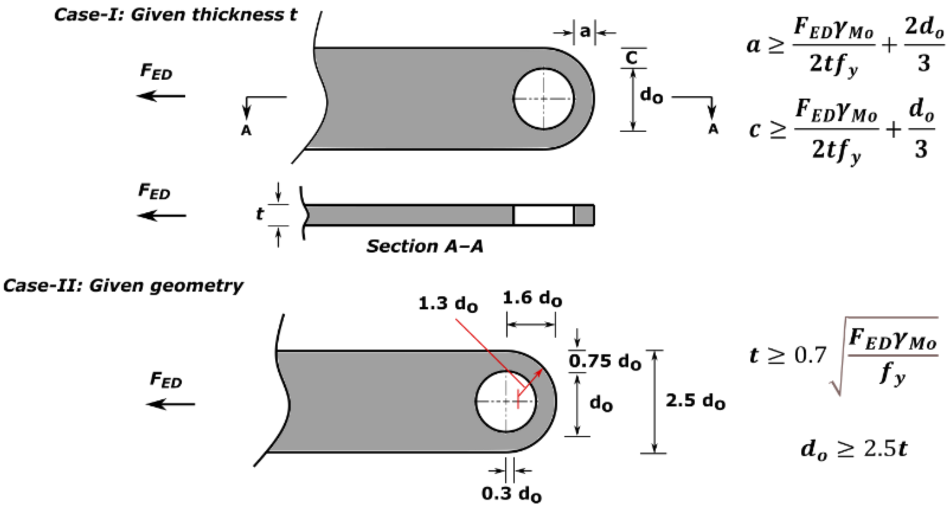

Figure 4.7. Edge distance and end distance requirement for pin connection according to EN 1993-1-8 (2006).

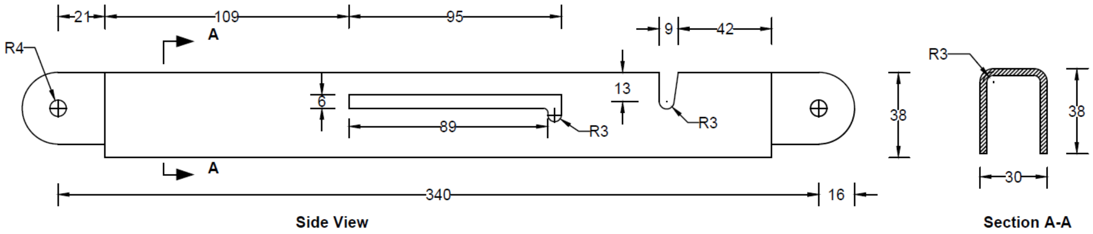

Figure 4.8. Details of primary folding link bars (all dimensions are in mm, steel plate gauge 11).

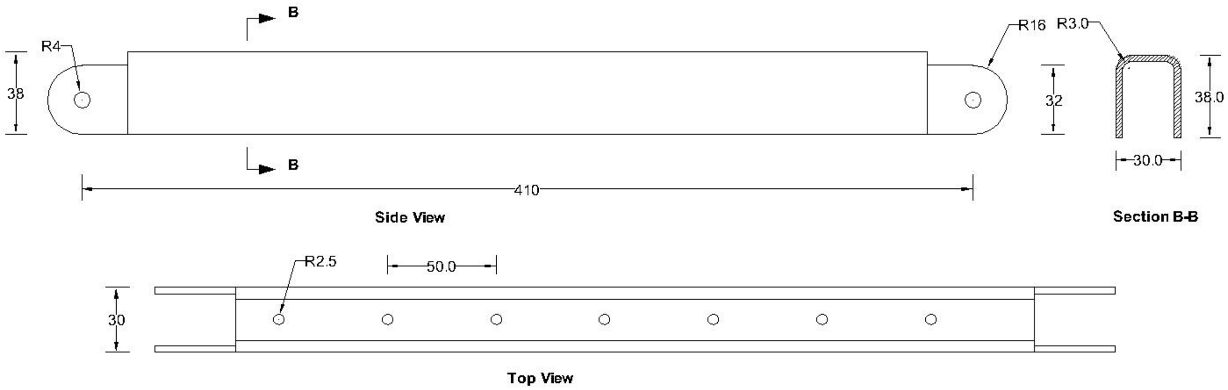

Figure 4.9. Details of Secondary bars (all dimensions are in mm, steel plate gauge 11).

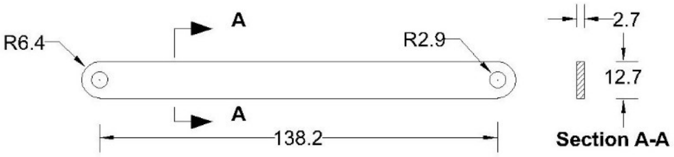

Figure 4.10. Details of Sidebars (all dimensions are in mm, steel plate gauge 12).

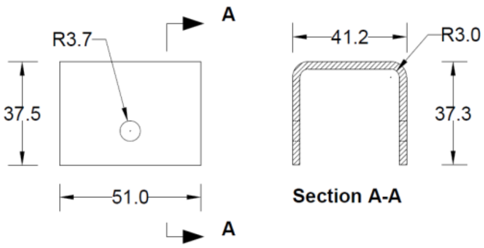

Figure 4.11. Details of main lock channel (all dimensions are in mm, steel plate gauge 11).

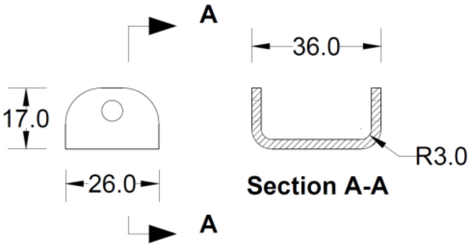

Figure 4.12. Details of secondary lock channel (all dimensions are in mm, steel plate gauge 12).

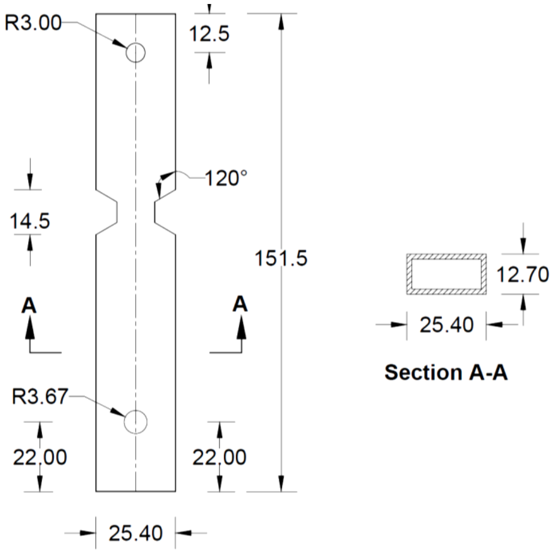

Figure 4.13. Details of Middle bar (all dimensions are in mm, HSS section).

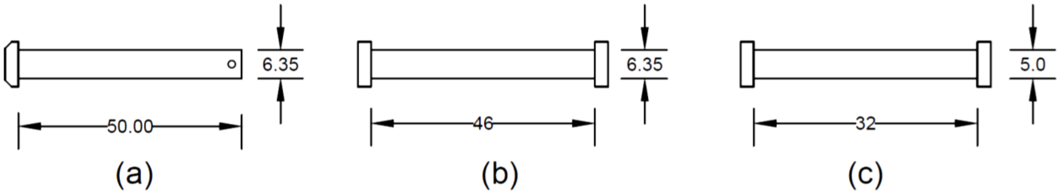

Figure 4.14. (a) Pin for connecting secondary bars at the apex point; (b) pin at the middle of the main link bar; and (c) Pin for sidebars.

4.3. Analysis of the Case Study Connection

As can be observed from Figure 4.3, the apex connection is installed to connect two panels and the main folding bar of the proposed connection at the unfolding state must resist the load at peak of the assembly. This system can be idealized as a statically indeterminate rafter system that has eave support with a collar strut (Figure 4.15). Using Castigliano's theorem on deflections with enforcement of displacement compatibility at the redundant reaction, unknown forces of the free body diagram shown in Figure 4.16 can be obtained using Equations (1) to (4) (Schmidt and Miller 2012).

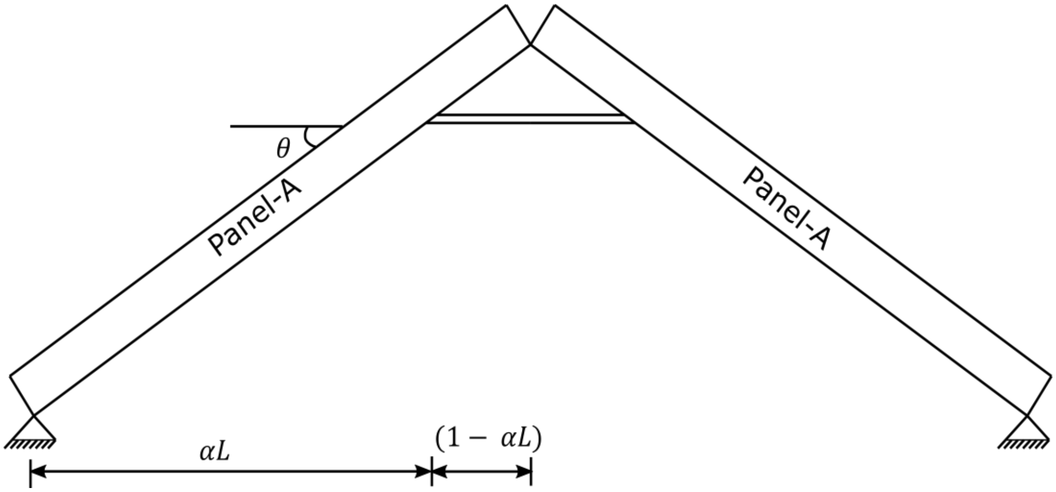

Figure 4.15. The apex connection idealized as rafter support system eave support with Collar Strut.

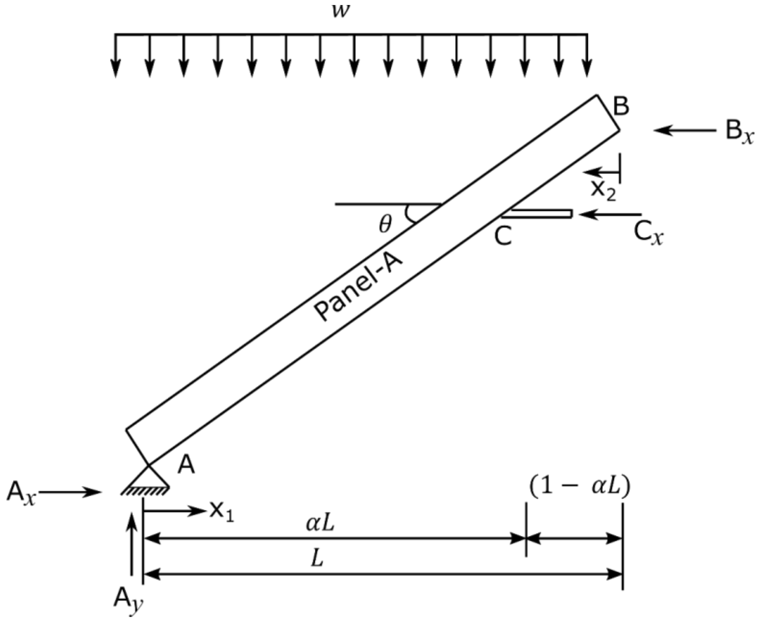

Figure 4.16. Free body diagram of the system under gravity load.

$$\boldsymbol{A_x} = \frac{\boldsymbol{wL}}{\boldsymbol{8tan\theta}}\left[\frac{-\alpha^2+5\alpha+1}{\alpha}\right], \qquad 1)$$

$$\boldsymbol{B_x} = \frac{\boldsymbol{wL}}{\boldsymbol{8tan\theta}}\left[\frac{\alpha^2-5\alpha+3}{(1-\alpha)}\right], \qquad 2)$$

$$\boldsymbol{C_x} = \frac{\boldsymbol{wL}}{\boldsymbol{8tan\theta}}\left[\frac{-\alpha^2+\alpha+1}{\alpha(1-\alpha)}\right], \qquad 3)$$

$$\boldsymbol{A_y} = \boldsymbol{wL}, \qquad 4)$$

where:

α = a span factor used to express the location of the interior support or attachment point of the folding link bar

L= horizontal projection of the distance from the eave to the Apex (the distance in the plan).

θ = roof pitch (rafter slope) relative to the horizontal.

x_1 *and* x_2 = span coordinates measured horizontally, as indicated in Figure 4.16

w = gravity load including the self-weight of the roof panel expressed as a uniformly distributed load

In this study, the apex connection design is demonstrated for a residential home package provided by an offsite construction company located in Alberta, Canada (11 m × 6.1 m Gabel roof footprint) with a slope of 8/12 and panel-A width of 1944 mm. Both gravity load case and wind load case were considered for a tributary area equal to the apex connection spacing. Assuming 600 mm c/c distance of the apex connections for a factored gravity load of 4 kPa, the axial force (C_x) in the bar and internal hinge force (B_x) at the apex location were calculated using Equations (2) and (3) and led to a solution of 5165 N and 1140 N respectively.

A 2-D finite element model was also developed utilizing commercially available general-purpose FE code, ABAQUS/CAE, distributed by SIMULIA Inc., USA. A two-node beam element (B31) was used to assemble the two LSL rafters with a cross-section of 140 mm × 38 mm and all the triangle apex connection components were made of steel C-channel section (30 mm × 40 mm × 40 mm) (Figure 4.17). It was assumed that the main folding bars connected by a pin in the actual connection setup act as one rigid link element. The three beams representing the apex connection, the secondary bar and the primary folding bar are connected by a hinge connector element (CONN3D2) (Points A, B and C in Figure 4.18). Then, the tie constraint was applied between the rafter and secondary bars of the apex connection. The tie constraint represents the screw connection between the rafter and the secondary bars, assuming that the number of screws provides sufficient rigidity to transfer the load from the rafter to the apex connection assembly. The same magnitude of gravity load was applied according to the previous analytical procedure and a comparison of the results shows that the FE model provides a reasonably close solution (axial force value in the main folding bar = 6570 N and apex hinge force at point B = 1879 N). Thus, the validation of this 2D FEM with the analytical model indicates that a more detailed modelling approach (e.g., contact simulation) can reveal the proper behaviour of this connection mechanism. However, this linear elastic analysis provides the basis to determine the internal forces and thereby an approximate diameter of the pins was obtained using Equation (5) (EN 1993-1-8 2006).

$$\text{Shear resistance of a pin, } F_v = \frac{0.6\, A\, f_{up}}{\gamma_{M2}}, \qquad 5)$$

where d is the diameter of the pin, f_{up} is the ultimate tensile strength of the pin and A is the cross-section area of a pin, and γ_{M2} is the safety factor.

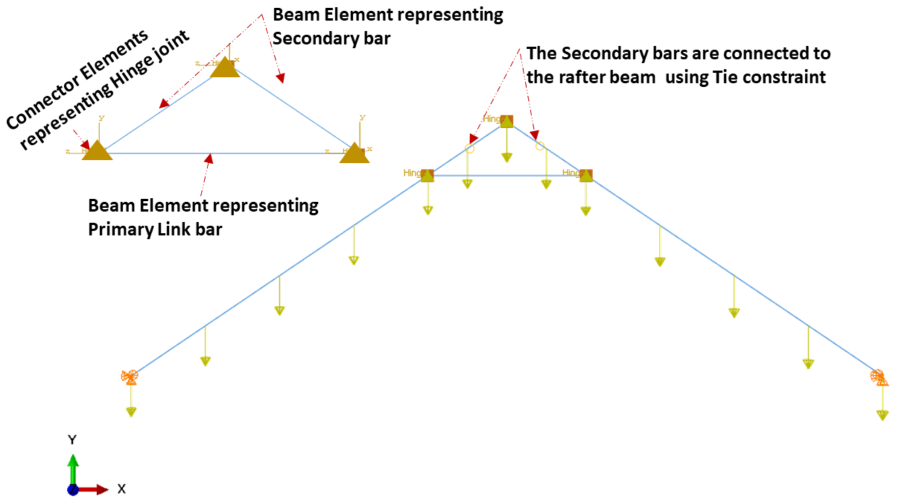

Figure 4.17. Loading and boundary condition 2-D numerical model of the apex connection.

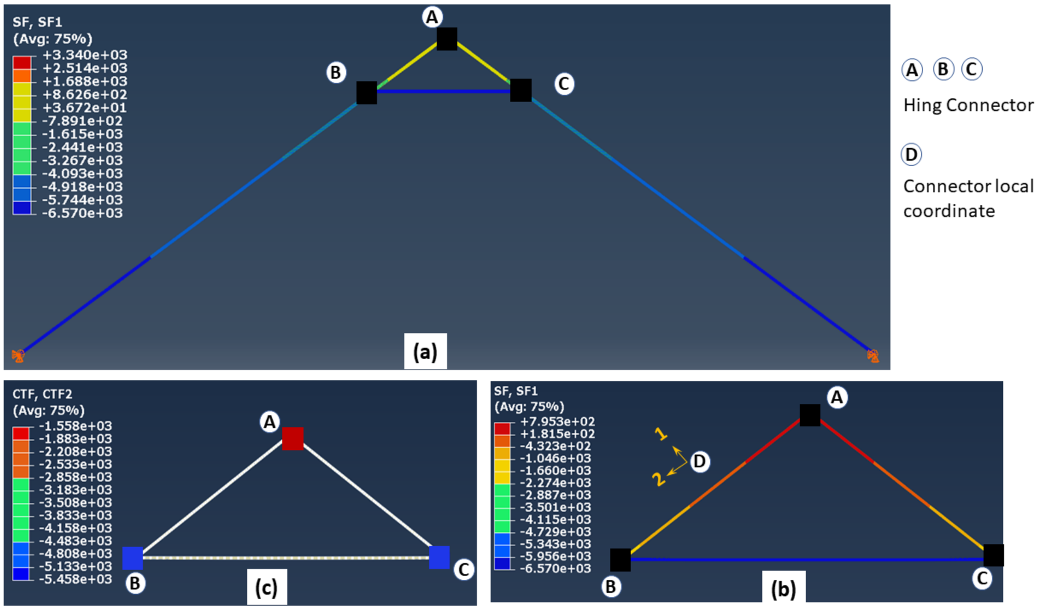

Figure 4.18. (a) Axial forces in the 2D assembly, (b) axial force in the apex connection, and (**c**) forces in the pins of apex connection (unit in the figure is N).

4.4. Screw Connection Requirement of Secondary Bars

In order to connect roof panels with the secondary bars of the proposed apex connection, commercially available screw (Simpson Strong-Tie SD screw), which is an alternative to common 10d nails, can be utilized. The screw nominal diameter and length of the screw are 4.5 mm and 38 mm, respectively. The in-plane component of load along the rafter plane must be resisted by the shear capacity of the screw connection between rafters and the secondary bars. Among all the load cases, gravity load has the highest magnitude. Thus, screw shear capacity was checked for the gravity load case only. Therefore, the number of holes in the secondary bar depends on the number of required screws. The analytical model for the nail and spike provided in CSA86-19 Equation (6) (CSA 2019) was used to predict the unfactored shear capacity of the screw connection between the secondary bar and rafter. The predicted unfactored shear capacity per screw was 1898 N with the failure mode (e) of Equation (6) (see Appendix-5 for calculation). In this case study of a roof slope of 8/12, the secondary bar has a dimension of 410 mm between the pin holes (Figure 4.9) and seven holes are provided to install the screws. Thus, with seven screws, the total factored shear capacity is 10.63 kN. The screw shear force (summation of components of hinge forces of points B and C along the rafter in-plane) was obtained from the 2D analysis (Figure 4.18c). For the governing load (factored gravity load of 4 kPa), the resultant screw shear was 7.02 kN. Therefore, the number of screws provided for apex connection is safe in the case of in-plane shear resistance. Details of shear capacity analysis can be found in the Appendix 5. The screw connection is also subjected to the highest withdrawal in case of wind load parallel to the ridge direction of the roof. According to the screw manufacturer’s technical data sheet, the design withdrawal capacity is 769.5 N per screw (ICC-ES 2021).

Additionally, the withdrawal force due to a wind withdrawal load is 2.1 kN. Thus, with seven screws, the withdrawal resistance is 5.4 kN. Further, the provided number of screws is sufficient to resist the hourly wind pressure of 0.85 kPa. Thus, providing seven holes in the secondary bar is sufficient to resist both the gravity and wind load in Edmonton, Alberta, Canada. The holes were provided at 50 mm c/c to avoid the splitting of the rafter of the roof panel. It is worthwhile to note that, to accommodate a higher load, the length of the secondary bar must be increased to provide proper screw spacing.

$$N_r = \phi\ N_u n_F\, n_s \tag{6}$$

where:

$N_u = n_u(K_D K_{SF} K_T)$

$\phi = resistance\ factor\ for\ yielding\ failures = 0.8$

$n_u = unit\ lateral\ resistance\ of\ screw$

$n_F\ = number\ of\ screw\ in\ connection$

$n_s = number\ of\ share\ planes\ per\ screw$

The unit lateral resistance of steel to timber screw connection per share plane is the smallest value calculated in accordance with the failure modes (a) to (f).

$$(a)\ f_1 d_F t_1 \tag{7}$$

$$(b)\ f_2 d_F t_2 \tag{8}$$

$$(c)\ f_1 {d_F}^2\left(\sqrt{\frac{1}{6}\frac{f_3}{(f_1+f_3)}\frac{f_y}{f_1}}+\frac{1}{5}\frac{t_1}{d_F}\right) \tag{9}$$

$$(d)\ f_1 {d_F}^2\left(\sqrt{\frac{1}{6}\frac{f_3}{(f_1+f_3)}\frac{f_y}{f_1}}+\frac{1}{5}\frac{t_2}{d_F}\right) \tag{10}$$

$$(e)\ f_1 {d_F}^2\frac{1}{5}\left(\frac{t_1}{d_F}+\frac{f_2}{f_1}\frac{t_2}{d_F}\right) \tag{11}$$

$$(f)\ f_1 {d_F}^2\sqrt{\frac{2}{3}\frac{f_3}{(f_1+f_3)}\frac{f_y}{f_1}} \tag{12}$$

where:

$t_1 = head - side\ member\ thickness\ (steel\ plate\ in\ this\ case)$

$d_F = screw\ diamenter$

$f_2 = embedment\ strength\ of\ point\ side\ member\ (LSL) = 50\ G(1-0.01d_F)$

$G = mean\ realtive\ density = 0.5\ for\ LSL$

$t_2 = length\ of\ screw\ penetration$

$f_3 =\ embedment\ strength\ of\ point\ side\ member\ when\ failure\ in\ screw\ yielding$
$= 110G^{1.8}(1-0.01d_F)$

$f_y = screw\ yield\ strength = 50(16-d_F)$

$f_1 = embedment\ strength\ of\ steel\ plate = K_{sp}(\phi_{steel}/\phi_{wood})f_u$

$K_{sp} = 2.7, \phi_{steel} = 0.80, \phi_{wood} = 0.8$

4.5. Finite Element Modelling of Apex Connection

The actual folding apex connection is inherently three-dimensional in nature and involves complex interactions between the parts. The folding mechanism of apex connections technically represents, in principle, an extremely complex and highly indeterminate analytical problem with a wide range of geometrical nonlinearity and mechanical parameters affecting its behaviour to transfer the force and moment. These parameters include the rectangular slots (95 mm long) and U-shape slots (13 mm × 9 mm) in the primary folding link bar, V-shape cuts (14.5 mm × 7 mm) in the Middle bar, contact between the main lock channel and primary link bars, contact between secondary lock channel and secondary link bars, pin bearing mechanism at the hole of main link bars and secondary bars, contact between the sidebar and main link bar (Figures 4.8–4.13). Hence, three-dimensional elements were utilized in the FEM to understand the structural behaviour of this connection. Proper element selection for steel connection design is critically important. Abaqus provides several types of elements, such as continuum solid element, shell elements, membrane elements, rigid elements, and beam elements that can be used to simulate steel connections. The behaviour of these elements is characterized by five criteria, such as family, degrees of freedom, number of nodes, formulation, and integration. For example, the solid element library includes first-order (linear) interpolation elements and second-order (quadratic) interpolation elements in one, two, or three dimensions classifying as triangles and quadrilaterals for two dimensions; and tetrahedra, triangular prisms, and hexahedra (“bricks”) in three dimensions. Each class of element provides a choice for first-order (linear) interpolation elements and modified second-order interpolation elements in two or three dimensions. It is critical to select the correct element for a particular application to avoid hourglassing, shear and volumetric locking, overly stiff behaviour in bending and slow convergence with mesh refinement. It should be noted that the proposed apex connection may have large plastic deformations and high strain gradients in the pinhole regions of connection, as well as the presence of contact between the lock channel and link bars. As suggested in previous studies (Daneshvar and Driver 2018; Liu et al. 2017; Zhao et al. 2021), first-order elements should be used to avoid mesh locking and convergence difficulties associated with contact, while modelling steel connection, 8-node linear brick (C3D8) element is preferable for the apex connection FEM. However, this element shows very high stiffness in bending; consequently, the incompatible mode of these elements (C3D8I) is implemented to improve their bending behaviour (Dassault Systèmes 2021).

For any numerical modelling, the definition of material property is the most critical step that affects connection ductility and capacity. A detailed literature review of steel connections suggests assuming that the steel in this study is homogenous and isotropic with an elastic modulus of 200 GPa and Poisson's ratio of 0.3 (Daneshvar and Driver 2018; Fan et al. 1997; Huynh et al. 2020; Mohamadi-shooreh and Mofid 2008). Since the variation of mechanical properties of steel is significantly low compared to other construction material, such as wood, in the absence of a coupon test, generic material properties specified in standards used for numerical simulation produces reasonably accurate results (Daneshvar 2013). According to ASTM A1008, drawing quality steel sheets (DS) have yield strengths between 150 to 240 MPa (ASTM 2014). While, for design purposes, selecting the nominal values is a conservative approach, the use of minimum nominal strength material property in numerical simulation underestimates the load-carrying capacity of the steel connection whereas adopting a maximum nominal strength property has the opposite effect (Daneshvar 2013). Thus, to obtain proper connection behaviour the typical stress-strain relationship as depicted in Figure 4.19 (Lenard 2014) is adopted for the elements of all the parts fabricated using steel plate and A36 steel for all pin components (Figure 4.20) (Daneshvar and Driver 2018). Since the main focus of the model is to understand the behaviour of the apex connection, the rafter material (LSL) was assumed to be isotropic with a Young's modulus of 9000 MPa and Poisson's ratio of 0.25.

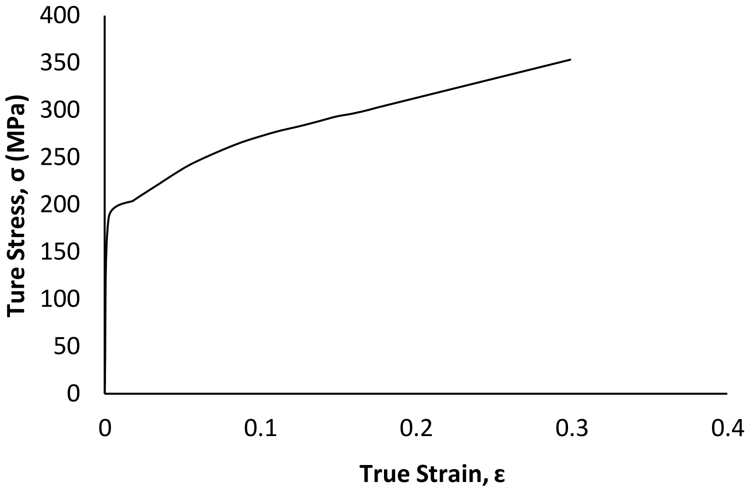

Figure 4.19. The true stress-true strain curves of an AISI 1008 steel (Data obtained with permission from Lenard (2014) Elsevier).

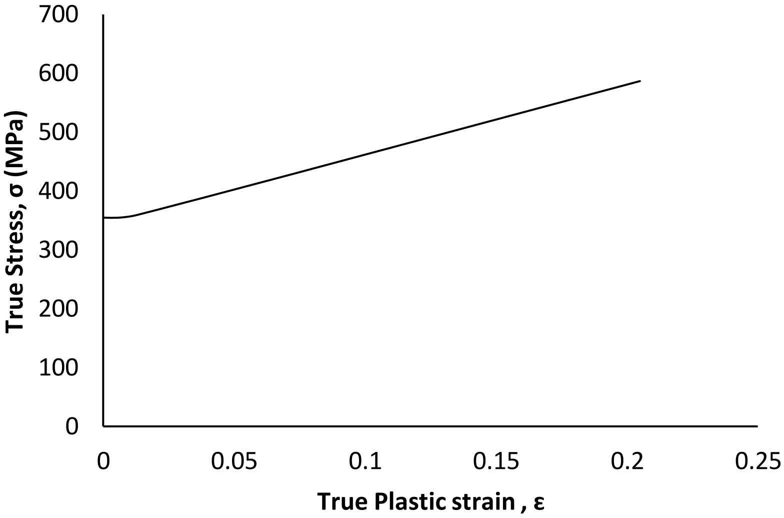

Figure 4.20. The true stress-true plastic strain curves of A36 steel (Daneshvar and Driver 2018).

In the structural analysis, it is common to make use of reduced or lower-dimensional element types with higher-dimensional element types in a single FE model, which is known as multiscale FEM. This approach is efficient and provides an improved solution to capture local structural features as well as global structural behaviour (Li et al. 2007). Figure 4.21 illustrates the complete mixed-dimensional FEM assembly of this study. To simplify the model, similar to the analytical approach, only two LSL rafters and the unfolded state of apex connection assembly were incorporated. However, all these components were modelled using solid 3D elements (8-node linear brick element). As can be observed from Figure 4.5, the apex connection has nine locations that require a hinge mechanism provided by steel pins. Despite well-established design rules and assembly procedures in American and European steel standards, numerous nonlinearities in the vicinity of the pinhole led to overly expensive calculations if fine-scale computation modelling is used. Consequently, to model this large assembly with a considerable number of pin joints, alternative computational strategies are a suitable option (Verwaerde et al. 2021). Abaqus provides the connector (CONN3D2) element to model any type of connection such as a hinge or a screw (Dassault Systèmes 2021). However, the connector element is a 1D element whereas the other components are 3D objects, so the number of degrees of freedom (DOFs) is not the same for all the objects. Hence, this multi-scale FE simulation requires a reasonable FE coupling method to blend mixed-dimensional finite elements at their interfaces to accomplish both displacement continuity and stress equilibrium. In this regard, the multipoint constraint (MPC) surface method is suitable for the static and dynamic analysis of linear or nonlinear structures and the interactions between the pin with the assembled elements can be modelled in an average sense with a more rigid way in ABAQUS (Verwaerde et al. 2021). The MPC method uses constraint equations for nodal displacements at the interface of mixed-dimensional elements. Thus, to model the hinge mechanism at all locations (as shown in Figure 4.22), reference points were generated on the center points of the connection and MPC-BEAM constraint was assigned to the hole surface with their corresponding reference point (RP). MPC-BEAM in ABAQUS uses a rigid interface method to connect nodes of different types of elements by creating rigid beams with respect to RP (Dassault Systèmes 2021). At each pin location connector element with a hinge, connection property was assigned to join corresponding parts. Tie constraint was applied at the interface between secondary bars and the LSL rafter assuming that the screw connection will act as a rigid joint. In the simulation of steel connection, the boundary condition is deemed to be significant and any inappropriate boundary conditions may cause completely different behaviour. Following the analytical model mentioned in the previous section, the lower two ends of the LSL rafter are assumed to be in the pinned ($U_x = U_y = U_z = 0$) support condition. In actual roof assembly, the OSB sheathing is nailed on the rafters, which provides stability against lateral buckling. To account for this lateral restraint, provided by the continuity of OSB sheathing panels, the rafter edges were assigned as the Z-symmetry coordinate system ($U_z = UR_x = UR_y = 0$), as shown in Figure 4.21.

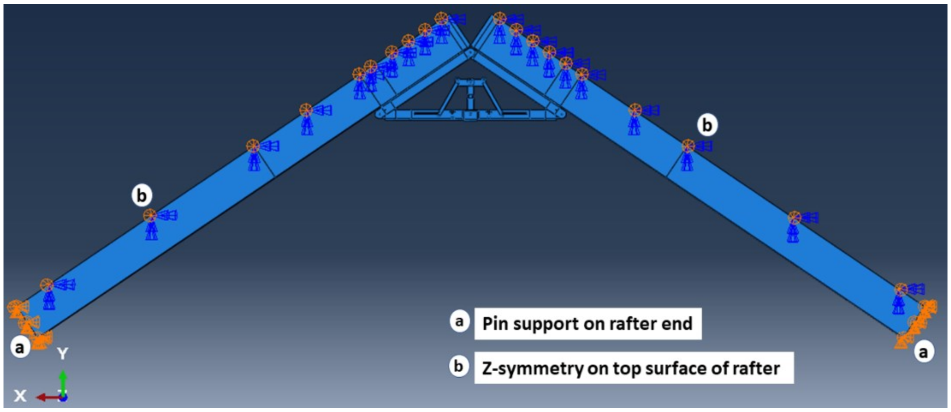

Figure 4.21. 3D assembly model and boundary condition.

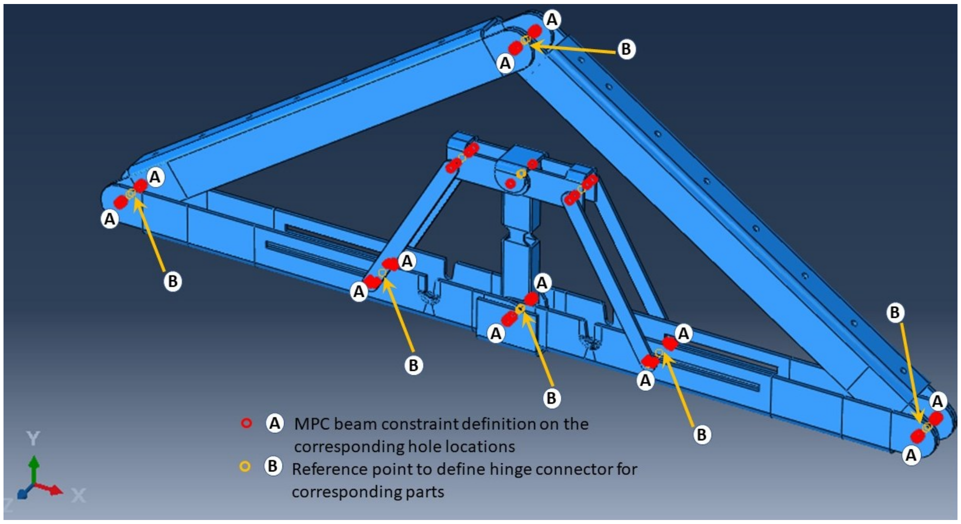

Figure 4.22. MPC beam constraint location for the hinge connection.

Properly refined element mesh is also an influencing factor for any finite element simulation to obtain reliable results. Due to the presence of slots and pinholes, it was required to partition the complex geometry into several segments and assign an advancing front or medial axis meshing algorithm to generate elements with proper shape factors. For example, the U-shape slot in the main link bar in Figure 4.23 was partitioned by offsetting the half-circular face of the slot at every 1 mm and creating radial lines at every 9° angle. This technique generated a very refined mesh with a proper shape factor around the face of the model.

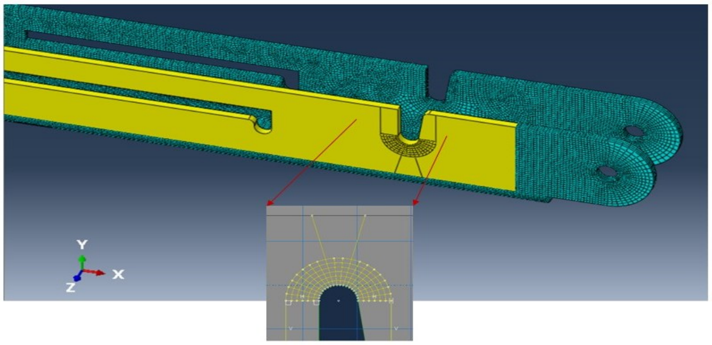

Figure 4.23. Advanced meshing application.

As mentioned previously, complex interactions exist between the surfaces of different parts of the apex connection to facilitate folding and self-locking mechanism, so this FE modelling requires contact simulations of different components to allow for a transmission of force from one part to another, specifically near the folding location where main lock channel and secondary lock channel provides a self-locking mechanism (Figure 4.24). In detail, a coulomb coefficient of friction equal to 0.3 is defined for sliding resistance in the surface-based contact approach. It should be noted that the interface of the contact surface must be close and the penalty technique enforcement was used in contact enforcement since this approach has more flexibility and recommended method in steel connection modelling (Daneshvar and Driver 2018).

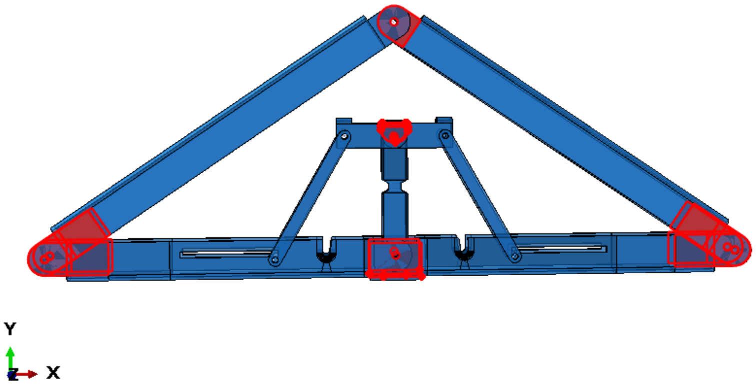

Figure 4.24. Contact surface interaction locations.

4.6. Results

Four governing loading combinations from the Canadian Building Code were considered for this numerical analysis. These load combinations account for all the combinations, including gravity load (dead, live and snow) and lateral load (wind load Figure 4.25), that will lead to maximum effects for both strength and serviceability. The design loads applied to the roof structure were assigned based on the National Building Code of Canada (NBCC) (NBCC 2020b) and the building location in Alberta, Canada. These were specified at a snow load of 2.25 kPa, other non-structural components account for another 0.5 kPa of dead load and hourly wind pressure of 0.85 kPa. Thus, the total factored gravity load was 4 kPa. Wind loads were calculated using the static procedure of NBCC and based on the gust effect and pressure coefficient (as illustrated in Figure 4.25) for both wind perpendicular to ridge and wind parallel to ridge direction. For both the gravity load and lateral load cases, the partial loading scenario was also checked following the NBCC. The uniformly distributed load was applied on the LSL assuming apex connection spacing of 600 mm c/c since the maximum spacing of the roof panel rafter must not exceed the corresponding value to take advantage of the load sharing system effect.

Load case a: 1.25D + 1.5S +1.0L

Load case b: 0.9D + 1.4W + 0.5S

Load case c: 0.9D + 1.5S + 0.4W

Load case d: 0.9D + 1.4W

where D = dead load, L = live load, S = snow load and W = wind load

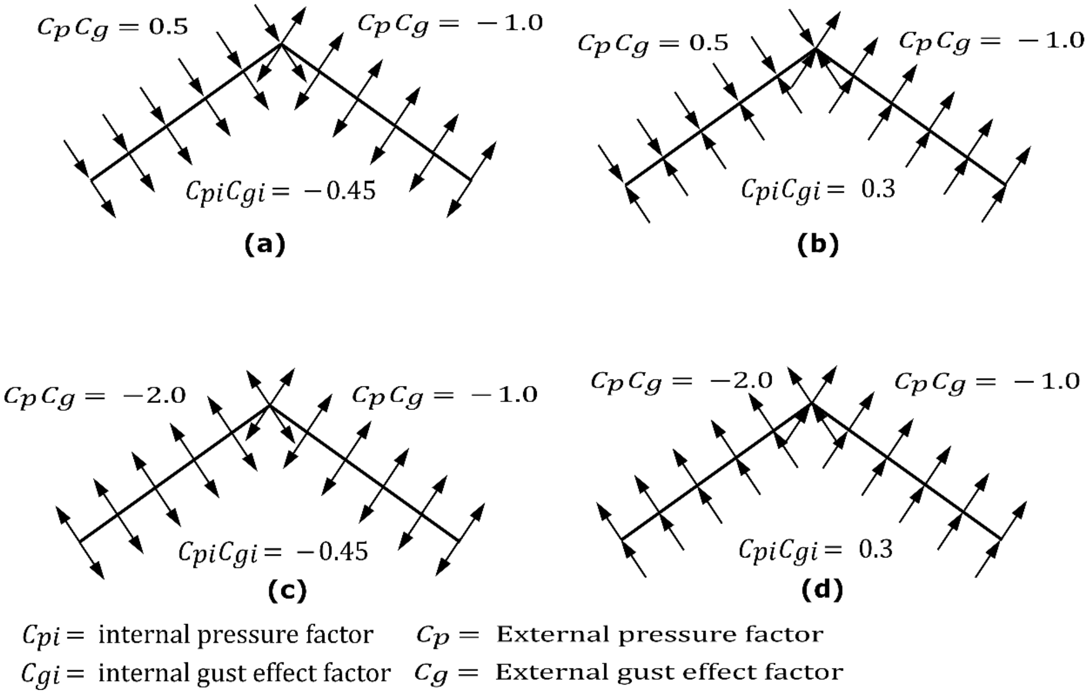

Figure 4.25. External and internal gust and pressure factors for wind load cases (a,b) for wind perpendicular to ridge and (c,d) for wind parallel to ridge.

Figures 4.26 and 4.27 show the deflected shape of the assembly under gravity load and von Mises stress of the apex connections parts. Table 4-1 summarizes the resultant von Mises stress and PEEQ value observed in different load cases. As the link assembly is subjected to both bending and compression for the gravity load, the maximum von Mises stress was observed around the U-slot of the primary folding link bar (Figures 4.28 and 4.29). It was observed that the load had the largest impact on the stress distribution in the proximity of the U-slot of the primary folding link bar. Figure 4.29 depicts the stress distribution near the U-slot indicating the highest stress concentration zone and probability of fracture initiation zone at ultimate failure load. A comparison of the stress contour plotted in Figure 4.30 shows that all other parts including the main lock channel, middle bar, secondary lock channel, sidebars and secondary folding link bars are within the elastic limit. As expected, among these components, maximum von Mises stress was observed in the contact zone of the main lock channel and secondary lock channel which confirms the effectiveness of the locking mechanism of the assembly. Maximum von Mises stress in the main lock channel and secondary lock channel were 55.2 MPa and 51.2 MPa respectively, whereas the ultimate strength of AISI 1008 is 353.3 MPa. Thus, the channels are well below the ultimate strength of the material for a factored gravity load of 4 kPa.

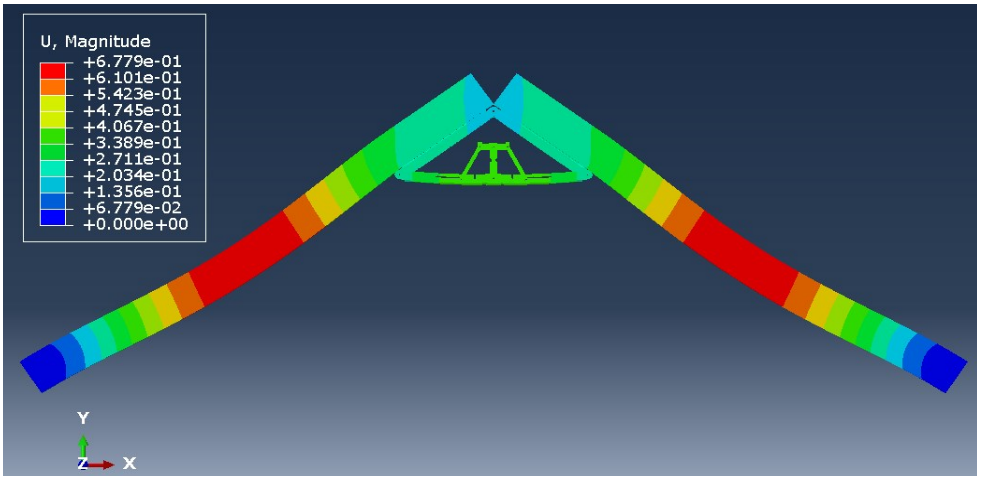

Figure 4.26. The deflected shape of the structure for a factored gravity load of 4 kPa.

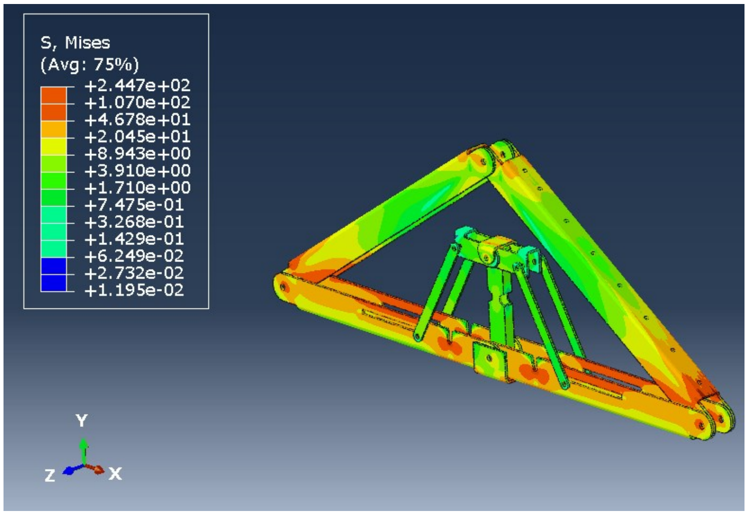

Figure 4.27. Von Misses stress (MPa) of the Apex connection (factored gravity load of 4 kPa).

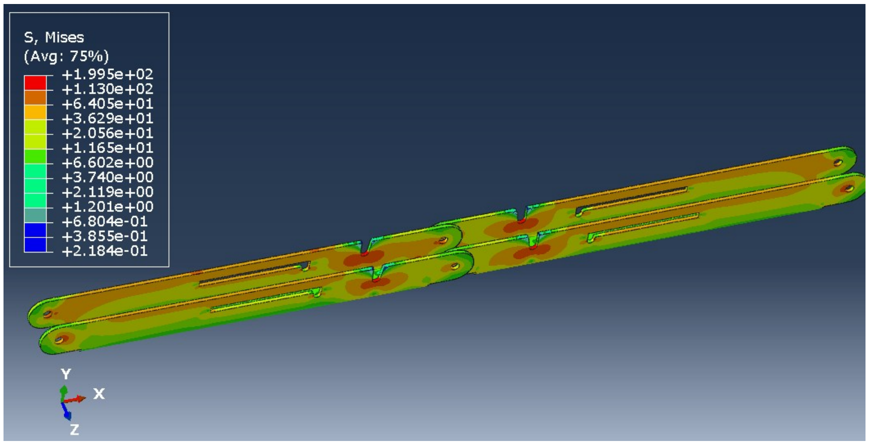

Figure 4.28. Von Mises Stress (MPa) of primary folding link bars (factored gravity load of 4 kPa).

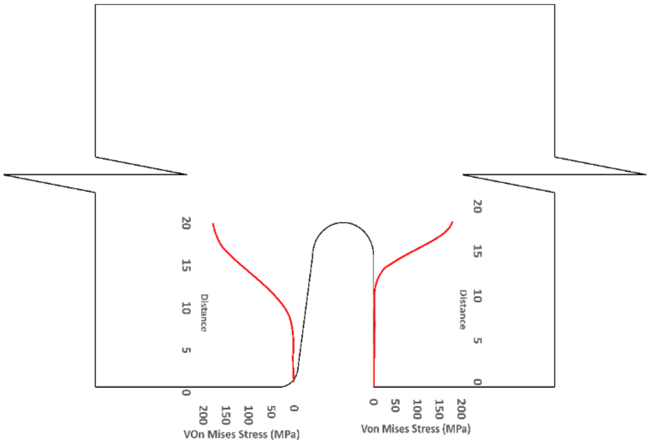

Figure 4.29. Stress (MPa) distribution near (red line) the vicinity of the U-slot of primary folding link bar.

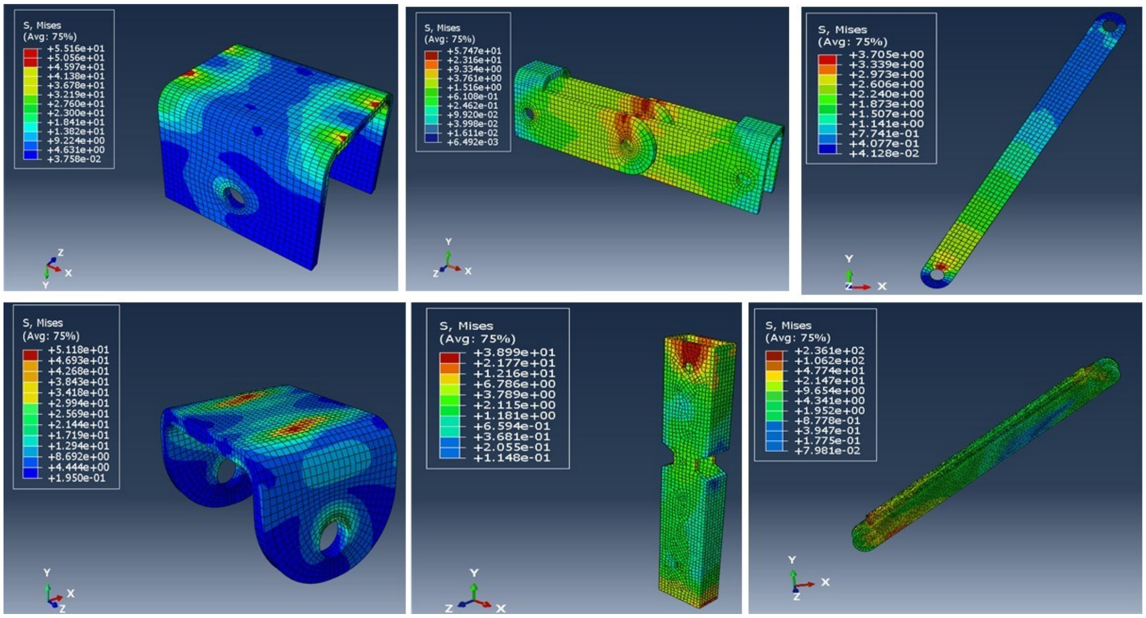

Figure 4.30. Stress (MPa) contour plot of different parts for a factored gravity load of 4 kPa.

In order to obtain the connection capacity, a benchmark for the failure mechanism and failure criteria for any numerical analysis are required. In the case of the experimental investigation of any connection, the failure point of an assembly can be distinct by observing a situation when the assembly exhibits a substantial loss in load-carrying capacity or the presence of a rupture mechanism. However numerical models continue to obtain results until it fails to converge on a solution which can be different from the actual failure state. Thus, it is important to establish proper failure criteria for the numerical modelling approach. The literature review has revealed that, in the case of steel connection, two types of failure criteria are considered, namely (a) strength criterion and (b) deformation criterion. For example, experimental studies on the bearing resistance of a connection adopted a design equation based on the maximum loads from tests in literature (Errera et al. 1974; Puthli and Fleischer 2001; Rogers et al. 1998; Winter 1956), even though significantly larger deformation in the specimen was observed. In contrast, according to the later criterion, failure is considered to be the applied load measured at a specific acceptable deformation level depending on the application (Salih et al. 2011). For instance, the bearing failure study of cold-formed steel bolted connections by Chung and Ip (2000) adopted a 3 mm extension limit. Additionally, Eurocode 3 design provisions for steel connections are based on a 3.0 mm deformation limit under ultimate conditions which ensures the deformation under service loads to be 1.0 mm (Salih et al. 2011). Thus, for design purposes, deformation-based criteria are more appropriate. Hence, the equivalent plastic strain of a material (PEEQ) in Abaqus, was adopted to implement as a design capacity criterion for the cross-section of the parts. PEEQ is a scalar measurement that is used to represent the material's inelastic deformation and if this variable is greater than zero, the material has yielded. Thus, PEEQ indicates the local ductility and fracture tendency of steel members (Peng et al. 2020). In the case of classical (Mises) plasticity, PEEQ is obtained by using the following equation:

$$PEEQ = \bar{\varepsilon_p}|_0 + \int_0^t \sqrt{\frac{2}{3}\dot{\varepsilon_p} : \dot{\varepsilon_p}}\, dt \tag{13}$$

where $\bar{\varepsilon_p}|_0$ is the initial equivalent plastic strain and
$\dot{\varepsilon_p}$ is the tensorial form of plastic strain rate.

In order to investigate the performance of the connection in service, the following hypothesis was adopted:

"The apex connection components must be sized so that all materials remain in the elastic range and their elastic deformations have negligible values. This ensures the deformation of the connection will be returned to its original state after the load is removed."

As can be observed from the deformation and stress distribution of the primary folding link bar, the possible mechanism of failure is fracture propagation near the U-slot. Thus, the design requires avoiding any form of localized plastic deformation near this zone. If the PEEQ value is zero, then it can be concluded that the assembly is in the elastic range under design load. Figures

4.30–4.33 illustrate the von Misses stress and PEEQ plot of the apex connection assembly in the most critical load cases. The PEEQ value analysis of all the critical load cases shows non-zero plastic strain for load case-a only (Figure 4.34). The PEEQ value for a factored gravity load of 4 kPa and the cumulative plastic deformation is concentrated in the middle location of the U-slot; 12 mesh (C3D8I) elements (approximately 64 mm^3 volume) near the U-slot of the primary folding link bar have PEEQ value greater than zero with a maximum value of 1.7810×10^{-3}. As can be observed from Figure 4.35, the computed strain levels in those 12 elements have exceeded the defined yield value and are in the strain hardening stage. Consequently, there will be a 0.185 mm permanent deformation near the U-slot zone of the one-side main folding link bar. Therefore, the main folding link has the probability of a total of 0.4 mm shortening for a specified gravity load of 4 kPa. This will cause tension force at the secondary bar, ultimately increasing the uplift force on the fastener used to connect the bar with the roof panels. Additionally, the relatively long winter in Canada poses a risk of fatigue and residual stress on the connection, so a PEEQ value equal to zero will be a safe option to ensure that the assembly components remain in the elastic zone. Therefore, it can be concluded that a revised cross-section is required to support a 4 kPa gravity load. However, at a factored load of 2.36 kPa, the cross-section shown in Figure 4.8 with PEEQ values equal to zero was observed. Thus, the primary folding link bar of the cross-section shown in Figure 4.8 can be used for a factored gravity load of 2.36 kPa. An enhanced cross-section (Figure 4.36) is required to support a factored gravity load of 4 kPa, which was obtained by running the numerical model with various trial cross-section sizes until the failure criterion was met. It is worthwhile to note that the initial primary folding link bar (as shown in Figure 4.8) has a cross-section of 30 mm × 38 mm, whereas the revised cross-section is 30 mm × 50 mm (as illustrated in

Figure 4.36). All other elements, such as the pinhole and u-slot, are the same as initially designed (Figure 4.8).

To observe the load-deflection behaviour of the apex connection assembly, a gravity load up to 12.7 kPa was applied since the load case-a is the governing case. Figure 4.37 illustrates the mid-point deflection vs. load plot of the primary folding link bars assembly, which ensures reasonably low deflection of the overall assembly at the factored gravity load of 4 kPa.

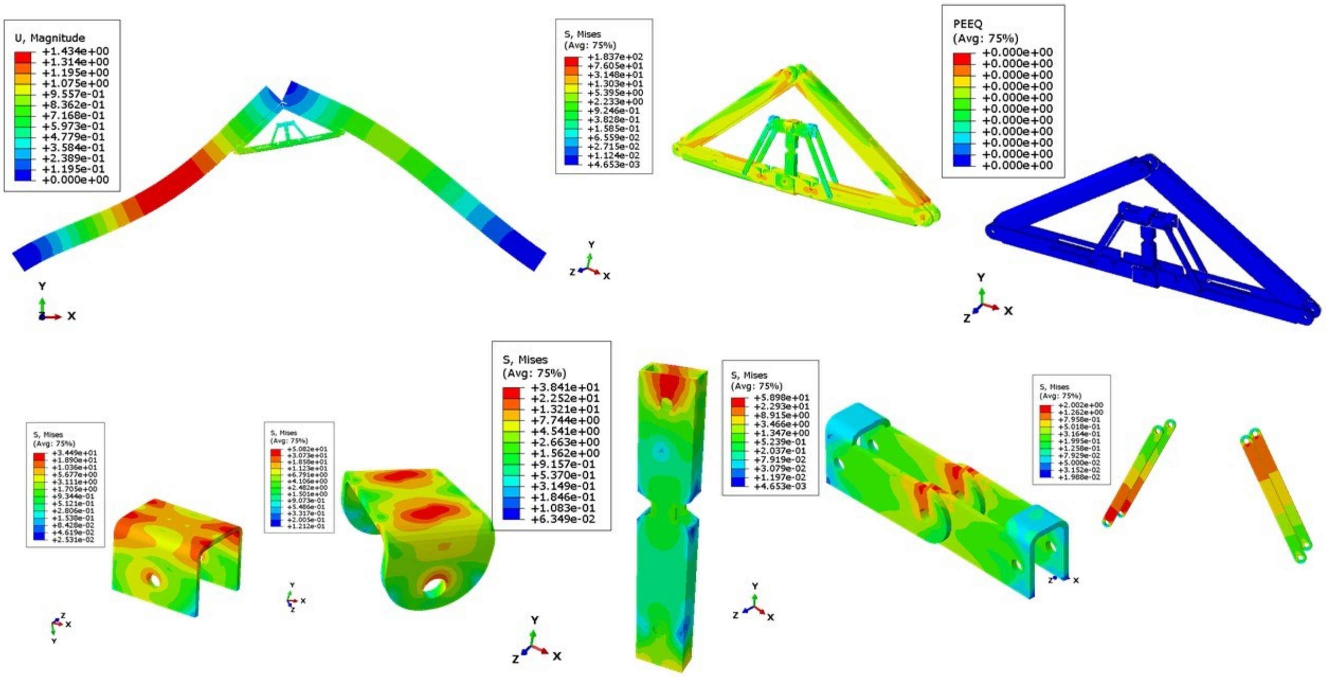

Figure 4.31. Stress (MPa) in wind load case (100% load removed from one side for hourly wind pressure of 0.85 kPa).

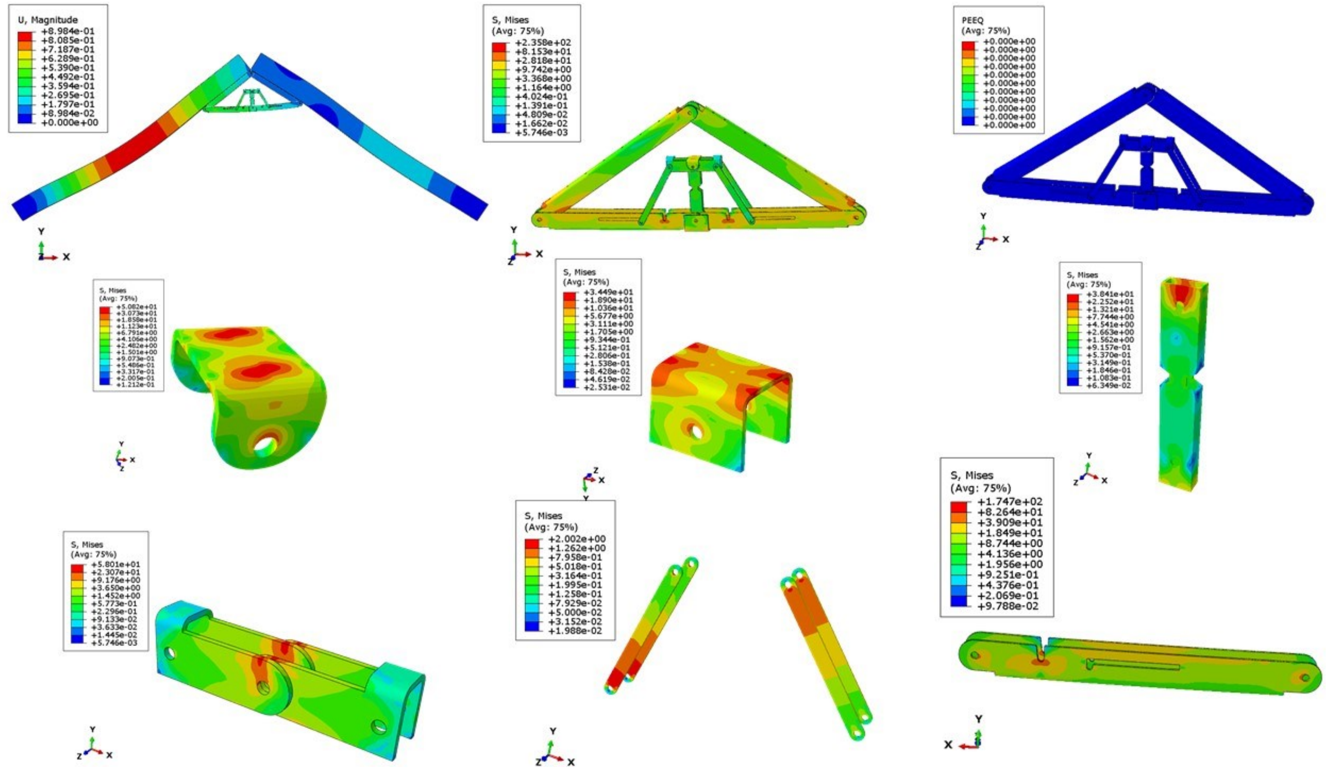

Figure 4.32. Stress (MPa) in different parts for partial snow load case (specified snow load of 2.25 kPa).

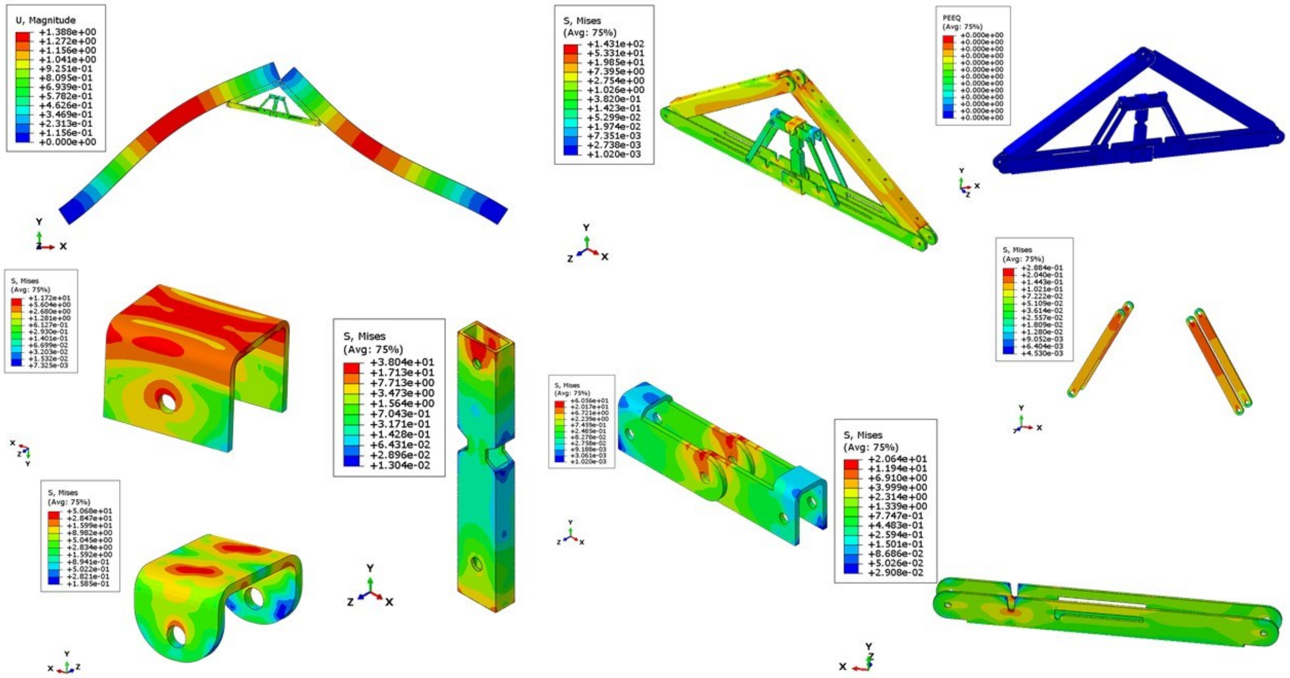

Figure 4.33. Stress (MPa) for partial wind load case uplift (hourly wind pressure= 0.85 kPa).

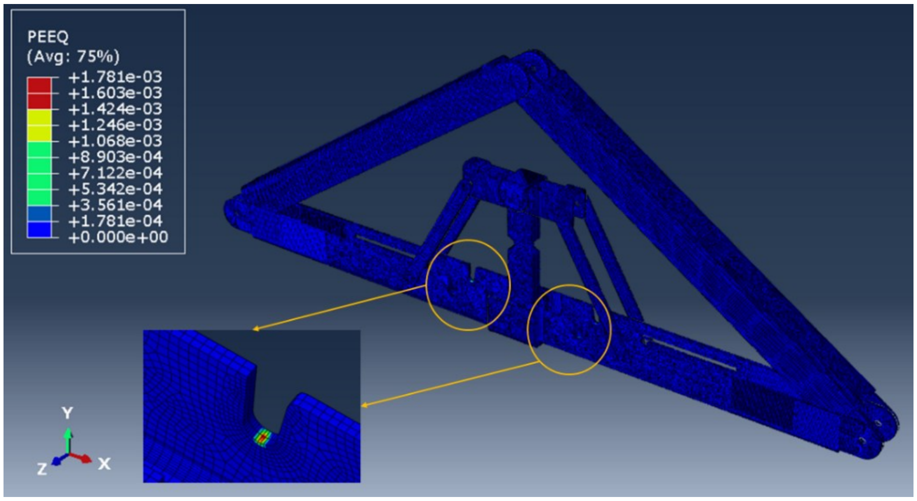

Figure 4.34. PEEQ value for the link assembly for a factored gravity loading of 4 kPa.

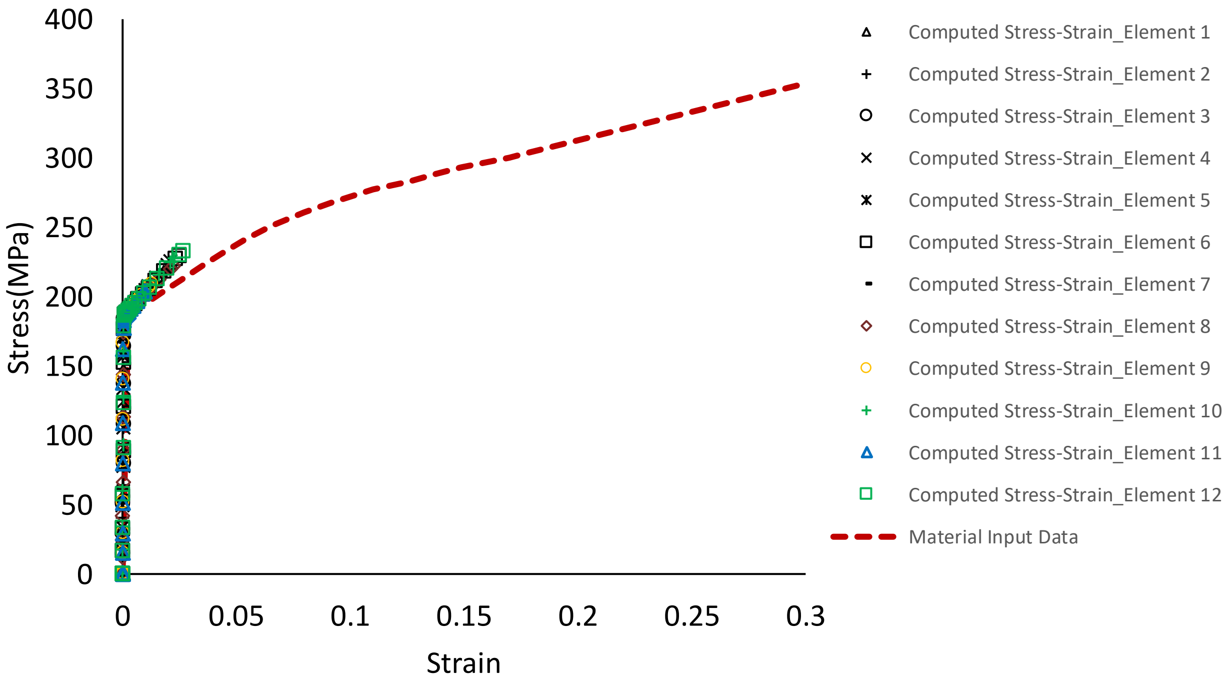

Figure 4.35. Stress-Strain near the U-slot of primary folding link bar.

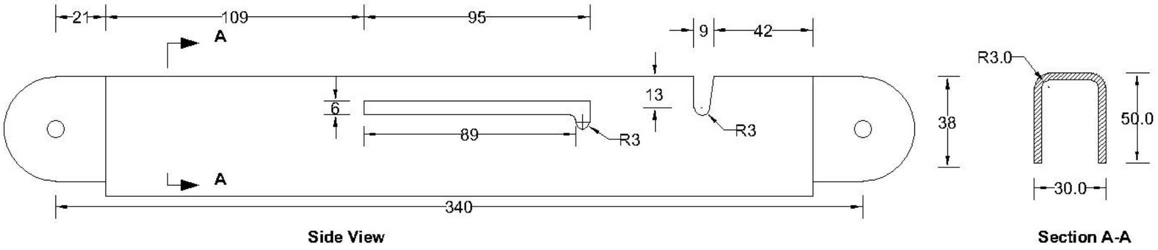

Figure 4.36. Revised primary folding link bar cross-section.

Table 4-1. Summary of results in different load cases.

Part Name	Load Case	Maximum Permissible Plastic Stain (PEEQ) (mm/mm)	Observed Maximum Plastic Strain (PEEQ) (mm/mm)	Maximum Permissible Von Mises Stress (MPa)	Observed Maximum Stress (MPa)
Primary folding link bar (30 mm × 38 mm c-section in Figure 4.8)	[1] Load case a	0	1.7810×10^{-03}	186.7	199.50
	[2] Load case b		0		81.03
	[2] Load case c		3.7910×10^{-05}		184.66
	[3] Load case d		0		177.56
Secondary bar	[1] Load case a	0	0	186.7	117.61
	[2] Load case b		0		112.95
	[2] Load case c		0		116.72
	[3] Load case d		0		186.76
Main lock channel	[1] Load case a	0	0	186.7	55.10
	[2] Load case b		0		33.59
	[2] Load case c		0		60.58
	[3] Load case d		0		47.75
Secondary lock channel	[1] Load case a	0	0	186.7	51.18
	[2] Load case b		0		50.79
	[2] Load case c		0		51.24
	[3] Load case d		0		50.84
Secondary Folding link bars	[1] Load case a	0	0	186.7	57.47
	[2] Load case b		0		59.18
	[2] Load case c		0		57.26
	[3] Load case d		0		62.61

Part Name	Load Case	Maximum Permissible Plastic Stain (PEEQ) (mm/mm)	Observed Maximum Plastic Strain (PEEQ) (mm/mm)	Maximum Permissible Von Mises Stress (MPa)	Observed Maximum Stress (MPa)
Side bars	[1] Load case a	0	0	186.7	3.70
	[2] Load case b		0		1.72
	[2] Load case c		0		3.81
	Load case d		0		2.48
Middle bar	[1] Load case a	0		186.7	38.99
	[2] Load case b		0		38.34
	[2] Load case c		0		39.09
	[3] Load case d		0		40.34

Note: [1] Gravity load case, total load = 4 kPa; [2,3] For the load cases wind pressure 0.85 kPa and specified snow load 2.25 kPa.

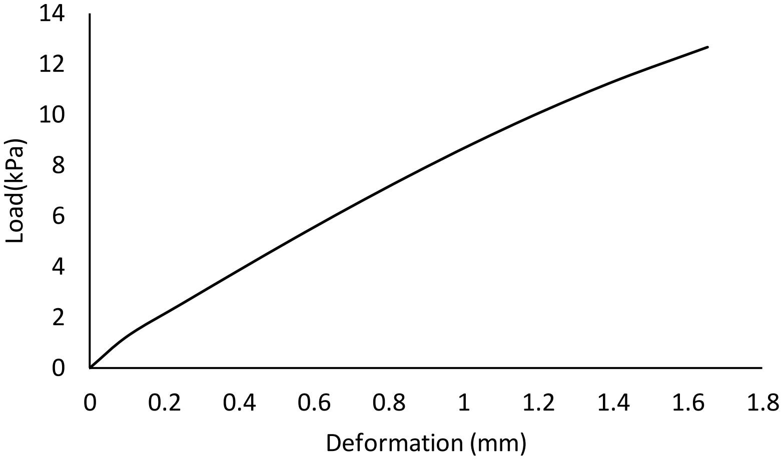

Figure 4.37. Deflection at the midpoint of the primary folding link bar assembly.

The design of the connection also requires checking the pin shear and bearing capacity of the steel sheet near the hole. Thus, another numerical model was developed to simulate a uniaxial tension test on the pin joint in the middle of the main link bar to observe the localized effect due to the interaction of the pin and the holes of the main link bar (Figure 4.38). In this case, the pin was modelled using a 3D solid element (C3D8I). Hard contact was defined between the pinhole of the folding bars and the pin. Figure 4.39 illustrates the von Mises stress distribution and PEEQ value due to the maximum applied load of 15 kN in this case. Using EN 1993-1-8 (2006) (Equation (5)) the predicted pin shear capacity was 8919 N, whereas the numerical model shows the shear capacity to be 8070 N, considering no plastic strain at any location of the pin (PEEQ = 0) (Figure 4.40). However, the literature review has shown that, in experimental investigation, connection capacity is defined based on certain deformation levels (Chung and Ip 2000; Errera et al. 1974; Puthli and Fleischer 2001; Rogers et al. 1998; Salih et al. 2011; Winter 1956). In the absence of the experimental test, it is a conservative design approach to adopt the PEEQ value equal to zero as the capacity benchmark for the pin. The maximum stress in the pin was 366.8 MPa (for PEEQ = 0 condition) and the ultimate stress for A-36 steel is 586.7 MPa. However, for a factored gravity load of 4 kPa (governing load for axial force), the axial force value in the main folding link bar was 6570 N. The maximum stress of the pin for this axial force was 286.9 MPa. Therefore, the pin section is safe in the case of the factored gravity load of 4 kPa and hourly wind pressure of 0.85 kPa.

For the pin connection, another important mode of failure is bearing for the steel plate and pin. It is required to have a benchmark to understand the bearing failure mechanism. Details of the bearing failure mechanism can be found in single-lap bolt connection studies. Ideally, bolts in a single-lap connection and the pin connection have similar structural behaviour such as shear failure, bearing failure and net section failure, the only difference is that the bolt connection has resistance due to clamping friction, whereas the pin provides free rotation. As the load is gradually applied to the bolted connection, the major force transfer would be friction between the contact surfaces. Once the applied force exceeds the friction capacity of the connected members slip relative to each other until they bear on the bolts, contact with the hole interaction dominates the connection performance similar to the pin connection. Thus, the bearing failure benchmark can be obtained from the bolted connection bearing stress review. The literature review has shown that, in the case of bearing failure, a 3 mm hole elongation level is considered to be the ultimate capacity of the connection, thereby ensuring 1 mm deformation at the serviceability limit state (Salih et al. 2011). Using EN 1993-1-8 (2006) (Equation (8)), the bearing resistance capacity for the plate and pin was calculated to be 12,527 N, however, at this load level, the numerical model shows hole elongation of 0.56 mm which is below the threshold limit for bearing failure criterion for serviceability limit state set by Eurocode. Additionally, the maximum design axial force (6570 N) for a factored gravity load of 4 kPa is less than the pin shear capacity (8070 N). Maximum bearing stress in the pinhole was 180.7 MPa (for PEEQ = 0) and the ultimate strength of ASIS 1008 steel was 353.4 MPa. Therefore, the assembly is safe in case of the factored gravity load of 4 kPa and wind pressure of 0.85 kPa in bearing. Thus, it can be concluded that the design capacity of the connection assembly is governed by the strain level near the U-slot of the main link bar.

Bearing resistance of the plate and the pin, $F_b = \frac{1.5\, t\, d\, f_y}{\gamma_{M0}}$, (14)

where d is the diameter of the pin, f_y the lower the yield strengths of the pin and the connected part, t is the thickness of the plate, and γ_{M0} is the safety factor.

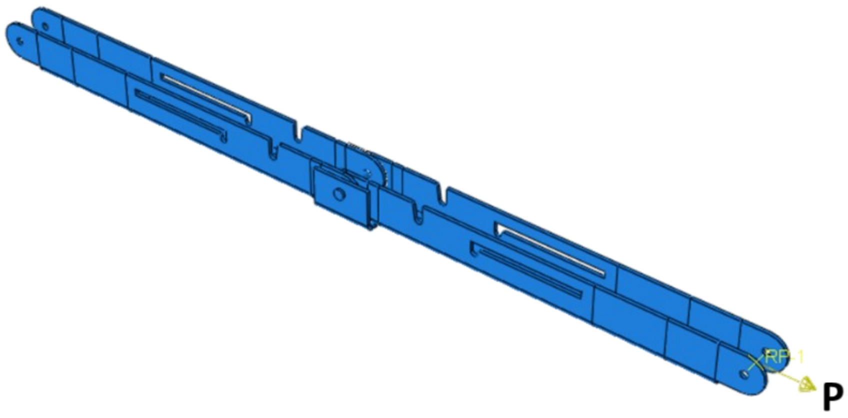

Figure 4.38. Uniaxial tension simulation of primary folding link bars for bearing and pin shear capacity.

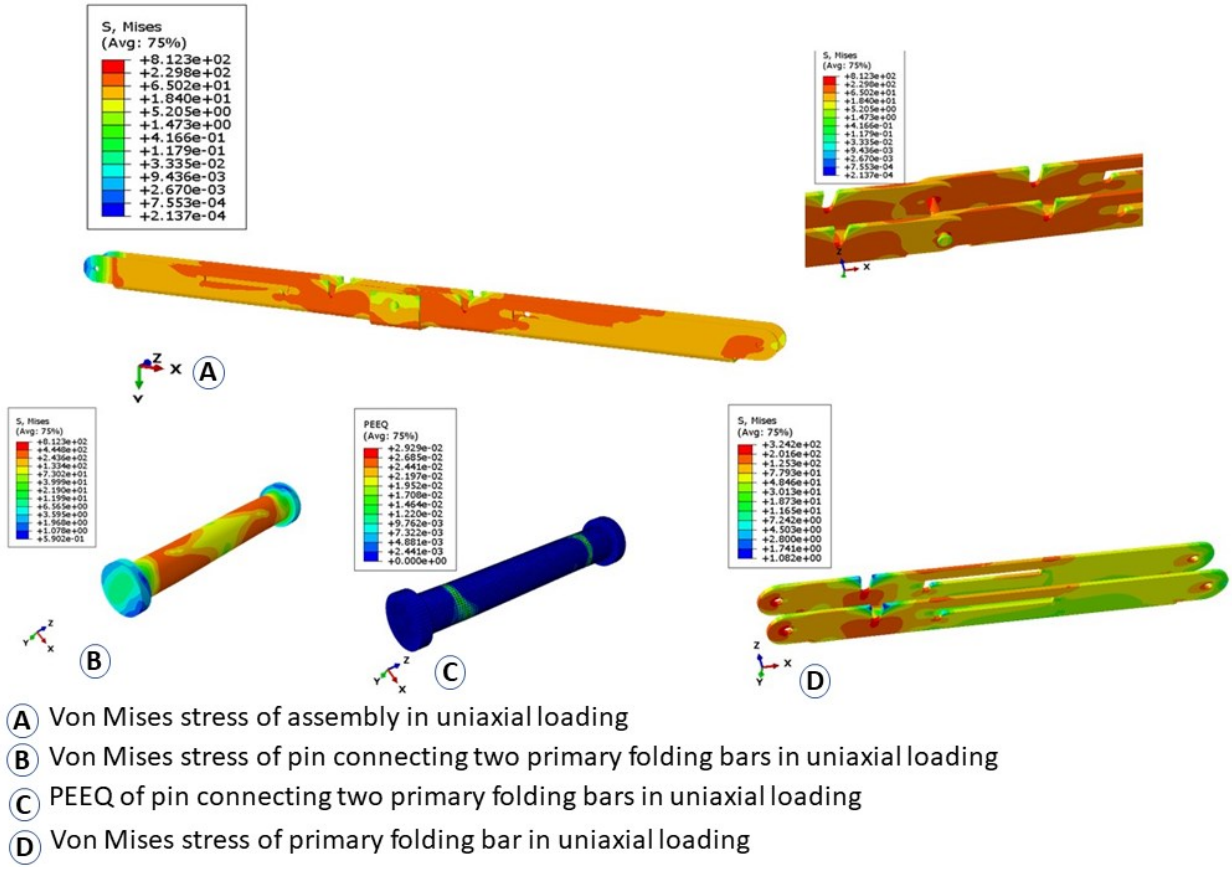

Ⓐ Von Mises stress of assembly in uniaxial loading

Ⓑ Von Mises stress of pin connecting two primary folding bars in uniaxial loading

Ⓒ PEEQ of pin connecting two primary folding bars in uniaxial loading

Ⓓ Von Mises stress of primary folding bar in uniaxial loading

Figure 4.39. Von Mises stress (MPa) and PEEQ plot of uniaxial loading of primary folding link bar and pin (P = 15,000N).

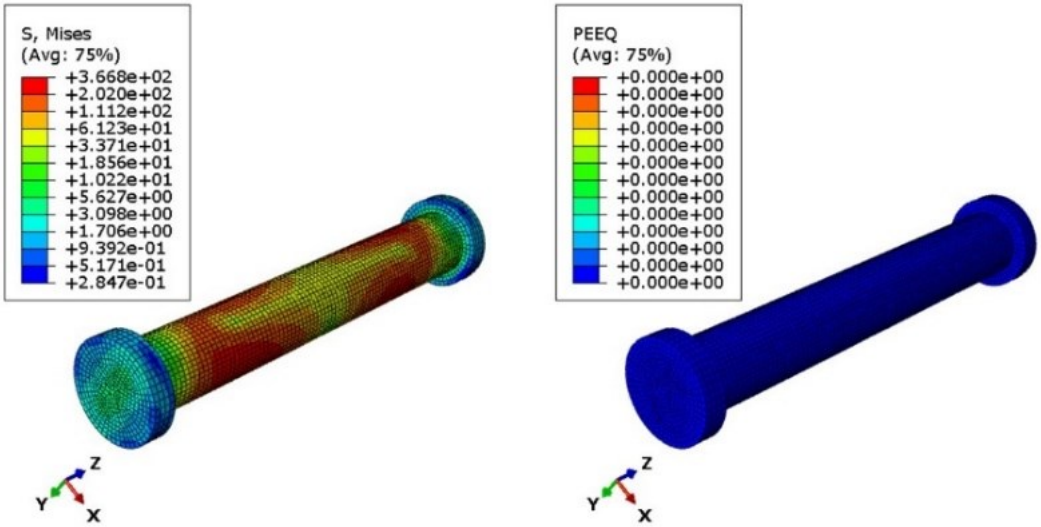

Figure 4.40. Von Mises stress (MPa) and PEEQ plot of the pin at the predicted design capacity using the EN 1993-1-8 equation (P = 8070 N).

4.7. Conclusions

A novel apex connection concept was presented in this chapter. The 3D printout of the assembly demonstrates connection effectiveness in providing the folding, unfolding and self-locking mechanism. The folding mechanism of the connection provides easy transportation of the roof panel assembly, and the self-locking mechanism reduces the onsite workload. The connection can be installed at the offsite facility. In order to reduce the onsite workload and enhance productivity, easy installation of the intercomponent connections is required. In this respect, the folding design of the apex connection will facilitate the erection of two panels simultaneously and reduces the crane lifting number. Furthermore, the self-locking mechanism removes the onsite installation activity of the apex connection. Consequently, this novel apex connection is expected to improve onsite productivity. However, the comparison with current truss base roof fabrication requires future time study for this panelized roof system with this folding apex connection.

The validation of 2D FEM with the analytical solution confirms the adequacy of the model for the connection force analysis. The 3D FEM results of PEEQ show that two different C-sections (30 mm × 38 mm and 30 mm × 50 mm) of the main folding bar are required for specified gravity loads of 2.36 kPa and 4 kPa, respectively. The shear capacity of the pin (d = 6.35 mm) obtained from the analytical model was higher than the predicted capacity of FEM since the former procedure is developed based on certain deformation levels in the experimental investigation. To obtain the ultimate strength of a steel connection, validation of the numerical model with an experimental test is necessary. This study was limited by the lack of material coupon tests and actual assembly tests. The benchmark of the PEEQ value equal to zero in determining the design capacity of the assembly is a conservative approach. Therefore, to establish the proper ultimate capacity and serviceability limit of the present connection, actual testing of the connection is recommended. However, the obtained cross-section from this study provides the basis for the fabrication and testing of the assembly in future.

As part of a future study, long-term performance, such as fatigue and durability of this connection, must be investigated. Following the industry practice of light frame connectors such as wood I-Joist hangers, the fabrication of components of the apex connection must use galvanized sheet metal to enhance weatherability.

Chapter 5 : System behaviour of panelized roof

This chapter presents the system behaviour of light-frame panelized gable roof. A detailed FEM was developed incorporating nonlinear load-slip response of the connections. The paper is based on a paper submitted to a peer-reviewed journal.

Finite element analysis of a light-frame wood panelized gable roof

Md Saiful Islam[1,2], Ying Hei Chui[1]
[1] University of Alberta, AB T6G 1H9, Canada
[2] mdsaiful@ualberta.ca

Abstract: A three-dimensional (3D) finite-element analysis of a light-frame wood panelized gable roof is presented. The study developed equivalent macro elements representing the major roof components, such as the roof panel and support wall, in the finite-element model (FEM) by utilizing analytical models of the diaphragm and shear wall of CSA 086-19. The most critical load response of the panelized roof structure was obtained by considering the governing load cases, including the partial load case for snow load. The load path analysis revealed that the panelized roof had a two-way load distribution due to the deep beam action of the support wall. The gable ends of the roof carry approximately one-third of the load. In the gravity load case, the in-plane shear governed the connection design at the eave and support wall lines. Self-tapping screws were very effective in resisting wind uplift forces due to their high withdrawal capacity. Furthermore, the deflection pattern of the ceiling joist revealed the effect of panelized construction on the load path.

Keywords: panelized roof, load path, system behaviour, finite-element model (FEM)

5.1. Introduction

Panelized fabrication of light-frame wood buildings is a popular construction method for home builders in North America because of reduced waste and construction time compared to traditional stick-built construction (Altaf et al. 2018a; National Association of Home Builders 2022). In this process, the fabrication of light-frame buildings is performed in an offsite construction facility. The entire building is subdivided into several panel components, such as wall and floor panels. The majority of construction activities take place following a controlled manufacturing principle. For example, an Alberta-based panelized home producer has several workstations to fabricate walls in their automated wall production line, whereas the floor is constructed in the floor line. However, due to its structural system, complete roof production is performed in several volumetric units. As illustrated in Figure 5.1, roof trusses are used to fabricate the several volumetric units and transported to the site using trailers. All the activities are manual and time intensive (Islam et al. 2022a). Consequently, roof production has a relatively low production rate compared to other components such as walls or floors. In addition, a single detached home with a 149 m^2 floor area requires four trailers hauling, thus increasing transportation costs (ACQBUILT Inc. 2019). Moreover, this roof fabrication process is not feasible in congested work site cases. Therefore, the roof is built at the site following the traditional stick-built process. Hence the overall project duration and the cost increases significantly.

To improve roof production of panelized construction, a holistic structural system is required that accounts for all the offsite construction factors such as fabrication constraints of a production line, transportation limitations, and onsite installation issues. In this regard, Islam et al. (2021, 2022a; b) have developed a panelized gable roof system that incorporated the production line factors of an Alberta-based prefab company and transportation limitations. The components of the panelized roof are illustrated in Figure 5.2. This holistic design enables the panelized gable roof components to be fabricated using the existing wall or floor production line, thereby leading to improved utilization of the prefabrication facility.


(a) Truss arrangement at roof production line (b) Complete one volumetric unit of a roof

Figure 5.1. Present state of roof production (a) Truss layout (b) Loaded roof component unit.

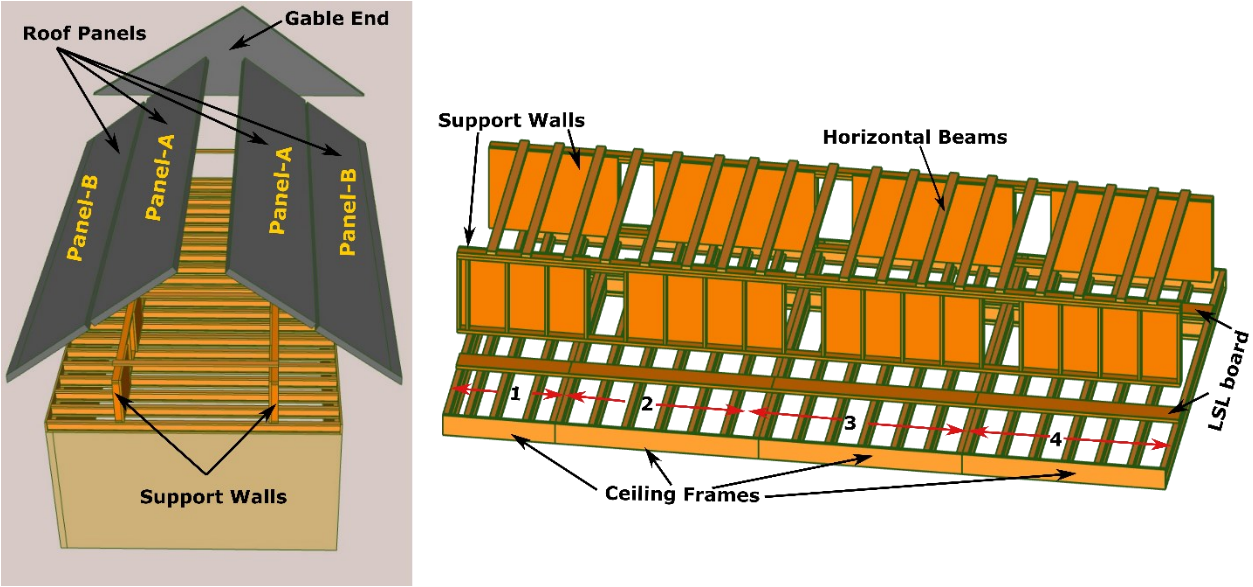

Figure 5.2. Panelized light frame roof.

As can be observed from Figure 5.2 for a 134 m^2 single detached home, the gable roof has four roof panels (two types: panel-A and panel-B), two support walls spanning from one gable end to another, four ceiling frames, two gable-ends and several horizontal beam elements spanning from one support wall to other. Most of these components can be produced using automated and semi-automated production lines. For instance, the production of roof panels in the wall line using Laminated Strand Lumber (LSL) rafters and Oriented Strand Board (OSB). Whereas the ceiling frame fabrication in the floor line using lumber or wood I-joists. It is worthwhile to note that producing these components using the corresponding production line does not require any modification to the existing work process. Consequently, this system is expected to have a higher production rate and be cost-competitive compared to the current roof system (Islam et al. 2021). The successful implementation of the panelized roof system requires efficient connections that can withstand the design load. Islam et al. (2022b) conducted an extensive experimental study on the short-term mechanical performance of light-frame wood panelized roof connections. Figure 5.3 shows the connections of a light frame wood panelized gable roof. The support wall-to-panel-A joint consists of a 200 mm screw connecting the top plates of the wall and roof panel (Figure 5.3 a). Whereas for panel-B, a wedge piece (210 mm × 140 mm × 76 mm) is attached to the support wall using two screws and the roof panel is attached to the wedge using L shape steel angle bracket (38 mm × 38 mm) and 38 mm long screws with a diameter equivalent to 10 d nails (Figure 5.3 b) (Islam et al. 2022b).

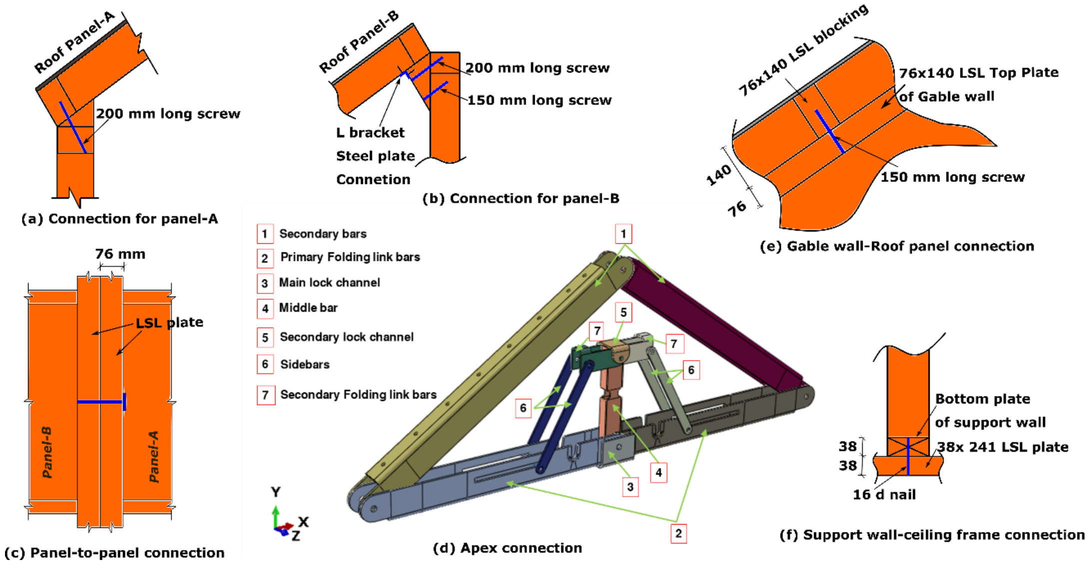

(a) Connection for panel-A

(b) Connection for panel-B

(e) Gable wall-Roof panel connection

(c) Panel-to-panel connection

(d) Apex connection

(f) Support wall-ceiling frame connection

Figure 5.3. Connections of panelized light frame wood roof.

The panel-to-panel connection uses 150 mm long screws to join the 76 mm thick LSL plates of the roof panels laterally (Figure 5.3 c). Similar joint configuration as support wall-to-panel-A is used for panel-B-to-ceiling frame connection at the eave line. The gable wall and roof panel connection require a 150 mm long screw (Figure 5.3e). Nails are used to connect the support wall and the ceiling frame, as indicated in Figure 5.3f. An in-depth design and analysis process of these connections can be found in (Islam et al. 2022b). The apex connection illustrated in Figure 5.3d facilitates a novel folding mechanism before installing the roof panels at the site. Details of this apex connection geometry and analysis can be found in (Islam et al. 2022c). In summary, this connection is fabricated using steel C section, and complete installation at the factory facilitates the transportation of the two roof panels as one vertical module. It also reduces the number of crane lifts by providing a self-locking mechanism at the service state of the connection (Islam et al. 2022c).

In order to implement this panelized roof system, it is essential to understand the global response of the complete assembly. Therefore, this study uses the commercially available FE program Abaqus to develop a 3D finite element model (FEM) of a panelized gable roof for a single detached home. This model revealed the overall global structural response, load sharing under gravity and wind loads, and connection requirements at the factored design load level, according to the National Building Code of Canada (NBCC 2020a).

5.2. FEM of light-frame wood building

Finite element models (FEMs) have proven to be a cost-effective method for evaluating the structural response of a wide range of light-framed wood buildings (Satheeskumar et al. 2017b). This method effectively solves complex and extensive structural systems by implementing super-element concepts and sub-structuring light-frame wood buildings (Kasal et al. 1994). He et al. (2001) used the shell, beam, and nonlinear spring elements to analyze the performance of 3D light-frame wood building component, including shearwalls, framing lumber and connections under static loading conditions. They validated two shear wall segments (2.4 m × 2.4 m) model with laboratory test results to observe the sensitivity of their FEM modeling technique, and then modelled the 3D building incorporating the nail connection test data as input for nonlinear spring elements. In light-framed structures, the inter-component connections influence the load-sharing and load-transfer of the structure (Chowdhury et al. 2013; Morrison 2010; Satheeskumar et al. 2016). Shivarudrappa and Nielson (2013) developed a numerical model of a gable roof comprising fink-trusses to understand the sensitivity of load distribution in light-framed wood roof systems in a highly detailed fashion, including the explicit modelling of each connector using commercial FE package Ansys (ANSYS 2013). The roof model consists of 13 fink-trusses spaced at 0.6 m (24 in.) c/c with a span of 9.1 m and a ridge height of 1.5 m. The truss members were modelled using the BEAM4 element: a frame element with tension, compression, torsion, and bending capabilities, whereas elastic shell elements (SHELL63) were used to model the sheathing panels, which captured the in-plane and out-of-plane action. Results from their analytical model indicate that the distribution of loads is sensitive to the overall stiffness of roof- to-wall (RWC) connections. Satheeskumar et al. (2017b) validated a 3D FEM full-scale test structure model using Abaqus FE software (Dassault Systèmes 2021). The FE model predicted load sharing, variation of stiffness of RWC with respect to the other elements (i.e., roof cladding and ceiling), and structural response within the elastic and post-elastic phases. Laboratory testing of roof-to-wall triple grip connections provided the force-displacement relationship input to model three nonlinear spring elements, which analytically represented each RWC (Satheeskumar et al. 2016, 2017b). The FEM model produced close results to full-scale structural test measurements with approximately 5–15% higher reaction coefficient for wind uplift and 10–15% for lateral load case. The authors concluded that the difference in the RWC stiffness input into the FEM and actual stiffness in the full-scale test might have contributed to this discrepancy.

Based on the above studies, it can be concluded that FEM analysis would be an effective means to understand the load-deformation response behaviour of the proposed panelized gable roof. However, before developing the complete FEM of the panelized gable roof, a validation exercise of an actual test on a light frame roof was performed to observe the effectiveness of the available elements of the FE software in predicting the load-deformation response of an assembly.

5.3. Validation of finite element model

As can be observed from Figure 5.2, the ceiling frame consists of repetitive timber joists spaced not more than 600 mm c/c, and Laminated Strand Lumber (LSL) boards are connected to the joists to provide a base for the support wall connection. This construction characteristic resembles the light-frame floor system where sheathing is attached to the joists by nailing. Therefore, the study by Doudak et al. (2005) was used to validate the system behaviour of light-frame roof joists using Abaqus. Their study monitored the structural response to environmental loads of a single-storey light-frame wood industrial shed in Sainte-Foy, Quebec, Canada. The roof of the monitored building had 457 mm deep wood I-joists spaced at 406 mm c/c and sheathed with plywood. All wood I-joists were seated on light gauge steel hangers and aligned directly with studs in supporting walls. During monitoring experiments, deformations of a continuous strip of the wall and roof were measured within the building. Apart from the monitoring experiment, load–deformation response under artificial static point loads was also measured on the roof (Figure 5.4). A point load of 3 kN was applied to the roof surface using weights placed on a square plate with a side length of 20 mm, as illustrated in Figure 5.4. The wood I-joist-2 loaded at mid-span and vertical deflection was measured along with the deflections of adjacent joists, as indicated in Figure 5.4, to investigate the degree of load sharing. A finite element model of this structure was developed in Abaqus. As shown in Figure 5.5, the three I-joists were modelled using linear beam element (B31: A 2-node linear beam in space), and roof plywood was modelled using shell element (S4). The information on nail spacing of the roof diaphragm was missing in the study. Therefore, the nail spacing for the plywood to I-joist connection was determined using back-calculation following the diaphragm design procedure of section 11.6.3.2 of CSA 086-19 (CSA 2019) (see section A-1.1 and calculation in Appendix-1). In this case, 150 mm nail spacing was obtained if the common 3-inch nail was used. The nail connection between the I-joist and plywood was modelled using the connector element of Abaqus.

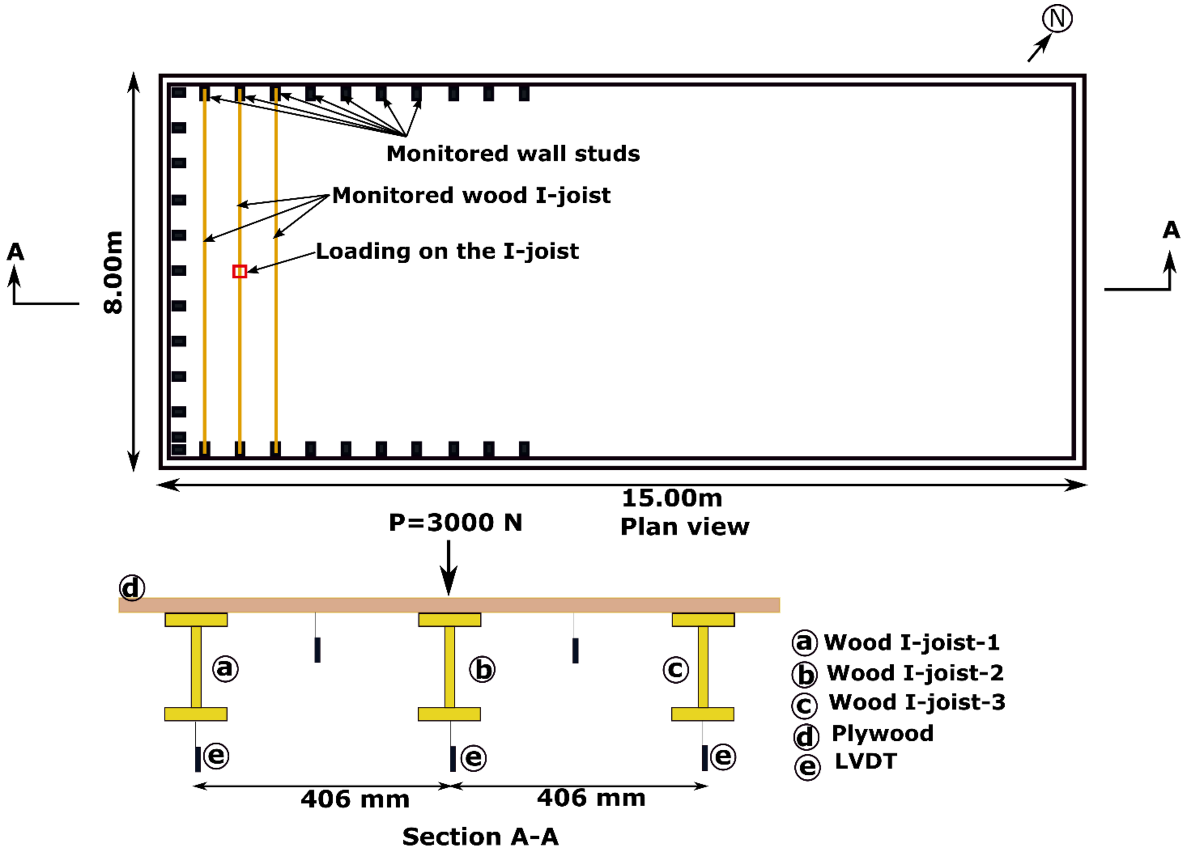

Figure 5.4. Experimental setup of load-sharing test.

Two linear springs were used to define the behaviour of the connector. Doudak et al. (2005) used a floor analysis program (FAP) developed by Foschi (1985) to model the load-sharing experiment under static point load and found a good correlation with test data. According to the FAP program, the nail connection stiffness value of 2625 N/mm can be used to predict wood floor deflections. So, this stiffness value was adopted for the spring properties in the connector element. Simply support boundary condition for the joists was assigned since they were seated on light gauge steel hangers in the building. Two sides of the plywood were assigned symmetry boundary conditions along the x-axis, as shown in Figure 5.5. A 20 mm × 20 mm area of the plywood was partitioned and constrained to a reference point to apply the 3kN point load to replicate the actual test setup. As can be observed from Table 5-2, overall, the FEM overpredicted the deflection of the loaded joist by 22.8%; however, it is very close to the actual test for the adjacent joists. Hence, it can be concluded that as long as proper element type, material and connection behaviour are incorporated in the model, FEM can simulate the load sharing of the light frame assembly.

Table 5-1. Materials properties

Material	E (MPa)	Poisson's ratio	Flexural rigidity, EI (kN m^2)	Connection stiffness (N/mm)
Plywood	7412	0.3	-	-
Wood I-joist	13778	0.3	4.8×10^{03}	-
Nail			-	2625

Table 5-2. Results of the FEM

	Deflection in Loading Test (mm)	Deflection in FEM (mm)	% Error
Loaded joist	1.45	1.78	22.8% (over prediction)
Adjacent Joist 1	0.780	0.77	1% (under prediction)
Adjacent Joist 2	0.844	0.77	9% (under prediction)

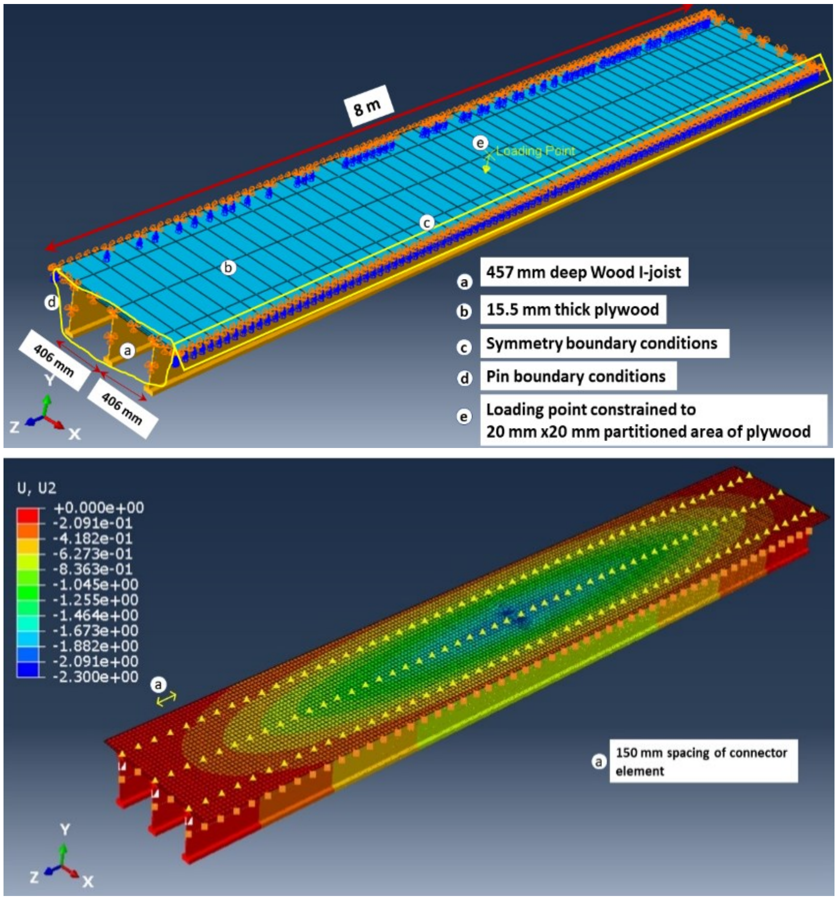

Figure 5.5. FEM of the test setup of Doudak et al. (2005).

5.4. FEM of light-frame wood panelized roof

The analysis presented in this study employs simple mechanics-based models for subassembly, such as shear walls of CSA 086-19 (CSA 2019) and finite-element techniques to characterize the responses of a panelized gable roof subjected to different load cases. In order to understand the load-deformation response of a panelized roof, a 3-D roof assembly of a typical two-storey single detached home with a gable roof was considered. The gable roof of the building has a footprint of 6.10 m × 11.0 m (20 ft × 36 ft) and a slope of 8/12 (Figure 5.6). Four governing loading combinations from the Canadian Building Code were considered for this numerical analysis. These load combinations account for all the combinations, including gravity load (dead, live and snow) and lateral load (wind load), that will lead to maximum effects for both strength and serviceability. The design loads applied to the roof structure were assigned based on the National Building Code of Canada (NBCC) (NBCC 2020a) and the building location is Edmonton, Alberta, Canada.

Load case a: 1.25D + 1.5S

Load case b: (1.25D or 0.9D) + 1.5S + 0.4W

Load case c: (1.25 D or 0.9D) + 1.4W + 0.5S

Load case d: 0.9D + 1.4W

where D = dead load, L = live load, S = snow load and W = wind load.

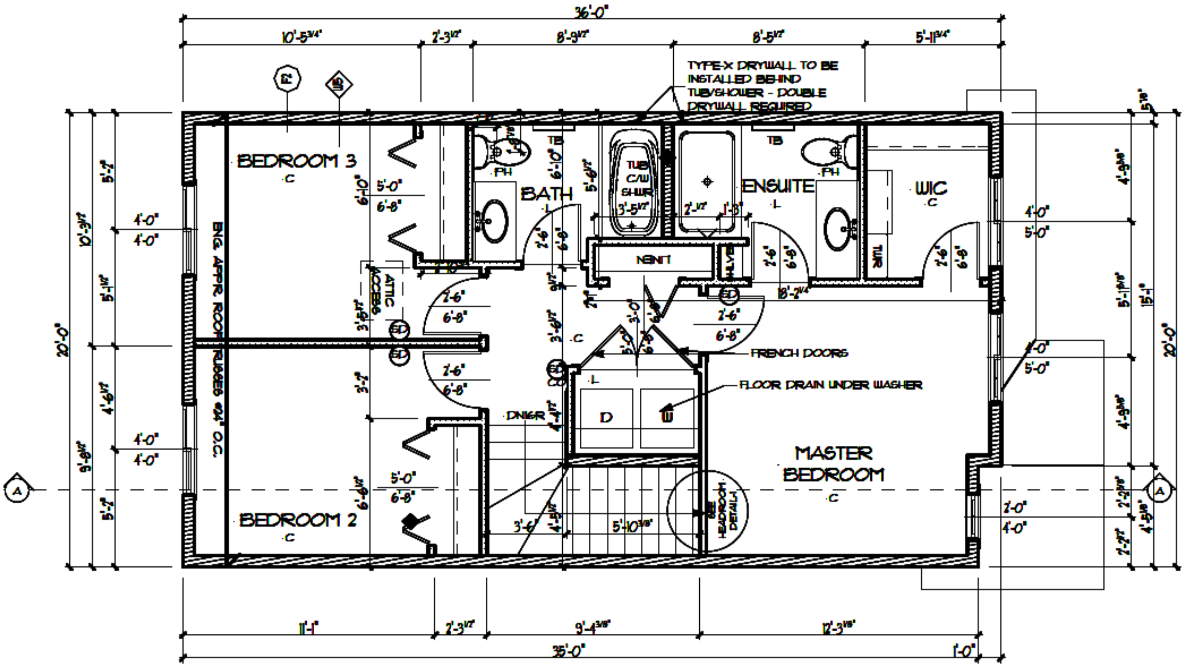

Figure 5.6. Second floor plan.

5.4.1. Roof Panel, Support wall, Ceiling frame and Connection components

The panelized roof is an assembly of several subsystems, such as diaphragms (panel-A and panel-B) and shear walls (support wall). The roof panels act as diaphragms when the system is subjected to wind load perpendicular to the ridge. In contrast, the support wall acts as a shear wall in wind load parallel to the ridge direction. The roof panels are produced on the wall line following the similar procedure used to fabricate the wall panel (Islam et al. 2021). As can be observed from

Figure 5.7, the components of the roof panel include 76 mm thick LSL top and bottom plates, 38 mm × 140 mm LSL or lumber rafters, and 9.5 mm thick oriented strand board (OSB) nailed on the framing (Islam et al. 2022a). The shear capacity of the roof panel is governed by the nailing of the sheathing-to-framing. The analytical model of diaphragm design explained in section 11.6.3.2 of CSA 086-19 (CSA 2019) was applied to determine the nailing requirement. Figure 5.8 illustrates the construction details of the support wall. Since the support wall acts as a shear wall in case of wind load parallel to the ridge, shear capacity is governed by the nailing of OSB to the stud (CSA 2019) , whereas the connection component geometry requirement for the roof panels governs the sections such of LSL top plates (Figure 5.8). As illustrated in Figure 5.7 and 5.8 roof panel and support wall consist of several types of timber components and nail connection; representing each component with fine-scale details in the FEM of complete assembly is computationally expensive and impractical.

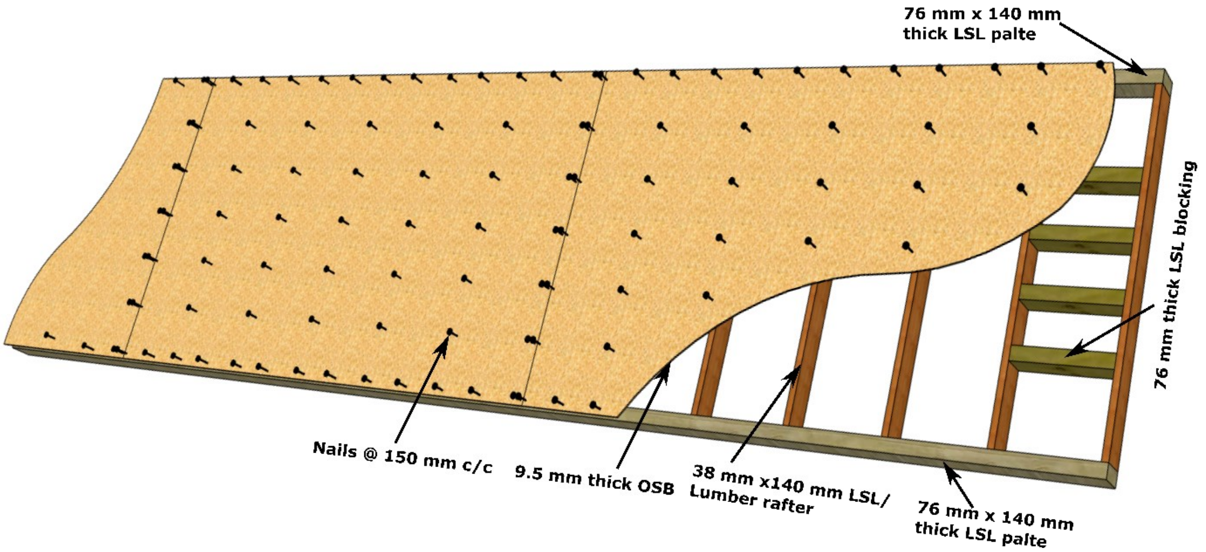

Figure 5.7. Roof panel construction details.

Therefore, a macro-element modelling approach as discussed herein, similar that adopted by Cárcamo et al. (2018) and Martin et al. (2011), was used to model the roof system, whereby the roof panel and support wall were modelled as macro-elements in Abaqus. In this study, roof panels and support walls were represented via shell elements with equivalent properties determined analytically and validated using the FEM of each diaphragm and shear wall component. The process is explained in the proceeding section.

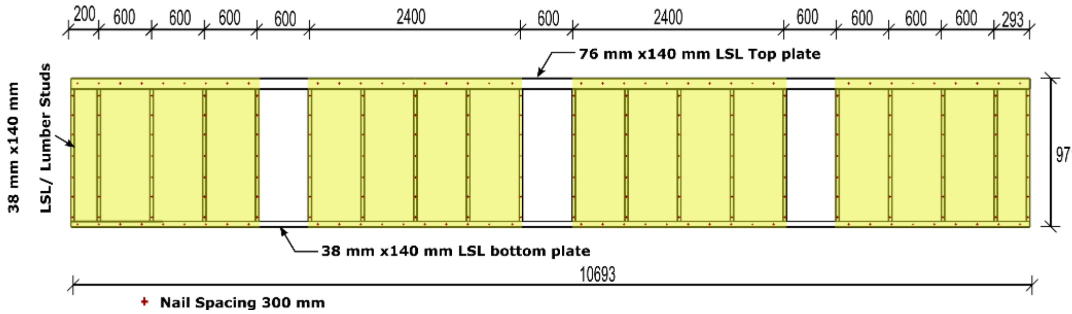

Figure 5.8. Support wall construction details.

5.4.2. Shell Element Behaviour

The roof panel and support wall were modelled via equivalent macro-elements developed from general-purpose shell elements (S4R) with orthotropic material properties. To account for the construction characteristics of roof panels, shell macro element properties were calibrated. The equivalent out-of-plane bending thickness (t_b) of shell elements of the roof panel and the short wall was obtained using the γ-method (Mohler 1956), following a similar procedure by Mosalam et al. (2002). The procedure accounts for the composite action between OSB (E= 7,425 MPa) sheathing and LSL framing (E= 8,965 MPa) connected by nails (see section A-1.2 and equations in Appendix-1). This equivalent thickness was used for calculating the plate out-of-plane bending and transverse shear stiffness.

The roof panel acts as a diaphragm to transfer in-plane load due to wind load. Therefore, the modulus of elasticity (E1 and E2) of the equivalent shell element was modified, assuming the roof panel as a deep beam, and the analytical method explained in CSA 086-19 was used to obtain a similar in-plane load-deformation response (CSA 2019). First, using the CSA 086-19 diaphragm equation, the deflection of the roof panel subjected to an in-plane shear load of 1 N/mm was determined ($\Delta_d = 0.88\ mm$) (CSA 2019). Then a deep beam with the same dimension as the roof panel was modelled, implementing shell elements in Abaqus with a simply supported boundary condition, and E1 and E2 values were calibrated to obtain the deflection as observed in the previous step. Figure 5.9 shows the deflection of the equivalent roof panel modelled using shell elements.

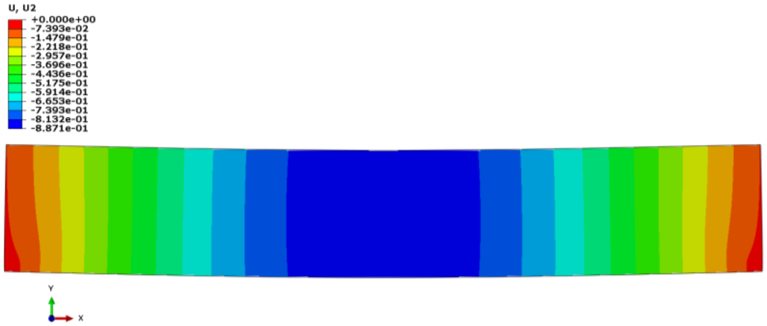

Figure 5.9. Deflection of deep beam modelled using shell element for roof panel.

The support wall in the roof panel assembly extends from one gable end to the other. A two-step process was performed to calibrate the support wall shell element properties. Initially, a deep beam spanning from one gable end to the other was modelled since it transfers load from the roof panel to the ceiling frame. First, using the CSA 086-19 (CSA 2019) diaphragm deflection equation, the midpoint deflection of simply supported support wall subjected to in-plane uniformly distributed load (1 N/mm) was obtained ($\Delta_d = 1.26\ mm$). Then using the shell elements, the same wall was modelled in Abaqus to calibrate the modulus of elasticity (E1 and E2) of the equivalent shell element (Figure 5.10a) such that the support wall had the same deflection as determined in the previous step. It should be noted that in this step, the opening of the support wall was ignored to have consistency with the CSA 086-19 analytical model (CSA 2019). However, in the case of wind load parallel to the ridge direction, the support wall behaves more like a shear wall. Hence, the deflection of the shear wall with opening subjected to unit lateral shear (1 N/mm) was obtained using the CSA 086-19 shear wall deflection equation (CSA 2019) ($\Delta_{sw} = 1.02\ mm$). Then the shear modulus (G12) of the shell element was calibrated to achieve the calculated shear wall deflection of the equivalent element in the previous step (Figure 5.10b). In actual roof assembly the support wall top and bottom plates are in contact with roof panel and LSL plate of ceiling frame. To prevent excessive distortion of the edges of the equivalent shell element, a stringer element with a cross section of 38 mm × 140 mm was defined during the calibration of properties. In Abaqus stringer element mathematically increases the stiffness of an edge of a two-dimensional planar part such as a shell.

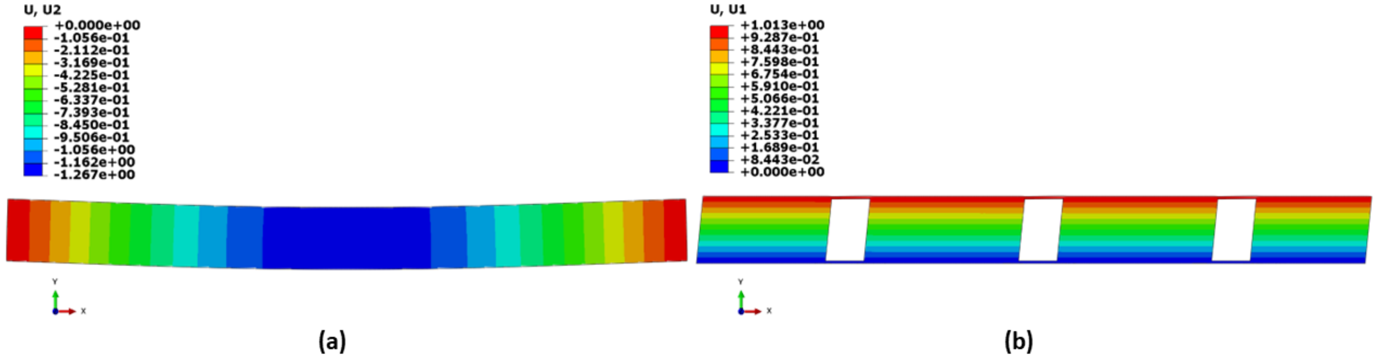

Figure 5.10. (a) E1 and E2 calibration (b) G12 calibration of support wall.

The gable end is a triangle-shaped shear wall. The components of the gable wall include a 76 mm × 140 mm LSL top plate, 38 mm × 140 mm lumber bottom plate, 38 mm × 140 mm lumber studs and 12 mm thick OSB. As can be observed from Figure 5.11, the vertical studs were spaced unevenly to facilitate the connection of the support wall ends. The nailing (100 mm c/c) of OSB boundary and intermediate support studs was governed by diaphragm shear due to wind load perpendicular to ridge direction. To assess the shear capacity of the gable wall, a 2D finite element was developed in Abaqus. The FE modelling methodology followed the techniques described by

Judd and Fonseca (2005) and Kuai et al. (2022). A 2-node beam element (B21) for the framing member and a 3-node triangular shell element (S3) for the OSB sheathing were utilized to model this assembly. The connector element available in the Abaqus library was used to define the OSB-to-framing and LSL plate-to-stud nail connections. This element in three-dimensional space (Conn3D2) is a two-node 1D element that effectively substitutes the active parts of a connection and defines a constitutive relationship between the degrees of freedom of the respective nodes (Dassault Systèmes 2021). To define the connector behaviours, nonlinear spring properties based on the actual nail connection test by Islam et al. (2022b) were incorporated. Figure 5.12 to 5.14 show the load-slip curves of three connections used in the 2D FEM to define the non-linear spring properties.

The material properties described in Table 5-3 were used for shell and beam elements. The gable wall was subjected to a lateral load (along the x-axis in Figure 5.11) that was equal to the calculated diaphragm shear force in the case of wind applied perpendicular to the ridge direction. The maximum slip and force resisted by the nail connection were 0.63 mm and 498.6 N, respectively (see the supplementary section A-1.2 of Appendix-1).

Table 5-3. Elastic Properties used in Abaqus for gable Wall FEM (CCMC 2019; Janowiak et al. 2001; Karacabeyli et al. 1996; Moses et al. 2003; Niederwestberg et al. 2018; Shahidul Islam et al. 2017)

	Modulus of elasticity (MPa)			Poisson’s ratio			Shear Modulus (MPa)		
	E_1	E_2	E_3	σ_{12}	σ_{13}	σ_{23}	G_{12}	G_{13}	G_{23}
OSB	5323	3231	130	0.183	0.364	0.312	1574	157.4	157.4
LSL	8965	996	1350	0.298	0.5	0.6	490	195	80

The factored shear resistance of the OSB-to-framing nail connection is 559 N based on the CSA-086 equation. Therefore, with OSB-to-framing nail spacing 150 mm and 12 mm thick OSB meets the design requirement. To simplify the assembly FEM, the gable wall was modelled using shell elements. Hence, equivalent shell element properties were calibrated to obtain the same lateral drift mentioned above. Table 5-4 summarizes all calibrated properties of all the shell elements used in this study.

Table 5-4. Elastic Properties used in ABAQUS for equivalent shell elements.

	Modulus of elasticity (MPa)			Poisson's ratio			Shear Modulus (MPa)			Thickness (mm)
	E_1	E_2	E_3	σ_{12}	σ_{13}	σ_{23}	G_{12}	G_{13}	G_{23}	
Support wall	9950	9950	8965	0.183	0.364	0.312	17	30	30	71.3
Roof Panel	3000	2000	8965	0.183	0.364	0.312	1574	157.4	157.4	75.8
Gable End	6550	6550	8965	0.2	0.2	0.2	565	157.4	157.4	25.2
LSL board	8965	996	1350	0.298	0.5	0.6	490	195	80	38

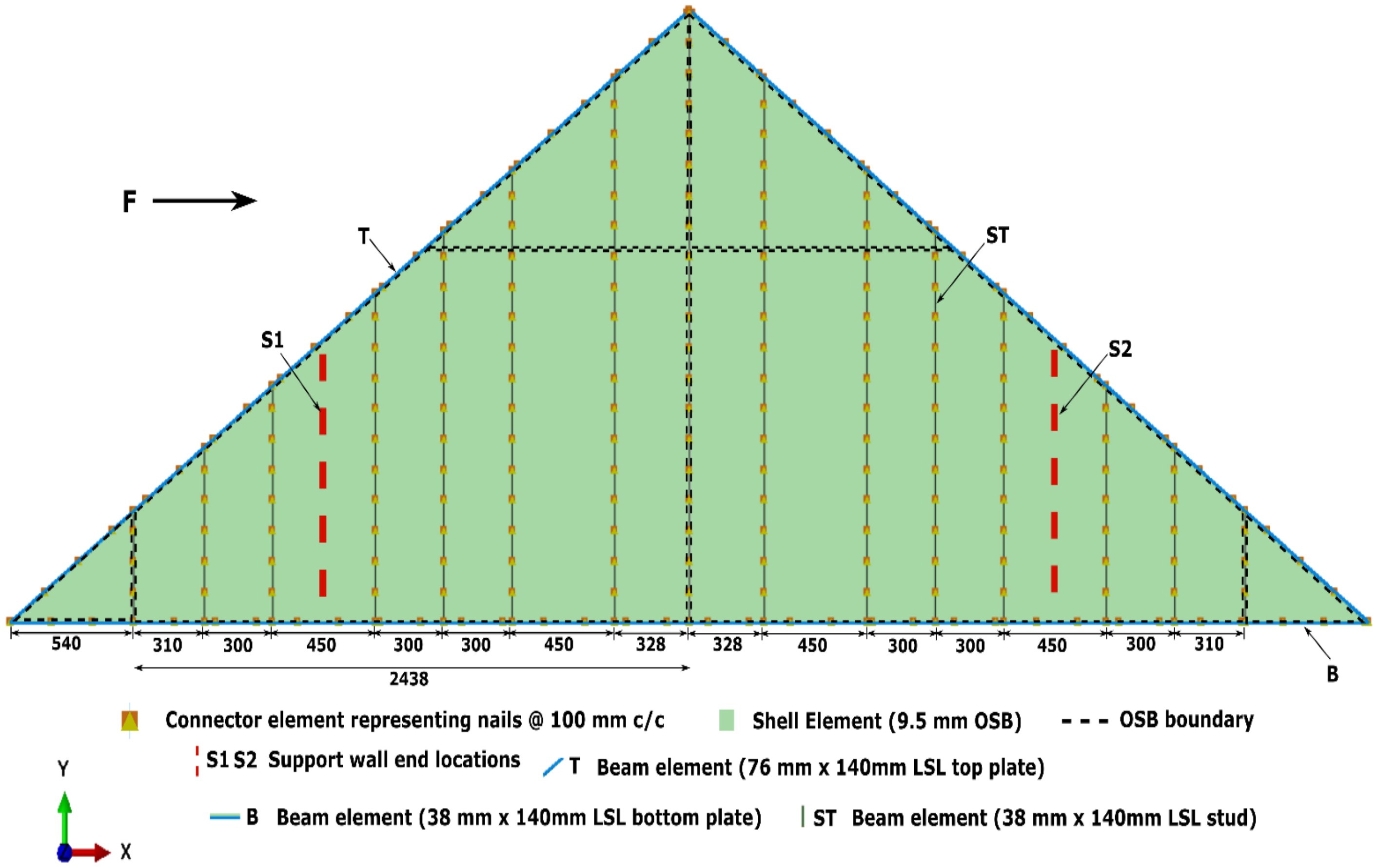

Figure 5.11. Gable wall analysis model (all dimensions are in mm).

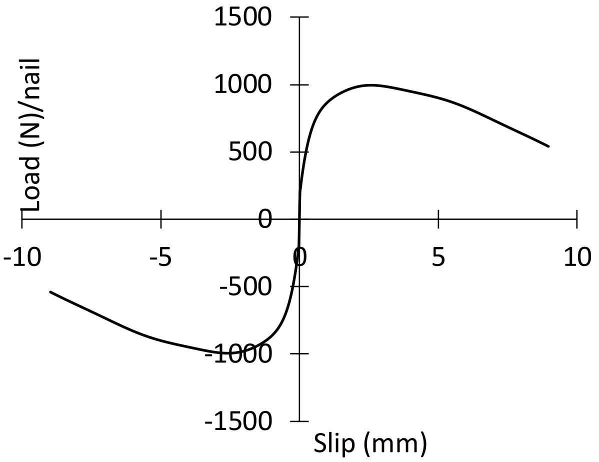

Figure 5.12. Load slip curve of OSB-LSL nail connection in shear along the x and y-axis.

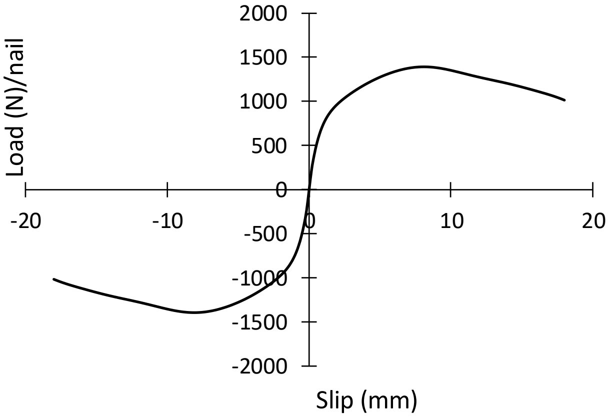

Figure 5.13. Load-slip curve LSL-LSL nail in shear along the x and z-axis.

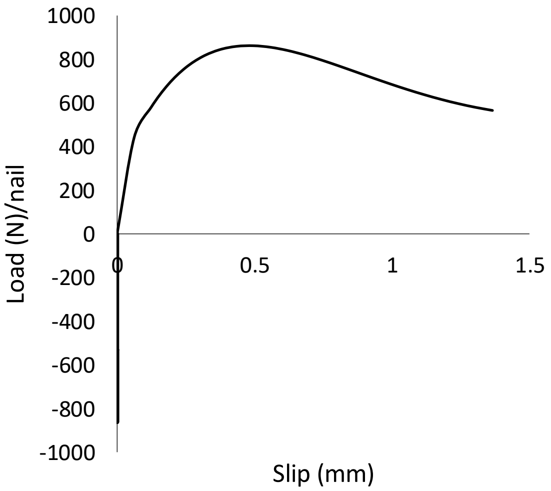

Figure 5.14. Load slip curve nail withdrawal/compression along the y-axis for LSL-LSL connection.

5.4.3. Modelling complete roof assembly

The 3D FE roof model consisted of four ceiling frames (Figure 5.15), two support wall parts, seventeen beams spanning between the two-support walls, four roof panels (Figure 5.16 to

5.18), and two gable end parts (Figure 5.17). As illustrated in Figure 5.15, ceiling frames were modelled as beam elements (B32) with isotropic material properties (Table 5-5). For the case study home, there were three 3.0 m wide (C1-C3) and one 1.2 m wide (C4) ceiling frame (Figure 5.15). The joist spacing of the ceiling frame was 600 mm. As indicated in Figure 5.18 (see note d), there were two joists in three locations of the roof assembly due to panelized construction. The width of the ceiling frame was determined considering the fabrication limitation of the offsite manufacturing facility (Islam et al. 2021). The ceiling joists and rim board are supported on the load-bearing shear wall of the second floor. So, reference points were generated on the ceiling joist at a location 70 mm from the rim board edge and the midpoint locations of each segment of the rim board, as indicated in Figure 5.15. The reference points were constrained to the 70 mm segment of partitioned joists and rim board segments. These reference points were assigned pinned boundary conditions (U1=U2=U3=0). Therefore, in post-processing of the FEM, these reference point nodes captured the reaction forces. The individual ceiling frame segments also have 38 mm × 241 mm LSL board attached at a location of roof span/4 distance (Islam et al. 2021).

The LSL board is connected to the ceiling joist using nails. Three nonlinear spring elements (aligned with the local x', y', and z' directions of the connector, as depicted in Figure 5.15) represented each LSL board-to-ceiling joist nail connection. The load-slip relationship for these spring elements (in the case of shear response along the x' and y' axis in Figure 5.13 and withdrawal according to Figure 5.14 in the z' axis direction) was obtained from laboratory testing (Islam et al. 2022a). Two nails connected the rim board and end edge of the ceiling joist. Hence, the shear response of this nail connection was defined by the graph shown in Figure 5.13 along the local y'' and Figure 5.15 along the z'' axis. The spring stiffness along x'' was set to infinity to represent the hard contact between the rim board and ceiling joist end. It is worthwhile to note that this nail connection was defined only to maintain the model connectivity in Abaqus.

Furthermore, the support walls were attached to the LSL board using nails, as illustrated in Figure 5.16. This connection was also defined using three nonlinear springs with load-slip properties, as shown in Figures 5.13 and 5.14 (shear response along the x' and y' axis and withdrawal/compression for the z' axis). The LSL beams spanning between the support wall were connected using nails. It was assumed that five nails were sufficient to resist the design load. Hence to represent this connection, the load-slip properties of Figures 5.13 and 5.14 were used (shear response along the x'' and y'' axes and withdrawal/compression for the z'' axis) for those five nails. The two roof panels (Panel-B1 and B2) are connected to the support wall wedge using an L-shape steel bracket and four screws. Although the screw diameter is the same as that of a 10d nail, it has a greater withdrawal capacity due to its geometry and material properties.

Therefore, linear spring along z' axis (Figure 5.17) represented this connection. The stiffness of this spring (3069 N/mm per screw) was set to the withdrawal stiffness of the nail obtained in the test by Islam et al. (2022a) . It is worthwhile to note that the test by Islam et al. (2022b) revealed that the withdrawal resistance of the screw governs rather than shear capacity in the case of the L bracket connection. However, the withdrawal test of these screws was not performed. Hence, a conservative approach is to assign withdrawal stiffness of 10d nails. Although this L bracket connection has small rotational stiffness, it was ignored by assigning the rotation stiffness of the spring defined along y' (Figure 5.17) close to zero (assigning absolute zero results numerical singularity in the stiffness matrix in Abaqus). The screw connection of the wedge piece of support was represented by defining a nonlinear spring along x' axis in Figure 5.17 for the gravity load case. The load-slip response of this spring was derived from laboratory testing of the wedge connection (as indicated in Figure 5.3b) by Islam et al. (2022b) (see the graph in Figure 5.19). In the case of lateral load, the stiffness along x' axis was set equal to the nail withdrawal in wind uplift since only the angle bracket connection provides resistance in this case.

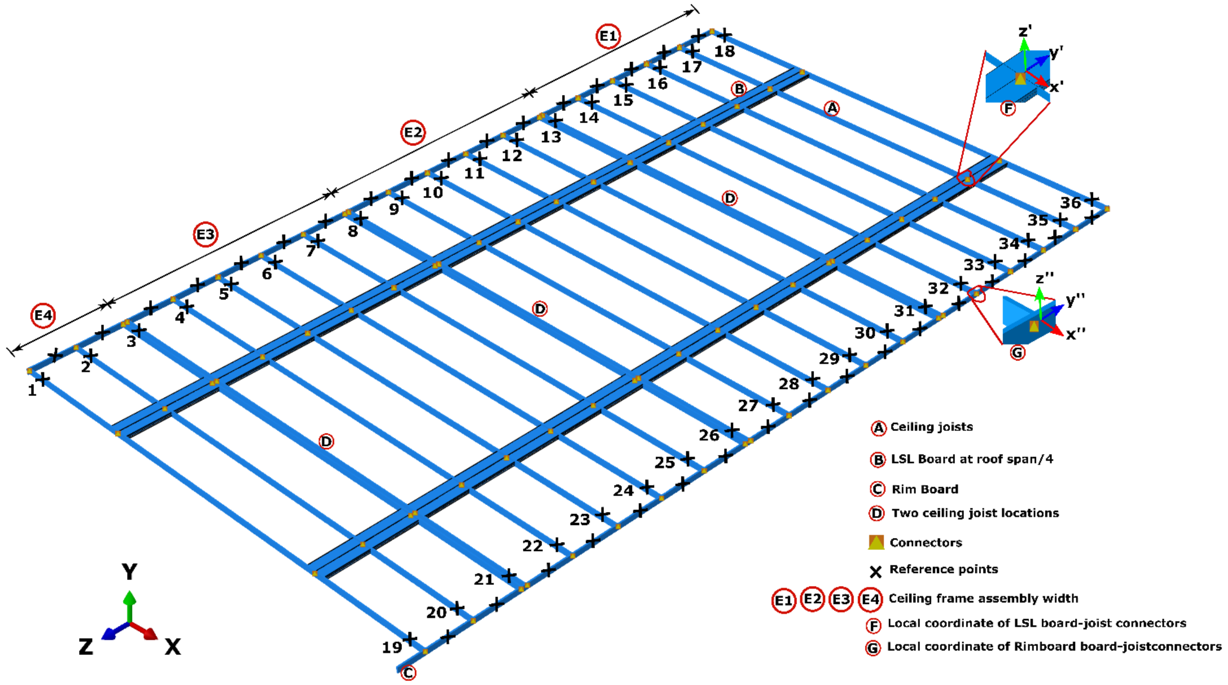

Figure 5.15. Ceiling frames in the model.

The eave line and panel-A-to-support wall screw connection were defined by two translational and one rotational spring according to the coordinate system, as indicated in Figures 5.17 and 5.18. The load-slip (Figure 5.20) response of the spring defined along y'' axis was obtained from laboratory testing (Islam et al. 2022b). The rotational stiffness along the x'' axis was obtained from finite element analysis of this screw connection (Figure 5.21) (Islam and Chui 2023). The spring stiffness along z'' axis was defined by the graph as illustrated in Figure 5.22.

The panel-to-panel connection was represented by two nonlinear springs and one spring with infinite rigidity, as illustrated in Figure 5.18 (see note d). The load-slip response for these springs along the local x''' and z''' axis of the connector was obtained from laboratory tests (Figures 5.23 and 5.24) (Islam et al. 2022b). The spring stiffness along the y''' axis was set to infinity to simulate the hard contact between the connected edges of the roof panel.

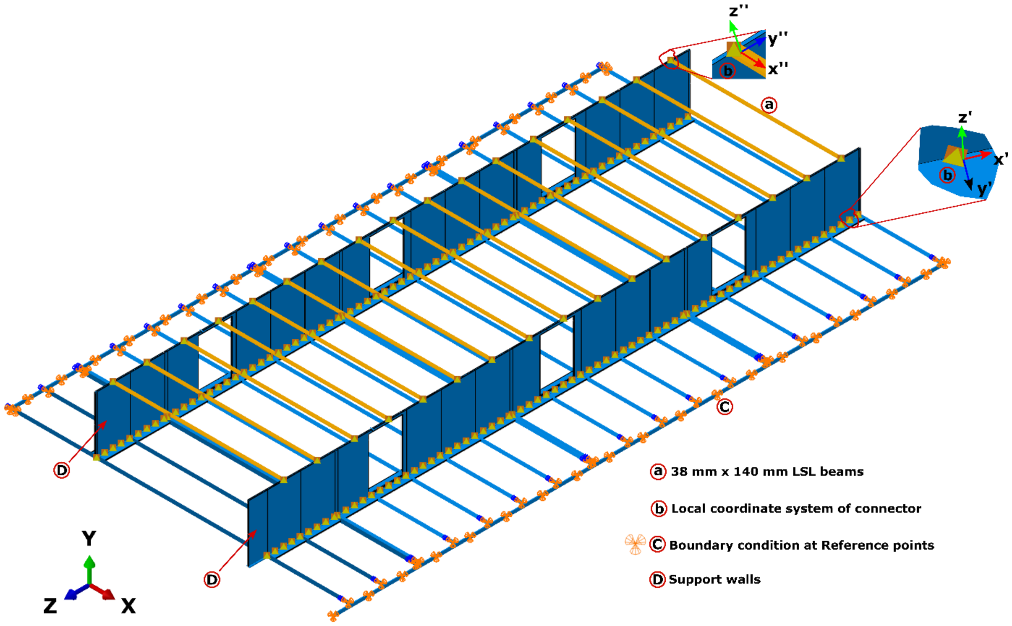

Figure 5.16. Support wall, LSL beam and Ceiling frame.

As explained in the previous section, the foldable self-locking apex connection acts as a rigid link between two roof panels (panel-A1 and A2) at service state; two types of connector mechanisms were used to define this connection. First, pin connectors were defined at the apex points, as illustrated in Figure 5.18 (see notes a and b), to allow free rotation about the local x' axis of the connector. Then rigid beam connectors were defined at the location of primary folding link bar element (see note 2 in Figure 5.3d) of the apex connection, as depicted in Figure 5.18. The gable end-to-roof panel connection was defined by the connectors according to the local coordinate, as indicated in Figure 5.18 (see note g). The spring stiffness was defined by the load-slip relationship illustrated in Figure 5.20 for y'''', Figure 5.21 for x'''' and Figure 5.22 for the local z''' axis of the connector. Finally, the gable end-to-support wall connection was defined assuming nine-nail connections. The three nonlinear springs with load-slip properties, as shown in Figures 5.13 and 5.14, defined this connector behaviour according to their local coordinate system. Table 5-5 summarizes the elastic properties of joists and beams assigned in the FEM. It is noteworthy that different types of trial sections, such as wood I-joists or SFP lumber, were assigned to optimize the final ceiling joist section.

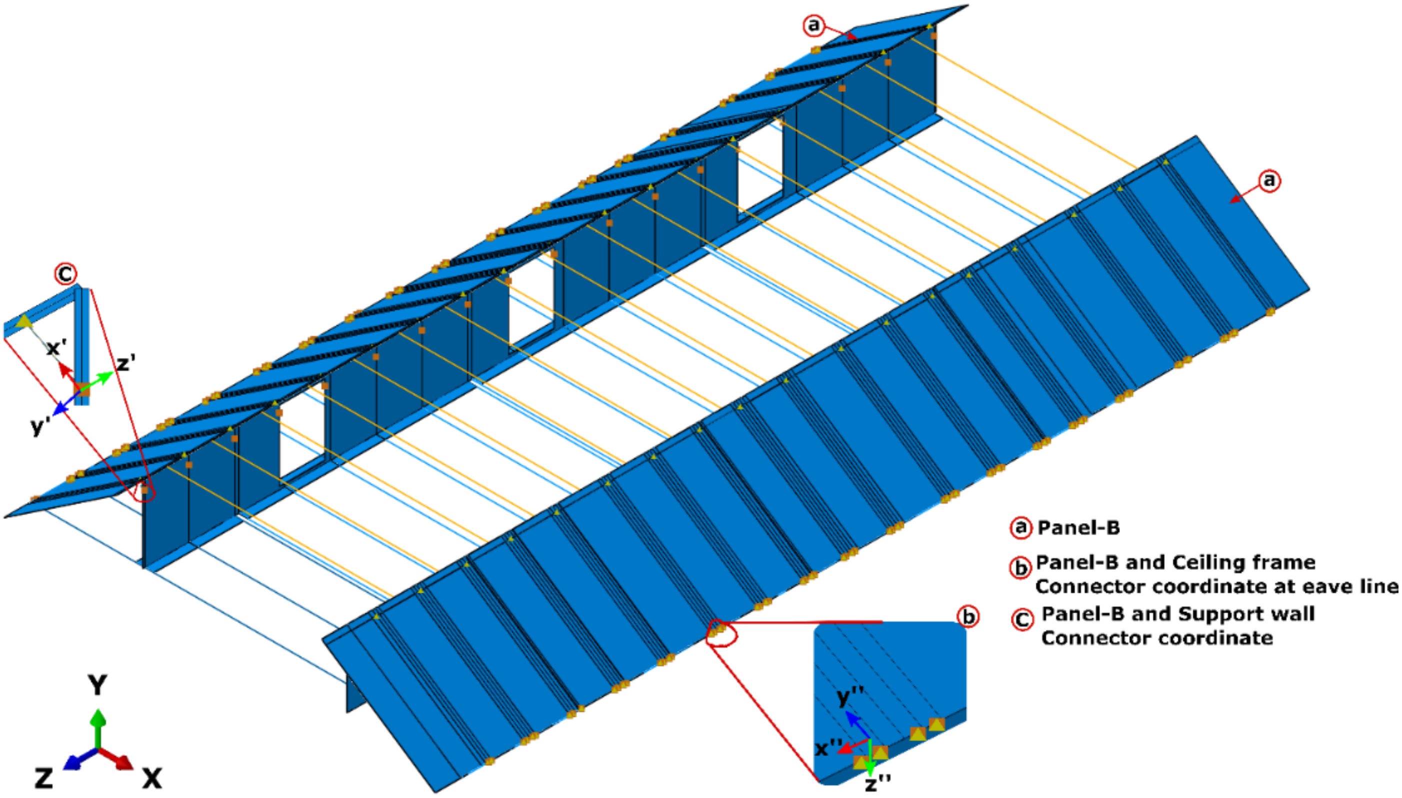

Figure 5.17. Partial model assembly with Roof panel-B, Gable ends, and Support wall.

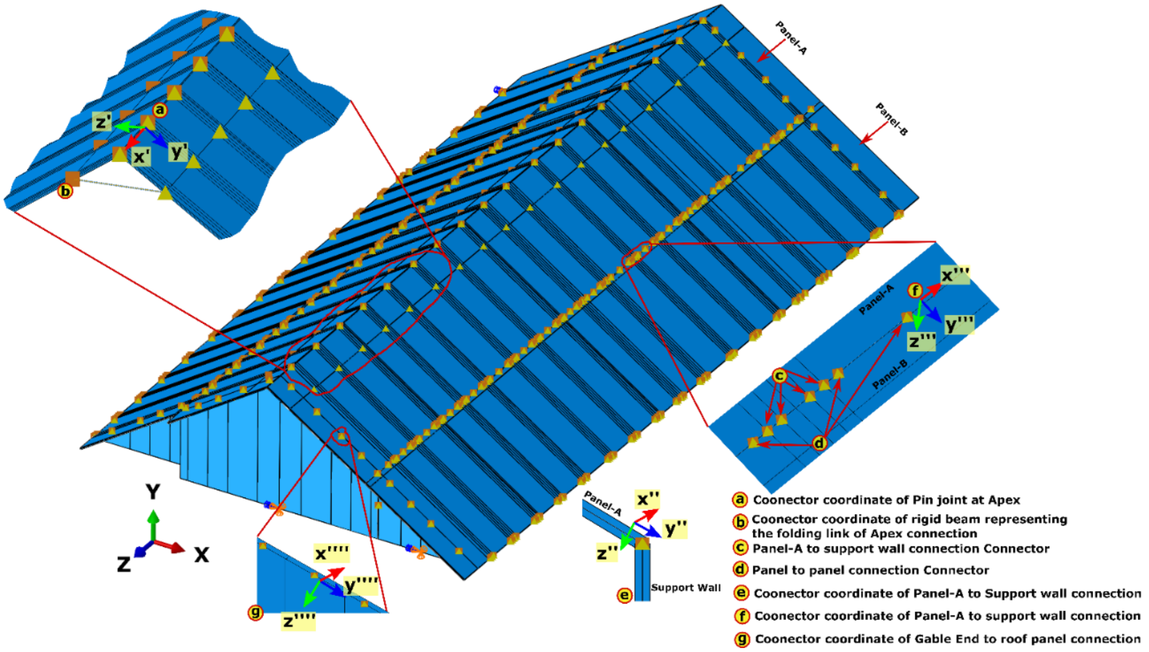

Figure 5.18. Complete roof assembly.

Table 5-5. Elastic Isotropic material properties used in the Abaqus model.

Item	Modulus of elasticity (MPa)	Poisson's ratio
S-P-F lumber	8831	0.4
Wood-I-joist	11328.8	0.3
LSL Beam	8965	0.3

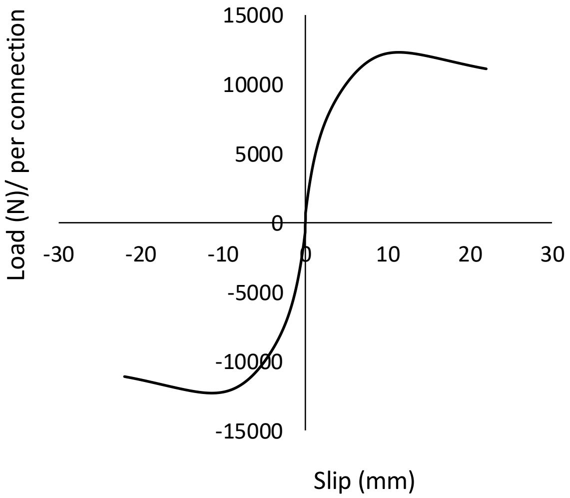

Figure 5.19. Support wall wedge screw connection stiffness along x' axis

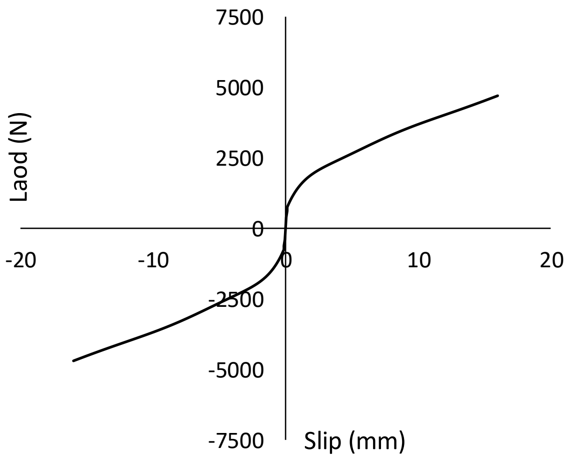

Figure 5.20. Load-slip response of screw connection at eave line and roof panel-support wall connection along y'' axis

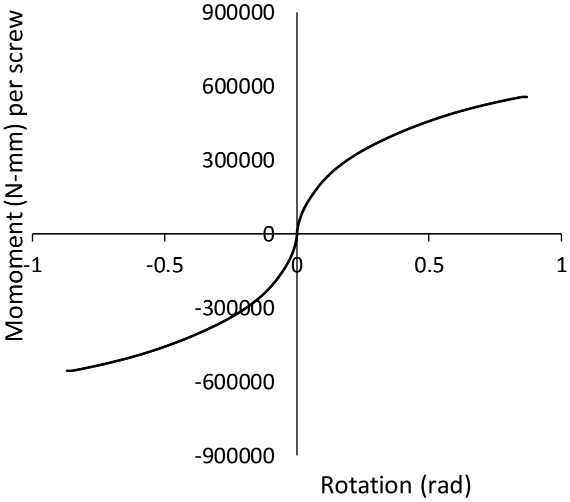

Figure 5.21. Rotational stiffness of screw connection at eave line and roof panel-support wall connection along x'' axis

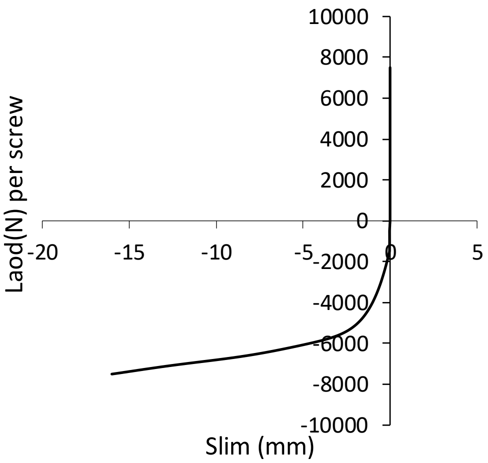

Figure 5.22. Load-slip response of screw in withdrawal or compression along z'' axis

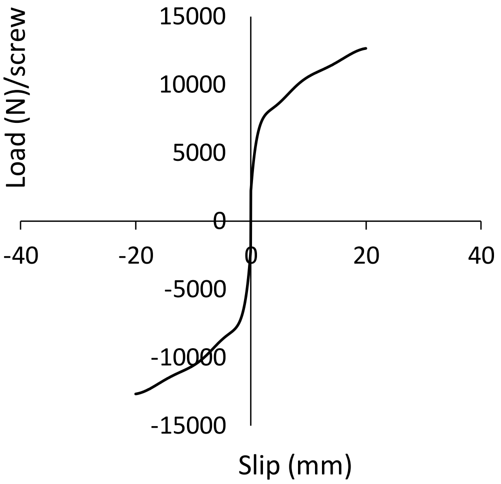

Figure 5.23. Panel-to-panel connection along x''' axis

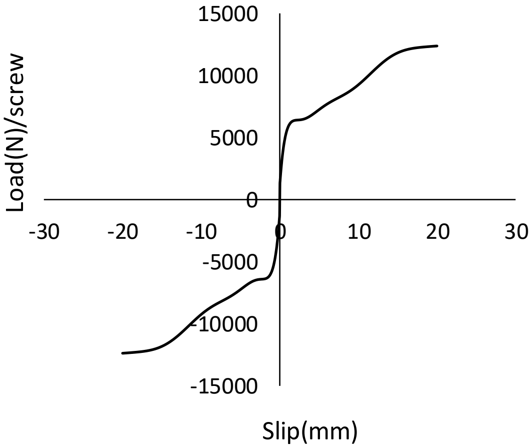

Figure 5.24. Panel-to-panel connection along z''' axis

5.5. Results and Discussion

One of the primary objectives of this study is to observe the gravity and wind load response of the panelized light frame roof. As mentioned earlier, the case study building was assumed to be located in Edmonton, Alberta, Canada. The specified snow load 1 in 50 years for this location is 1.035 kPa. Additionally, 0.5 kPa dead load was assumed on the roof panels considering waterproofing and permanent roof features such as air vents outlets. Furthermore, 0.5 kPa deadload was assigned for the ceiling joist, assuming gypsum board drywall as the ceiling material.

5.5.1 Gravity Load Response

The governing load case for gravity load was the combination of dead and snow load (1.25 D+ 1.5 S). As can be seen from Figure 5.25, the deflection shape of the roof assembly indicates two-way load distribution when it is subjected to gravity load. Moreover, the comparison of vertical reaction values of load-bearing shear wall sides and gable end sides revealed that shear wall side reactions are twice the magnitude of those in gable ends (Figure 5.26*)*. Hence it can be concluded that 33% of the total load is being transferred to the gable ends through the deep beam action of the support wall element in the panelized roof assembly. Figures 5.27 and 5.28 depict the vertical reaction profile of the reference points of the ceiling joist. Due to penalization, a higher magnitude of the reactions was observed in the locations with two side-by-side ceiling joists (as indicated in Figure 5.15). Since load is attracted to stiffer elements in an assembly, the location shown in Figure 5.15 with relatively high stiffness than their adjacent ceiling joists exhibits low deflection. Therefore, panelized construction method significantly impacts the load path of the light frame panelized roof. Maximum deflection with a magnitude of 9.56 mm in the case of ceiling joists (Figure 5.29) was observed for the ceiling frame E2 as indicated in Figure 5.15, again indicating the load flow by the two-way distribution. According to Part 9 of the NBCC deflection limit for the ceiling joist is Span/360 (16.2 mm), and the observed deflection for governing serviceability load case was 9.6 mm (NBCC 2020b). Thus, using SPF lumber (38 mm x 140 mm) to fabricate ceiling joists is adequate to satisfy the serviceability limit. This finding differs from the deflection results obtained in Islam et al. (2021), where I-Joists of 241 mm depth ceiling joist was required to comply with the serviceability limit state. Hence, the 3D FEM model indicates the system effect and different load path for gravity load case compared to the 2D simplified analysis in Islam et al. (2021). The panel-to-panel hard contact transfers a higher percentage of load in plane than the load transfer through the panel-A-to-support wall connection. The ceiling frame joists undergo bending and, at the same time, act as tie beams for the load-bearing shear wall of the building at the eave line. Therefore, ceiling frame joists resist the outward horizontal thrust of the load-bearing shear wall in the system. Maximum horizontal thrust was observed for the reference points (51, 52 and 57 in Figure 5.30 and 70, 74 and 64 in Figure 5.31) closer to the location with two ceiling joists (see note b in Figure 5.15), confirming more load flow in the stiffer zone of the structure. Also, the maximum axial force was observed for the ceiling joist in frame E2 (Figure 5.32). A maximum bending moment of 407 kN-mm was observed in the ceiling joist. Design checks were performed for the ceiling joist, LSL beam and support wall (see supplementary section A-4.3 in Appendix-4). All the defined sections, including the ceiling joist (38 mm×140 mm), LSL beam (76 mm ×140 mm) and support wall stud (38 mm×140 mm) and bottom plate (38 mm×140 mm), were adequate to sustain the design load.

In the case of the roof panel-B-to-ceiling frame at the eave line and panel-A-to-support wall connection, four screws were defined close to the rafter location of the roof panels (Figures 5.17 and 5.18). The maximum shear load (1.7 kN) on the screw connection at the eave line was observed for load case b (Figure 5.33). According to the CSA 086 analytical model factored (ϕ=0.8) shear capacity of this crew connection is 1.83 kN (Islam et al. 2022b). Therefore, four screws per rafter, as defined in the model, have sufficient capacity to withstand the design load at the eave line. Figure 5.34 illustrates the maximum connector force output for the panel-A-to-support wall connection. The factored (ϕ=0.8) shear capacity for this connection is also 1.83 kN (Islam et al. 2022b), and the maximum shear in case of load case b was 1.2 kN. Hence, four screws per rafter, as defined in the model, have sufficient capacity to withstand the design load for this connection as well.

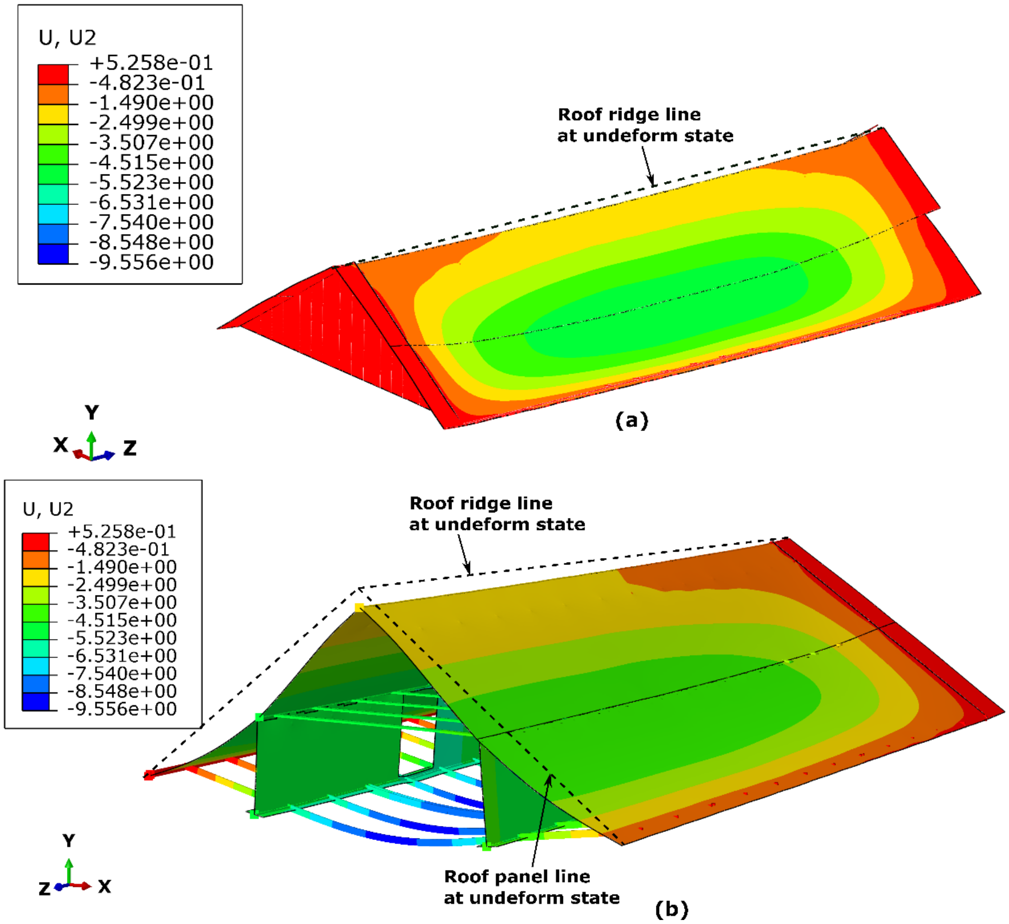

Figure 5.25. Deflection of (a) roof assembly at ultimate limit state (b) section cut of the assembly (deflection scale: 100).

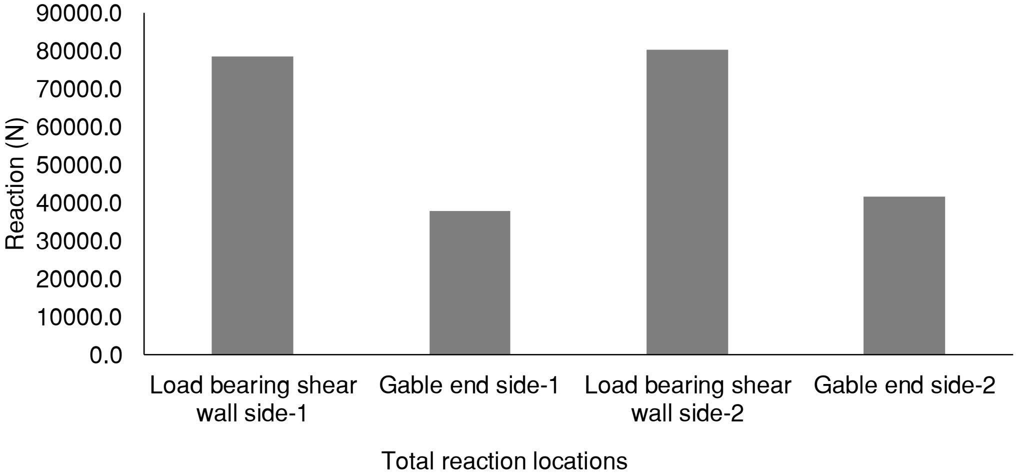

Figure 5.26. Reaction distribution of load-bearing shear wall side and gable end side.

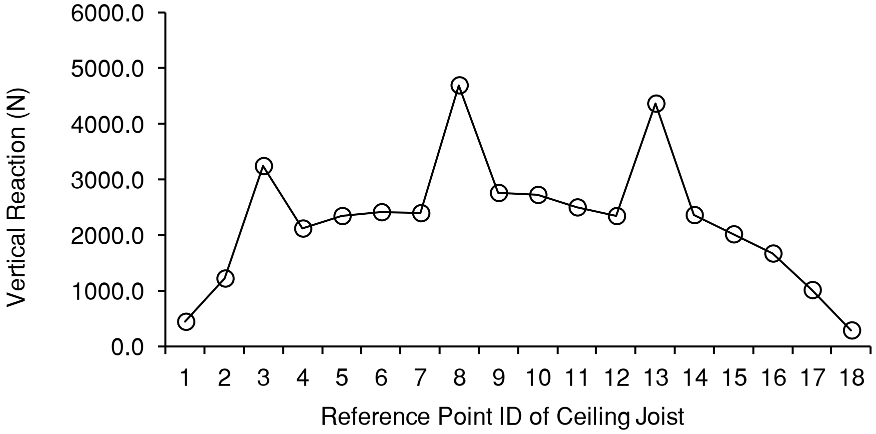

Figure 5.27. Vertical Reaction profile of joist end side 1.

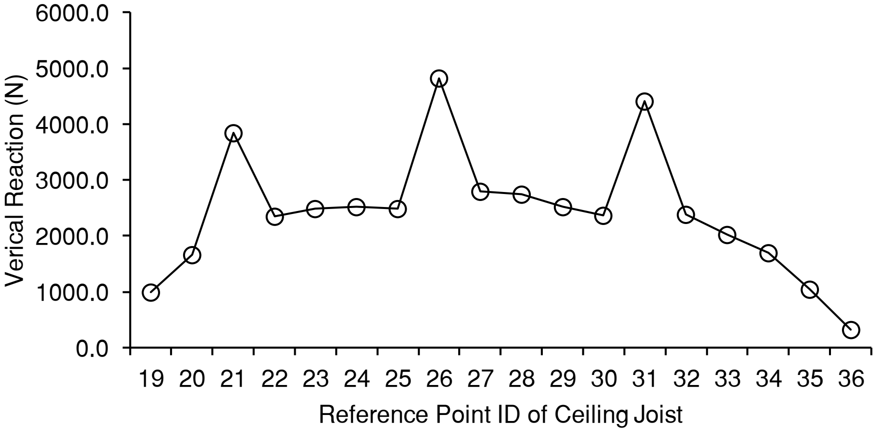

Figure 5.28. Vertical profile of joist end side 2.

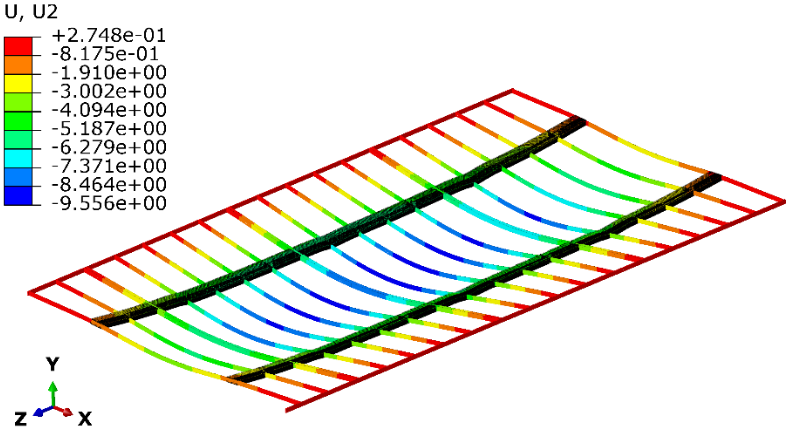

Figure 5.29. Ceiling frame deflection for serviceability limit state (1.0 D+1.0S+0.4 W) (deflection scale: 100).

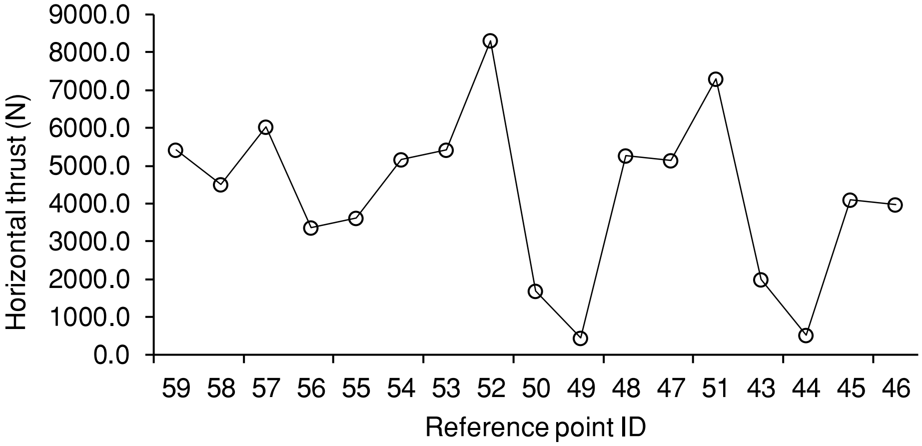

Figure 5.30. Horizontal thrust distribution in ceiling frame side 1.

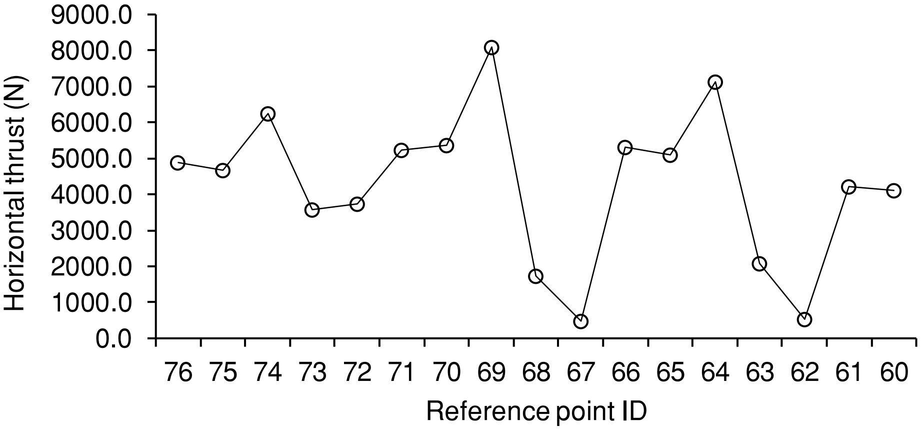

Figure 5.31. Horizontal thrust distribution in ceiling frame side 2.

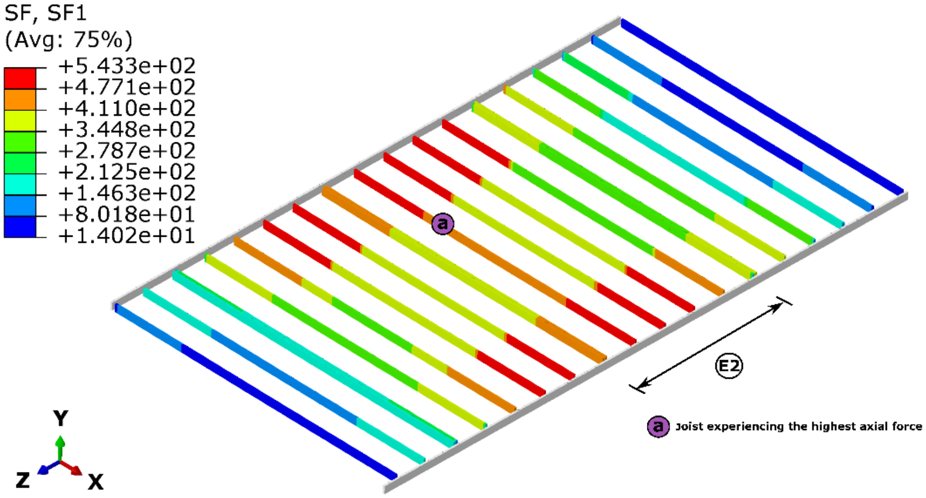

Figure 5.32. Axial force in Ceiling frame joists.

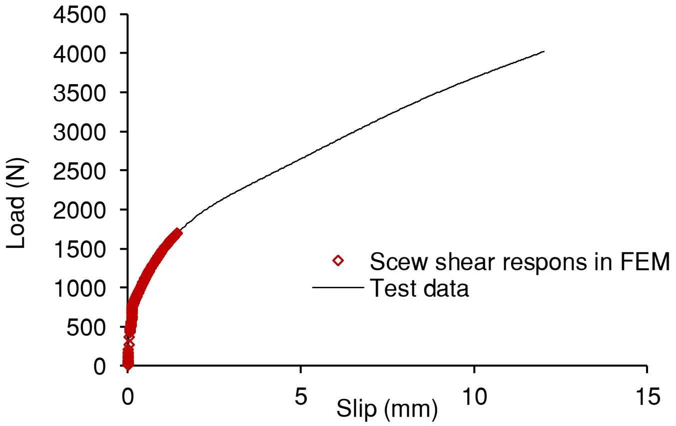

Figure 5.33. Average maximum screw connection response along y" axis at the eave line (for load case 1.25D+1.5S+0.4W).

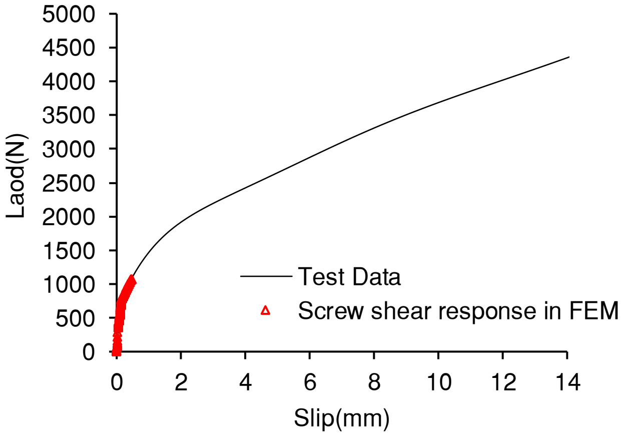

Figure 5.34. Average maximum screw connection response along y" axis at Support wall-to-panel-A connection (for load case 1.25D+1.5S+0.4W).

5.5.2. Wind Load Response:

Figure 5.35 represents the deformed shape of the roof in the case of wind load (0.9D+1.4W) perpendicular to the ridge direction. As the windward side of the roof has positive pressure build-up and the leeward side in suction, the ceiling joist deflection indicates the existence of a point of contraflexure in the bending moment diagram of the ceiling joists. The joist of ceiling frame E2, located near the mid-span of the roof's longer direction (along the global Z axis), exhibits the highest upward and downward deflection, as depicted in Figure 5.35. This observation again highlights the two-way load distribution in the panelized gable roof assembly.

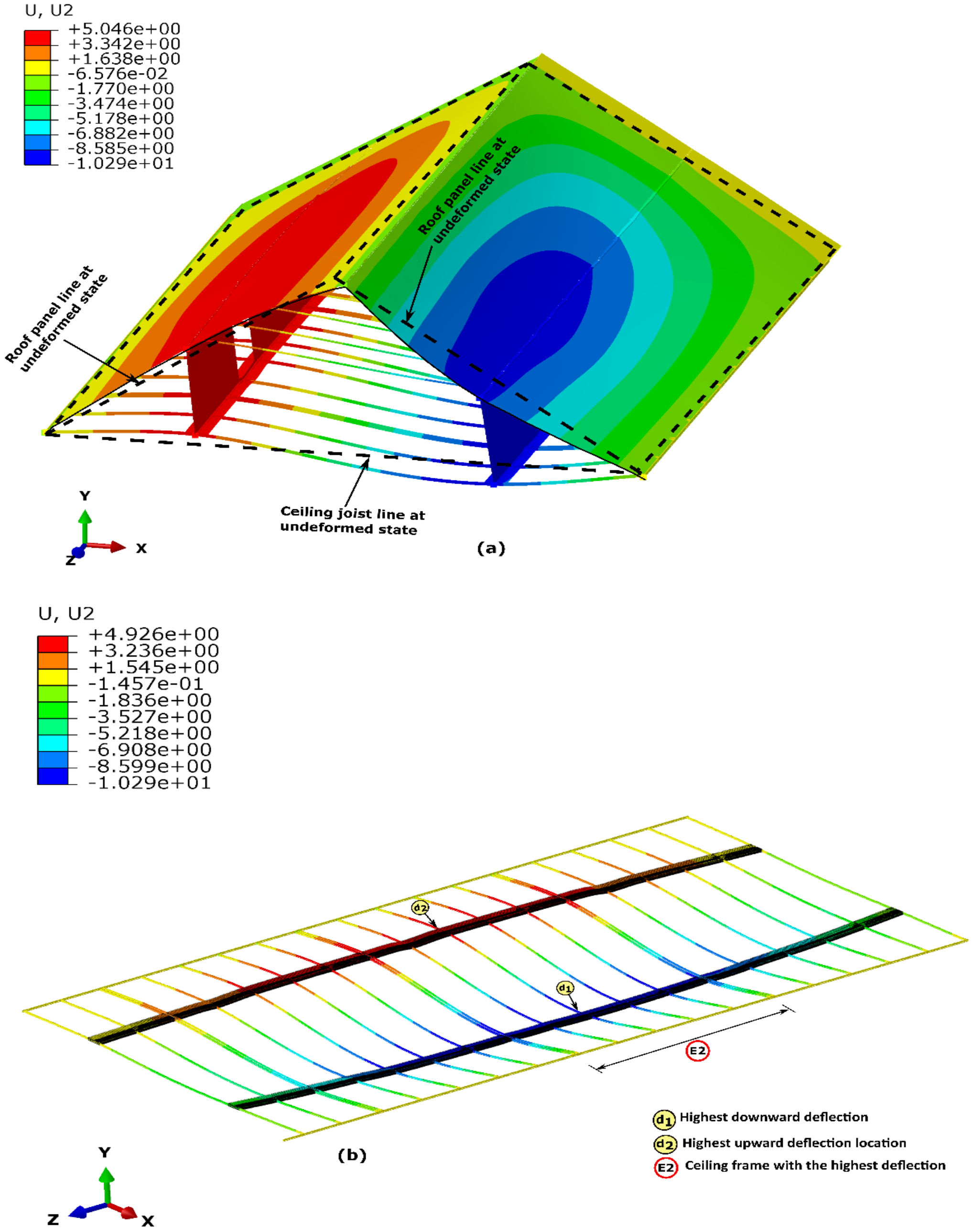

Figure 5.35. Deformation under wind load perpendicular to the ridge (a) 3D sectional view (b) ceiling joists deflection (0.9 D+1.4W load case) (deflection scale: 100).

The LSL beams effectively transfer the lateral load component from the windward side support wall to the suction side support wall. This load is then transmitted to the ceiling frame rim board via in-plane transfer through panel-B on the suction side. In this load case, the lateral drift of the roof resulted in higher withdrawal force (799.6 N) on the base connectors of the support wall located on the windward side (specifically, the connection between the support wall and the LSL board as shown in Figure 5.3e). As a result, to withstand this force, five nails are necessary. Table 5-6 summarizes the governing connection forces and the corresponding requirements for connection design.

Results for load case d (0.9D+1.4W wind parallel to ridge direction), considering the dead load of the structure and wind loading only, reflect the behaviour of the roof when additional gravity loads (snow) are not present to assist in the resistance of uplift. The analysis of the vertical uplift response between the eave line and gable wall side revealed that the gable ends were transferring 32% of the load. The gable end walls exhibited a load intensity (i.e., spike) directly beneath (reference point 78 in Figure 5.36) the peak of the roof, which resulted from load accumulating in the roof structure, delivered via the ridgeline to the bottom of the wall for wind load (0.9D+1.4W) parallel to the ridge. As can be observed from Figure 5.36, the reference point (77) in the end zone of the roof has a higher uplift reaction than the other reference point (79). The eave line withdrawal response in the screw connection is shown in Figure 5.37, indicating the effectiveness of these self-tapping screws with high withdrawal capacity. Hence, the design of screw connections at the eave and support wall lines is governed by the shear capacity requirement for the gravity load case. Figures 5.38 to 5.41 illustrate the connection layout and sectional details based on this complete analysis discussed herein. For the apex link element, force varied between 3866 N to 4866 N except for the connector close to the gable end, where the roof panel is extended beyond the wall (432 mm tributary length). The force in this connector was 8195 N. Hence two apex connections are recommended near the gable end zone. Roof panel details to accommodate the apex connection are illustrated in Figure 5.40c (see note c in the figure).

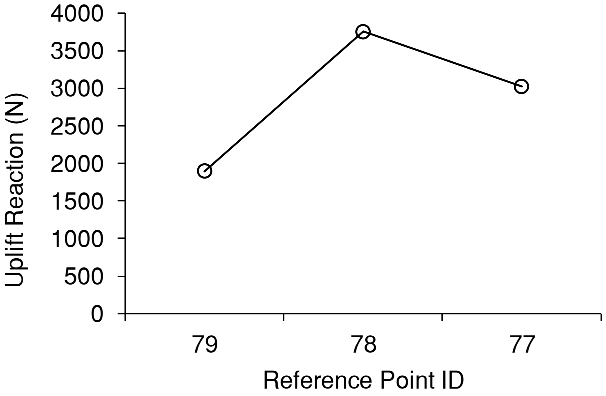

Figure 5.36. Uplift reaction profile of gable end wall (09D+1.4W load case).

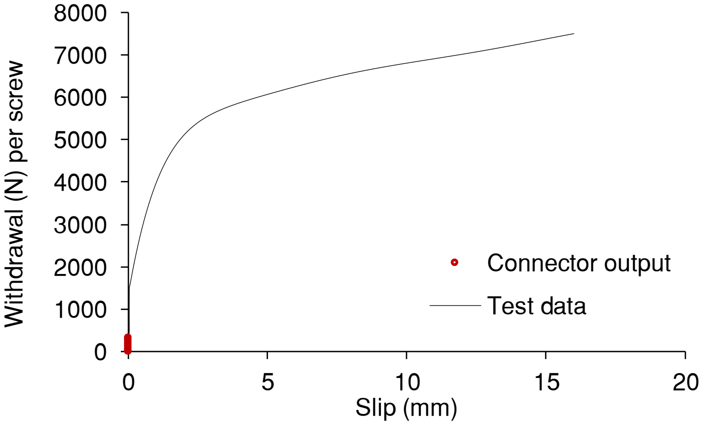

Figure 5.37. Screw withdrawal response at the eave line (0.9D+1.4W load case).

Table 5-6. Connection Design Summary

Connection Type	**Max Force (N)**	**Connection Design Capacity(N)**	**Governing Load Case**	**Fastener Note**
Support wall wedge screw shear per connection	993	5880	1.25D+1.5S+0.4W	Fabricate this wedge connection with one 150 mm and 200 mm long screw with a 6mm nominal diameter, as shown in Figure 5.3c.
Support wall wedge Steel Angle Screw withdrawal per connection	876	3960	0.9D+1.4 W	Use four commercially available SD screws to connect the L bracket
Gable End-to-Roof panel screw shear in the plane of roof panel (y') per screw	1589	2286	1.25D+1.5S+0.4W	Four screws per roof panel (see details in Figure 5.3c). Use a flat head screw/ washer for tapper head screws.

Connection Type	Max Force (N)	Connection Design Capacity(N)	Governing Load Case	Fastener Note
Gable End-to-Roof Panel screw shear in the plane of roof panel (x') per screw	608	2286	1.25D+1.5S+0.4W	Four screws per roof panel. See details in Figure 5.3c. Use a flat head screw/ washer for the tapper head screws.
Gable End-to-Roof panel screw withdrawal (z') per screw	1075	2628	0.9D+1.4 W	Four screws per roof panel. See details in Figure 5.3c. Use a flat head screw/ washer for the tapper head screws.
Panel-Panel connection per screw	1574	2288	1.25D+1.5S+0.4W	Use two screws per rafter with an 8 mm diameter (see details in Figure 38 d)
Eave line screw shear per screw	1700	1832	1.25D+1.5S+0.4W	Use 4- 8 mm nominal diameter of self-tapping screw (see details in Figure 5.38b)
Eave line screw withdrawal per screw	331	1090	0.9D+1.4 W	Use 4- 8 mm nominal diameter of self-tapping screw per rafter Figure 38b)
Roof panel-A-to-support Wall screw shear per screw	1120	1832	1.25D+1.5S+0.4W	Use 4- 6 mm nominal diameter of self-tapping screw per rafter (see details in (Figure 5.38c)
Roof Panel-A-to-support wall screw withdrawal per screw	366	1090	0.9D+1.4 W (Wind parallel to ridge)	Use 4- 6 mm nominal diameter of self-tapping screw per rafter
Support wall base-to-LSL board nail connection withdrawal	800	1083	0.9D+1.4 W (Wind perpendicular to ridge)	Use five nails as indicated in Figure 5.40a
Support wall base-to-LSL board nail connection Shear	86	1361	0.9D+1.4 W (Wind perpendicular to ridge)	Nails defined as the model is okay
LSL board-to-Ceiling frame connection withdrawal	895	1300	0.9D+1.4 W (Wind perpendicular to ridge)	Six Nails defined in the model are okay (see details in Figure 5.39d)
LSL board-to-Ceiling frame connection shear	146	1361	0.9D+1.4 W (Wind perpendicular to ridge)	Nails defined as the model is okay
LSL Beam-to-support wall shear	3947	5445	1.25D+1.5S+0.4W	Use 5 Nails as defined in the model
Gable End-to-support wall connection Shear	5040	12251	1.25D+1.5S+0.4W	Use 9 Nails as defined in the model
Apex connection link	4866	5898.00	1.25D+1.5S+0.4W	Use seven commercially available SD screws to

Connection Type	**Max Force (N)**	**Connection Design Capacity(N)**	**Governing Load Case**	**Fastener Note**
				connect the folding connection to the rafter.
Ceiling frame-to-load bearing shear wall connection per nail	405	846	1.25D+1.5S+0.4W	Use nails @ 85 mm c/c as shown in Figure 41(a)
Gabel Wall-to-load bearing shear wall connection per nail	52	217	0.9D+1.4 W (Wind parallel to ridge)	Use nails @ 85 mm c/c as shown in Figure 41(b)

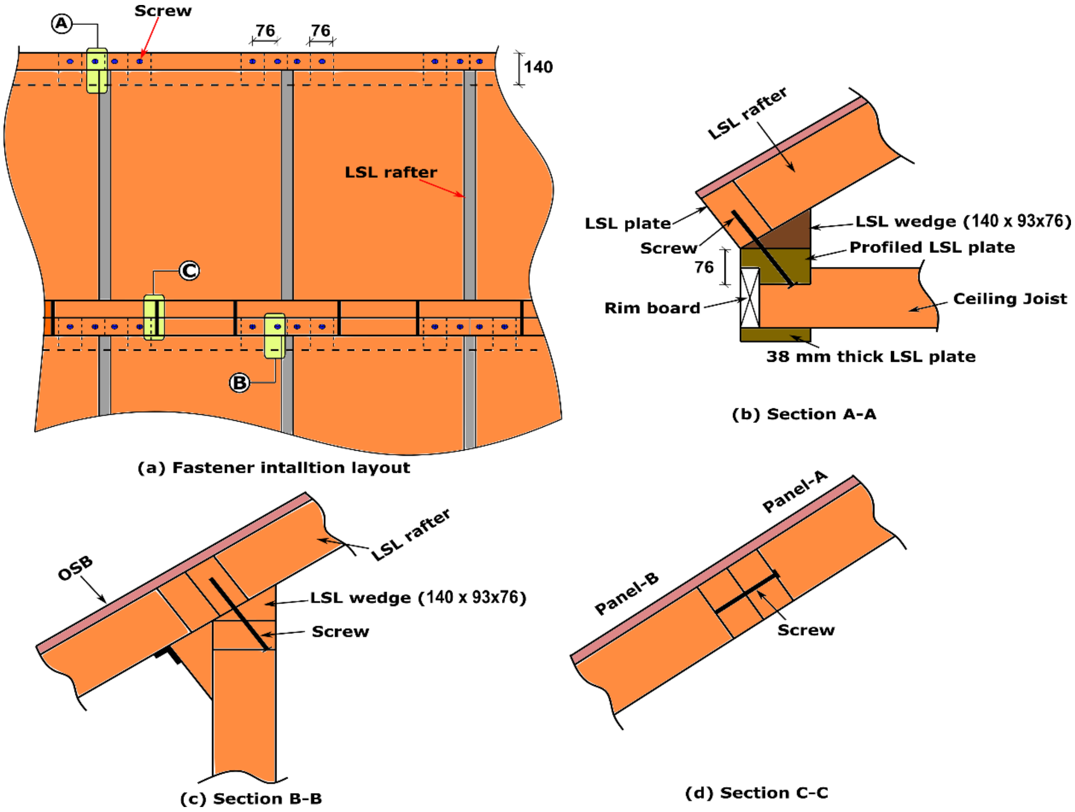

(a) Fastener intalltion layout

(b) Section A-A

(c) Section B-B

(d) Section C-C

Figure 5.38. Fastener details (all dimensions are in mm).

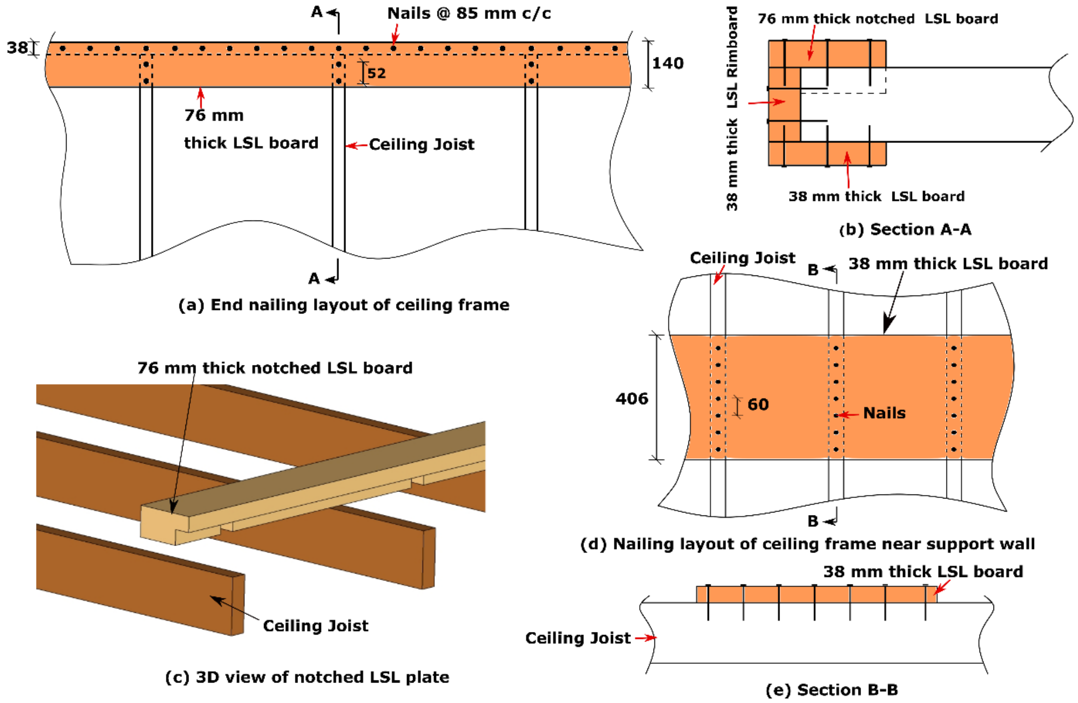

Figure 5.39. Ceiling frame nailing details (all dimensions are in mm).

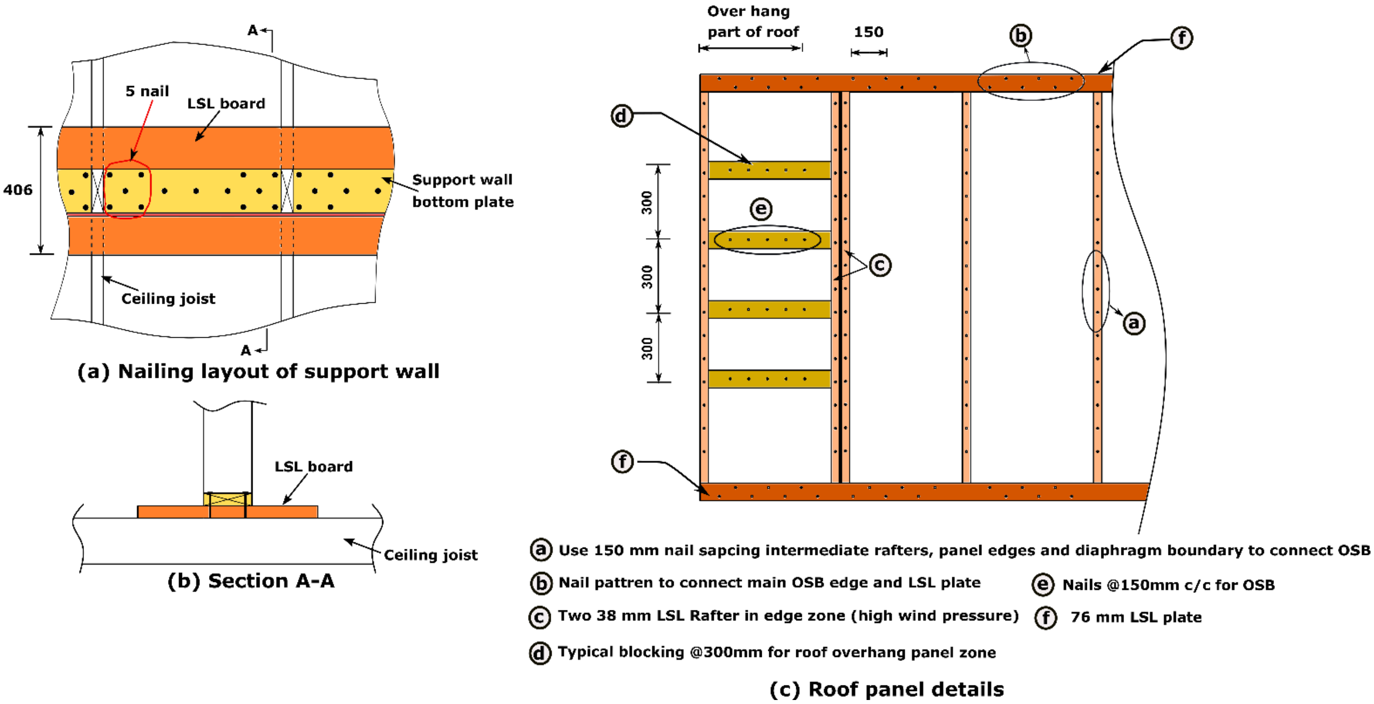

Figure 5.40. (a) (b) Support wall nailing details, and (c) Roof Panel details (all dimensions are in mm).

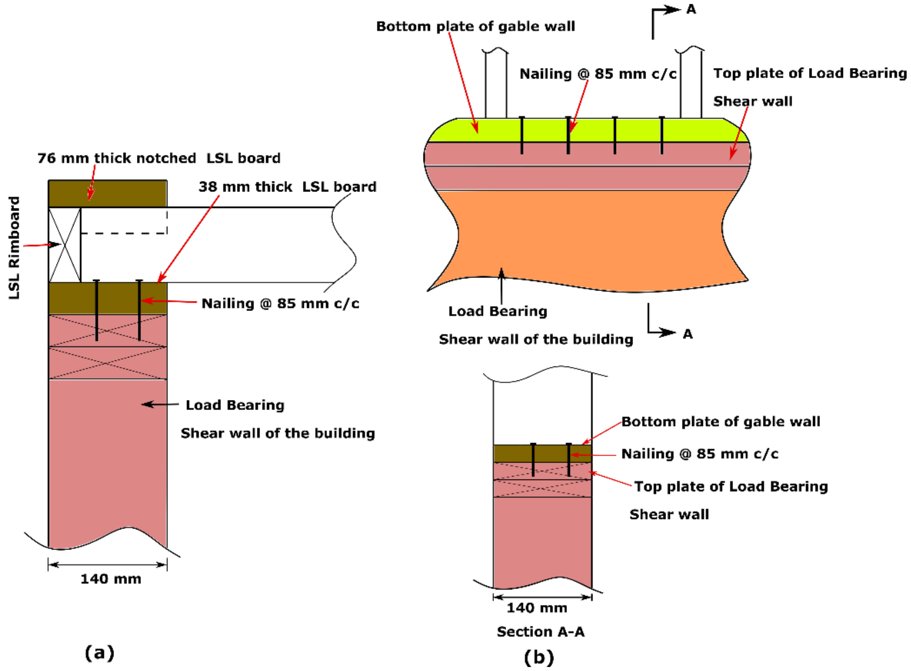

Figure 5.41. (a) Ceiling Frame-to-Load bearing Shear wall connection (b) Gable Wall-to-Load Bearing Shear wall connection.

5.6. Conclusions

A 3D FEM model using Abaqus was developed for a light frame wood panelized gable roof. The connection properties between components in the model were derived from individual connection tests (Islam et al. 2022b). The numerical analysis in governing load cases provided the connection design requirements and member sections such as ceiling joist for the case study roof in Edmonton, Alberta, Canada. The following conclusions were reached from the FEM analysis:

- The vertical reaction force for gravity and wind uplift load case indicates two-way load distribution in the panelized roof. In the case of gravity and lateral load, the gable ends transmit 33% and 32% of the load, respectively.
- In order to transfer horizontal thrust, the eave line connection design requires either more screws or four screws with a larger diameter in contrast to the support wall line screw connection. The possible reason is the higher percentage of in-plane load flow

in the system. Hence, the connection design of the eave line and support wall-to-panel-A is governed by the shear load demand in the gravity load case.

- The self-tapping screws are very effective in resisting wind uplifts due to their higher withdrawal capacity than traditional fasteners such as toe nailing.
- The ceiling joists are engaged as tie beams for the eave line load-bearing walls for all load cases. It also undergoes bending due to the load transfer from the support wall.
- The load path analysis indicates the influence of panelized construction in the overall system. Consequently, the joists where two ceiling frame meets exhibited lower deflection in contrast to their adjacent joists.
- The deep beam action of the support wall component influence in the load path of the panelized roof. The combined system behaviour of the support wall, roof panel-B and ceiling frame components enforces a higher percentage of in-plane load flow.

Chapter 6 : Fabrication, onsite installation, and replicability of the system

6.1 Introduction

This chapter summarizes incorporating the developed panelized roof production in an existing offsite fabrication facility, onsite installation factors, and replicability of this panelized roof system as a potential solution for the Northern Canada housing crisis.

6.2 Incorporation of Roof Production Elements into Existing Fabrication Line

The workflow in offsite manufacturing of light-frame wood buildings as a panelized form entails multiple concurrent and iterative tasks, structured production sequences, and diverse degrees of automation, which differs significantly from the construction sequence, use of equipment and machinery, and activities involved in traditional stick-built construction workflows (Altaf et al. 2018a; Arif and Egbu 2010; Ayinla et al. 2022, 2020; Quale et al. 2012; Youyi et al. 2020). Application of automation, advanced sensor and radio frequency identification (RFID) in real-time to achieve desired construction elements is a core aspect of productivity gain in panelized off-site manufacturing (Altaf et al. 2018a; Ayinla et al. 2022). For instance, in the wall production line of an Alberta-based home manufacturer, wall panels pass through various workstations, consuming different amounts of time at each station based on the design parameters of the given panel, such as framing height and sheathing orientation. In summary, this construction process is a very complex industrialized manufacturing setting. Therefore, understanding the production process requires an effective tool called process mapping, which is frequently used in business process modelling (Anjard 1998; Ayinla et al. 2022; Wang et al. 2020b). Process mapping is a technique to visualize and document the steps, activities, and decisions of an industrialized production procedure (Biazzo 2002; Hussain et al. 2017; Sott et al. 2020). The construction industry uses process mapping to identify inefficiencies and streamline processes in various construction areas, including design, procurement, construction, and project management (Altaf 2016; Anjard 1998; Ayinla et al. 2022, 2020; Biazzo 2002; Hussain et al. 2017; Quale et al. 2012; Shafa 2012; Sott et al. 2020; Wang et al. 2020b; Youyi et al. 2020). The roof production scenario is based on the Alberta-based offsite manufacturing facility. As mentioned in previous chapters, the panelized roof components are produced using the existing wall and floor production line; the current operational activities of the different production lines were analyzed to obtain the current process map. Then the additional activities to fabricate the roof component were identified from the structural design explained in previous chapters. Since the roof panel elements, such as rafter and LSL plates, are arranged similarly for wall framing, fabricating the panels will follow most of the activities performed in the current state of the wall line. However, new activities must be incorporated into the existing production line work process. As can be observed from Figure 6.1, the future state of the wall line requires additional activity called "Transfer the roof panel to roof production jig" (see the end of Figure 6.1b). The produced roof panel is transferred to the roof production section in the activity mentioned above. The wall line and the roof production section are in two adjacent buildings (see Figure 6.2). Each production section works independently and does not share any synchronized activity to produce any component. However, in the future state, the roof section will depend on the wall line to produce the panels first. Then, it will connect two panels to the apex connection in the existing roof jig platform. Therefore, in the future state, there will be a lag time for the roof panel production in receiving the finished panel due to the transfer process from one building to another.

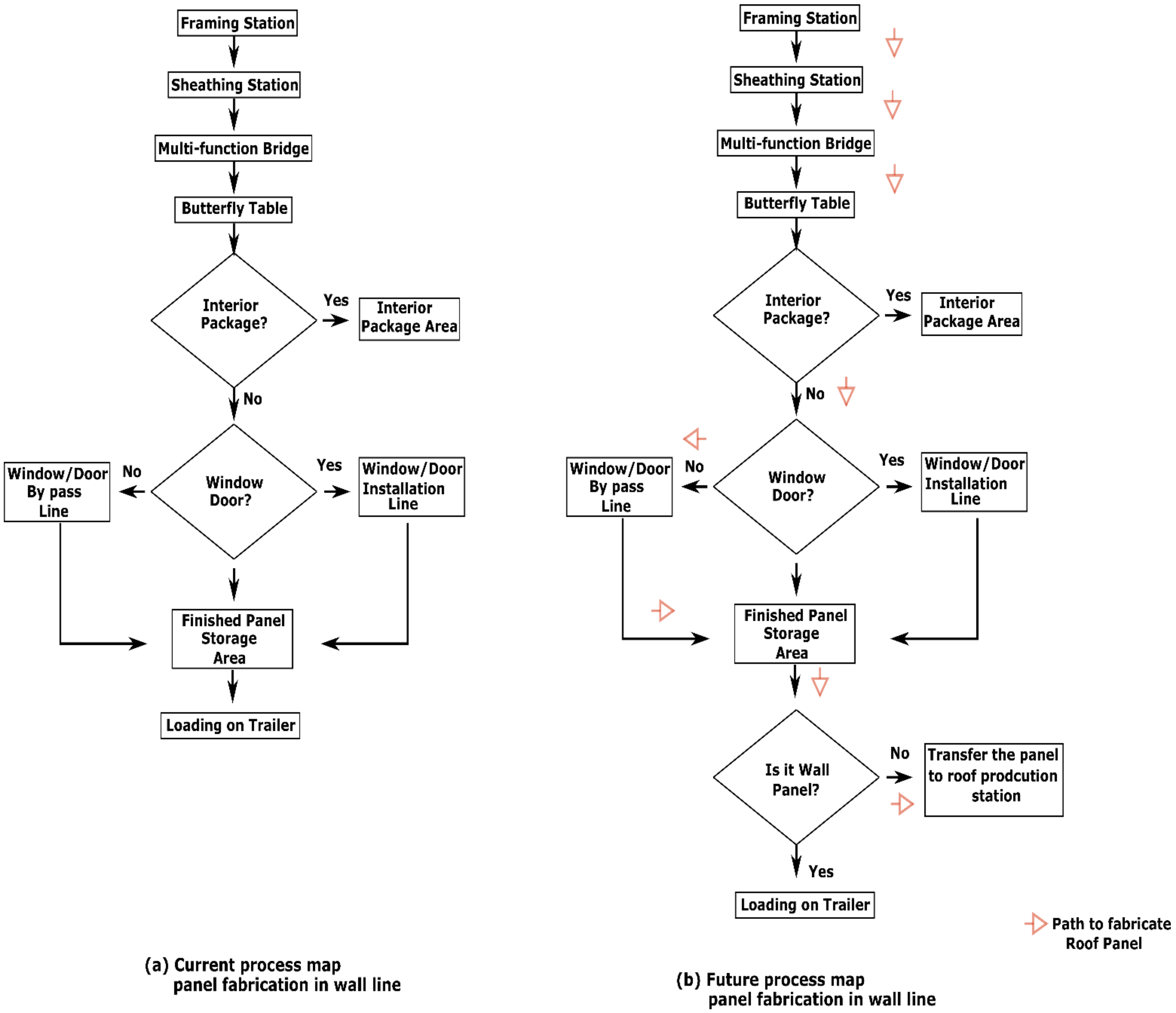

(a) Current process map panel fabrication in wall line

(b) Future process map panel fabrication in wall line

Figure 6.1. Process map of the current and future state in the wall line.

Figure 6.3 illustrates the current and future state of the floor line. Currently, the floor production line only uses wood I-joists; hence the material storage section stores only I-joists. However, in the future state, it will store lumber joists for ceiling frame production. Also, notched LSL plates will be stored. The profiling activity of this LSL plate will be accommodated in the CNC machine located in building-1 (Figure 6.2). Ceiling frame fabrication can be partially done using the existing pin table of the floor line. The remaining tasks to produce a complete ceiling frame will be performed in the current roof jig platform. As can be observed from Figure 6.4a, the ceiling frame produced in the previous step requires a flipping task to attach the bottom LSL plate component. Hence, the flipping rotary system, as indicated in Figure 6.5, must be installed on the existing overhead crane of the roof section.

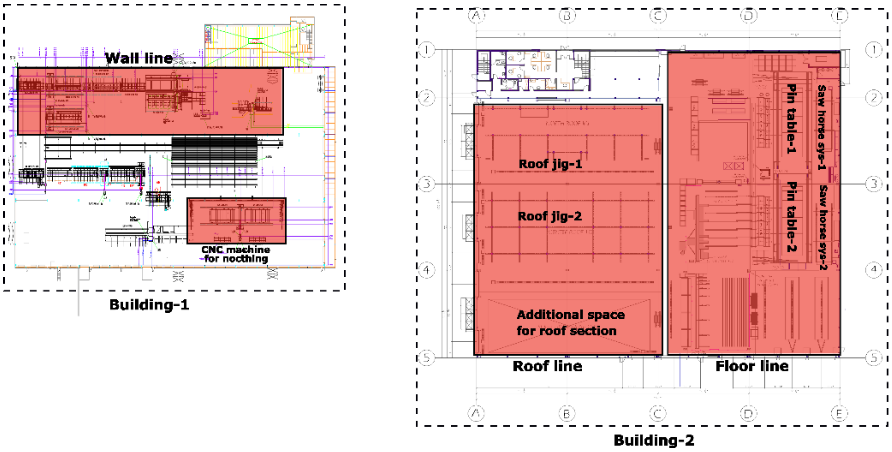

Figure 6.2. Buildings of the existing offsite facility.

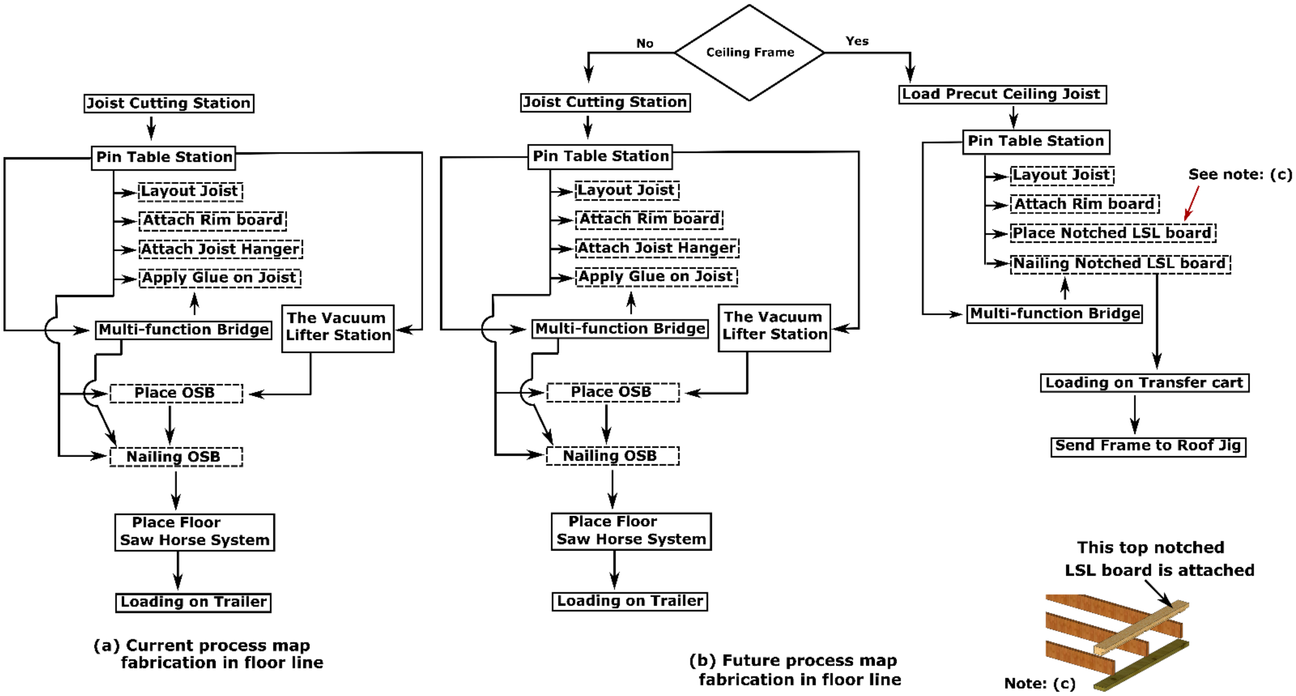

(a) Current process map fabrication in floor line

(b) Future process map fabrication in floor line

Figure 6.3. The current and future state of floor line.

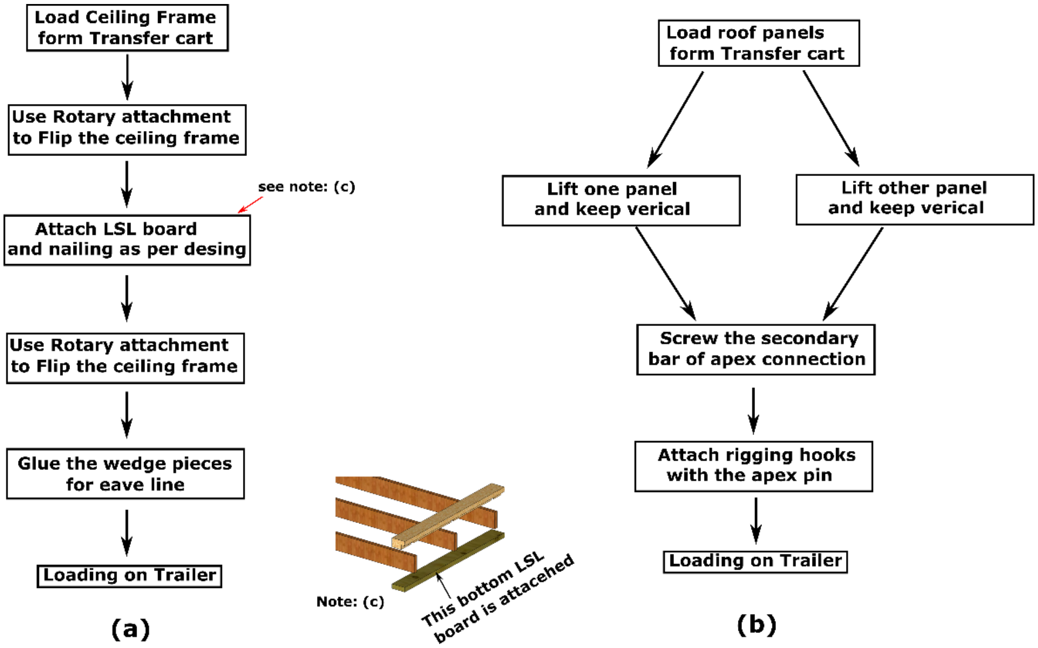

Figure 6.4. Future process map in the roof line.

Figure 6.6 illustrates the existing roof production jig facilitated with overhead cranes. This station can be used to perform the new task of installing the apex connection (for the process map, see Figure 6.4 b). In this process, panel lifting must follow the sequence and pick points on two opposite sides, as shown in Figure 6.7 and 6.8. Lifting the panel following the lift points as depicted facilitates the vertical position of two roof panels, as described in Figure 6.9, such that a worker can install the apex connection easily (Figure 6.10). After installing the apex connection, the two-roof panel forms a module (Figure 6.11) due to the folding action of the apex connection. At this stage, the rigging assembly, including the beam and slings with S-hook, are mounted (see Figure 6.12 for details of the S-hook). The design requirement of the S-hook is explained in the proceeding section. Installing a rigging system at the offsite facility reduces the onsite workload for crane maneuvering.

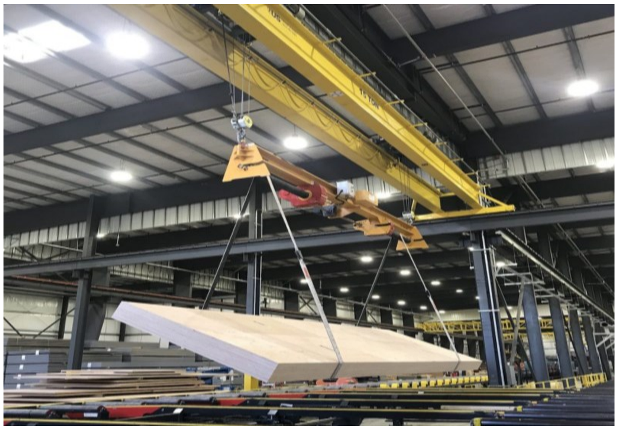

Figure 6.5. Flipping rotary system (Source: Caldwell Posi-Turner 2023).

Figure 6.6. Existing roof production jig line with overhead crane.

An additional workstation must be developed to install the wedge pieces in the support wall element and the ceiling frame of the panelized roof (Figure 6.13). As explained in previous chapters, the wedge is connected to the support wall via two screws. Although this is a manual job, it will require a platform to maintain proper connection alignment. It is worth noting that any angle cut can be done in the existing wall CNC cutting machine of building 1. From the above discussion, it is evident that panelized roofs can be produced in the existing production line with some modification and addition of activities. However, this may impact the overall production status of the offsite facility. For instance, roof panel dimensions differ from the regular wall framing, which may require adjusting the width of framing platform. This process requires additional setup time for the framing station of the wall line. Hence a reassessment of existing production planning is recommended to obtain optimized efficiency.

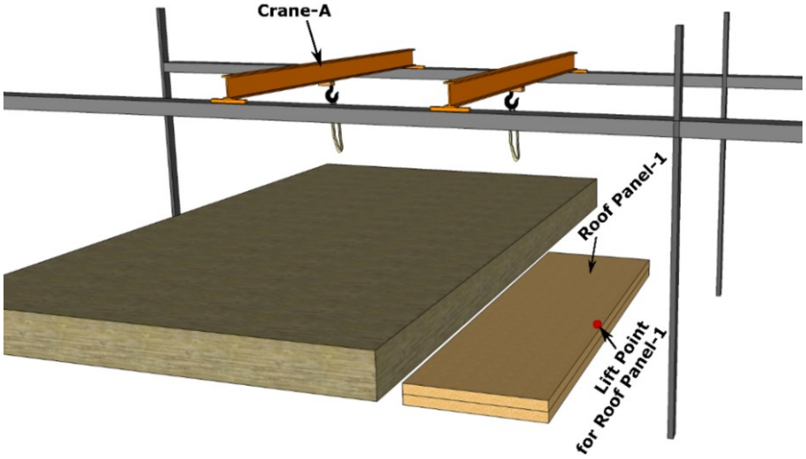

Figure 6.7. Roof panel lifting point for panel-1.

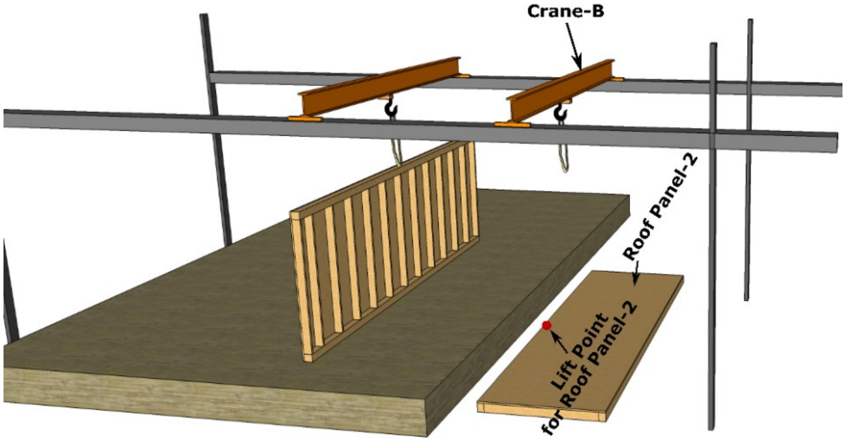

Figure 6.8. Roof panel lifting for panel-2.

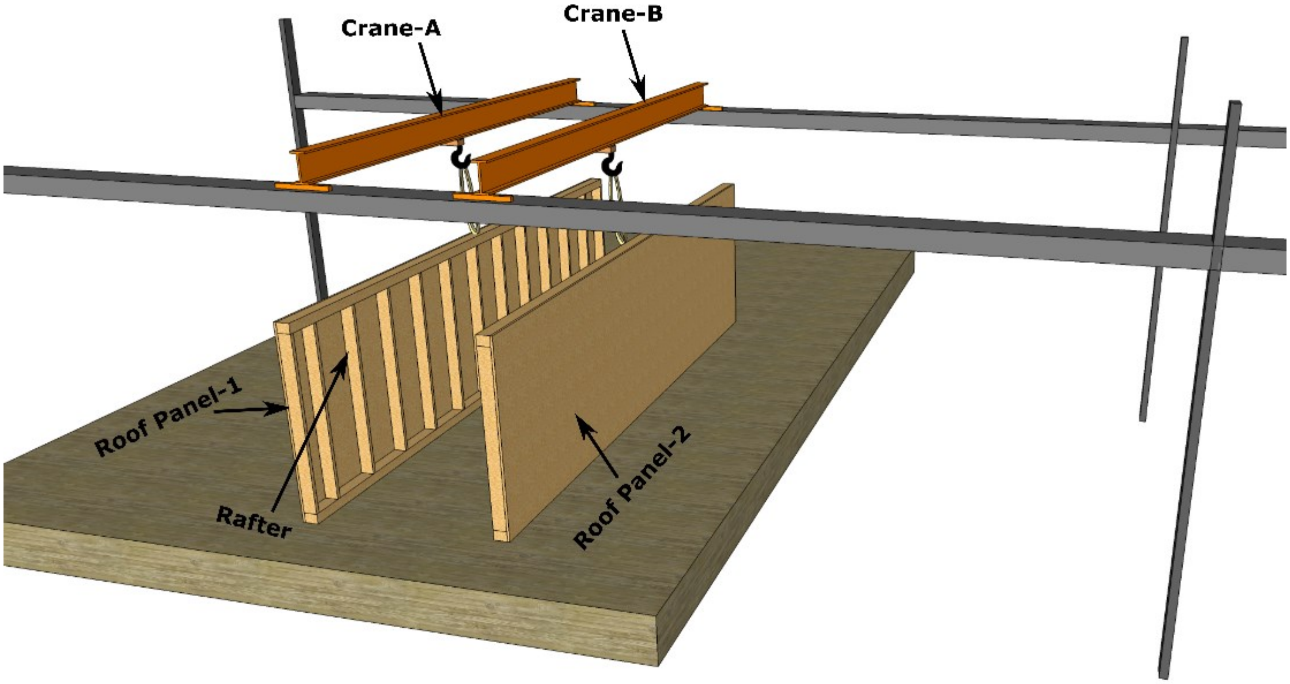

Figure 6.9. The vertical position of panels to connect apex connection.

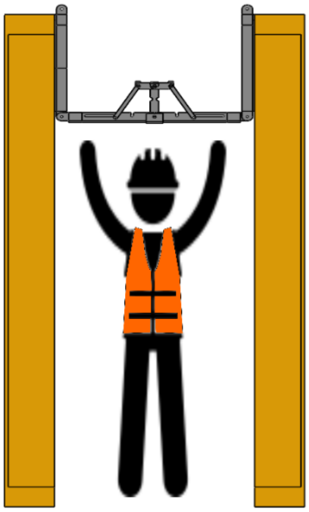

Figure 6.10. Installing the apex connection.

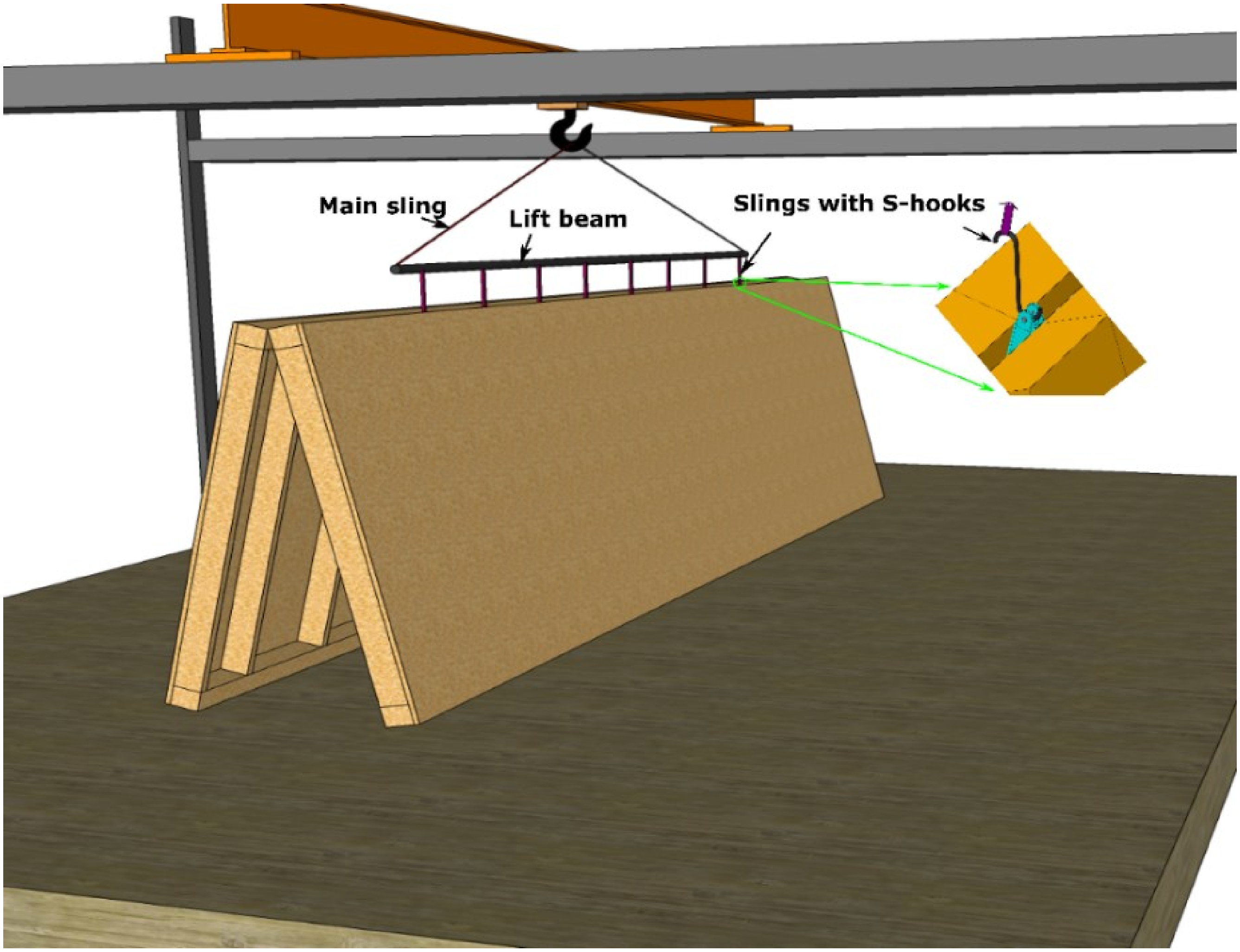

Figure 6.11. Attaching rigging slings with S-hooks to the panel assembly.

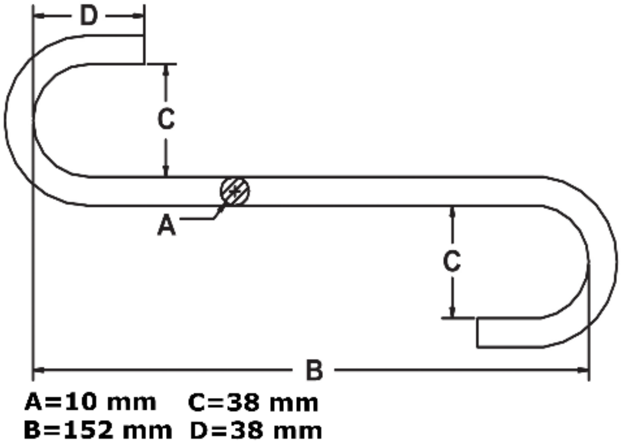

Figure 6.12. S-hook to connect rigging slings (Source: CMWORKS 2023).

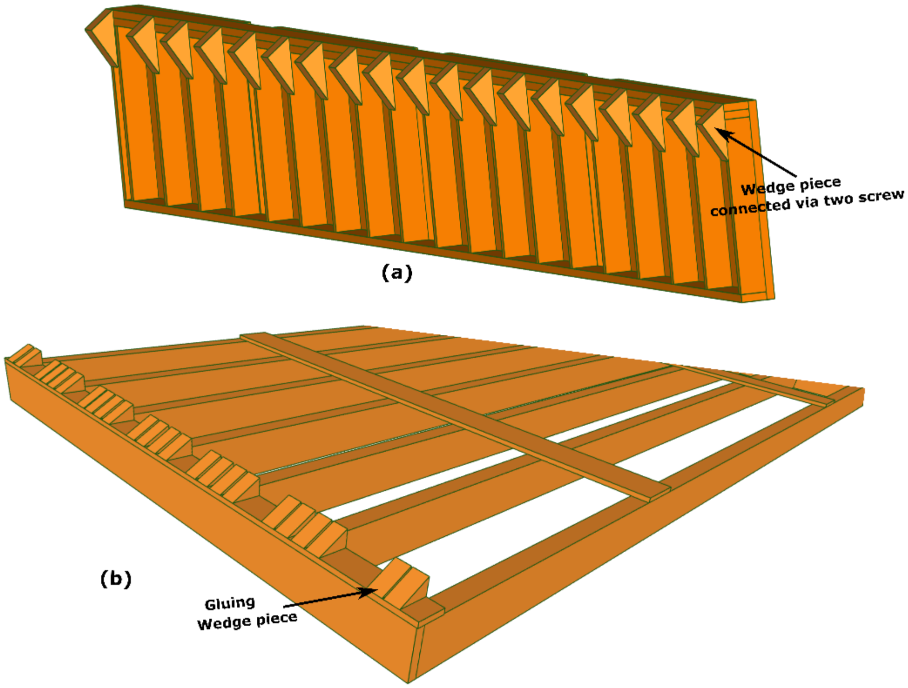

Figure 6.13. (a) Attaching wedge pieces to support wall (b) Gluing the wedge pieces to the ceiling frame.

6.3 Crane Rigging Hook and Apex Connection Actions

The apex connection can facilitate hooks, as shown in Figure 6.12, to connect the rigging slings. The rigging assembly shown in Figure 6.11 consists of main slings, lift beam, and slings with S-hooks. The one end of the S-hook illustrated in Figure 6.12 is attached to the peak pin of the self-locking apex connection. The other end of the hook is connected to the lift beam via slings, as shown in Figure 6.14. This hook is commercially available. According to the manufacturer’s technical specification, the design factor of the S-hook is 4:1, which means it can carry four times the rated working load limit (CMWORKS 2023). Therefore, by calculating the dead load of the panel assembly number of S-hooks was determined in this case study. The number of hooks required for the panel assembly was 8 to lift the panel. It is worth noting that for this S-hook arrangement, the apex pin and the screw connections have a capacity factor of safety of 3.3 and

7.4, respectively. Hence, the hooks working load capacity governs the lifting assembly. This study provides the gross estimate of hook requirement for crane lifting to demonstrate the advantage of the folding mechanism of apex connection. However, more factors, such as rigging sling strength and arrangement, must be considered for actual crane lifting. Therefore, proper rigging design is recommended for future studies. Also, a proper crane lifting plan assessment is recommended for panelized roof installation.

The conceptual crane deployment sequence is depicted in Figures 6.14 and 6.15. As mentioned above, the low-angle panel module is delivered to the site with the rigging system attached. On the site, the crane rigging system has a double-action winch system. This system facilitates two slings that are attached to the eave line of roof panels. The ground site crew installs the rigging device, as shown in Figure 6.16, at the eave line point. The crane operator lowers the double-action winch, and simultaneously the jig fixed to the apex pins lowered away from the attachment points of the slings opening up the roof panel. Since the apex connection is self-locking, the panel assembly automatically stops changing the opening angle at the proper roof pitch. This process is performed by lifting the panel assembly slightly up from the ground at the site. After the panel assembly reaches the appropriate roof pitch, it is ready to lift and place on the support walls of the gable roof.

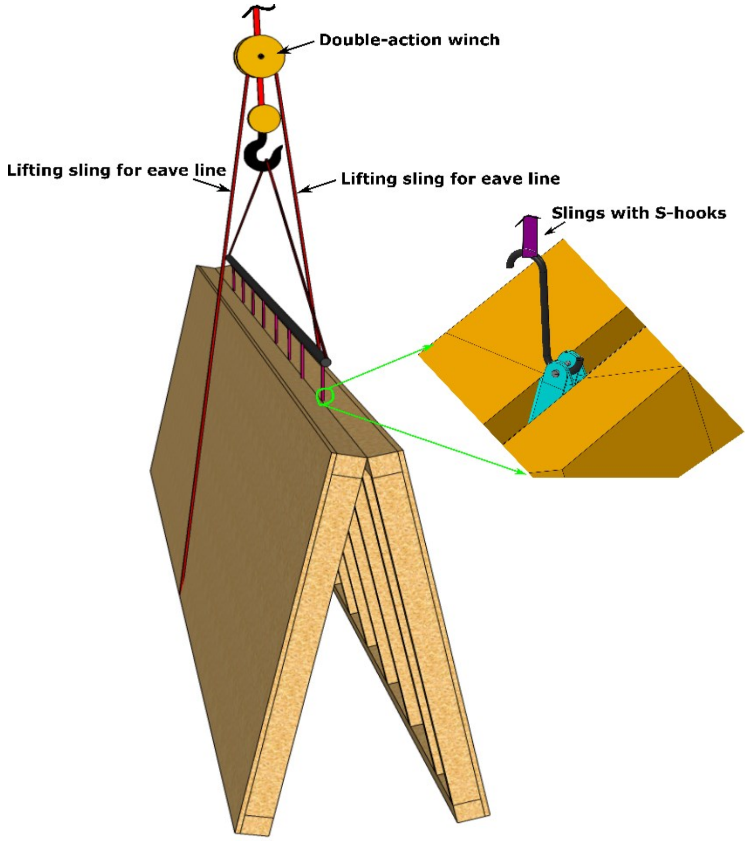

Figure 6.14. Attach the lifting slings at the eave line to open the roof panel.

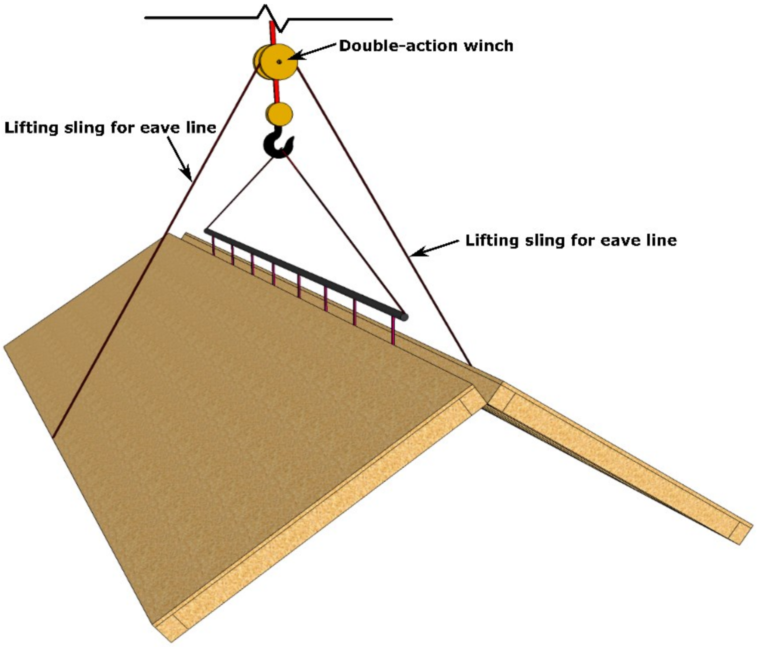

Figure 6.15. Roof panel at proper angle by double-action winch rigging system.

Figure 6.16. Material Handling System for Lightweight Wood Elements (Source: MTC Solution 2023).

6.4 Replicability of Panelized Roof System in the Context of the Northern Canada Housing Crisis

This section summarizes the replicability of the novel panelized gable roof system in the context of a different fabrication process using a robotic facility and remote construction site.

6.4.1 Panelized Fabrication Solution to Solve Northern Canada Housing Crisis

Northern Canada is facing a significant challenge with the need for sufficient housing. The harsh arctic climate, short construction season, limited local resources, high materials and labour costs (2 to 3 times as much as they cost in south Canada), and climate change make constructing and maintaining housing a difficult task (Daley 2016; Semple 2008). On average, the cost of building in Canadian North cities is 150 percent higher than in the rest of Canada, with the actual expenses likely to be even more elevated in isolated communities (National Aboriginal Economic Development Board 2014; Semple 2008). Traditional stick framing construction requires a large quantity of material, workforce, and equipment mobilization to build homes. In this construction method, each architectural component of a light-frame building framework is cut and assembled on the construction site, including the walls, roof, and floor systems. Hence, this process requires relatively higher manhours of on-site labour in cutting and measuring individual components. Due to the manual work process, building projects executed following this construction method exhibit high reworks and waste of construction materials, which leads to a prolonged construction schedule. Consequently, home building using the traditional stick-built process is a significant cost driver in Northern Canada.

On the other hand, panelized construction uses the manufacturing principle to pre-fabricate building off-site in a factory setting. A building is constructed in the form of a wall and floor panel. These panels are then delivered to the construction site, assembled and erected on a foundation. Hence, panelized construction significantly reduces on-site labour and time since the pre-manufactured panels can be quickly assembled using a crane. Thus, the offsite fabrication of homes could be a cost-effective solution for Northern Canada. However, there is no such offsite construction facility in Northern Canada that can serve locations such as Northwest Territories, Yellowknife and Nunavut. In this regard, an Edmonton-based startup company is currently working on IoT based robotic construction factory as a potential solution for Northern Canada. The robotic facility conceptualizes a factory in a box that can be shipped using two containers. Setting up requires a relatively small space compared to the conventional CNC-based offsite facility. Figure 6.17 illustrates the proposed factory setting where two robotic arms are trained to fabricate light frame wood assembly. It can fabricate any size of light-frame wood panels to manufacture panelized homes. However, panel size is restricted to the available standard shipping container dimension.

Figure 6.17. Robotic workstation (Source: Promise Robotics 2023).

As shown in Figure 6.18, the maximum interior clearance height is 2.7 m (8' 10"); any panel width or height is restricted to this dimension to comply with this container shipping. Therefore, the developed panelized roof is a solution to efficiently building homes with gable roofs since it can facilitate fully panelized construction. In the proceeding section case study, a single detached house is presented in the context of a remote northern location to demonstrate the replicability of the light frame wood panelized gable roof system.

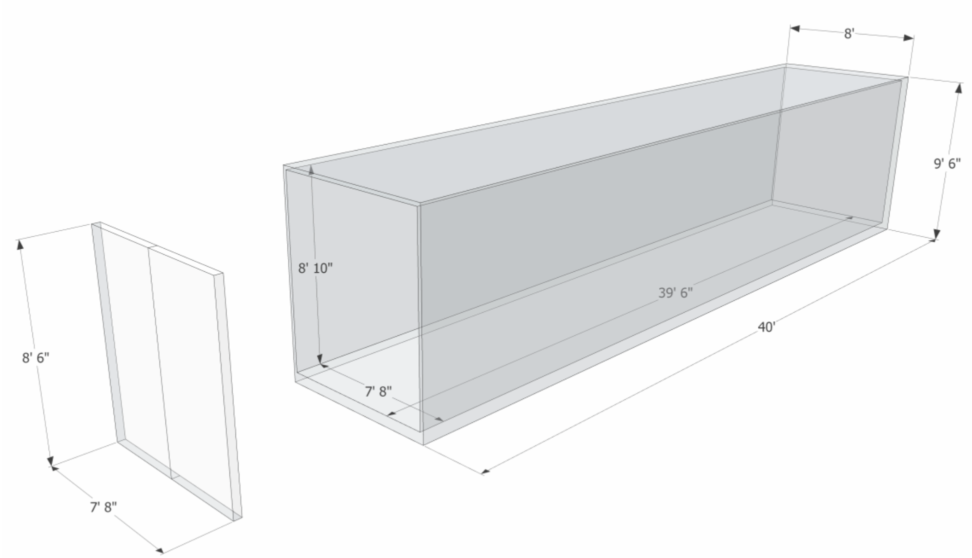

Figure 6.18. Standard high cub shipping container dimension (Source: Discover Containers 2023).

6.4.2 Prefabricated Panelized Gable Roof Case Study in the Context of Northern Canada

Home building in northern Canada is becoming more challenging due to the impact of climate change impact. In the last few decades, arctic Canada has been warming at about three times the global rate (Government of Canada 2023). Due to climate change, the construction season is getting much shorter in the North than elsewhere in Canada (GNTW 2021). Transporting construction materials to community project sites is served only by annual sealifts, summer barges, or winter roads (GNTW 2021). In some remote locations, the only means of transport are barges. Therefore, an efficient way to improve panelized home construction is to consider transporting building components in small packages that can be fit into shipping containers. A case study home on Salliq (Coral Island) of Nunavut was adopted to demonstrate the replicability of the panelized roof system. As can be observed from Figure 6.19, the location is very remote, and the only way to transport home packages is using a shipping container.

Single detached homes account for more than 50% of housing in major northern cities such as Whitehorse, Yellowknife, and the demand for more unit sales remains high (CMHC 2022). Therefore, a case study of a single-family home is presented herein. The case study home has a roof footprint of 66.9 m^2 and a slope of 8/12. The panelized roof concept is similar to the one presented in the previous chapter. However, some component sizes were modified due to transportation limitations, such as ceiling frame width. As can be observed from Table 6-1 maximum package height for the ceiling frame and folded roof panel are 2.4 m and 1.7 m, respectively. The triangle-shaped gable end has a base length of 6.1 m and a height of 2.2 m. Therefore, it can be concluded that the panelized roof can be transported in a standard shipping container.

Figure 6.19. Location of the case study area (Salliq).

Using the same FEM process explained in Chapter -5, sectional details for this case study were determined. In the case of any building located in Salliq (Coral Island) specified snow load, 1 in 50 years, was 2.29 kPa. Additionally, 0.5 kPa dead load was assumed on the roof panels considering waterproofing and permanent roof features such as air vents outlets. Furthermore, 0.5 kPa deadload was assigned for the ceiling joist, assuming gypsum board drywall as the ceiling material. As per the recommendation in GNTW(2021), 1 in 50 years of wind pressure (0.58 kPa) was also considered. The following design load scenarios applied to the roof structure were assigned based on the National Building Code of Canada (NBCC 2020a).

Load case a: 1.25D + 1.5S
Load case b: (1.25D or 0.9D) + 1.5S + 0.4W
Load case c: (1.25 D or 0.9D) + 1.4W + 0.5S
Load case d: 0.9D + 1.4W
where D = dead load, L = live load, S = snow load and W = wind load.

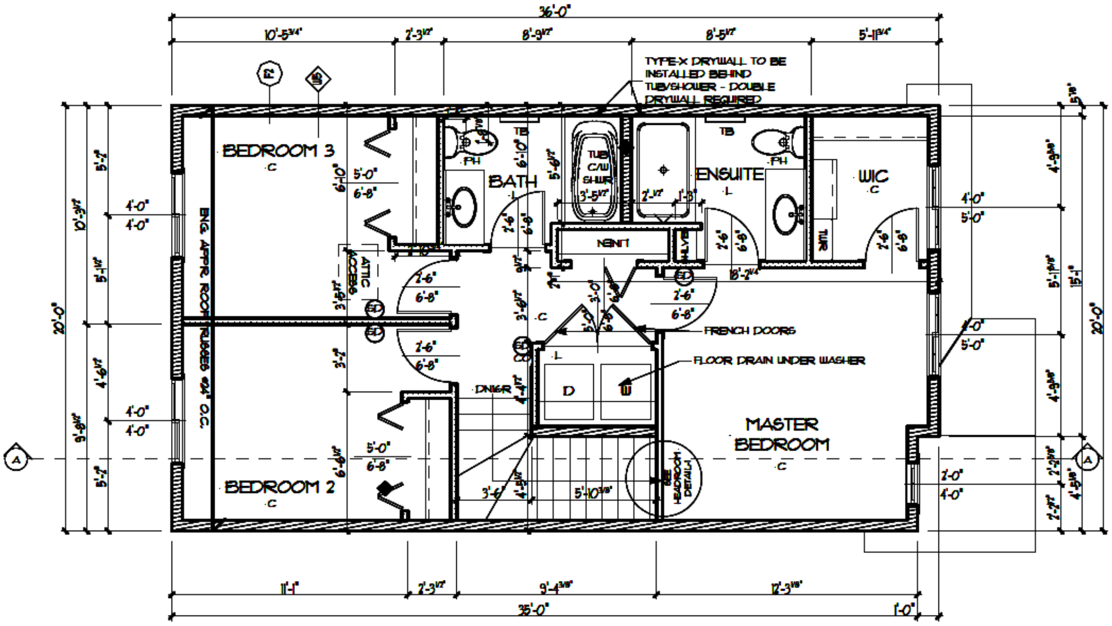

Figure 6.20. Case study home roof footprint.

Table 6-2 summarizes all the construction details to fabricate the panelized roof component. Due to the specified snow load of more than 2 kPa, minimum 15 mm OSB thickness for roof panel is recommended (CWC 2014). Also, the ceiling frame construction requires two rim boards to obtain proper nailing requirements due to high horizontal thrust. As can be observed from Figure 6.22 a total of five ceiling frames are required for this case study home, where three ceiling frames are 2.4 m wide, and the rest are 1.8 m and 1.2 m, respectively. Figure 6.23 shows the construction details of individual ceiling frames. The ceiling joist span is in the short direction of the building. Two notched 76 mm thick and 184 mm wide LSL board is attached at the top face near the end of the joist span (see the plan and section view of Figure 6.23). Also, two 38 mm thick and 403 mm wide LSL board is attached using a 6 mm screw at the location of span/4 distance, which provides the base for the support wall component. To facilitate the folding apex connection, rafter spacing for panel-A is 300 mm, whereas in the case of panel-B is 600 mm (Figures 6.24 and

6.25). Due to the high wind uplift in the roof overhang zone, eight blocking is required for each roof panel.

Table 6-3 summarizes the connection requirements for the case study. Due to the higher snow load, six screws per rafter location must be installed at the eave line. For the ceiling frame, a maximum of 12 mm deflection was observed with 38 mm × 184 mm joists (Figure 6.26). To comply with the serviceability limit state maximum of 16 mm deflection is allowed (NBCC 2020b). Therefore, this cross-section of joists is sufficient in this case.

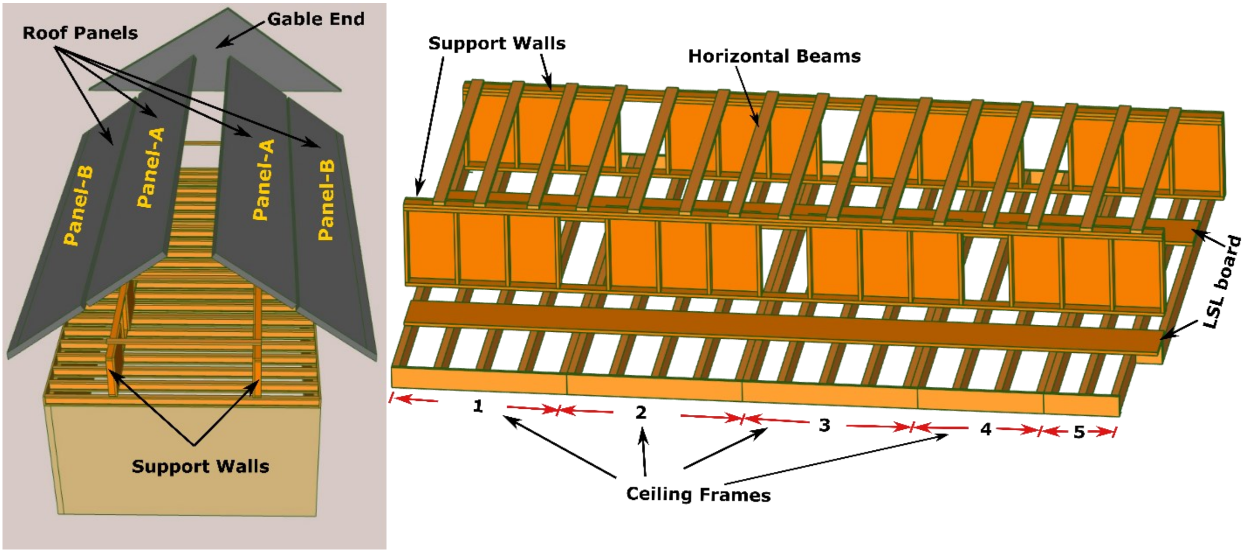

Figure 6.21. Panelized roof component for Salliq.

Table 6-1. Component size of the panelized roof

Roof Component	Width	Length	Package height
Roof Panel-A	1.9 m	11.6 m	1.8 m
Roof Panel-B	1.7 m	10.9 m 11.6 m	1.7 m

Roof Component	Width	Length	Package height
Ceiling frames	Three frames 2.4 m One frame 1.8m One frame 1.2 m	6.1 m	Maximum 2.4 m
Gable End	-	6.1 m	2.2 m

Table 6-2. Panelized roof component construction details for the Salliq case study.

Roof Panel construction details	
Minimum OSB thickness	15 mm
Nailing	150 mm c/c on the edges and intermediate rafter
LSL Plates at the edges of the rafter	76 mm × 140 mm
Rafter section	LSL/Lumber or a mix of both. Cross section 38 mm × 140 mm
Support wall construction details	
Minimum OSB thickness	9.5 mm
Nailing	150 mm c/c
Top plate	76 mm × 140 mm
Bottom plate	38 mm × 140 mm
Gable End Construction details	
OSB	15 mm
Top plate	76 mm × 140 mm
Nailing	100 mm c/c at edges of OSB and intermediate studs
Ceiling frame construction details	
SPF Joist	38 mm × 184 mm
Rim board	38 mm × 184 mm
Notched LSL plate	76 mm × 140 mm
Standard LSL plate	38 mm × 140 mm

Table 6-3. Connection requirements

Connection Type	Max Force (N)	Connection Design Capacity(N)	Governing Load Case	Fastener Note
Support wall wedge screw shear per connection	1425	5880	1.25D+1.5S+0.4W	Fabricate this wedge connection with one 150 mm and 200 mm long screw with a 6mm nominal diameter, as

Connection Type	**Max Force (N)**	**Connection Design Capacity(N)**	**Governing Load Case**	**Fastener Note**
				shown in Figure 5.3c of Chapter 5.
Support wall wedge Steel Angle Screw withdrawal per connection	1267	3960	0.9D+1.4 W (Wind parallel to ridge)	Use four commercially available SD screws to connect the L bracket
Gable End-to-Roof panel screw shear in the plane of roof panel (y') per panel	17750	18288	1.25D+1.5S+0.4W	Eight screws per roof panel (see details of Figure 5.3c). Use a flat head screw/ washer for tapper head screws.
Gable End-to-Roof Panel screw shear in the plane of roof panel (x') per panel	2500	18288	1.25D+1.5S+0.4W	Eight screws per roof panel (see details in Figure 5.3e of Chapter 5). Use a flat head screw/ washer for the tapper head screws.
Gable End-to-Roof, panel screw withdrawal (z') per panel	4462	8720	0.9D+1.4 W (Wind parallel to ridge)	Four screws per roof panel (see details in Figure 5.3e of Chapter 5). Use a flat head screw/ washer for the tapper head screws.
Panel-Panel connection per rafter	5352	9152	1.25D+1.5S+0.4W	Use four screws per rafter with an 8 mm diameter (see typical details in Figure 5.38 d of Chapter 5)
Eave line screw shear per rafter	9446	10992	1.25D+1.5S+0.4W	Use 6- 8 mm nominal diameter of self-tapping screw (see typical details in Figure 5.38b of Chapter 5)
Eave line screw withdrawal per rafter	1464	6540	0.9D+1.4 W (Wind parallel to ridge)	Use 6- 8 mm nominal diameter of self-tapping screw per rafter (see typical details in Figure 5.38b of Chapter 5)
Roof panel-A-to-support Wall screw shear per rafter	4160	7328	1.25D+1.5S+0.4W	Use 4- 8 mm nominal diameter of self-tapping screw per rafter (see typical details in Figure 5.38c of Chapter 5). If rafter spacing is 150 mm, use 2-8 mm diameter of self-tapping screw per rafter
Roof Panel-A-to-support wall screw withdrawal per rafter	1528	4360	0.9D+1.4 W (Wind parallel to ridge)	Use 4- 8 mm nominal diameter of self-tapping screw per rafter

Connection Type	**Max Force (N)**	**Connection Design Capacity(N)**	**Governing Load Case**	**Fastener Note**
Support wall base-to-LSL board nail connection withdrawal	859	1083.09	0.9D+1.4 W (Wind perpendicular to ridge)	Use five nails as indicated in (see typical details in Figure 5.40a of Chapter 5).
Support wall base-to-LSL board nail connection Shear	65	1361	0.9D+1.4 W (Wind perpendicular to ridge)	Nails defined as the model is okay
LSL board-to-Ceiling frame connection withdrawal	2194	3270	0.9D+1.4 W (Wind perpendicular to ridge)	Use 3- 6mm dia 100 mm long HBS screw (see details in Figure 6.23)
LSL board-to-Ceiling frame connection shear	100	5640	0.9D+1.4 W (Wind perpendicular to ridge)	Withdrawal governs. Use 6mm dia 100 mm long HBS screw (see details in Figure 6.23)
LSL Beam-to-support wall shear	5106	5445	1.25D+1.5S+0.4W	Use 5 Nails as defined in the model
Gable End-to-support wall connection Shear	8409	12250.45	1.25D+1.5S+0.4W	Use 9 Nails as defined in the model
Apex connection link	8331	11796	1.25D+1.5S+0.4W	Use seven commercially available SD screws to connect the folding connection to the rafter.
Ceiling frame-to-load bearing shear wall connection per nail	400	846	1.25D+1.5S+0.4W	Use nails @ 75 mm c/c as shown in (see typical details in Figure 5.41a of Chapter 5). Use two rows of nail.
Gabel Wall-to-load bearing shear wall connection per nail	109	216.6	0.9D+1.4 W (Wind parallel to ridge)	Use nails (3.3 mm dia) @ 85 mm c/c as shown in (see typical details in Figure 5.41b of Chapter 5). Use two rows of nail.

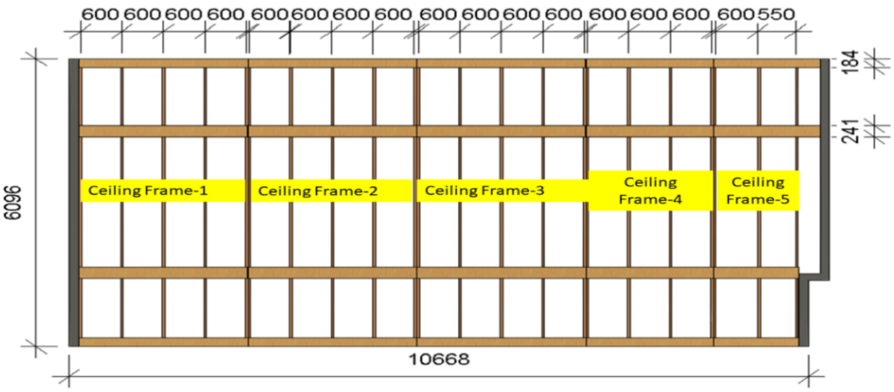

Figure 6.22. Ceiling Frame Layout.

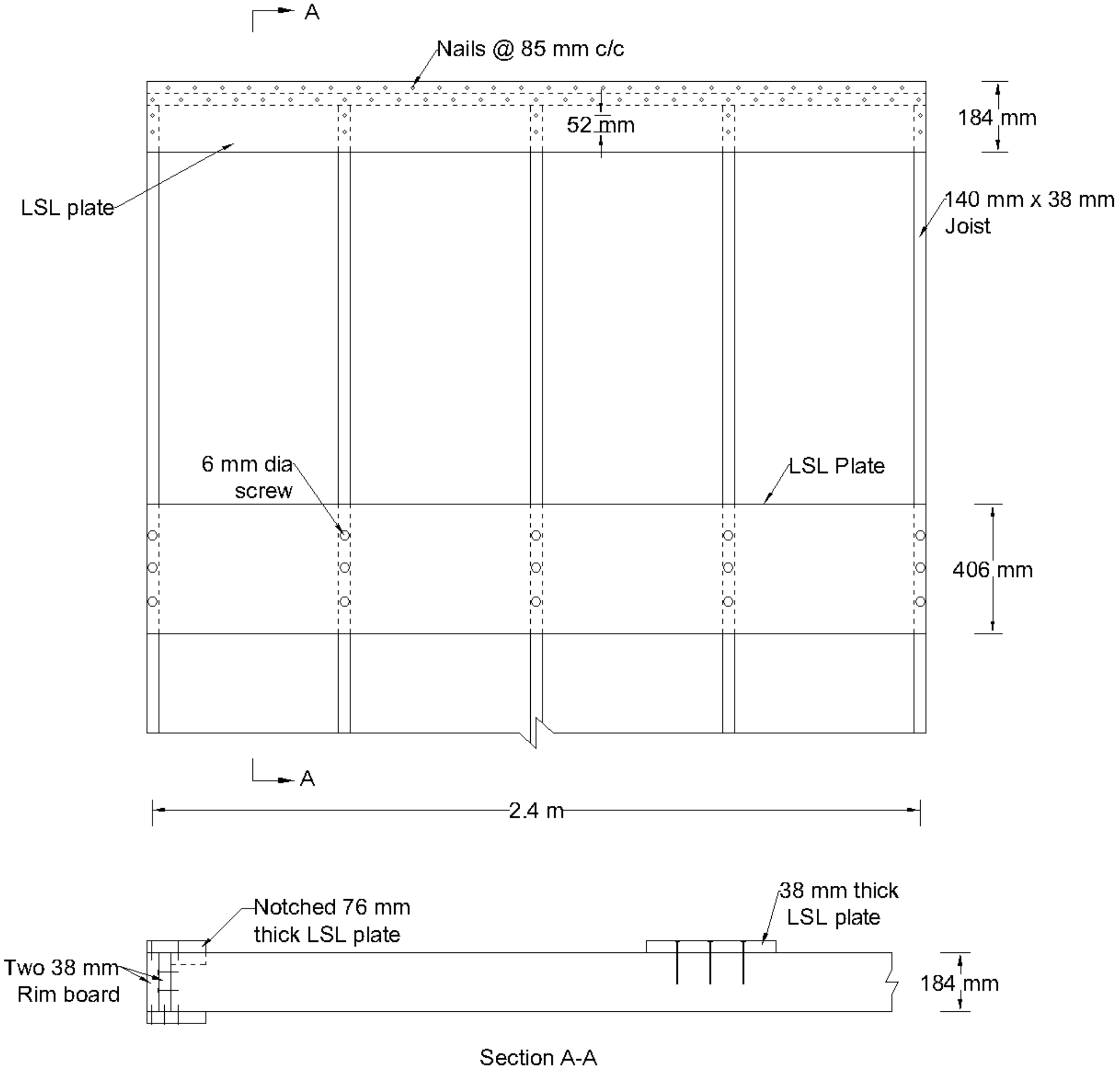

Figure 6.23. Ceiling Frame nailing details.

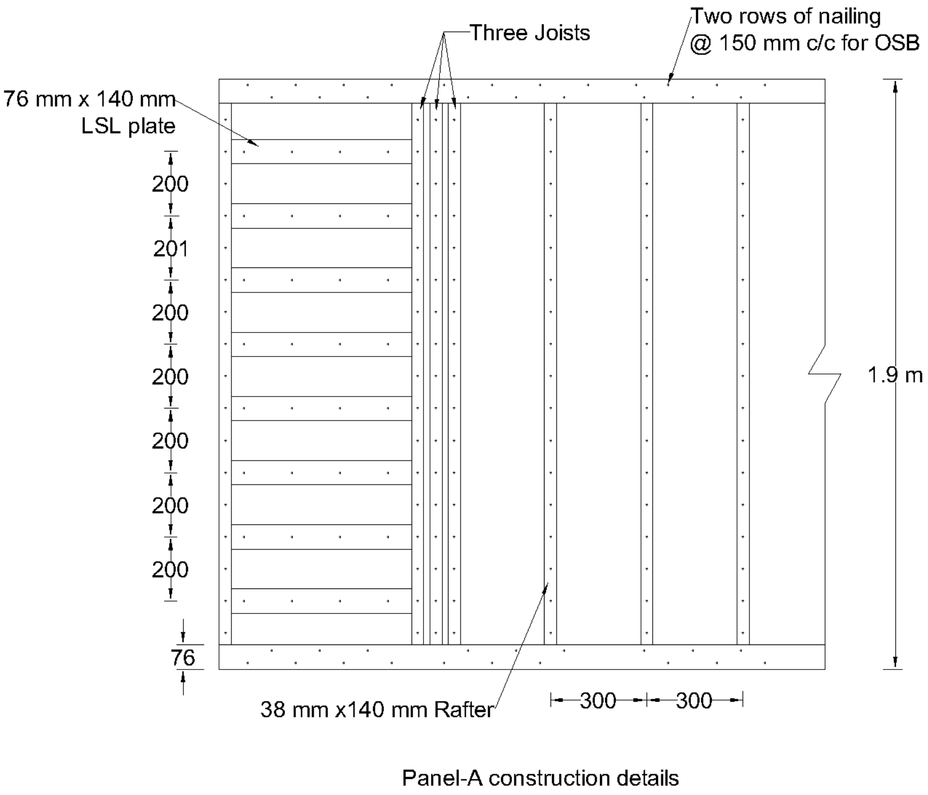

Figure 6.24. Roof Panel-A fabrication details.

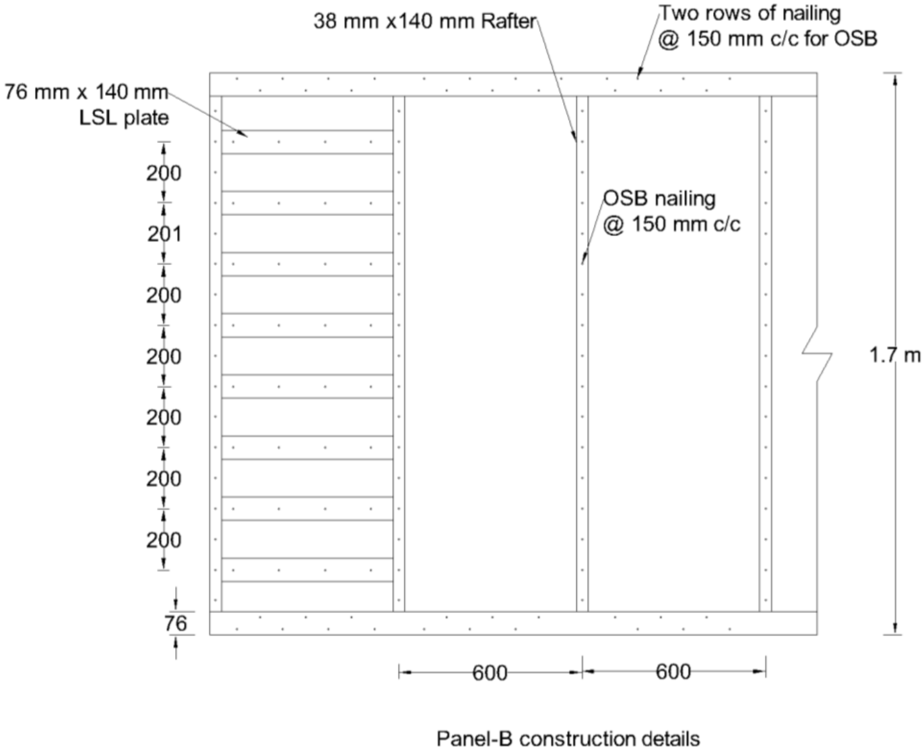

Figure 6.25. Panel-B construction details.

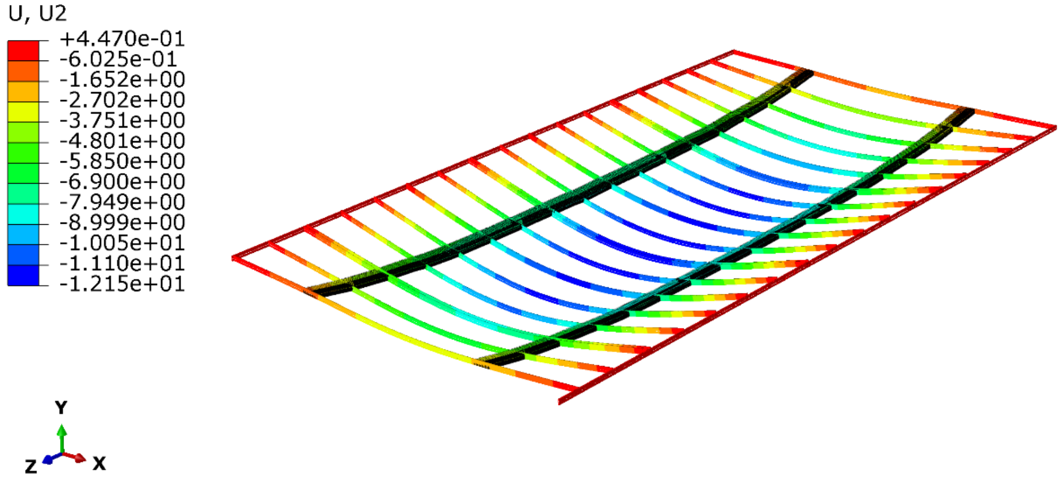

Figure 6.26. Ceiling frame deflection in load case 1.0 D+1.0 S+0.4 W.

6.4. Conclusion

It is evident from the above discussion that the panelized gable roof presented in this research is replicable in any location regardless of the offsite factory process. With the Industrial 4.0 revolution, Canada is expected to move towards more robotic construction technology. Hence, the panelized roof could be a potential solution for constructing homes in remote locations with high transportation costs.

Chapter 7 : Conclusion

7.1 Research Summary

This thesis focuses on developing a novel light-frame wood gable roof by considering offsite fabrication constraints, transportation limitations and onsite installation factors. The ultimate research goal of the thesis is to facilitate partially panelized home building in North America to transition towards fully panelized construction by developing a light-frame wood panelized gable roof. Different components of the panelized roof were idealized first for a gable roof that can be fitted to construct using the existing work stations. In this process, input from the current offsite facility partner was incorporated into the design process. A case study of a two-story home with an 8/12 slope was selected to implement the idea. This slope is common in residential roofs all over North America built with trusses.

Then nail connection test was performed on timber structural composites such as laminated strand lumber (LSL) and oriented strand board (OSB). Based on this experimental study, roof panel analysis was performed. Finite element analysis of the roof panel shows panels fabricated using the existing wall line using LSL, and OSB can sustain the design loads.

In the next phase, the screw connection configuration was developed to facilitate an efficient connection mechanism for roof panels. A detailed test setup was designed to obtain the load-slip curve of screw connections. Two types of screws were utilized in the test to observe their performance. These screw connections are intended for connecting roof panels at the eave line and support wall line. The head-side wedged piece member geometry will vary according to the slope of the roof. The test data provided the connection strength and stiffness in screw shear and withdrawal. Analytical models from the literature were utilized to predict connection strength and verified with test results.

A novel apex connection was invented in this research. The connection has unique features that allow a self-locking and folding mechanism. Using 3D CAD modelling, several designs were conceptualized. The final design was 3D printed on the full scale. This 3D print model demonstrates the full functionality of the connection in folding and self-locking mechanism. 2D FE analysis of the apex connection was performed to obtain internal forces on the connection. The FE results were verified by using an analytical model. Screw connection design was performed based on CSA 086-19 (CSA 2019) to connect the apex connection components with the roof panel. A full-scale 3D FEM model of the apex connection was developed to obtain the cross-sections of steel c-sections required to sustain the design load as specified in NBCC (NBCC 2020a).

A complete 3D FEM of the roof assembly was developed. In this process, the connection test data were implemented to capture the non-linear behaviour due to the screw and nails in the assembly. The governing load cases explained in NBCC (NBCC 2020a) were analyzed to see the most critical effect of the roof assembly. The loading was applied for two locations where one had a snow load of less than 2.0 kPa and the other with a snow load higher than 2.0 kPa. Connection details and configuration were presented for both case studies.

Finally, process maps were developed to incorporate the panelized roof production into the existing manufacturing workstations of an offsite facility. Reviewing the existing process revealed that roof components could be produced without altering the current wall and floor lines production process. However, the existing roof production section requires some modifications and the incorporation of new activities. This study also reviewed the replicability of this novel panelized roof production in the case of other types of offsite facilities with robotic arms. A feasibility study was performed for home buildings in remote locations of Canada, such as Arctic locations, including Nunavut. Preliminary findings show that this panelized roof could be a potential solution to building a gable roof in a remote area where shipping containers are the only transportation medium.

7.2 Research Contributions

Several studies have been conducted on the roof panel in the light frame structure. This research specifically focused on developing an integrated roof system for the prefabricated home building industry, which requires specific attention for its unique manufacturing process. The study developed a holistic methodology to design a panelized roof system that accounts for manufacturing variables in the prefabrication process and the efficiency of the on-site construction process. At the same time, it complies with the structural requirements mandated in building codes. The developed methodology can be applied to analyze and design other roof layouts and dimensions. The main contributions of this thesis are summarized below:

i. The fabrication of panelized roof components can be incorporated into the existing production process of any offsite facility with some adjustments.

ii. Roof panel analysis was performed based on experimental studies on nail connection of structural composites. Finite element analysis of the roof panel shows that any panel fabricated in the existing wall line using LSL and OSB can sustain design loads. The analysis shows 38 mm × 140 mm LSL rafters with 11 mm OSB can be used for snow load less than 2.0 kPa. In case of snow load, only 15 mm OSB is required.

iii. From the experimental evaluation of self-tapping screw connection strength prediction using CSA 086-19 (CSA 2019) and other analytical models such as Bejttka and Blaß (2002) can provide a reasonable connection capacity for any different slope of the roof.

iv. The invented novel apex connection can facilitate easy transportation of gable roofs to the site. Due to the folding and self-locking mechanism, it provides easy roof panel installation at the site. To the best of the author's knowledge, this is the first type of connection with such a unique mechanism with load-carrying capacity, according to NBCC (NBCC 2020a). A design process based on CSA 086-19 (CSA 2019) was developed to connect this connection to the roof panel.

v. Finite element analysis of complete assembly revealed the overall system behaviour of such a panelized roof. The panel-to-panel in-plane load component is higher than the load transfer from the support wall component. The ceiling frame joist acts as a tie beam for the load-bearing shear wall that resists the horizontal thrust.

vi. The panelized roof could be a potential solution to build roofs following the offsite construction method where transportation cost is higher due to remote distance, such as in Northern Canada.

7.3 Future Recommendations

The research work in this thesis demonstrates promising outcomes regarding the holistic design approach of light-frame wood panelized gable roof design. However, due to some limitations in the study, the following are recommended for future research:

a) The roof panel design was investigated only for engineered wood products. Nevertheless, some remote areas may require using dimensional lumber due to local availability. Hence, further study is needed to explore the challenges in fabricating roof panels using regular lumber because of the dimensional variability issues.

b) The screw connection test was performed only for LSL material and 8/12 slope. No material test was performed in this research. As a consequence, screw connection capacity prediction depended on literature and manufacturers' guide. However, analytical model validation requires extensive testing with more samples and material tests. Hence, the connection strength validation should be investigated to improve the strength prediction of screw shear connections. Also, the use of dimension lumber products in screw connections should be explored for an economical solution by incorporating locally available materials. A new analytical model is recommended to predict the inclined screw connection capacity, specifically for the wedge piece connected to the support wall. This would require extensive testing of screw connection tests for various angles.

c) An experimental study on the novel apex connection was not performed due to resource constraints. The lack of testing resulted in a conservative design capacity for this connection. The ultimate limit state of this connection needed to be established. Since it is a steel connection, experimental testing could provide insight to optimize the steel c-sections of the connection further and thereby obtain an economical section. Also, the long-term loading effect of this connection is still unknown. Therefore, future studies should perform a full-scale test on an assembly of roof panels connected by this novel connection. Figure 7.1 illustrates a uniaxial test setup of the apex connection. The uniaxial tension-compression test will be performed on the primary folding link bar by following the cyclic loading protocol described in ASTM E2760 – 19^{e1} (ASTM 2020). As can be observed from Figure 7.1, an extensometer will be used to measure the elongation of the assembly. The test will also include a Digital Image Correlation (DIC) system to measure the strain distribution near the U-slot and long-slot zone of the primary folding link bars.

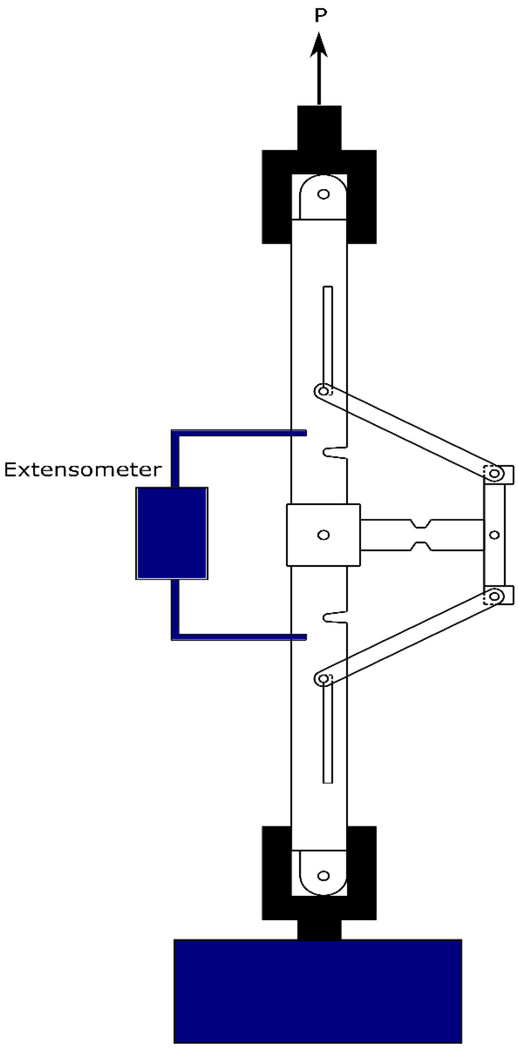

Figure 7.1. Uniaxial test setup of primary folding link bar of Apex connection

d) A full-scale test on a segment of a case study panelized roof should be investigated to obtain the system behaviour of this design to optimize the structural design further. Figure 7.2 to 7.4 show the test configuration for a complete roof assembly for a 1600 x 6096 mm complete assembly of the proposed system. The assembly will be fabricated with all the connections, including the screw and apex connection. Since the structural system of the test assembly is symmetric, the loads will only be applied to one side of the roof at a time, as shown in Figure 7.4, for the lateral load case. Tests will be conducted at three different stages of loading conditions. In the first stage, the gravity load will be applied to the roof panel, and the vertical deflection of the ceiling frames will be measured. Later static lateral load will be applied to simulate the wind-load effect on the roof panel and record the lateral reactions. Finally, the roof will be loaded vertically again until failure is observed in the assembly. This final test of roof assembly will characterize assembly performance beyond design load. The roof assembly will be supported by load cells under the top plate of the load-bearing wall to record the reaction forces, and linear variable differential transformers (LVDT) will be attached at specific connection locations on the test structure to obtain deflection.

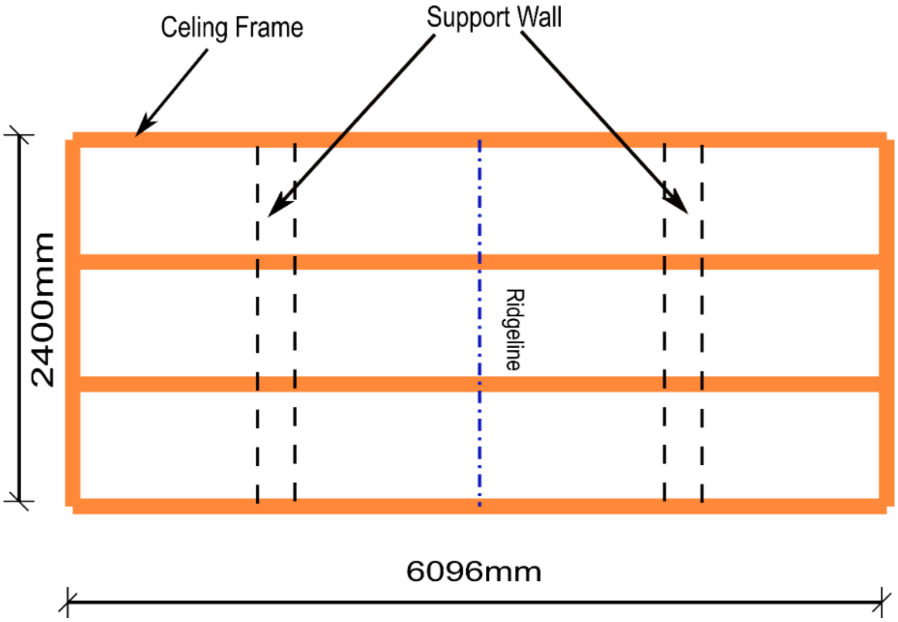

Figure 7.2. Plan view of the roof assembly test segment.

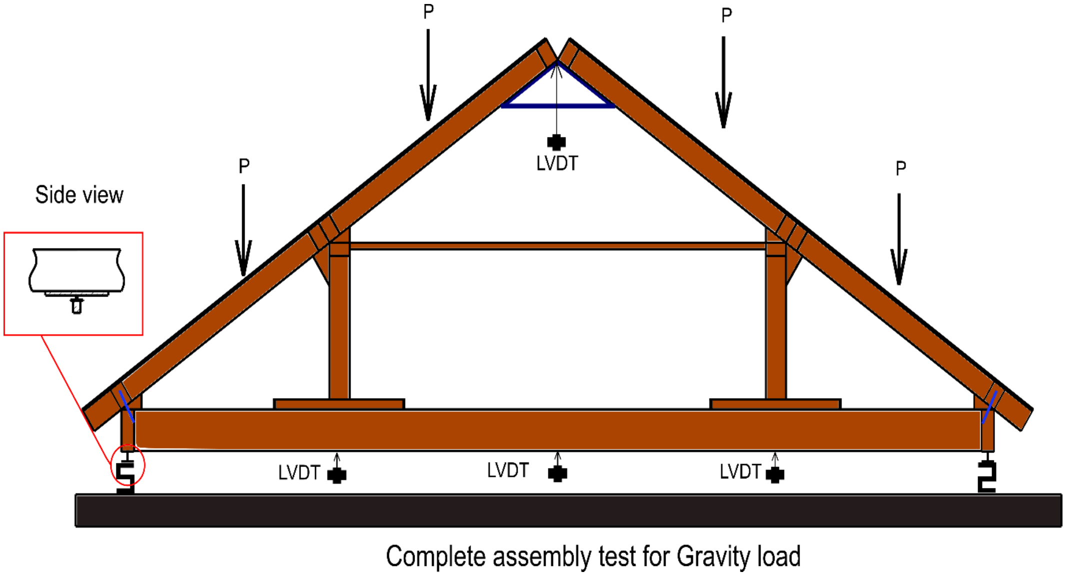

Figure 7.3. Gravity load tetst setup on roof assembly.

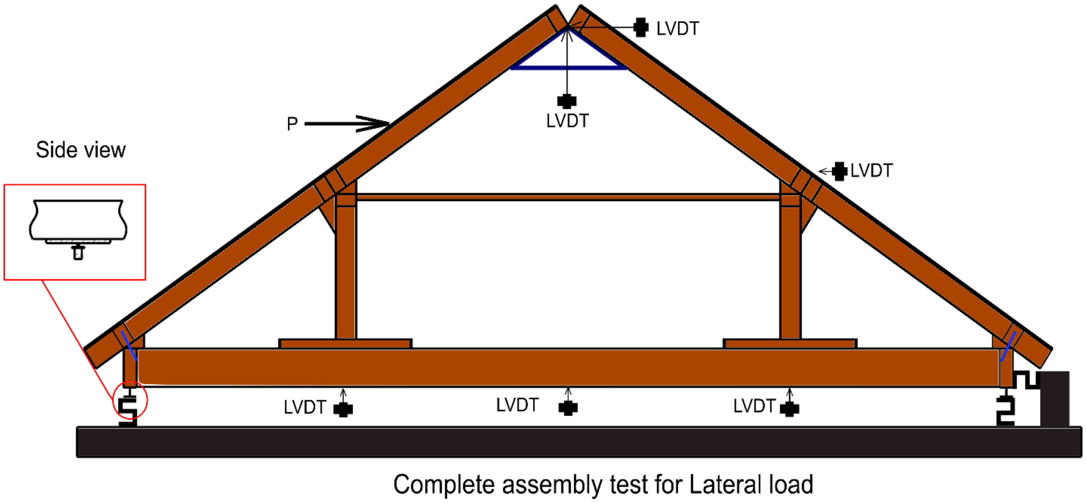

Figure 7.4. Lateral load test setup for the roof assembly.

e) Only gable roofs were investigated in this study. Therefore, future research should address this holistic approach in fabricating other types of roofs, such as hip roofs.

Bibliography

ACQBUILT Inc. (2019). "Company database and personal visits for images." <http://www.acqbuilt.com/> (Nov. 3, 2019).

Ahn, S. J. (2019). "Transportation Framework in Panelized Construction for Residential Building." PhD Thesis, University of Alberta, Canada.

Ahn, S., SangUk, H., and Mohamed, A.-H. (2019). "2D Drawing Visualization Framework for Applying Projection-Based Augmented Reality in a Panelized Construction Manufacturing Facility: Proof of Concept." *Journal of Computing in Civil Engineering*, 33(5), 4019032.

Alhawamdeh, B., and Shao, X. (2020). "Uplift Capacity of Light-Frame Rafter to Top Plates Connections Applied with Elastomeric Construction Adhesives." *Journal of Materials in Civil Engineering*, 32(5), 04020078.

Almeida de, A. C., and Melo Moura de, J. D. (2022). "Mechanical Behavior of GFRP Dowel Connections to Cross Laminated Timber-CLT Panels." *Forests*, 13(2), 1–13.

Altaf, M. S. (2016). "Integrated Production Planning and Control System for Prefabrication of Panelized Construction for Residential Building." PhD Thesis, University of Alberta, Canada.

Altaf, M. S., Bouferguene, A., Liu, H., Al-Hussein, M., and Yu, H. (2018a). "Integrated production planning and control system for a panelized home prefabrication facility using simulation and RFID." *Automation in Construction*, 85(2018), 369–383.

Altaf, M. S., Han, S. H., Lei, Z., Demirer, S., and Al-Hussein, M. (2018b). "A case study: Prefabricated wood framed panelized roof system for single family home." *WCTE 2018 - World Conference on Timber Engineering*, 1–6.

Altaf, M. S., Han, S. H., Lei, Z., Demirer, S., and Al-Hussein, M. (2018c). "A case study: Prefabricated wood framed panelized roof system for single family home." *WCTE 2018 - World Conference on Timber Engineering*, Seoul, Republic of Korea, 1–6.

Anjard, R. (1998). "The primary mapping project phases include: Team development and framework." *Facilities*, 16(3), 79–81.

ANSYS. (2013). "ANSYS 12 [Computer software]. Canonsburg, PA, ANSYS."

Arif, M., and Egbu, C. (2010). "Making a case for offsite construction in China." *Engineering, Construction and Architectural Management*, 17(6), 536–548.

Asiz, A., Chui, Y. H., Doudak, G., Ni, C., and Mohammad, M. (2011). "Contribution of plasterboard finishes to structural performance of multi-storey light wood frame buildings." *Procedia Engineering*, 14, 1572–1581.

ASTM. (2012). *Standard Test Methods for Mechanical Fasteners in Wood Designation: D1761 - 12*. ASTM International, USA.

ASTM. (2014). *Standard Specification for Low-Alloy , High-Strength Low-Alloy with Improved Formability , Solution Hardened , and Bake Hardenable 1*. *ASTM International*, ASTM International, USA.

ASTM. (2018). *ASTM D5764-97a: Standard Test Method for Evaluating Dowel-Bearing Strength of Wood and Wood-*. ASTM International, USA.

ASTM. (2020). *Designation: E2760 − 19e1-Standard Test Method for Creep-Fatigue Crack Growth Testing*. ASTM International.

Ayinla, K., Cheung, F., and Skitmore, M. (2022). "Process Waste Analysis for Offsite Production Methods for House Construction: A Case Study of Factory Wall Panel Production." *Journal of Construction Engineering and Management*, 148(1).

Ayinla, K. O., Cheung, F., and Tawil, A.-R. (2020). "Demystifying the concept of offsite manufacturing method." *Construction Innovation*, 20(2), 223–246.

Bejttka, I., and Blaß, H. (2002). "Joints with Inclined Screws." *Proceedings of CIB-W18 Timber Structures, Meeting 35*, 35-7–4.

Biazzo, S. (2002). "Process mapping techniques and organisational analysis: Lessons from sociotechnical system theory." *Business Process Management Journal*, 8(1), 42–52.

Briscoe, C. R., Mantell, S. C., Davidson, J. H., and Okazaki, T. (2011). "Design Procedure for Web Core Sandwich Panels for Residential Roofs." *Journal of Sandwich Structures & Materials*, 13(1), 23–58.

Brown, R. (2020). "Production Improvements in Offsite Construction Facilities Using Simulation and Lean Principles." MSc Thesis, University of Alberta, Canada.

Browne, M. (2015). "Chapter 1: The challenge of construction logistics." *Supply Chain Management and Logistics in Construction: Delivering Tomorrow's Built Environment*, G. Lundesjo, ed., Kogan Page, London ; Philadelphia, 9–23.

Caldwell Posi-Turner. (2023). "Timber Company Turns Panels with Caldwell Posi-Turner." <https://www.caldwellinc.com/timber-company-turns-panels-with-caldwell-posi-turner/> (Feb. 8, 2022).

Canino, I., Chowdhury, A. G., Mirmiran, A., and Suksawang, N. (2011). "Triaxial Load Testing of Metal and FRP Roof-to-Wall Connectors." *Journal of Architectural Engineering*, 17(3), 112–120.

Cárcamo, S., María, H. S., and Zisis, S. (2018). "Wood frame shear wall model for a finite element program thruogh a shell element." *WCTE 2018 - World Conference on Timber Engineering*, Seoul, Republic of Korea.

CCMC. (2018). "Evaluation Report 13132-R TJI® SERIES JOISTS." Canadian Construction Materials Centre, Canada.

CCMC. (2019). "Evaluation Report of Canadian Construction Materials Centre (CCMC) 12627-R Timber Strand LSL." Canadian Construction Materials Centre, Canada.

CEN. (1991). *EN 26891: Timber structures – Joints made with mechanical fasteners – General principles for the determination of strength and deformation characteristics,* European Committee for Standardization. Brussels, Belgium.

CEN. (2004). *EN 1995-1-1: Eurocode 5 - Design of timber structures - General - Common rules and rules for buildings*. European Committee for Standardization, Brussels, Belgium.

Chowdhury, A. G., Canino, I., Mirmiran, A., Suksawang, N., and Baheru, T. (2013). "Wind-Loading Effects on Roof-to-Wall Connections of Timber Residential Buildings." *Journal of Engineering Mechanics*, 139(3), 386–395.

Chung, K. F., and Ip, K. H. (2000). "Finite element modeling of bolted connections between cold-formed steel strips and hot rolled steel plates under static shear loading." *Engineering Structures*, 22(10), 1271–1284.

CMHC. (2022). "Northern Housing Report." Canada Mortgage and Housing Corporation, Canada.

<https://publications.gc.ca/collections/collection_2022/schl-cmhc/NH12-321-2022-eng.pdf> (Feb. 1, 2023).

CMWORKS. (2023). “Alloy ‘S’ Hook herc-alloy 800 working load limit.” <WWW.CMWORKS.COM> (Jan. 11, 2023).

Crosbie, M. J. (2009). “Making Connections : Innovative Integration of Utilities in Panelized Housing Design.” *Wood Structures Symposium*, 186–204.

Crowley, J., Dentz, J., Morse-Fortier, L., and Parent, M. (1993). “Reinventing Wood Frame Construction: Development of an Innovative Roof Component System.” *Forest products journal*, 43(7), 27–35.

CSA. (2019). *CSA 086 19 Engineering design in wood.* CSA Group, Mississauga, Canada.

CWC. (1994). *Canadian Lumber Properties*. (E. Jones, ed.), Canadian Wood Council.

CWC. (2014). *Engineering guide for wood frame construction*. Canadian Wood Council.

Daley, K. (2016). “Meeting the northern housing challenge.” <https://www.canada.ca/en/polar-knowledge/publications/polarleads/vol1-no1-2016.html> (Nov. 3, 2023).

Daneshvar, H. (2013). “One-sided Steel Shear Connections in Column Removal Scenario.” Phd Thesis, University of Alberta, Edmonton.

Daneshvar, H., and Driver, R. G. (2018). “Modelling benchmarks for steel shear connections in column removal scenario.” *Journal of Building Engineering*, 16, 199–212.

Dassault Systèmes. (2021). “ABAQUS 2021 Documentation.” *ABAQUS User manual*, <https://help.3ds.com/2021/english/dssimulia_established/simacaematrefmap/simamat-c-

anisoyield.htm?contextscope=all> (Jan. 1, 2021).

Dentz, J. L. (1991). “The design of a panelized roof system for residential construction.” MSc Thesis, Massachusetts Institute of Technology (MIT), USA.

Discover Containers. (2023). “Shipping Container Size Basics.” <https://www.discovercontainers.com/shipping-container-dimensions/> (Feb. 2, 2023).

Doudak, G., McClure, G., and Smith, I. (2012). “Experimental Evaluation of Load Paths in Light-Frame Wood Structure.” *Journal of Structural Engineering*, 138(2), 258–265.

Doudak, G., McClure, G., Smith, I., Hu, L., and Stathopoulos, T. (2005). “Monitoring Structural Response of a Wooden Light-Frame Industrial Shed Building to Environmental Loads.” *Journal of Structural Engineering*, 131(5), 794–805.

Ellingwood, B. R., Rosowsky, D. V., Li, Y., and Kim, J. H. (2004). “Fragility Assessment of Light-Frame Wood Construction Subjected to Wind and Earthquake Hazards.” *Journal of Structural Engineering*, 130(12), 1921–1930.

EN 1993-1-8. (2006). *Eurocode 3: Design of Steel Structures, Part 1–8: Design of Joints.* European Committee for Standardization. Brussels , Belgium.

Errera, S. J., Popowich, D. W., and Winter, G. (1974). “Bolted and Welded Stainless Steel Connections.” *ASCE Journal of the Structural Division*, Clairol, Inc, 100(6), 1279–1296.

ETA. (2019). “European Technical Assessment ETA-11/0030-Rotho Blaas Self-tapping screws and threaded rods.” ETA-Danmark, Nordhavn.

Fam, A., and Sharaf, T. (2010). “Flexural performance of sandwich panels comprising polyurethane core and GFRP skins and ribs of various configurations." *Composite Structures*, 92(12), 2927–2935.

Fan, L., Rondal, J., and Cescotto, S. (1997). "Finite element modelling of single lap screw connections in steel sheeting under static shear." *Thin-Walled Structures*, 27(2), 165–185.

Foschi, R. O. (1985). "Wood Floor Behavior: Experimental Study." *Journal of Structural Engineering*, 111(11), 2497–2508.

Goodier, C., and Gibb, A. (2007). "Future opportunities for offsite in the UK." *Construction Management and Economics*, 25(6), 585–595.

Government of Canada. (2023). "Climate change adaptation in Canada." <https://natural-resources.canada.ca/climate-change/what-adaptation/10025>.

GNTW. (2021). *Good Building Practice for Northern Facilities design guide 4th Edition*. Government of the Northwest Territories.

Gutknecht, M. P., and Macdougall, C. (2019). "Withdrawal resistance of structural self-tapping screws parallel-to-grain in common canadian timber species." *Canadian Journal of Civil Engineering*, 46(10), 952–962.

He, M., Lam, F., and Foschi, R. (2001). "Modeling Three-Dimensional Timber Light-Frame Buildings." *Journal of Structural Engineering*, 127(8), 901–913.

He, W. X., and Hong, H. P. (2012). "Probabilistic characterization of roof panel uplift capacity under wind loading." *Canadian Journal of Civil Engineering*, 39(12), 1285–1296.

Hussain, R. S., Ruikar, K., Enoch, M. P., Brien, N., and Gartside, D. (2017). "Process mapping for road works planning and coordination." *Built Environment Project and Asset Management*, 7(2), 157–172.

Huynh, M. T., Pham, C. H., and Hancock, G. J. (2020). "Experimental behaviour and modelling of screwed connections of high strength sheet steels in shear." *Thin-Walled Structures*, 146.

ICC-ES. (2021). "Evaluation Report ESR-3046 for Simpson Strong-Tie Inc." <https://ssttoolbox.widen.net/view/pdf/lo69jw45jn/ICCES_ESR3046.pdf?t.download=true&u=cjmyin> (Nov. 3, 2021).

Islam, M. S., and Chui, Y. H. (2023). "Numerical Investigation of Timber Screw Connection for Panelized Light Wood Frame Roof." *Proceedings of the Canadian Society for Civil Engineering Annual Conference 2023*, Moncton, Canada.

Islam, M. S., Chui, Y. H., Al-Hussein, M., and Altaf, M. S. (2022a). "A New Panelized Roof Design Approach for Offsite Fabrication of Light-Frame Wood Residential Construction Projects." *Proceedings of the Canadian Society of Civil Engineering Annual Conference 2021*, S. Walbridge, M. Nik-Bakht, K. T. W. Ng, M. Shome, M. S. Alam, A. el Damatty, and G. Lovegrove, eds., Springer Singapore, Singapore, 451–463.

Islam, M. S., Chui, Y. H., and Altaf, M. S. (2021). "A Holistic Design Approach for Innovative Panelized Light-Wood Frame Roof Construction." *WCTE 2021 - World Conference on Timber Engineering 9-12 August*, Chile.

Islam, M. S., Chui, Y. H., and Altaf, M. S. (2022b). "Design and Experimental Analysis of Connections for a Panelized Wood Frame Roof System." *Buildings*, 12(6).

Islam, M. S., Chui, Y. H., and Chen, Z. (2022c). "Novel Apex Connection for Light Wood Frame

Panelized Roof." *Materials*, 15(21).

Janowiak, J. J., Hindman, D. P., and Manbeck, H. B. (2001). "Orthotropic behavior of lumber composite materials." *Wood and Fiber Science*, 33(4), 580–594.

Jellen, A. C., and Memari, A. M. (2019). "Structural Design of a Typical American Wood-Framed Single-Family Home." *Timber Buildings and Sustainability*, G. Concu, ed., IntechOpen, Rijeka.

Johansen, K. W. (1949). "Theory of Timber Connections." *IABSE: International Association of Bridge and Structural Engineering*, 9, 249–262.

Judd, J. P., and Fonseca, F. S. (2005). "Analytical Model for Sheathing-to-Framing Connections in Wood Shear Walls and Diaphragms." *Journal of Structural Engineering*, 131(2), 345–352.

Karacabeyli, E., Lau, P., Henderson, C. R., Meakes, F. V., and Deacon, W. (1996). "Design rated oriented Strandboard in CSA standards." *Canadian Journal of Civil Engineering*, 23(2), 431–443.

Kasal, B., Leichti, R. J., and Itani, R. Y. (1994). "Nonlinear Finite-Element Model of Complete Light-Frame Wood Structures." *Journal of Structural Engineering*, 120(1), 100–119.

Khan, R., Niederwestberg, J., and Chui, Y. (2021). "Influence of insertion angle, diameter and thread on embedment properties of self-tapping screws." *European Journal of Wood and Wood Products*, 79(3), 707–718.

Koo, K., Lafond, C., and Abasian, F. (2020). "Industrialized construction program machining optimization : equipment and software suppliers." <https://library.fpinnovations.ca/fr/permalink/fpipub53064> (Nov. 1, 2021).

Kuai, L., Ormarsson, S., Vessby, J., and Maharjan, R. (2022). "A numerical and experimental investigation of non-linear deformation behaviours in light-frame timber walls." *Engineering Structures*, 252(2022), 113599.

Kucirka, M. J. (1989). "Analysis and Design of Sandwich Panel Residential Roof Systems." MSc. Thesis, Massachusetts Institute of Technology (MIT), USA.

Lam, F. (2001). "Modern structural wood products." *Progress in Structural Engineering and Materials*, 3(3), 238–245.

Lenard, J. G. (2014). *Primer on Flat Rolling*. (J. G. Lenard, ed.), Elsevier.

Li, H., Chan, G., Wong, J. K. W., and Skitmore, M. (2016). "Real-time locating systems applications in construction." *Automation in Construction*, 63, 37–47.

Li, H. X., Esfahani, M. N., Gul, M., Yu, H., Mah, D., and Al-Hussein, M. (2014). "Carbon Footprint of Panelized Construction: An Empirical and Comparative Study." *Construction Research Congress 2014*, 140–149.

Li, Z. X., Zhou, T. Q., Chan, T. H. T., and Yu, Y. (2007). "Multi-scale numerical analysis on dynamic response and local damage in long-span bridges." *Engineering Structures*, 29(7), 1507–1524.

Liu, X. C., Pu, S. H., Zhang, A. L., and Zhan, X. X. (2017). "Performance analysis and design of bolted connections in modularized prefabricated steel structures." *Journal of Constructional Steel Research*, 133, 360–373.

Martin, K. G., Gupta, R., Prevatt, D. O., Datin, P. L., and van de Lindt, J. W. (2011). "Modeling System Effects and Structural Load Paths in a Wood-Framed Structure." *Journal of*

Architectural Engineering, 17(4), 134–143.

MBI. (2015). “First, let’s describe what modular construction is.” <https://www.modular.org/what-is-modular-construction/> (Jan. 1, 2019).

Mohamadi-shooreh, M. R., and Mofid, M. (2008). “Parametric analyses on the initial stiffness of flush end-plate splice connections using FEM.” *Journal of Constructional Steel Research*, 64(10), 1129–1141.

Mohamadzadeh, M., Hindman, D. P., and Whaley, A. G. (2019). “Rotational Stiffness of Wood Truss Joints in Lateral and Diagonal Bracing and Truss–Wall Connections.” *Journal of Architectural Engineering*, 25(1), 4019003.

Mohler, K. (1956). “Das Tragverhalten von Beigeträgern und Druckstäben mit Zusammengesetzten Querschnitten und Nachgieben Verbindungsmitteln.” Technische Hochschule Fridericiana (Karlsruhe, Germany).[in German]

Morrison, M. J. (2010). “Response of a two-story residential house under realistic fluctuating wind loads.” PhD Thesis, University of Western Ontario, Canada.

Mosalam, K. M., Machado, C., Gliniorz, K.-U., Naito, C., Kunkel, E., and Mahin, S. A. (2002). *Seismic evaluation of an asymmetric three-story woodframe building*. Richmond, CA.

Moses, D. M. (2000). “Constitutive and analytical models for structural composite lumber with applications to bolted connections.” PhD Thesis, University of British Columbia, Canada.

Moses, D. M., Prion, H. G. L., Li, H., and Boehner, W. (2003). “Composite behavior of laminated strand lumber.” *Wood Science and Technology*, 37(1), 59–77.

MTC Solution. (2023). “Material Handling System for Lightweight Wood Elements.” <https://mtcsolutions.com/products/mini-yoke/> (Jan. 1, 2023).

Mullens, M. A., and Arif, M. (2006). “Structural Insulated Panels: Impact on the Residential Construction Process.” *Journal of Construction Engineering and Management*, 132(7), 786–794.

Murty, B., Smith, I., and Asiz, A. (2007). “Wood and Engineered Wood Product Connections Using Small Steel Tube Fasteners: Applicability of European Yield Model.” *Journal of Materials in Civil Engineering*, 19(11), 965–971.

Nahmens, I., and Reichel, C. (2013). “Adoption of high performance building systems in hot-humid climates - lessons learned.” *Construction Innovation*, 13(2), 186–201.

National Aboriginal Economic Development Board. (2014). "Study on Addressing the Infrastructure Needs of Northern Aboriginal Communitie*s*." <http://www.naedb-cndea.com/reports/northern-infrastructure-report.pdf>(Jan. 1, 2022).

National Association of Home Builders. (2022). “Building Systems Councils E-Brochures.” <https://www.nahb.org/-/media/NAHB/nahb-community/docs/councils/bsc/brochures/nahb-bsc-panelized-home-brochure.pdf>(Jan. 1, 2022).

naturally:wood. (2022). “What is light-frame construction?” <https://www.naturallywood.com/topics/light-frame-construction/> (Jan. 1, 2022).

NBCC. (2020a). *National Building Code of Canada Part-4 Structural design*. National Research Council of Canada, Canada.

NBCC. (2020b). *National Building Code of Canada Part-9 Housing and Small Building*. National

Research Council of Canada, Canada.

Niederwestberg, J., Zhou, J., Chui, Y. H., and Gong, M. (2018). "Bending properties of innovative multi-layer composite laminated panels." *WCTE 2018 - World Conference on Timber Engineering*.

Pan, W., and Goodier, C. (2012). "House-Building Business Models and Off-Site Construction Take-Up." *Journal of Architectural Engineering*, 18(2), 84–93.

Peng, H., Ou, J., and Mahin, S. (2020). "Design and numerical analysis of a damage-controllable mechanical hinge beam-to-column connection." *Soil Dynamics and Earthquake Engineering*, 133, 106149.

Plesnik, T., Erochko, J., and Doudak, G. (2016). "Nailed Connection Behavior in Light-Frame Wood Shear Walls with an Intermediate Layer of Insulation." *Journal of Structural Engineeringing*, 142(7), 1–9.

Promise Robotics. (2023). "Robotic workstation." <https://promiserobotics.com/> (Mar. 3, 2023).

Puthli, R., and Fleischer, O. (2001). "Investigations on bolted connections for high strength steel members." *Journal of Constructional Steel Research*, 57(3), 313–326.

Qi, B., Razkenari, M., Costin, A., Kibert, C., and Fu, M. (2021). "A systematic review of emerging technologies in industrialized construction." *Journal of Building Engineering*, 39.

Quale, J., Eckelman, M. J., Williams, K. W., Sloditskie, G., and Zimmerman, J. B. (2012). "Construction Matters: Comparing Environmental Impacts of Building Modular and Conventional Homes in the United States." *Journal of Industrial Ecology*, 16(2), 243–253.

Rogers, C. A., Masc, B., and Hancock, G. J. (1998). “New Bolted Connection Design Formulae for G550 and G300 Sheet Steels Less Than 1.0 mm Thick.” Sydney, <http://www.civil.usyd.edu.au/> (Jan. 1, 2021).

Rothoblaas. (2021). “HBS SOFTWOOD countersunk screw with under-head ribs.” <https://www.rothoblaas.com/products/fastening/screws/screws-carpentry> (Nov. 3, 2021).

Salih, E. L., Gardner, L., and Nethercot, D. A. (2011). “Bearing failure in stainless steel bolted connections.” *Engineering Structures*, 33(2), 549–562.

Satheeskumar, N., Henderson, D. J., Ginger, J. D., and Wang, C. H. (2016). “Wind Uplift Strength Capacity Variation in Roof-to-Wall Connections of Timber-Framed Houses.” *Journal of Architectural Engineering*, 22(2), 4016003.

Satheeskumar, N., Henderson, D. J., Ginger, J. D., and Wang, C. H. (2017a). “Finite element modelling of the structural response of roof to wall framing connections in timber-framed houses.” *Engineering Structures*, 134, 25–36.

Satheeskumar, N., Henderson, D. J., Ginger, J. D., and Wang, C. H. (2017b). “Three-Dimensional Finite-Element Modeling and Validation of a Timber-Framed House to Wind Loading.” *Journal of Structural Engineering*, 143(9), 4017112.

Schiro, G., Giongo, I., Sebastian, W., Riccadonna, D., and Piazza, M. (2018). “Testing of timber-to-timber screw-connections in hybrid configurations.” *Construction and Building Materials*, 171, 170–186.

Schmidt, R. J., and Miller, J. F. (2012). “Considerations for Design of Rafters in Timber Buildings.” *Practice Periodical on Structural Design and Construction*, 17(3), 127–132.

Semple, B. (2008). "A Sustainable House for the Canadian Arctic." <http://www.homeenergy.org/show/article/id/503/viewFull/yes> (Nov. 3, 2023).

Shafa, L. (2012). "Simulation Based Process Flow Improvement for Wood Framing Home Building Production Lines." MSc Thesis, University of Alberta, Canada.

Shahidul Islam, M., Islam, M. N., and Shahria Alam, M. (2017). "Properties of oriented strand board (OSB), and timber to evaluate the stiffness of timber L-joist." *6th International Conference on Engineering Mechanics and Materials 2017*, 790–801.

Sharaf, T., and Fam, A. (2011). "Experimental Investigation of Large-Scale Cladding Sandwich Panels under Out-of-Plane Transverse Loading for Building Applications." *Journal of Composites for Construction*, 15(3), 422–430.

Shivarudrappa, R., and Nielson, B. G. (2013). "Sensitivity of Load Distribution in Light-Framed Wood Roof Systems due to Typical Modeling Parameters." *Journal of Performance of Constructed Facilities*, 27(3), 222–234.

Simpson Strong-Tie. (2022). "ICC-ES Evaluation Report ESR-3046 Wood, Plastic, and composite Fastenings." <https://ssttoolbox.widen.net/view/pdf/lo69jw45jn/ICCES_ESR3046.pdf?t.download=true&u=cjmyin> (Nov. 3, 2021).

Simpson Strong-Tie. (2019). *Evaluation Report Number: 192 Evaluation SUBJECT: SIMPSON STRONG-DRIVE® SDW22, SDWS22DB, SDWH19DB, SDWS22, SDWS19, SDWH27G, and SDWS16 WOOD SCREWS*.

Sott, M. K., Furstenau, L. B., Kipper, L. M., Reckziegel Rodrigues, Y. P., López-Robles, J. R., Giraldo, F. D., and Cobo, M. J. (2020). “Process modeling for smart factories: using science mapping to understand the strategic themes, main challenges and future trends.” *Business Process Management Journal*, 27(5), 1391–1417.

Spasojevic, M., Daneshvar, H., Chen, Y., and Chui, Y. H. (2021). “Lateral Resistance of Sheathing-to-Framing Nailed Joints with an Intermediate Insulation Layer.” *Journal of Structural Engineering*, 147(6), 1–11.

Stevenson, S. A., El Ansary, A. M., and Kopp, G. A. (2019). “A practical modelling technique to assess the performance of wood-frame roofs under extreme wind loads.” *Engineering Structures*, 191, 640–648.

Thomas, D., Mantell, S. C., Davidson, J. H., Goldberg, L. F., and Carmody, J. (2006). “Analysis of Sandwich Panels for an Energy Efficient and Self-Supporting Residential Roof.” *Journal of Solar Energy Engineering*, 128(3), 338.

Tomasi, R., Crosatti, A., and Piazza, M. (2010). “Theoretical and experimental analysis of timber-to-timber joints connected with inclined screws.” *Construction and Building Materials*, 24(9), 1560–1571.

U.S. Department of Housing and Urban Development. (2017). *Residential Structural Design Guide*. *Coulbourne Consulting*.

UES. (2022). “Uniform Evaluation Service Report 192: Evaluation subjects Simpson Strong-Tie Strong Drive, SDW, SDWS, SDWH, and SDWV screws.” California, <https://ssttoolbox.widen.net/view/pdf/96lrxjfxjn/IAPMO_UES_ER192.pdf?t.download=true&u=cjmyin> (Nov. 3, 2021).

Verwaerde, R., Guidault, P. A., and Boucard, P. A. (2021). “A non-linear finite element connector model with friction and plasticity for the simulation of bolted assemblies.” *Finite Elements in Analysis and Design*, 195, 103586.

Vessby, J., Serrano, E., and Olsson, A. (2010). “Coupled and uncoupled nonlinear elastic finite element models for monotonically loaded sheathing-to-framing joints in timber based shear walls.” *Engineering structures*, 32(11), 3433–3442.

Wang, M., Altaf, M. S., Al-Hussein, M., and Ma, Y. (2020a). “Framework for an IoT-based shop floor material management system for panelized homebuilding.” *International Journal of Construction Management*, 20(2), 130–145.

Wang, S., Tang, J., Zou, Y., and Zhou, Q. (2020b). “Research on production process optimization of precast concrete component factory based on value stream mapping.” *Engineering, Construction and Architectural Management*, 27(4), 850–871.

Weyerhaeuser. (2021). “TimberStrand LSL TJ-9500 Specifier’s Guide.” <https://www.weyerhaeuser.com/woodproducts/engineered-lumber/timberstrand-lsl/> (Jan. 1, 2021).

Winter, G. (1956). “Tests on Bolted Connections in Light Gage Steel.” *Journal of the Structural Division*, 82(2), 920–1.

Xu, J., Zhang, S., Wu, G., Gong, Y., and Ren, H. (2021). “Withdrawal properties of self-tapping screws in japanese larch (Larix kaempferi (lamb.) carr.) cross laminated timber.” *Forests*, 12(5), 1–13.

Youyi, Z., Zhen, L., SangHyeok, H., Ahmed, B., and Mohamed, A.-H. (2020). “Process-Oriented

Framework to Improve Modular and Offsite Construction Manufacturing Performance." *Journal of Construction Engineering and Management*, 146(9), 4020116.

Zenkert, D. (1997). *The Handbook of Sandwich Construction*. EMAS, Cradley Heath, UK.

Zhao, J., Peng, Y., Su, W., and Dong, J. (2021). "Finite element analysis of the shear capacity of stainless-steel blind-rivet connections." *Journal of Constructional Steel Research*, 179, 106558.

Zhu, E. (2003). "Modelling the structural behaviour of OSB webbed timber I-beams." PhD Thesis, University of Brighton, UK.

Zhu, E. C., Guan, Z. W., Rodd, P. D., and Pope, D. J. (2005). "A constitutive model for OSB and its application in finite element analysis." *Holz als Roh - und Werkstoff*, 63(2), 87–93.

Appendix-1

A-1.1. Supplementary section for section 5.3 of Chapter 5

The following calculation was performed for spacing of the Sheathing-to-framing connection described in section 5.3 of chapter-5:

Try 15.5 plywood 3.66 mm nail diameter (3 in long)

$$V_{rs} = \phi\ v_d J_D J_s J_f J_{ud} L_D$$

$$v_d = N_u / s$$

$$N_u = n_u (K_D K_{SF} K_T$$

$n_u = 791\ N$, equation (d) of CSA 086 Clause 12.9.3.2 governs.

$$N_u = 791(1.15 \times 1.0 \times 1.0) = 910\ N$$

$$v_d = \frac{910}{150} = 6.07\ N/mm$$

$$V_{rs} = 0.8 \times 6.07 \times 1.3 \times 1.0 \times 1.0 \times 0.89 \times 8 = 44.95\ kN$$

Use 15.5 plywood with 3.66 mm diameter (3 in long) common nails spaced at 150 mm c/c at the diaphragm boundary and other panel edges.

A-1.2. Supplementary section for section 5.4.2 of Chapter 5

The following equations of the Gamma Method were used to obtain the out plane bending thickness of the roof panel and support wall elements:

$$I_{effective} = n\, I_1 + n\, \gamma\, A_1\, {e_1}^2 + I_2 + A_2 {e_2}^2 \text{ .... (1)}$$

$$t_b = \sqrt[3]{12\, I_{effective}}/a_1 \text{ .... (2)}$$

$$\gamma = \frac{1}{(1+p)} \text{ .... (3)}$$

$$p = E_1 \left(\frac{\pi}{l}\right) \frac{1}{k} \frac{A_1 A_2}{A_2 + n A_1} \text{ .... (4)}$$

$$n = \frac{E_1}{E_2} \ldots\ldots\ldots\ldots\ldots\ldots (5)$$

$$e_1 = \frac{1}{2} t \frac{A_2}{A_2 + nA_1} \ldots\ldots\ldots\ldots\ldots\ldots (6)$$

$$e_2 = \frac{1}{2} t \frac{A_1}{A_1 + nA_2} \ldots\ldots\ldots\ldots\ldots\ldots (7)$$

$$k = \frac{K}{s} \ldots\ldots\ldots\ldots\ldots\ldots (8)$$

$$K = OSB - LSL\ nail\ connection\ stiffness\ of\ fastner, \frac{N}{mm}$$

$$s = connector\ spacing, mm$$

$$k = smeared\ connection\ stiffness, N/mm/mm$$

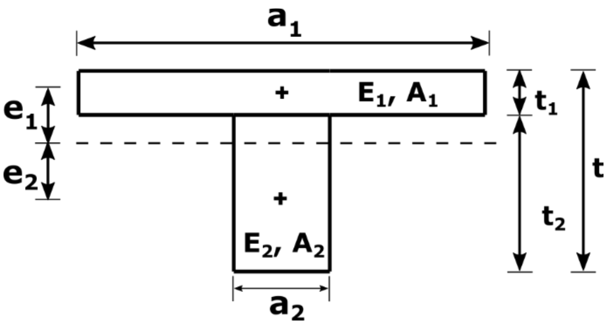

Figure A-4.1. Composite action of OSB-nail-Stud

Figure A-4.2 illustrates the connector out of gable wall FEM described in section 5.4.2 of Chapter 5. The shear in the nail connection is well below the factor design resistance of sheathing to lumber connection. Maximum lateral displace of 0.7 mm was observed in load case d (wind perpendicular to ridge direction)

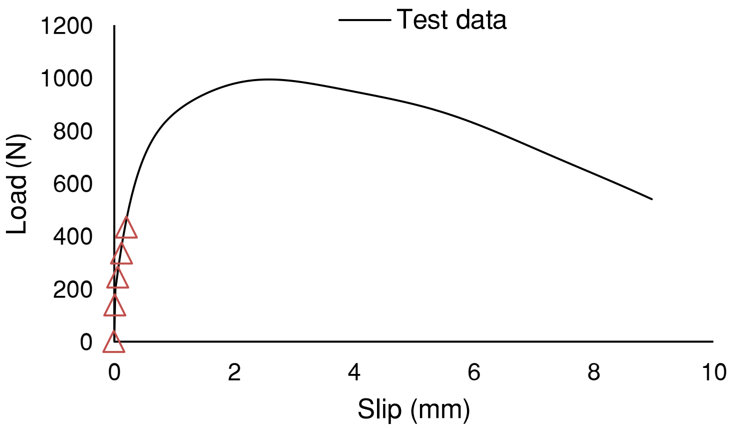

Figure A-4.2. Connector output of gable wall sheathing to lumber connection

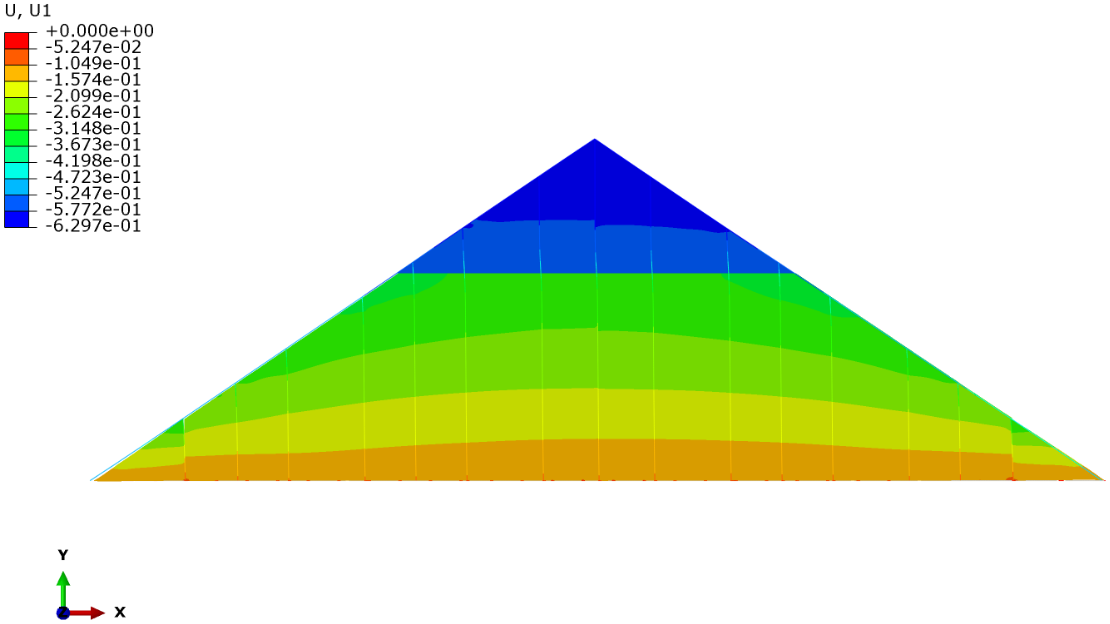

Figure A-4.3. Displacement of Gable wall FEM

A-1.3. Supplementary section for section 5.5.1 of Chapter 5

LSL beam spanned between two support wall checks:

The axial force out shows the LSL beam in plank orientation is in compression; therefore, checks for compressive strength were performed. The 76×140 mm LSL beam section is required to sustain the buckling of the beam. Tables A-4.1 and A-4.2 show the strength checks for LSL beam and ceiling joists.

Table A-1.1. Strength check of LSL beam

Highest axial force from FEM, P=	3946.95 N		Highest moment from FEM, M=	29728.3 N-mm	
b	76 mm		b	76 mm	
d	140 mm		d	140 mm	
ϕ	0.8		f_b	24.2MPa	Use strength properties in Plank orientation
A	10640		s	124133.3	
fc	15.4 MPa		k_{zb}	1.4	
L	2980 mm		k_l	1	
K_{zcb}	1.1713746		Fb	24.2 MPa	
K_{zcd}	1.2681968	<1.3	ϕ	0.9	
C_{cb}	39.210526		f_v	5.15	
C_{cd}	21.285714		M_r	3785074 N-mm	> M_f Ok
K_{cb}	0.0980041				
K_{cd}	0.5592634				
E_{05} (use Dfir-L property)	7000 MPa				
P_{rb}	15048.467	>P_f oK			
P_{rd}	95304.215				
Use 76 x 140 mm LSL					

Table A-1.2. Strength check of Ceiling Joists

Bending Capacity check		Shear Capacity Check		Bearing Capacity Check	
Maximum bending moment from FEM, M =	407181 N-mm	Maximum shear force from FEM, V =	586.1 N	Reaction in bearing location from FEM, Q_f =	2930.18 N
b	38 mm			f_{cp}	5.3
d	140 mm	A	5320 mm^2	A_b	3876
f_b	11.8 MPa			ϕ	0.8
s	124133.3	V_r	10054.8 N > V_f oK	Q_r	16434.24 N > Q_f ok
k_{zb}	1.4				

kl	1	
F_b	11.8 MPa	
ϕ	0.9	
f_v	1.5	
M_r	1845614	$>M_f$ oK

Table A-2.3. Strength check of the support wall stud and bottom plate

Compressive strength check			Bearing Check bottom plate		
Highest axial force from FEM, P=	998.074 N		ϕ	0.8	
b	38		f_{cr}	5.45 MPa	
d	140		F_{cp}	5.45 MPa	
ϕ	0.8		k_b	1.25	
A	5320		d/b	1.842105	
f_c	15.4		K_{zcp}	1.15	
L	1000		A_b	5320 m^2	
K_{zc}	1.5994427	>1.3	Q_r	33343.1 N	$> Q_f$ Ok
C_c	7.1428571				
K_c	0.9710819				
E05 (use Dfir-L)	7000				
P_{rd}	82741.15	$>P_f$ Ok			

A maximum bending moment of 407 kN-mm was observed in the ceiling joist. Design checks were performed for the ceiling joist, LSL beam and support wall. All the defined sections, including the ceiling joist (38 mm×140 mm), LSL beam (76 mm ×140 mm) and support wall stud (38 mm×140 mm) and bottom plate (38 mm×140 mm), were adequate to sustain the design load.

Appendix-2

A-2.1 Wind load calculation for Edmonton:

External Wind Load P= $I_w\, q\, C_e\, C_t\, C_g\, C_p$

Table A-2.1. C_pC_g Value

	Zone											
Case I	2	2E	3	3E	5	1	4	6	1E	4E	5E	6E
	0.4	0.5	-0.8	-1	0	1.05	-0.7	0	1.15	-0.9	1.15	-0.8
	Zone											
Case II	2	2E	3	3E	5	1	4	6	1E	4E	5E	6E
	-1.3	-2	-0.7	-1	0.75	-0.85	-0.85	-0.55	-0.9	-0.9	1.15	-0.8

Table A-2.2. Internal Pressure

Internal Pressure		
I_w	1	
Wind pressure, q (kPa)	0.45	
h	7.9	
C_{ei}	0.617493	Use 0.7
C_t	1	
C_{pi}	-0.45	0.3
C_{gi}	2	
p_i	$= I_w\, q\, C_{ei}\, C_t\, C_{gi}\, C_{pi}$	
Suction, p1	-0.2835	
Pressure, p2	0.189	

Table A-2.3. Wind Pressure for Wind perpendicular to ridge direction

Zone	External Pressure (kPa)	Net Pressure (Suction internal case)	Net Pressure (Pressure internal case)
P_2	0.126	0.4095	-0.063
P_{2E}	0.1575	0.441	-0.0315
P_3	-0.252	0.0315	-0.441
P_{3E}	-0.315	-0.0315	-0.504
P1	0.33075	0.61425	0.14175
P1E	0.36225	0.64575	0.17325
P4	-0.2205	0.063	-0.4095
P4E	-0.2835	0	-0.4725

Table A-2.4. Wind Pressure for Wind parallel to ridge direction

Zone	External Pressure (kPa)	Net Pressure (Suction internal case)	Net Pressure (Pressure internal case)
P_2	-0.4095	-0.126	-0.5985
P_{2E}	-0.63	-0.3465	-0.819
P_3	-0.2205	0.063	-0.4095
P_{3E}	-0.315	-0.0315	-0.504
P5	0.23625	0.51975	0.04725
P5E	0.36225	0.64575	0.17325
P1	-0.26775	0.01575	-0.45675
P1E	-0.2835	0	-0.4725
P4	-0.26775	0.01575	-0.45675
P4E	-0.2835	0	-0.4725
P6	-0.17325	0.11025	-0.36225
P6E	-0.252	0.0315	-0.441

Appendix-3

A-3.1 Roof Panel Diaphragm wind load analysis

Table A-3.1. Roof Panel Diaphragm wind load analysis

	Roof Panel				Building length, L (m)	10.973
	Interior Zone		End Zone		End Zone length, y (m)	6
	Windward	Leeward	Windward	Leeward	Roof Panel Width	1.8
p(kpa)	-0.063	-0.441	-0.0315	-0.504	L-y	4.973
Total factored	0.5292		0.6615			
	Average Pressure	0.6015			height of roof (m)	2.032
					Second floor height (m)	2.7432
	Wall pressure Wind perpendicular to ridge					
	Interior Zone		End Zone			
	Windward	Leeward	Windward	Leeward		
P (kPa)	0.14175	-0.4095	0.17325	-0.4725		
Total factored	0.7718		0.90405			
Average Pressure	0.8441					
	W_{roof} (kN/m)	1.7689				
	Factored Shear force, V_f (N)	9705.1869				
	M_f (kN-m)	26.6237				
	T_f (kN)	14.7909				

A-3.2 Roof Panel Diaphragm Design Checks

Table A-3.2. Sheathing to framing connection check

Failure Mode in nail connection					
				G (OSB)	0.42
a	917.48	N		G (LSL)	0.5
b	3310.77	N		d_f (mm)	3.3
d	616.61	N	Governs		
e	1234.71	N			
f	845.65	N		f_1 (MPa)	29.3
g	866.23	N		f_2 (MPa)	24.175
				f_3 (MPa)	30.54676

n_u (N)	616.61			f_y (MPa)	635	
N_u (N)	709.11			t_1 (mm)	9.5	
v_d (N/mm)	4.73			t_2 (mm)	41.5	
V_{rs} (N)	20080.37	>Vf	= 9705.19 N	Nail length (mm)	51	
				Nail spacing, s	150	
				ϕ	0.8	
				J_d	1.3	
				L_D (m)	6.096	
				J_{ud}	0.67	
				J_s	1	since s >= 150mm
				J_f	1	since it is unblocked

Table A-3.3. Panel Buckling check

			Assumed 2.4 m ×1.2 m OSB	
$B_{a,0}$ (N/mm)	44000		a	2400
$B_{a,90}$ (N/mm)	33000		b	1200
α	1.86121		B_v (N/mm)	10000
η	0.524864		L_D (m)	6.096
K_{pb}	1.298135		t	9.5
			ϕ	0.8
v_{pb} (kN/m)	11.38972		kD	1.15
			K_s	1
V_{rs}/L_D	10.47854		K_T	1
V_{rs}	63877.19	> V_f =9705.187		

Table A-3.4. Chord Member Check

b (mm)	76
d(mm)	140
An(mm2)	10640
ft (Mpa)	13.7
ϕ	0.9
K_D	1.15
K_H	1
K_{St}	1
K_T	1
K_{zt}	1
T_r	150869.9 N

	150.8699 kN > T_f= 14.79097

A-3.3 Support wall Analysis

Table A-3.5. Support Wall wind Load Analysis

	Interior Zone		End Zone	
	Windward	Leeward	Windward	Leeward
Wind pressure p (kPa)	0.04725	-0.36225	0.17325	-0.441
Total factored	0.5733		0.85995	

End zone length (m)	1
Interior Zone length (m)	5.096
Width of house (m)	6.096
Effective short wall length Ls (m)	8400
height of roof (m)	2.032
A_{gable} (m^2)	6.1935
Second Floor height) (m)	2.7432
Support wall height (m)	1
Length of house	10.97
Span/4	1.524

Average pressure	
P(kPa)	0.6203

W_{roof} (kN/m)	1.4811

Roof diaphragm shear force, V1 (kN)	4.5143
Roof diaphragm shear force, V2 (kN)	2.2572
Total Shear force (kN)	6.7715

Unit Shear force in the short wall(N/mm)	0.8061
M (kN-m)	6.7715
P (kN)	0.61728

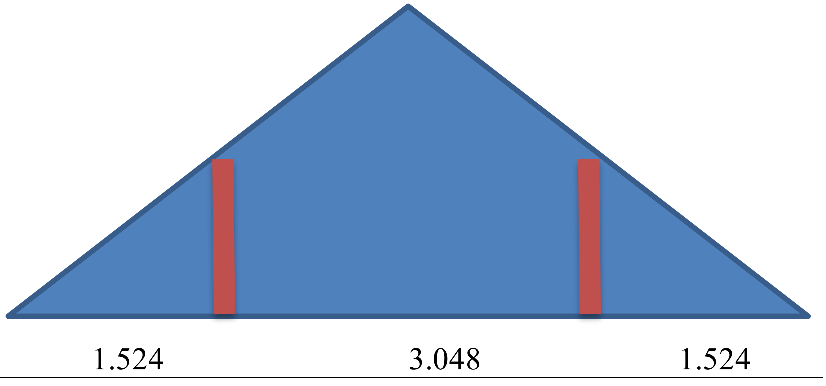

A-3.4 Support Wall Design Checks

Table A-3.6. Sheathing to framing connection check

Failure Mode in nail connection					G (OSB)	0.42
a	917.48	N	H_s (mm)	1000	G (LSL)	0.5
b	3310.77	N	L_s(mm)	8400	d_f (mm)	3.3
d	616.61	N	P_{ij} (kN)	1.2755		
e	1234.72	N	V_{hd} (kN)	41.30		
f	845.65	N	J_{hd}	0.9027	f_1 (MPa)	29.3
g	866.23	N	s	150	f_2 (MPa)	24.175
mode d governs			J_s (for LSL)	0.8	f_3 (MPa)	30.54676
					f_y (MPa)	635
					t_1 (mm)	9.5
n_u (N)	616.61				t_2 (mm)	41.5
N_u (N)	709.11				Nail length (mm)	51
v_d	4.73				Nail spacing, s	150
					ϕ	0.8
Vrs/L_s (N/mm)	4.92				J_d	1.3
Adjusted shear for no hold down situation					J_{us}	0.5
Vrs/L_s (N/mm)	1.78		> V_f/L_s= 0.81			

Table A-3.7. Panel Buckling

$B_{a,0}$ (N/mm)	44000		a	2400
$B_{a,90}$ (N/mm)	33000		b	1000
α	2.2335		Bv (N/mm)	10000
η	0.5249		Ls	8400
K_{pb}	1.2083		t	9.5
			ϕ	0.8
v_{pb} (kN/m)	12.7223			
V_{rs}/L_s (N/mm)	10.18	> V_f/L_s=0.81		

Table A-3.8. Chord Member Check

M	6.771508
h	8400
T_f=M/h (N)	806.132
f_t (LSL) (MPa)	13.7
ϕ	0.9
K_{zt}	1.07
K_D	1.15

K_H	1.04	
K_T	1	
A_n	5320	
F_t (Mpa)	16.3852	
T_r (N)	83944	$> T_f$

Table A-3.9. Support Wall Deflection Check

600 mm segment		2400 mm segment	
v(N/mm)	0.81	v(N/mm)	0.81
H_s (mm)	1000	H_s (mm)	1000
E(Mpa)	8965	E(Mpa)	8965
A(mm^2)	5320	A(mm^2)	5320
L_s (mm)	600	L_s (mm)	2400
B_v(N/mm)	10000	B_v(N/mm)	10000
s (mm)	150	s (mm)	150
d_f(mm)	3.3	d_f(mm)	3.3
e_n	0.0208	e_n	0.0208
P_{ij}(N)	617.28	P_{ij}(N)	617.28
K_m	1	K_m	1
n_u	616.612	n_u	616.612
d_a	0.1046	d_a	0.00991
Δ_{sw} (mm)	0.2973	Δ_{sw}	0.1172
Total (mm)	0.95		

Appendix-4

A-4.1 2D Analysis of Ceiling frame

Table A-4.1. 2D joist analysis of Ceiling frame

Ceiling Frame parameters		Panel Parameters	
Panel height (mm)	3200	x (mm)	2978
ULS Check		y(mm)	1489
Tributary area for a joist (mm)	600	z(mm)	993
Support Wall Self-weight (kN/m)	0.054026444	Joist Span	5956
DL drywall (kPa)	0.5		
I Joist Self Wt. (kN/m)	0.041		
UDL from drywall+ Self (kN/m)	0.42625		
Load from roof panel (kpa)	1.9275		
Load to Support wall (kN/m)	1.1565		
Concentrated Load (P) (kN)	2.58		
Load for UDL (P) (kN/m)	0.341		
P1	0.86		
Reaction R1 (kN)	3.596		
Reaction R2 (kN)	3.956		
V (kN)	3.956	Assumed NI-80 (9-1/2) I-joist manufactured by Nordic Structures	
M (kN-m)	2.978	M_r = 6.765	From the manufacturer's technical report
EI(N-mm^2)	9.300 E+11		
SLS Check (Deflection)			
Support Wall Self-weight (kN/m)	0.054026444		
DL drywall (kPa)	0.5		
Self wt. (kN/m)	0.041		
UDL from drywall (kN/m)	0.3		
Load from roof panel (kPa)	1.535		
Load to Support wall (kN/m)	3.482448944		
Concentrated Load (P) (kN)	2.089469367		
UDL from drywall + Self wt (kN/m)	0.341		
Span, L	5956		
24EI	2.232 E+13		
Pa	3111219.887		
(3l^2-4a^2)	97553324		
Deflection due to Concentrated load	13.59811		
Deflection due to UDL	6.00799	Total deflection Limit=33.1	Live load deflection limit=16.6

Total deflection	19.61	oK
Concentrated Load	1.419419367	
Pa	2113515.437	
Deflection for only snow load	9.24	oK

Table A-4.2. Support Wall location analysis.

Support wall location, y (mm)	No of LSL Joist (44.5 mm × 241 mm)	Roof Panel B Size (mm)	Roof Panel A Size (mm)	Support Wall height (mm)	Deflection (mm)	Note
1050	2	1262	2313	700	24.50	Panel-B dimension less than the minimum width requirement for wall line
1200	2	1442	1778	800.30	29.64	Panel-B dimension less than the minimum width requirement for wall line
1350	4	1623	1957	867	17.47	
1489	4	1790	1790	992	19.95	Span/4 distance
1750	4	2103	1476	1017	24.54	Panel-A dimension less than the minimum width requirement for wall line

Appendix-5

A-5.1 SD screw connection analysis of Apex Connection:

According to the manufacturer's technical data sheet (ICC-ES 2021) SD Connector screw is specifically designed to replace nails and the screw used in this study is equivalent to 10d common nails. Hence, the analytical model of timber connection using nails and spikes in CSA86-19 is applicable for the connection analysis.

The factored lateral strength resistance of a connection with nails or spikes, Nr, shall be greater than or equal to the effect of the factored loads, and shall be calculated using Equation (6) of main text.

The unit lateral resistance of steel to timber screw connection per share plane is the smallest value calculated in accordance with failure mode (a) to (f) of Equation 7 to 12 of main text.

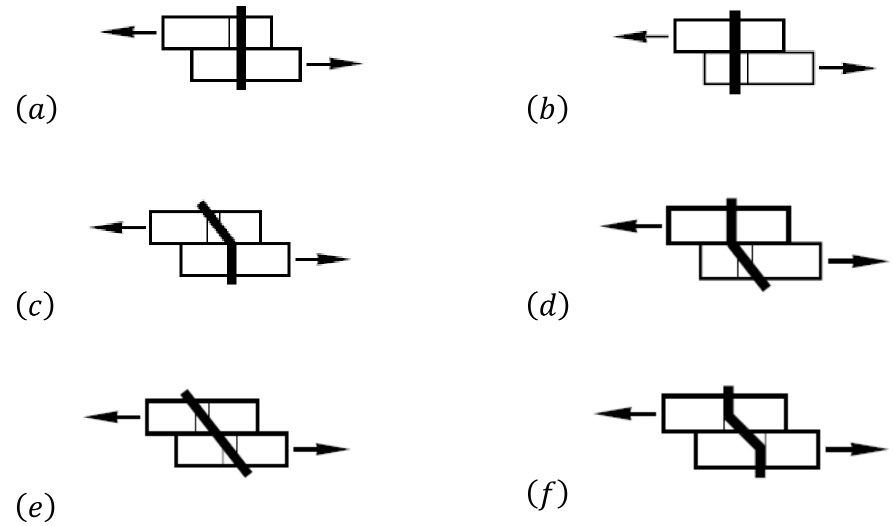
(a) (b) (c) (d) (e) (f)

Figure A-5.1: Different failure modes of the screw connection

Table A1 explains all the parameters values used in the calculating the screw connection capacity and Table A2 presents the results of the connection analysis. As can be observed from Table A2 the failure mode has the lowest connection capacity, so the connection is governed by this failure mode.

Table A-5.1. Input parameters of the connection analysis.

Mean relative density, G (LSL)	0.5
Screw diameter, d_f (mm)	4.5
Factor for light gauge steel, K_{sp}	2.7
Resistance factor for light gauge steel, ϕ_{steel}	0.4
Resistance factor for wood member, ϕ_{wood}	0.8
Ultimate tensile strength of steel fu (MPa)	310
Embedment strength of steel side plate, f_1 (MPa)	418.50
Embedment strength of LSL, f_2 (MPa)	23.88
Embedment strength of main member where failure is screw yielding, f_3 (MPa)	30.17
Screw yield strength, f_y (MPa)	575
Head side member thickness, t_1 (mm)	3.04
Length of screw penetration, t_2 (mm)	35.06
Resistance factor for the lateral resistance of the connection, ϕ	0.8
Number of fasteners, n	7

Table A-5.2. Strength in different failure mode.

Failure mode	Strength
(a)	5725.08 N
(b)	3766.759 N
(c)	2196.59 N
(d)	14,256.92 N
(e)	1898.37 N
(f)	2103.15
Governing failure mode	(e)
Unit lateral strength resistance, n_u	1898.37 N
The factored lateral strength resistance, N_u	10,630.86 N

Video link of Apex connection: https://www.youtube.com/watch?v=VL3aDW-k3Vw&t=5s

Appendix-6

A-6.1 Model prediction bar chart figure with error bar

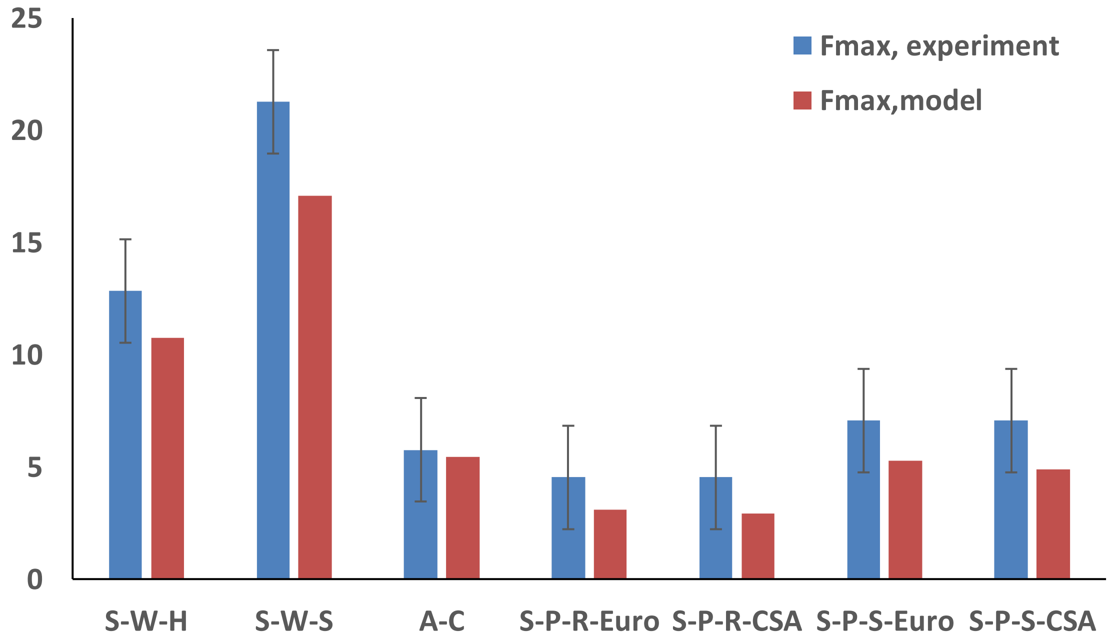

Figure. A-6.1 Model prediction versus test results.

The European model over-predicted for HBS screw shear connection for some samples (see error bar in Fig A-6.1). The sample size of the connection test varied between 3 to 7. Therefore, more elaborate testing is recommended to calibrate the model. The limitation of analytical model validation was the need for more material test data. No embedment test of LSL was performed. Embedment strength depends on the screw diameter and density of the wood. The embedment strength equation used here is primarily developed for wood products, and the LSL density was regarded as the equivalent of Douglas Fir wood species. Consequently, further validation of embedment strength is required before implementing the analytical models. Another limitation was the lack of testing of screw properties. Therefore, future studies should include embedment strength equation development for LSL and experimental evaluation of fastener yield strength in bending.

Appendix-7

Summary of the input properties to the FE models

A-7.1 Input Properties of Roof panel FEM of Chapter 2

The following properties were used for OSB and LSL materials for the roof panel finite element model. The OSB sheathing properties were adopted from Karacabeyli et al. (1996), Zhu (2003), and Shahidul et al. (2017) and LSL wood properties were defined based on the test results of Moses et al. (2003), CCMC (2019), Niederwestberg et al. (2018), and Janowiak et al. (2001) as indicated in the table.

Table A-7.1. Elastic material properties for OSB and LSL

Property	OSB	LSL
E_1 (MPa)	5323[a]	8,965[c]
E_2(MPa)	3231 [a]	996[d]
E_3 (MPa)	130[b]	1,350[e]
G_{12}(MPa)	1,574 [a]	490[f]
G_{13}(MPa)	157.4 [a]	195 [f]
G_{23}(MPa)	157.4 [a]	80 [f]
υ_{12}	0.183 [b]	0.298 [f]
υ_{13}	0.364 [b]	0.500 [f]
υ_{23}	0.312 [b]	0.6 [f]

[a] (Shahidul Islam et al. 2017); [b](Zhu et al. 2005); [c](CCMC 2019); [d](Janowiak et al. 2001); [e](Niederwestberg et al. 2018); [f](Moses 2000); [g](Karacabeyli et al. 1996)

The following load-slip curves were used to define the spring properties of the connectors used in the FEM.

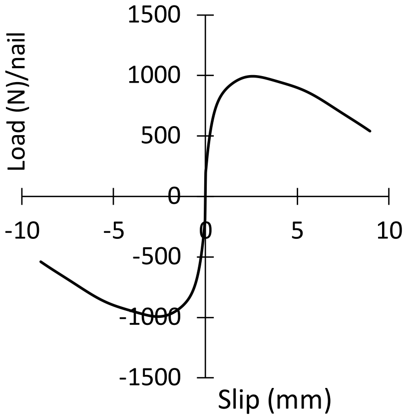

Figure. A-7.1 Load slip curve of OSB-LSL nail connection in shear along the x and y-axis.

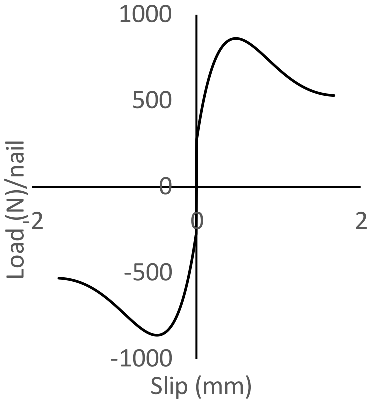

Fig. Load-slip curve LSL-LSL nail in shear along the local x-axis of the connector

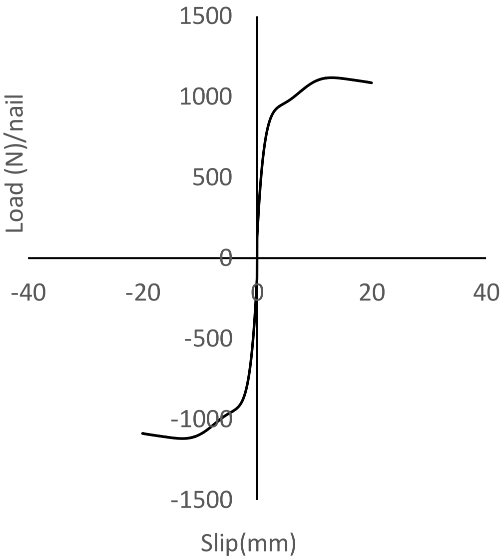

Fig. Load-slip curve LSL-LSL nail in shear along the local y-axis of the connector.

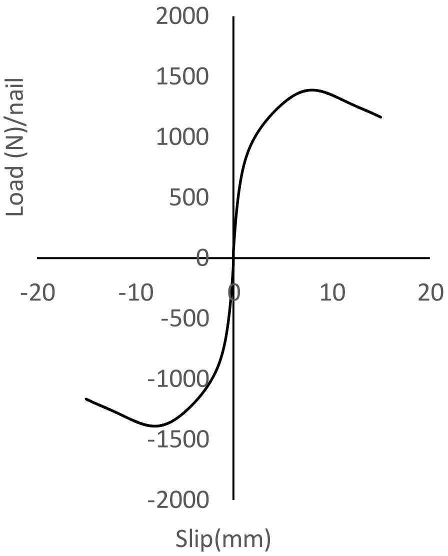

Fig. Load-slip curve LSL-LSL nail in shear along the local z-axis of the connector.

A-7.2 Input Properties of Apex Connection model FEM of Chapter 4

The following properties were used to model the Apex connection using ASIS 1008 steel plates and A36 steel for pins.

Table A-7.2. AISI 1008 steel elastic properties

Modulus of elasticity, E	200000
Poisson’s ratio, σ	0.3

Table A-7.3. AISI 1008 steel plastic properties

Yield Stress	Plastic Strain
186.6609859	0
204.0451529	0.01542624
211.5999235	0.022330613
222.2772679	0.032424094
231.1487709	0.040638474
241.4372872	0.05090961
250.6480852	0.062495817
260.7292832	0.076719587
267.8915929	0.088374905
277.1051126	0.106968547
283.0825606	0.122274322
288.2632225	0.134413693
293.2957278	0.145761175
296.3301478	0.15603879
300.4393484	0.166835733
303.1368195	0.172815091
353.35678	0.295656907

Table A-7.4. A36 steel elastic properties

Modulus of elasticity, E	210000
Poisson’s ratio, σ	0.3

Table A-7.5. A36 steel plastic properties

True Yield Stress	True Plastic Strain
371.6	0
376.5	0.013
586.7	0.205

A-7.3 Input Properties of Assembly model FEM of Chapter 5

Table A-7.6. OSB-LSL properties to calculate equivalent bending thickness using the γ-method.

OSB	7,425 MPa[g]
LSL	8,965 MPa[c]

Table A-7.7. Elastic Properties used in Abaqus for gable Wall FEM

	Modulus of elasticity (MPa)			Poisson's ratio			Shear Modulus (MPa)		
	E_1	E_2	E_3	σ_{12}	σ_{13}	σ_{23}	G_{12}	G_{13}	G_{23}
OSB	5323[a]	3231[a]	130[b]	0.183[b]	0.364[b]	0.312[b]	1574[a]	157.4[a]	157.4[a]
LSL	8965[c]	996[d]	1350[e]	0.298[f]	0.5[f]	0.6[f]	490[f]	195[f]	80[f]

[a] (Shahidul Islam et al. 2017); [b](Zhu et al. 2005); [c](CCMC 2019); [d](Janowiak et al. 2001); [e](Niederwestberg et al. 2018); [f](Moses 2000); [g](Karacabeyli et al. 1996)

Item	Modulus of elasticity (MPa)	Poisson's ratio
S-P-F lumber	8831[i]	0.4
Wood-I-joist	11328.8[h]	0.3
LSL Beam	8965[c]	0.3

[h](CCMC 2018); [i](CWC 1994)

Appendix-8

A-8.1 Details of the iterative analysis of the apex connection

In developing the apex connection, several iterations were performed to obtain the c-section of the main folding bars. From the 3D assembly model analysis, it was observed that the U-slot of the primary folding link bar was subjected to failure due to high deformation and stress distribution near the U-slot. Therefore, the numerical model to simulate a uniaxial tension test on the pin joint in the middle of the primary link bars was used to obtain the proper section of the primary folding link bar. In this model, the pin was modelled as a 3D solid element (C3D8I) to account for the interaction of the pin and the holes of the primary link bar. The PEEQ and the stress status near the primary folding link bars were observed to quantify the connection capacity. It should be noted that steel connection capacity is defined based on certain deformation levels in experimental evaluation (Chung and Ip 2000; Errera et al. 1974; Peng et al. 2020; Puthli and Fleischer 2001; Rogers et al. 1998; Salih et al. 2011; Winter 1956). However, this study adopted a conservative design approach and obtained connection capacity by considering the PEEQ value equal to zero as the capacity benchmark. For the c-section 30 mm×38 mm, the model was loaded up to 15 kN of force, and PEEQ and Von Mises stress in each time step were observed to identify the capacity of this cross-section. As can be observed from Fig. A-8.1 and A-8.2, for time step 0.1875 PEEQ value for all elements is zero, and at time step 0.2375, only six elements have nonzero PEEQ. Observing the nodal PEEQ and von Mises stress output revealed that the average value was 2.18×10^{-05} (this value is very close to zero) and 138 MPa, respectively (see Table A-8.1). The axial force value (3400 N) is between these two-time steps due to factored gravity load of 2.36 kPa. Therefore, it can be concluded that cross-section 30 mm×38 mm can sustain the factored gravity load of 2.36 kPa.

In the 30 mm×50 mm cross-section case, the model was loaded up to 10kN. The PEEQ value for all elements was zero in time-step 0.4875, whereas only four elements in the U-slot have nonzero in time-step 0.5375. Fig A-8.4 shows the elements in U-slot with a nonzero value in time step 0.5375. As seen from Table A-8.2, nodal PEEQ and von Mises stress of the four elements have average values of 3.93×10^{-06} (this PEEQ value is very close to zero) and 130.34 MPa, respectively, in the time step 0.5375. The axial force (5165 N) is between these two-time steps due to factored gravity load 4.0 kPa. Therefore, it can be concluded that the cross-section 30 mm×50 mm can sustain the factored gravity load of 4.0 kPa.

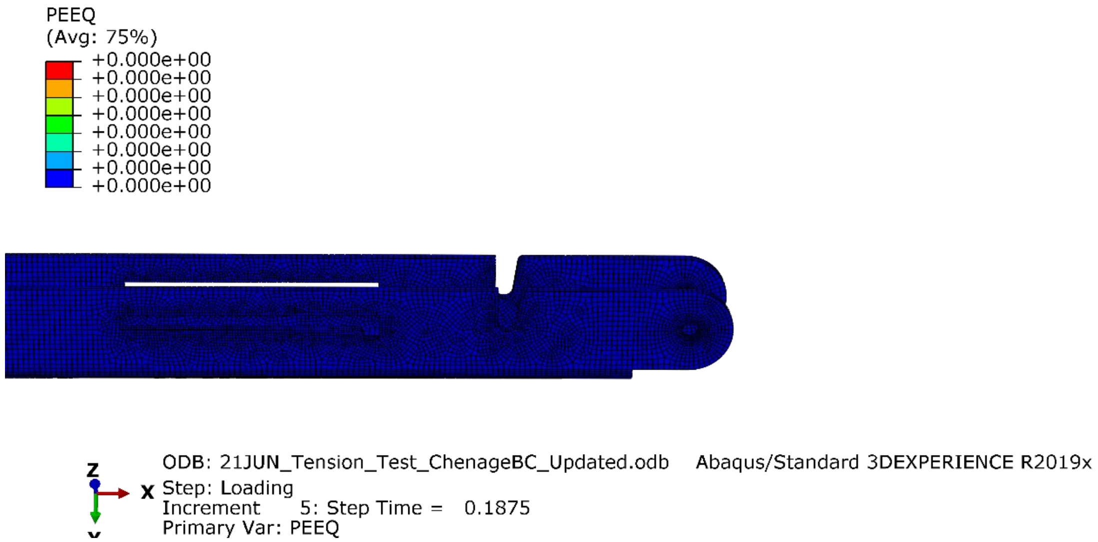

Fig A-8.1. PEEQ output for 30 mm×38 mm section at time step 0.1875 (applied load =2820 N)

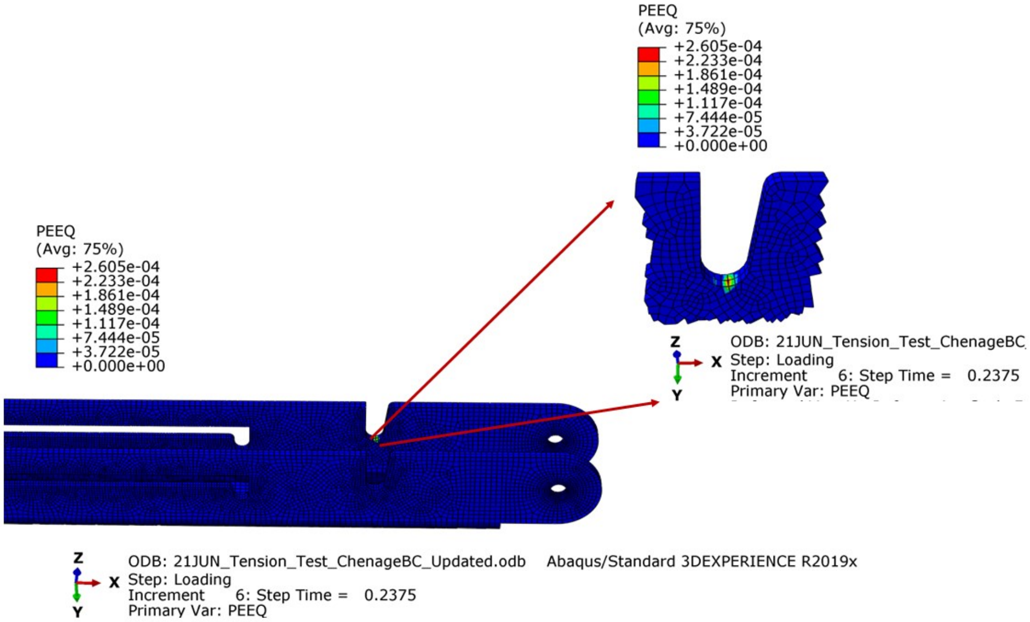

Fig A-8.2. PEEQ output for 30 mm×38 mm section at time step 0.2375 (applied load =3600 N)

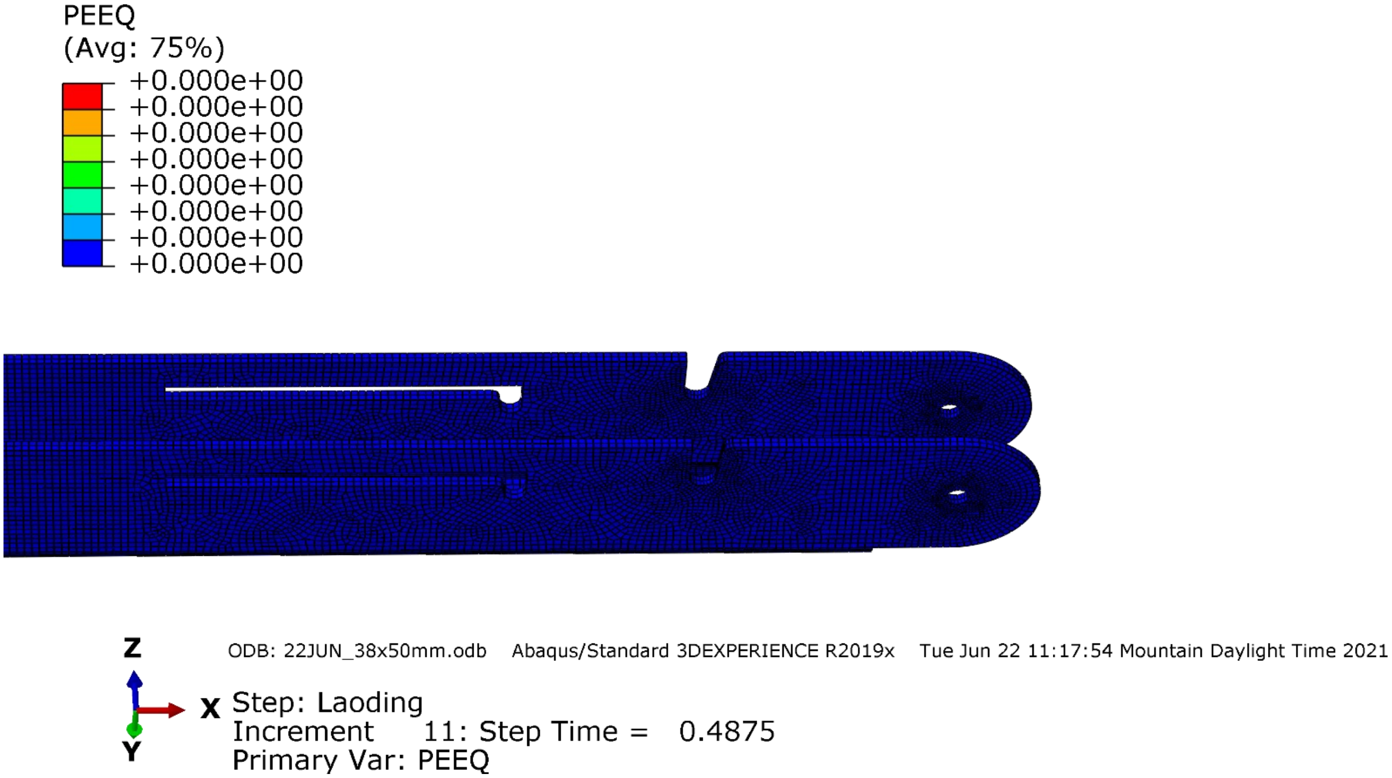

Fig A-8.3. PEEQ output for 30 mm×50 mm section at time step 0.4875 (applied load =4875 N)

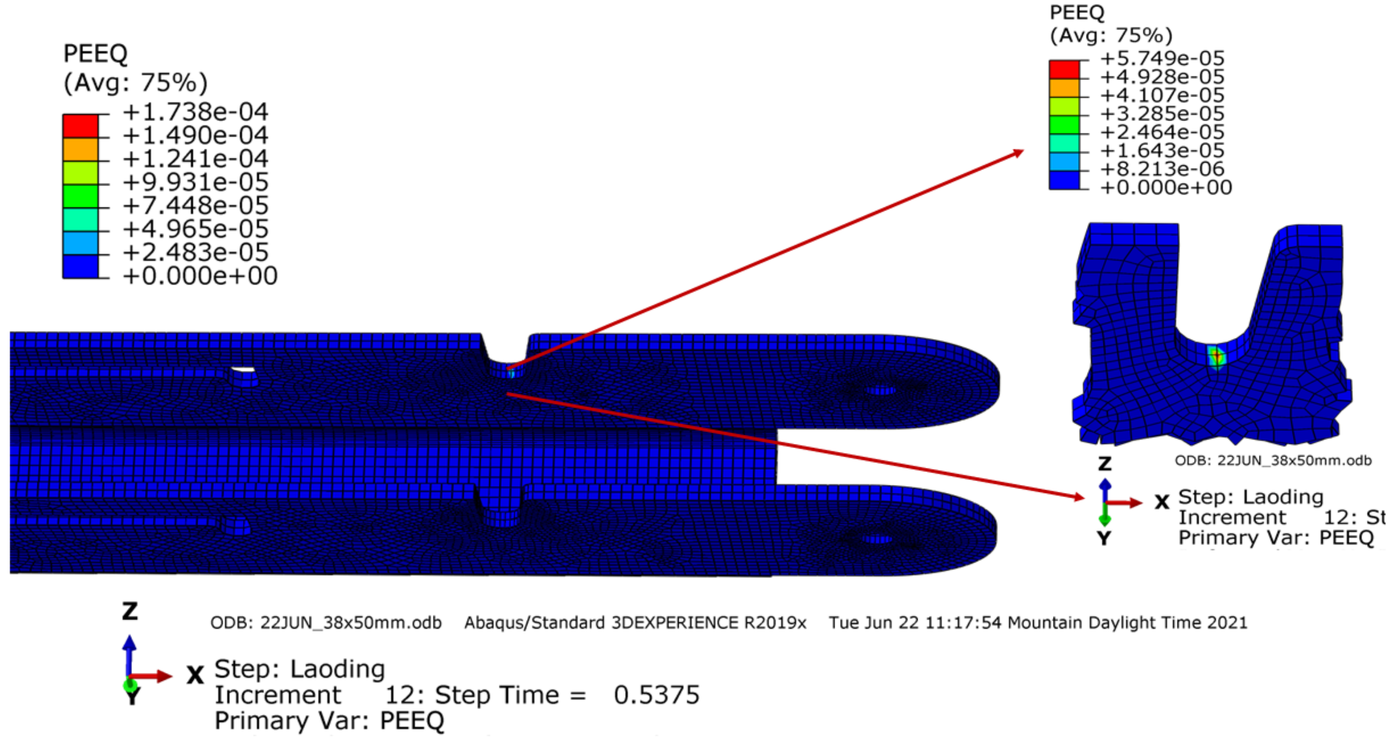

Fig A-8.4. PEEQ output for 30 mm ×50 mm section at time step 0.5375 (applied load =5375 N)

Table A-8.1. Nodal PEEQ and von Mises stress output of the element of concern in time step 0.2375 for 30 mm × 38 mm section.

Node ID	Attached elements	PEEQ	von Mises Stress (MPa)
2400	12841	0	199.686
2400	13729	0	199.686
2401	12841	8.44E-07	167.214
2401	12842	8.44E-07	167.214
2401	13730	8.44E-07	167.214
2402	13284	9.97E-05	206.107
2402	13730	9.97E-05	206.107
2403	12843	1.30E-05	198.04
2403	13284	1.30E-05	198.04
2474	15789	6.09E-05	199.789
2474	16230	6.09E-05	199.789
2475	16230	2.19E-04	198.823
2475	16676	2.19E-04	198.823
2476	15787	0	179.787
2476	15788	0	179.787

Node ID	Attached elements	PEEQ	von Mises Stress (MPa)
2476	16676	0	179.787
2477	15787	4.55E-05	199.725
2477	16675	4.55E-05	199.725
16280	12842	2.80E-06	99.3639
16280	13283	2.80E-06	99.3639
16280	13730	2.80E-06	99.3639
16280	13754	2.80E-06	99.3639
16596	12840	6.33E-07	105.295
16596	12841	6.33E-07	105.295
16596	13729	6.33E-07	105.295
16596	13755	6.33E-07	105.295
16597	12841	0	100.846
16597	12842	0	100.846
16597	13755	0	100.846
16597	14012	0	100.846
16598	13283	0	114.411
16598	13284	0	114.411
16598	13730	0	114.411
16598	13756	0	114.411
18428	12843	0	113.394
18428	12844	0	113.394
18428	13284	0	113.394
18428	13756	0	113.394
18994	15788	4.53E-06	106.543
18994	16229	4.53E-06	106.543
18994	16676	4.53E-06	106.543
18994	16700	4.53E-06	106.543
19310	15786	0	113.964
19310	15787	0	113.964
19310	16675	0	113.964
19310	16701	0	113.964
19311	15787	1.63E-06	106.912
19311	15788	1.63E-06	106.912
19311	16701	1.63E-06	106.912
19311	16958	1.63E-06	106.912
19312	16229	0	127.692
19312	16230	0	127.692
19312	16676	0	127.692
19312	16702	0	127.692
21142	15789	0	122.84
21142	15790	0	122.84

Node ID	Attached elements	PEEQ	von Mises Stress (MPa)
21142	16230	0	122.84
21142	16702	0	122.84
21731	12843	8.36E-05	198.528
21731	13284	8.36E-05	198.528
21731	15789	8.36E-05	198.528
21731	16230	8.36E-05	198.528
21732	13284	2.61E-04	196.576
21732	13730	2.61E-04	196.576
21732	16230	2.61E-04	196.576
21732	16676	2.61E-04	196.576
21733	12841	0	181.239
21733	12842	0	181.239
21733	13730	0	181.239
21733	15787	0	181.239
21733	15788	0	181.239
21733	16676	0	181.239
21734	12841	5.02E-05	199.675
21734	13729	5.02E-05	199.675
21734	15787	5.02E-05	199.675
21734	16675	5.02E-05	199.675
38070	12842	2.33E-06	108.388
38070	13283	2.33E-06	108.388
38070	13730	2.33E-06	108.388
38070	13754	2.33E-06	108.388
38070	15788	2.33E-06	108.388
38070	16229	2.33E-06	108.388
38070	16676	2.33E-06	108.388
38070	16700	2.33E-06	108.388
38386	12840	0	112.813
38386	12841	0	112.813
38386	13729	0	112.813
38386	13755	0	112.813
38386	15786	0	112.813
38386	15787	0	112.813
38386	16675	0	112.813
38386	16701	0	112.813
38387	12841	1.80E-06	106.443
38387	12842	1.80E-06	106.443
38387	13755	1.80E-06	106.443
38387	14012	1.80E-06	106.443
38387	15787	1.80E-06	106.443

Node ID	Attached elements	PEEQ	von Mises Stress (MPa)
38387	15788	1.80E-06	106.443
38387	16701	1.80E-06	106.443
38387	16958	1.80E-06	106.443
38388	13283	0	131.547
38388	13284	0	131.547
38388	13730	0	131.547
38388	13756	0	131.547
38388	16229	0	131.547
38388	16230	0	131.547
38388	16676	0	131.547
38388	16702	0	131.547
40218	12843	0	124.877
40218	12844	0	124.877
40218	13284	0	124.877
40218	13756	0	124.877
40218	15789	0	124.877
40218	15790	0	124.877
40218	16230	0	124.877
40218	16702	0	124.877
Average		2.18E-05	138.1852

Table A-8.2. Nodal PEEQ and von Mises output of the element of concern in time step 0.5375 for the 30 mm×50 mm section.

Node ID	Attached elements	PEEQ	Von Mises Stress (MPa)
2359	14577	0	145.99
2359	14778	0	145.99
2359	14823	0	145.99
2360	14275	2.85E-05	209.13
2360	14823	2.85E-05	209.13
2361	14275	0	165.37
2361	14276	0	165.37
2361	14825	0	165.37
2653	16871	1.18E-06	158.83
2653	16872	1.18E-06	158.83
2653	17421	1.18E-06	158.83
2654	16871	0	208.05
2654	17419	0	208.05

Node ID	Attached elements	PEEQ	Von Mises Stress (MPa)
2655	17173	0	140.03
2655	17374	0	140.03
2655	17419	0	140.03
17406	14275	1.02E-06	103.88
17406	14824	1.02E-06	103.88
17406	14825	1.02E-06	103.88
17406	16316	1.02E-06	103.88
17411	14577	0	101.89
17411	14818	0	101.89
17411	14823	0	101.89
17411	14863	0	101.89
19088	14275	0	108.04
19088	14823	0	108.04
19088	14824	0	108.04
19088	14863	0	108.04
19815	16871	0	99.67
19815	17420	0	99.67
19815	17421	0	99.67
19815	18912	0	99.67
19820	17173	0	97.81
19820	17414	0	97.81
19820	17419	0	97.81
19820	17459	0	97.81
21497	16871	8.85E-07	102.04
21497	17419	8.85E-07	102.04
21497	17420	8.85E-07	102.04
21497	17459	8.85E-07	102.04
22034	14275	0	171.80
22034	14276	0	171.80
22034	14825	0	171.80
22034	16871	0	171.80
22034	16872	0	171.80
22034	17421	0	171.80
22035	14275	5.75E-05	208.83
22035	14823	5.75E-05	208.83
22035	16871	5.75E-05	208.83
22035	17419	5.75E-05	208.83
22036	14577	0	147.59
22036	14778	0	147.59
22036	14823	0	147.59
22036	17173	0	147.59

Node ID	Attached elements	PEEQ	Von Mises Stress (MPa)
22036	17374	0	147.59
22036	17419	0	147.59
40654	14275	2.06E-06	105.99
40654	14824	2.06E-06	105.99
40654	14825	2.06E-06	105.99
40654	16316	2.06E-06	105.99
40654	16871	2.06E-06	105.99
40654	17420	2.06E-06	105.99
40654	17421	2.06E-06	105.99
40654	18912	2.06E-06	105.99
40659	14577	0	102.76
40659	14818	0	102.76
40659	14823	0	102.76
40659	14863	0	102.76
40659	17173	0	102.76
40659	17414	0	102.76
40659	17419	0	102.76
40659	17459	0	102.76
42336	14275	0	110.87
42336	14823	0	110.87
42336	14824	0	110.87
42336	14863	0	110.87
42336	16871	0	110.87
42336	17419	0	110.87
42336	17420	0	110.87
42336	17459	0	110.87
Average		3.93207E-06	130.34

The studies on steel connection show that connection capacity is defined based on certain deformation levels in experimental investigation (Chung and Ip 2000; Errera et al. 1974; Puthli and Fleischer 2001; Rogers et al. 1998; Salih et al. 2011; Winter 1956) . In lieu of any experimental benchmark, by observing the PEEQ, a conservative judgment was made to find out the sections for apex connection assembly. Therefore, a further experimental investigation is recommended for future study.